HELLENIC REPUBLIC
UNIVERSITY OF IOANNINA
SCHOOL OF ENGINEERING
DEPARTMENT OF MATERIALS SCIENCE AND ENGINEERING

Towards the development of novel self-sensing and self-healing methodologies in polymer matrix composites

DIMITRIOS G. BEKAS
MATERIALS ENGINEER

Thesis for the degree of Doctor of Philosophy

IOANNINA, 2017
GREECE

ΕΛΛΗΝΙΚΗ ΔΗΜΟΚΡΑΤΙΑ
ΠΑΝΕΠΙΣΤΗΜΙΟ ΙΩΑΝΝΙΝΩΝ
ΠΟΛΥΤΕΧΝΙΚΗ ΣΧΟΛΗ
ΤΜΗΜΑ ΜΗΧΑΝΙΚΩΝ ΕΠΙΣΤΗΜΗΣ ΥΛΙΚΩΝ

Ανάπτυξη καινοτόμων μεθόδων αυτό-διάγνωσης και αυτό-ίασης της υποβάθμισης σε σύνθετα υλικά πολυμερικής μήτρας

ΔΗΜΗΤΡΙΟΣ Γ. ΜΠΕΚΑΣ
ΜΗΧΑΝΙΚΟΣ ΕΠΙΣΤΗΜΗΣ ΥΛΙΚΩΝ

ΔΙΔΑΚΤΟΡΙΚΗ ΔΙΑΤΡΙΒΗ

ΙΩΑΝΝΙΝΑ 2017
ΕΛΛΑΔΑ

HELLENIC REPUBLIC
UNIVERSITY OF IOANNINA
SCHOOL OF ENGINEERING
DEPARTMENT OF MATERIALS SCIENCE AND ENGINEERING

Towards the development of novel self-sensing and self-healing methodologies in polymer matrix composites

DIMITRIOS G. BEKAS
MATERIALS ENGINEER

Thesis for the degree of Doctor of Philosophy

IOANNINA, 2017
GREECE

«Η έγκριση της διδακτορικής διατριβής από το Τμήμα Μηχανικών Επιστήμης Υλικών της Πολυτεχνικής Σχολής του Πανεπιστημίου Ιωαννίνων δεν υποδηλώνει αποδοχή των γνωμών του συγγραφέα Ν. 5343/32, άρθρο 202, παράγραφος 2».

Application date of Mr. Dimitrios Bekas: 18.09.2012

Appointment date for the three-membered advisory committee: 28.09.2012 & 16.01.2014
Members of the three-membered advisory committee:

Supervisor
Alkiviadis S. Paipetis, Professor at the Dept. of Materials Science and Engineering, School of Engineering, University of Ioannina
Members
Theodore Matikas, Professor at the Dept. of Materials Science and Engineering, School of Engineering, University of Ioannina

Evaggelia Kontou-Drouga, Professor at the School of Applied Mathematical & Physical Sciences, National Technical University of Athens

Subject appointment date: 28.09.2012

"Novel strategies towards triggering and monitoring the self-healing process in composite materials"

Date of subject change: 10.05.2017

"Towards the development of novel self-sensing and self-healing methodologies in polymer matrix composites"

APPOINTMENT DATE FOR THE SEVEN-MEMBERED ADVISORY COMMITTEE: 18.07.2017

1. **Alkiviadis S. Paipetis**, Professor at the Dept. of Materials Science and Engineering, School of Engineering, University of Ioannina,
2. **Theodore Matikas**, Professor at the Dept. of Materials Science and Engineering, School of Engineering, University of Ioannina,
3. **Evaggelia Kontou-Drouga**, Professor at the School of Applied Mathematical & Physical Sciences, National Technical University of Athens,
4. **Apostolos Avegopoulos**, Professor at the Dept. of Materials Science and Engineering, School of Engineering, University of Ioannina,
5. **Konstantinos Beltsios**, Professor at the Dept. of Materials Science and Engineering, School of Engineering, University of Ioannina,
6. **Nektaria-Marianthi Barkoula**, Associate Professor at the Dept. of Materials Science and Engineering, School of Engineering, University of Ioannina,
7. **Leonidas Gergidis**, Assistant Professor the Dept. of Materials Science and Engineering, School of Engineering, University of Ioannina.

The Ph.D. thesis was awarded with grade "EXCELENT" at **28.09.2017**

The Head of the Department **The Secretary of the Department**

Alkiviadis Paipetis **Maria Kontou**

Ημερομηνία αίτησης του κ. Δημητρίου Μπέκα: 18.09.2012

Ημερομηνία ορισμού Τριμελούς Συμβουλευτικής Επιτροπής: **28.09.2012 & 16.01.2014**

Μέλη Τριμελούς Συμβουλευτικής Επιτροπής:

Επιβλέπων

Αλκιβιάδης Παϊπέτης Καθηγητής του Τ.Μ.Ε.Υ. της Πολυτεχνικής Σχολής του Πανεπιστημίου Ιωαννίνων

Μέλη

Θεόδωρος Ματίκας Καθηγητής του Τ.Μ.Ε.Υ. της Πολυτεχνικής Σχολής του Πανεπιστημίου Ιωαννίνων,

Ευαγγελία Κοντού-Δρούγκα, Καθηγήτρια της Σ.Ε.Μ.Φ.Ε. του Ε.Μ.Π.

Ημερομηνία ορισμού θέματος: **28.09.2012**

"Ενεργοποίηση και παρακολούθηση της αυτό-ίασης σε σύνθετα υλικά με προηγμένες μεθόδους".

Ημερομηνία τροποποίησης θέματος: **10.05.2017**

"Ανάπτυξη καινοτόμων μεθόδων αυτο-διάγνωσης και αυτό-ίασης της υποβάθμισης σε σύνθετα υλικά πολυμερικής μήτρας".

ΔΙΟΡΙΣΜΟΣ ΕΠΤΑΜΕΛΟΥΣ ΕΞΕΤΑΣΤΙΚΗΣ ΕΠΙΤΡΟΠΗΣ: 18.07.2017

1. **Αλκιβιάδης Παϊπέτης** Καθηγητής του Τ.Μ.Ε.Υ. της Πολυτεχνικής Σχολής του Πανεπιστημίου Ιωαννίνων,
2. **Θεόδωρος Ματίκας** Καθηγητής του Τ.Μ.Ε.Υ. της Πολυτεχνικής Σχολής του Πανεπιστημίου Ιωαννίνων,
3. **Ευαγγελία Κοντού-Δρούγκα,** Καθηγήτρια της Σ.Ε.Μ.Φ.Ε. του Ε.Μ.Π.,
4. **Απόστολος Αυγερόπουλος,** Καθηγητής του Τ.Μ.Ε.Υ. της Πολυτεχνικής Σχολής του Πανεπιστημίου Ιωαννίνων,
5. **Κων/νος Μπέλτσιος,** Καθηγητής του Τ.Μ.Ε.Υ. της Πολυτεχνικής Σχολής του Πανεπιστημίου Ιωαννίνων,
6. **Νεκταρία-Μαριάνθη Μπάρκουλα,** Αναπλ. Καθηγήτρια του Τ.Μ.Ε.Υ. της Πολυτεχνικής Σχολής του Πανεπιστημίου Ιωαννίνων,
7. **Λεωνίδας Γεργίδης**, Επίκουρος Καθηγητής του Τ.Μ.Ε.Υ. της Πολυτεχνικής Σχολής του Πανεπιστημίου Ιωαννίνων.

Έγκριση Διδακτορικής Διατριβής με βαθμό **«ΑΡΙΣΤΑ»** στις **28.09.2017**

Ο Πρόεδρος του Τμήματος	**Η Γραμματέας του Τμήματος**
Αλκιβιάδης Παϊπέτης **Καθηγητής**	**Μαρία Κόντου**

Στους γονείς μου Γιώργο και Βούλα
και στον αδερφό μου Εύδοξο

Abstract

Fibre reinforced polymer (FRP) composites are becoming excellent candidates to address significant weight reductions in several industrial sectors such as the aerospace, automotive, naval and renewable energy. The Achilles' heel of advanced FRP composites centers around the poor interlaminar fracture toughness that may lead to undetected damage within the microstructure deteriorating the mechanical performance.

The purpose of the present work unfolds in two axes, (i) to develop a novel Non-Destructive Evaluation technique based on Impedance Spectroscopy for the damage assessment of nanomodified FRP composites. This study aims to providing an insight in the damage mechanisms that occur in FRPs during their active lifetime under different loading scenarios (mechanical or environmental loading), (ii) to develop and employ three “tailor-on-demand” self-healing strategies to counterbalance the aforementioned damage mechanisms and restore specific functionalities in the composite. The healing performance of all the adopted self-healing concepts showed remarkable results both at polymer and composite level.

Acknowledgments

During my Ph.D. research, I had the opportunity to collaborate with several remarkable people who significantly contributed to the realization of this research and I would like to dedicate the following paragraphs to acknowledge them.

First and foremost, I would like to express my special appreciation and thanks to my advisor, Alkiviadis Paipetis, Professor at the Dept. of Materials Science and Engineering (MSE) who kept me focused throughout my graduate career and was patient through all of the rookie mistakes I made as a graduate student. I appreciate the scientific discussions as well as the opportunities he has opened up for me. His advice on both research as well as on my career have been priceless and without his support it would not be possible to conduct this research.

I want to express my gratitude to Theodore Matikas, Professor at the Dept. of MSE for his participation as a member of the advisory committee. In addition, I would like to thank him for giving me access to the mechanical testing equipment and the optical microscope.

I wish also to thank Evagelia Kontou, Professor at the Dept. of Theoretical and Applied Mechanics, of the National Technical University of Athens for her participation on my advisory committee.

At this point I want to express my sincere gratitude to Nektaria-Marianthi Barkoula, Associate Professor at the Dept. of MSE, for her scientific advices and for our many insightful discussions. Her contribution to my research career was more than precious.

Furthermore, I would like to thank Konstantinos Beltsios, Professor at the at the Dept. of MSE, for introducing me to composite materials during my undergraduate studies and for honoring me with his participation to my committee. My sincere thanks also goes to Apostolos Avgeropoulos, Professor at the Dept. of MSE, for his guidance and scientific advice regarding the reversible polymers. His suggestions and comments were crucial and expanded my knowledge on polymeric materials. I would like to deeply thank Leonidas Gergidis, Assistant professor at the Dept. of MSE, for honoring me with his presence as a member of my committee. I want also to thank Tiverios Vaimakis, Professor at the Dept. of Chemistry for his assistance on the Differential Scanning Calorimetry experiments. Lastly, I would like to thank Alexandros Karantzalis, Assistant Professor at the Dept. of MSE for his assistant on Scanning Electron Microscopy.

I have to express my thanks to my two companions in this journey, Kyriaki Tsirka and Dimitrios Baltzis, Ph.D. candidates at the Dept. of MSE for their friendship, full support, collaboration and of course their patience. It was a great pleasure and a privilege working with them in a daily basis.

I want to express my sincere gratitude to my *senpai*, Dr. Sotirios Grammatikos, of for his precious friendship, guidance and collaboration. Our stimulating discussions cautiously encouraged me to explore new things. His advices were more that precious. Along with Sotirios I gratefully thank my second *senpai*, Dr. Georgios Gkikas for his precious friendship and for the opportunities he gave me during my research. It was a privilege working with him.

I also owe my special thanks to my friend and colleague Dimitrios Exarchos, Ph.D. candidate at the Dept. of MSE, for his excellent collaboration and his precious assistance regarding the Infrared thermography method. I want also to thank Ilias Tragazikis, Theodoti Kordatou, Panagiota Alafogianni and Panagiota Dalla, Ph.D. candidates at the Dept. of MSE for their friendship and their collaboration. In addition, I am also grateful to Dr. Dimitrios Moschovas, post-doctoral researcher at the Dept. of MSE, for his assistance on Size exclusion chromatography.

At this point I want to thank all of my friends and colleges at the Composite and Smart Materials Laboratory (CSML): Vasilios Spais, Katerina Garavela, Dimitrios Vaimakis, Christos Saganas, Maria Vlacha, Maria Kosarli, Antigoni Katsiki, Giorgos Fotinidis, Panagiota Tsilimiga, Katerina Giovanaki, Christina Kouimtzi, Maria Karadimou, Apostolos Parlamas, Theodoros Tosounidis, Michaela Konstantinidou, Katerina Vlachaki, Christos Drougas, Mariliza Kouli, Kiriakos Magdalis, Danai Douka and Giorgos Tzachristas for their support and collaboration.

In addition, I want to express my gratitude to my dearest friends for their understanding and their support during my studies: Giorgos Kosmopoulos, Vasilios Pantos, Anastasios Tsipas, Dimitrios Iliopoulos, Nikos Vlachopoulos, Kostas Tzaralis and Giwrgos Thodis. I also like to thank a special girl, Maria Antoniou, for her support, especially during the writing stage of this thesis.

Last but not least, I want to deeply thank my father Giorgos, my mother Voula and my brother Evdoxos for providing me with everything I needed, for giving me strength and

courage to carry on with my personal goals and for making me believe in myself. I wouldn't be here without their help.

The current Ph.D. thesis was funded by a European 'HIPOCRATES' (FP7 2013-2016) and the Greek 'THALES' (ΕΣΠΑ 2007-2013) research projects:

I. Project acronym: HIPOCRATES
   Project full title: "Self-Healing Polymer for Concepts on self-Repaired Aeronautical composites"
   Grant Agreement Number: ACP3-GA-2013-605412

SEVENTH FRAMEWORK PROGRAMME

HIPOCRATES PROJECT · EU

II. Project full title: «Ανάπτυξη σύνθετου υλικού και συναφών τεχνικών εφαρμογής και παρακολούθησης δομικής ακεραιότητας για αεροπορικές εφαρμογές και διερεύνηση δυνατότητας αυτοΐασης»
    Grant Agreement Number: 68/1134

Ευρωπαϊκή Ένωση
Ευρωπαϊκό Κοινωνικό Ταμείο

ΕΠΙΧΕΙΡΗΣΙΑΚΟ ΠΡΟΓΡΑΜΜΑ
ΕΚΠΑΙΔΕΥΣΗ ΚΑΙ ΔΙΑ ΒΙΟΥ ΜΑΘΗΣΗ
επένδυση στην κοινωνία της γνώσης
ΥΠΟΥΡΓΕΙΟ ΠΑΙΔΕΙΑΣ & ΘΡΗΣΚΕΥΜΑΤΩΝ, ΠΟΛΙΤΙΣΜΟΥ & ΑΘΛΗΤΙΣΜΟΥ
ΕΙΔΙΚΗ ΥΠΗΡΕΣΙΑ ΔΙΑΧΕΙΡΙΣΗΣ
Με τη συγχρηματοδότηση της Ελλάδας και της Ευρωπαϊκής Ένωσης

ΕΣΠΑ
2007-2013
πρόγραμμα για την ανάπτυξη
ΕΥΡΩΠΑΪΚΟ ΚΟΙΝΩΝΙΚΟ ΤΑΜΕΙΟ

TABLE OF CONTENTS

List of Figures

CHAPTER 1

Introduction

1.1. Overview

Due to their excellent mass-specific mechanical properties as well as their “tailor-to-order” strength and stiffness, fiber reinforced polymer (FRP) composites are widely used in several industrial sectors such as the automotive, aerospace, naval and renewable energy. There is, however, an important drawback when FRPs are subjected to mechanical loading which concerns the susceptibility of these materials to micro-cracking or delamination that may be created deep within the microstructure, due to their poor through-thickness strength and toughness.

Nondestructive evaluation (NDE) is a vital tool for damage detection and prevention of high value or critical polymer matrix composite (PMC) structures. NDE assesses the state of structural health and, through appropriate data processing and interpretation, predicts the remaining life of a structure. Among NDE techniques, the ones that relate electrical properties to the mechanical response and/or the durability of the structure are of great interest due to the sensitivity of the electrical properties to internal degradation. Full exploitation of the aforementioned NDE concepts, necessitates an in depth understanding of the principles that govern coupled property interaction between electrical and mechanical properties in the case of PMCs reinforced with a conductive phase such as carbon nanotubes (CNTs) [1–3].

As aforementioned, electrical properties act as a potential indicator for the evaluation of the structural integrity of the composite. Numerous researchers have attempted a direct correlation between the inherent structural integrity and the variation of electrical properties. Whilst reversible changes in the electrical properties relate solely to strain, irreversible electrical resistance change relates to internal damage of the composite material [4–7].

The initial aim of the current thesis is unfolding in Chapter 2 and is concerned with the development of novel strategies towards the on-line monitoring of the structural integrity of nanomodified fibre reinforced composites using impedance spectroscopy (IS). This step was essential in order to gain insight on the damage mechanisms that initiate and propagate within a composite material during its operating lifetime. For that purpose, carbon nanotube (CNT)-modified epoxy resins and their hybrid composites subjected to different levels damage via hygrothermal exposure and mechanical step loading respectively. The IS measurements were performed using a simple two-electrode method with no specialized modifications. The Electrode polarization (EP) effect which normally impedes impedance measurements for dielectric materials have been addressed via the incorporation of the conductive nanophase which tailors conductivity to the desired levels. The presence of CNTs shifted the electrical response of the material to AC towards higher frequencies resulting in a higher signal-to-noise ratio. The AC frequency response of the composites revealed a direct correlation between the level of damage as verified by optical microscopy and the hysteretic behaviour of the studied materials. Induced damage has been successfully modeled using a simple RC circuit in parallel providing an insight of the internal state of the material.

Apart from the conventional damage tolerant design philosophies, the self-healing concept has attracted great interest in the research community over the last decade [8–10]. Inspired by living organisms, self-healing composites possess the remarkable ability to detect and heal damage and, as a result, to restore their initial performance (fully or partially). Figure 1.1 depicts the autonomous functionalities of an ideal synthetic material that is capable of maintaining and recover its initial performance throughout its functional life.

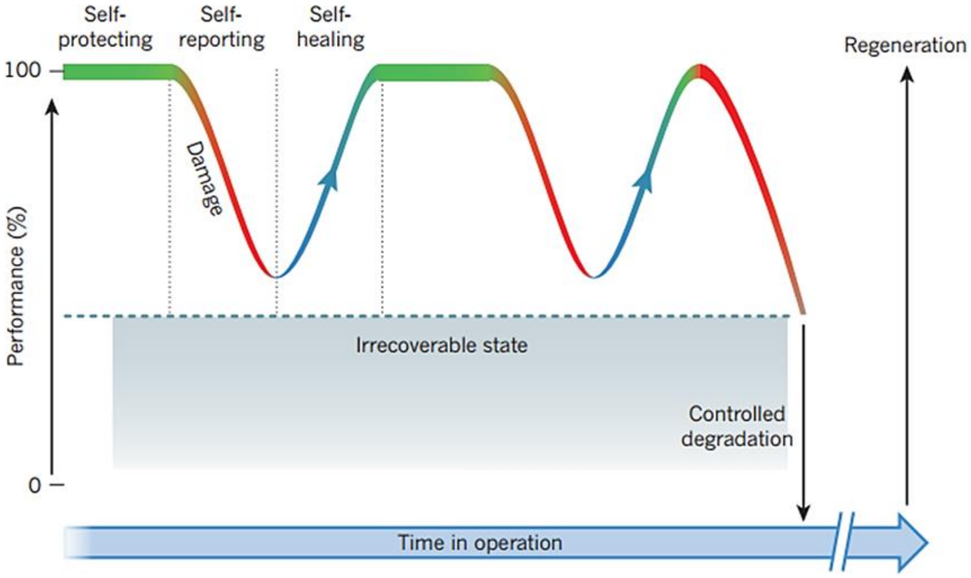

Figure 1.1 The life cycle of polymers with autonomous healing functions.

Self-protection refers to the protection of a material against damaging factors in hostile environments, i.e. mechanical or electrical load, chemical corrosion etc.; self-reporting functionality ensures the promptly detection of performance loss and finally autonomous self-healing is responsible of recovering the performance and thereby increase the materials lifetime [11]. Based on the adopted approach and employed chemistry of self-healing polymers/ polymer composites, these materials can be divided into two classes: (i) autonomous and (ii) non-autonomous self-healing materials. As their name indicates, the autonomous self-healing materials, are capable of regaining specific functionalities without external intervention e.g. heating. On the other hand, non-autonomous self-healing materials need external intervention.

Self-healing composites or materials in general, can be categorized into three conceptual approaches, the intrinsic, the vascular and the capsule-based. The intrinsic self-healing approach exploits the inherent ability of a composite to restore its initial properties, at the molecular level, through physical or chemical reversible bonding, theoretically for an infinite number of repetitions [12–16]. The capsule-based concept is an extrinsic self-healing mechanism that involves the embedment of capsules, which contain an active liquid i.e. the healing agent, within the host material. When the composite is damaged, the capsules are ruptured, releasing the liquid agent at the damage site thus repairing the material [17–19]. An alternative route towards developing self-repairing composites is by mimicking the blood vessels of living organisms. This approach, involves the fabrication of a vascular network composed of micro-channels or hollow fibers whereby the healing agent is manually or automatically introduced into the host matrix [20,21]. Upon damage of the vascular network in the presence of crack propagation phenomena, healing is performed as the healing agent is delivered to the damaged area. In the case where the healing agent is injected in the vascules via an external intervention, this approach deviates from a per se self-healing process.

In Chapters 3,4 and 5 efforts to expand our knowledge on these three self-healing approaches have been made by introducing beyond-the-state-of-the-art methodologies for the development, characterization and incorporation of the self-healing scenarios to the composite materials. In these chapters, a brief introduction on theoretical considerations and recent advances on self-healing composites will be presented.

In more detail, Chapter 3 is concerned with the nano-reinforcement of an epoxy healing agent for vascular self-repairing fiber reinforced composites. Multi Wall Carbon Nanotubes (MWCNTs) have been selected, as the nanoscaled reinforcing phase of a low-viscosity epoxy healing agent, in three different weight contents. The rheological behavior of the nanomodified epoxies was evaluated via apparent dynamic viscosity measurements and adjusted accordingly. The resulted nanocomposites were infused via a vascular network, to Double Cantilever Beam (DCB) fractured Glass Fiber Reinforced Composites (GFRPs) specimens in order to assess the effect of the MWCNTs on the healing efficiency (η), in terms of maximum bearing load and interlaminar fracture toughness (G_{Ic}) recovery. The employment of the nano-enhanced healing agent increased the calculated healing efficiency (n_{GIc}) up to circa 190%, through the introduction of additional energy consumption mechanisms that were confirmed via a comparative Scanning Electron Microscopy (SEM) study.

The work presented in Chapter 4 is unfolding into two main axes: (i) the synthesis and characterization of poly(urea–formaldehyde) (UF) microcapsules and (ii) the incorporation of the produced microcapsules within a polymeric material to access the healing efficiency of the system using several testing protocols and configurations. The characterization of the UF capsules was achieved using Thermogravimetric Analysis (TGA), Differential Scanning Calorimetry (DSC), Scanning Electron Microscopy (SEM) and Raman spectroscopy, while capsule-based self-healing systems have been tested at polymer and composite levels. Obtained results indicated that capsules proved thermally stable at elevated temperature while the rough external wall material enhanced the interlocking between the capsules and the host matrix. At matrix level, the capsule-based self-healing polymer was able to restore its initial fracture toughness at 72% while in the case of GFRP specimens, the healing efficiency was almost the same reaching at 77.84%. The modification of a polymeric adhesive using UF microcapsules has been proved as a reliable route towards up-scaling the employment of capsule-based self-healing methodologies to more complicated composite structures.

Chapter 5 is concerned with the synthesis and characterization of three reversible epoxy resins. The reversible cross-link network realized using three bis-maleimide oligomers with different molecular masses. The produced healing systems, were characterized using DSC and Raman spectroscopy while the healing performance of the three systems was assessed via 2 different testing configurations. The obtained results, indicated a remarkable healing efficiency when the reversible polymers employed as adhesives at a lap strap geometry. A satisfying healing performance in terms of fracture toughness was also recorded in the case where the investigated systems were employed as interlayers in Glass Fiber Reinforced Composite coupons.

The concluding remarks of this study along with future suggestions and recommendations related to the field of the study are reported in the final part, Chapter 6.

References

[1] V. Kostopoulos, A. Vavouliotis, P. Karapappas, P. Tsotra, A. Paipetis, Damage Monitoring of Carbon Fiber Reinforced Laminates Using Resistance Measurements. Improving Sensitivity Using Carbon Nanotube Doped Epoxy Matrix System, J. Intell. Mater. Syst. Struct. 20 (2009) 1025–1034. doi:10.1177/1045389X08099993.

[2] A. Vavouliotis, A. Paipetis, V. Kostopoulos, On the fatigue life prediction of CFRP laminates using the Electrical Resistance Change method, Compos. Sci. Technol. 71 (2011) 630–642. doi:10.1016/j.compscitech.2011.01.003.

[3] D. Bekas, S. a Grammatikos, C. Kouimtzi, a S. Paipetis, Linear and non-linear electrical dependency of carbon nanotube reinforced composites to internal damage, IOP Conf. Ser. Mater. Sci. Eng. 74 (2015) 12002. doi:10.1088/1757-899X/74/1/012002.

[4] M. Nofar, S. V. Hoa, M.D. Pugh, Failure detection and monitoring in polymer matrix composites subjected to static and dynamic loads using carbon nanotube networks, Compos. Sci. Technol. 69 (2009) 1599–1606. doi:10.1016/j.compscitech.2009.03.010.

[5] Y. Shindo, Y. Kuronuma, T. Takeda, F. Narita, S.Y. Fu, Electrical resistance change and crack behavior in carbon nanotube/polymer composites under tensile loading, Compos. Part B Eng. 43 (2012) 39–43. doi:10.1016/j.compositesb.2011.04.028.

[6] M. Park, H. Kim, J.P. Youngblood, Strain-dependent electrical resistance of multi-walled carbon nanotube/polymer composite films, Nanotechnology. 19 (2008) 55705. doi:10.1088/0957-4484/19/05/055705.

[7] Y. Song, A. Hehr, V. Shanov, N. Alvarez, N. Kienzle, J. Cummins, D. Koester, M. Schulz, Carbon nanotube sensor thread for distributed strain and damage monitoring on IM7/977-3 composites, Smart Mater. Struct. 23 (2014) 75008. doi:10.1088/0964-1726/23/7/075008.

[8] Y. Wang, D.T. Pham, C. Ji, E. Harkin-Jones, Self-healing composites: A review, Cogent Eng. 2 (2015) 1075686. doi:10.1080/23311916.2015.1075686.

[9] B.J. Blaiszik, S.L.B. Kramer, S.C. Olugebefola, J.S. Moore, N.R. Sottos, S.R.

White, Self-Healing Polymers and Composites, (2010). doi:10.1146/annurev-matsci-070909-104532.

[10] D.G. Bekas, K. Tsirka, D. Baltzis, A.S. Paipetis, Self-healing materials: A review of advances in materials, evaluation, characterization and monitoring techniques, Compos. Part B Eng. 87 (2016) 92–119. doi:10.1016/j.compositesb.2015.09.057.

[11] J.F. Patrick, M.J. Robb, N.R. Sottos, J.S. Moore, S.R. White, Polymers with autonomous life-cycle control, Nature. 540 (2016) 363–370. doi:10.1038/nature21002.

[12] V. Kostopoulos, A. Kotrotsos, S. Tsantzalis, P. Tsokanas, T. Loutas, A.W. Bosman, Toughening and healing of continuous fibre reinforced composites by supramolecular polymers, Compos. Sci. Technol. 128 (2016) 84–93. doi:10.1016/j.compscitech.2016.03.021.

[13] V. Kostopoulos, A. Kotrotsos, S. Tsantzalis, P. Tsokanas, A.C. Christopoulos, T. Loutas, Toughening and healing of continuous fibre reinforced composites with bis-maleimide based pre-pregs, Smart Mater. Struct. 25 (2016). doi:10.1016/j.compscitech.2016.03.021.

[14] T.S. Coope, D.H. Turkenburg, H.R. Fischer, R. Luterbacher, H. van Bracht, I.P. Bond, Novel Diels-Alder based self-healing epoxies for aerospace composites, Smart Mater. Struct. 25 (2016) 84010. doi:10.1088/0964-1726/25/8/084010.

[15] W. Zhang, J. Duchet, J.F. Gérard, Self-healable interfaces based on thermo-reversible Diels-Alder reactions in carbon fiber reinforced composites, J. Colloid Interface Sci. 430 (2014) 61–68. doi:10.1016/j.jcis.2014.05.007.

[16] D.G. Bekas, D. Baltzis, K. Tsirka, D. Exarchos, T. Matikas, A. Meristoudi, S. Pispas, A.S. Paipetis, Self-healing polymers: evaluation of self-healing process via non-destructive techniques, Plast. Rubber Compos. 45 (2016) 147–156. doi:10.1080/14658011.2016.1151987.

[17] A.J. Patel, N.R. Sottos, E.D. Wetzel, S.R. White, Autonomic healing of low-velocity impact damage in fiber-reinforced composites, Compos. Part A Appl. Sci. Manuf. 41 (2010) 360–368. doi:10.1016/j.compositesa.2009.11.002.

[18] T. Yin, M.Z. Rong, M.Q. Zhang, J.Q. Zhao, Durability of self-healing woven glass fabric/epoxy composites, Smart Mater. Struct. 18 (2009) 74001. doi:10.1088/0964-1726/18/7/074001.

[19] T. Yin, L. Zhou, M.Z. Rong, M.Q. Zhang, Self-healing woven glass fabric/epoxy composites with the healant consisting of micro-encapsulated epoxy and latent curing agent, Smart Mater. Struct. 17 (2008) 15019. doi:10.1088/0964-1726/17/01/015019.

[20] A.P. Esser-Kahn, P.R. Thakre, H. Dong, J.F. Patrick, V.K. Vlasko-Vlasov, N.R. Sottos, J.S. Moore, S.R. White, Three-dimensional microvascular fiber-reinforced composites., Adv. Mater. 23 (2011) 3654–8. doi:10.1002/adma.201100933.

[21] R.S. Trask, G.J. Williams, I.P. Bond, Bioinspired self-healing of advanced composite structures using hollow glass fibres., J. R. Soc. Interface. 4 (2007) 363–71. doi:10.1098/rsif.2006.0194.

CHAPTER 2

Damage monitoring in nano-enhanced composites using impedance spectroscopy

2.1 Introduction

Coupled property interaction in engineering structures may administer multiple functionalities. In order to exploit coupled field interaction for application such as Non-destructive evaluation, an in depth understanding of the principles that relate structural integrity to internal properties is indispensable. Typical example is the electromechanical coupling which relates electrical properties to the mechanical response and/or the durability of the structure in the case of composites reinforced with a conductive phase such as carbon nanotubes (CNTs) [1–3].

Electrical properties of epoxy resin-based CNT composites were extensively studied by many research groups over the last years [4–11]. A key feature of the electrical properties is that they can act as a very sensitive indicator for the evaluation of composite structural integrity. Numerous efforts have focused on the correlation of DC electrical properties (i.e. electrical resistance, electrical conductivity) to structural degradation within the lifetime of the composite material or structure. It has been established that, reversible changes in the electrical properties relate solely to strain, while irreversible electrical resistance changes relate to internal damage of the composite material [12–16]. Thostenson and Chou [17] established that the change in the size of reinforcements, from conventional micronsized fiber reinforcement to carbon nanotubes with nanometer-level diameters, enables a unique opportunity for the creation of multi-functional in situ sensing capability. By combining these reinforcements of different scales, carbon nanotubes can penetrate the matrix-rich areas between fibers in individual bundles as well as between adjacent plies and can achieve a percolating nerve-like network of sensors throughout the arrays of fibers in a composite, as depicted in Figure 2.1.

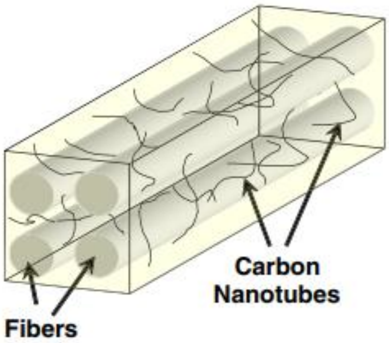

Figure 2.1 Three-dimensional model showing the penetration of nanotubes

In another work, T. Takeda and F. Narita [18] presented a study on the Mode I fracture behavior and crack monitoring of bonded carbon fiber reinforced polymer (CFRP) composite joints with carbon nanotube (CNT)-based polymer adhesive layer. Bonded joints were fabricated using woven carbon/epoxy composite substrates and CNT-based epoxy adhesives while the electrical resistance of the bonded joint specimens was monitored during Mode I fracture toughness tests Figure 2.2. They showed that the normalized resistance change can be utilized as a quantitative measure of crack extension amount and application of this crack sensing technique in real aerospace structures may provide confidence in using adhesively bonded joints.

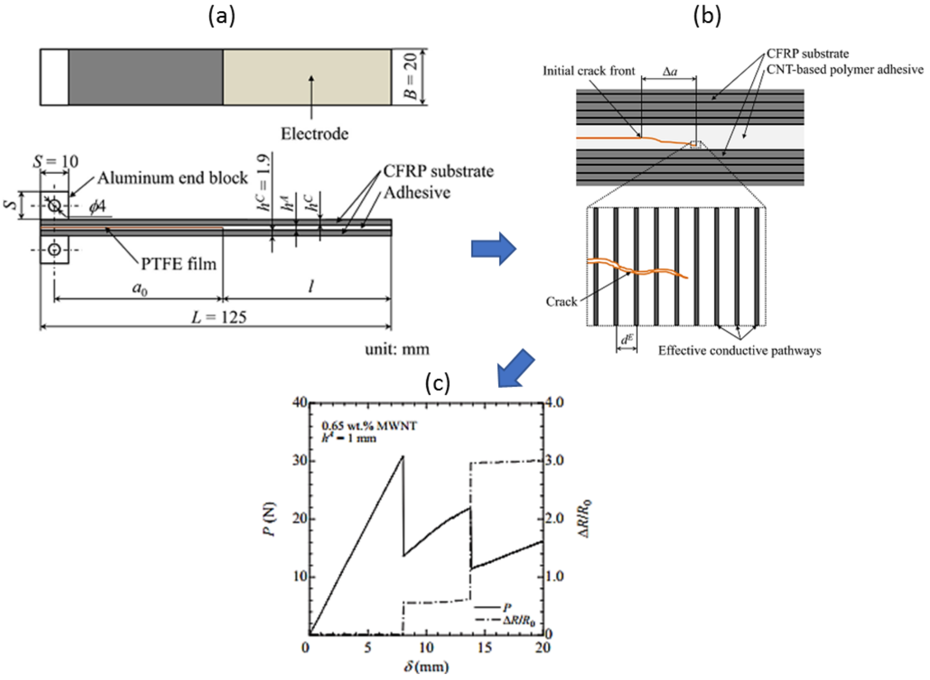

Figure 2.2 (a) Schematic of DCB bonded joint specimen, (b) illustration of crack region in DCB bonded joint specimen with CNT-based polymer adhesive layer and (c) load and normalized resistance change versus load point displacement plots for MWNT/epoxy adhesive joint specimen showing cohesive fracture

In a more recent work, the structural integrity of Carbon Fibre Reinforced Polymers (CFRPs) with Multi Walled CNTs (MWCNTs) in the matrix phase was evaluated concurrently with the self-sensing abilities of the hybrid composite. The adopted experimental setup for the electrical measurements is depicted in Figure 2.3. Self-sensing was achieved via the electrical network of CNTs within the insulating matrix which perform as inherent sensors in the composite structure. Changes in the electrical resistance of nano-composites and CFRPs, when subjected to load, provided a direct measure for strain and damage accumulation [19].

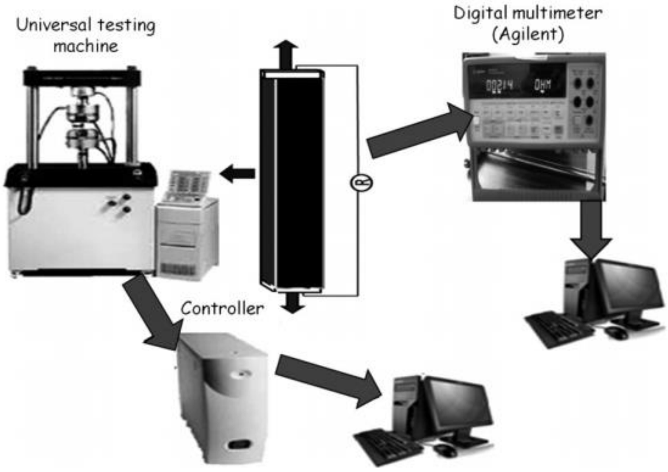

Figure 2.3 Experimental setup of electrical resistance change method.

More recently, electrical based methodologies utilizing AC configurations are gaining acceptance as more effective non-destructive evaluation (NDE) method for damage assessment in PMCs. AC methodologies increase the dimensionality of the problem adding additional variables compared to the DC techniques, which is virtually the monitoring of a potential function. This dimensionality increase may prove very useful in the inverse problem solution i.e. in the case of electrical topography [20,21].

The study of the impedance properties of composites which contain conductive reinforcing fibers in an insulating matrix have been extensively studied due to the fact that the conductive fiber can act as a working electrode or when the fiber volume fraction is above the percolation threshold, the entire composite specimen may act as the working electrode itself [22–25]. In a typical study, Slipher et al. [26] employed Electrical Impedance Spectroscopy (EIS) for damage detection in CFRPs. Impedance magnitude at low frequencies and impedance phase at high frequencies proved to be particularly useful as damage metrics showing significant sensitivity to the structural deterioration of the material due to mechanical loading. The adopted experimental setup is illustrated in Figure 2.4

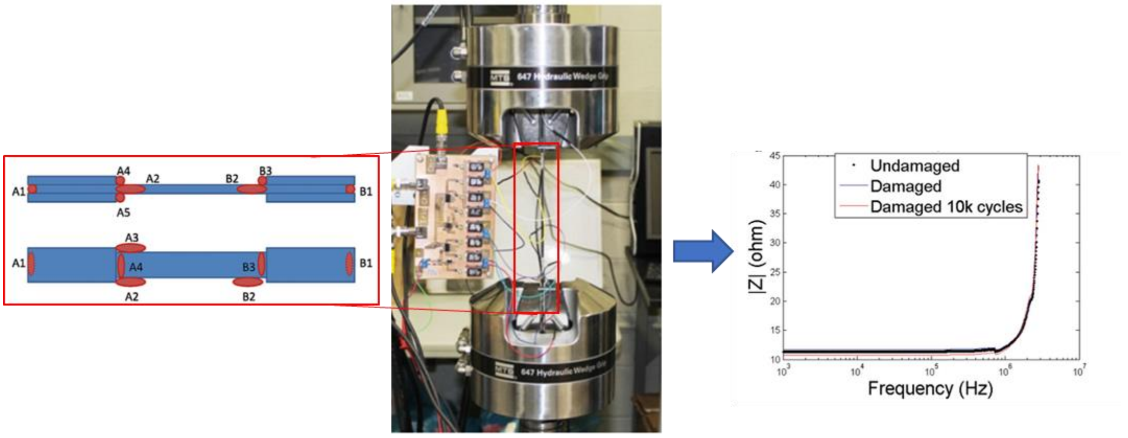

Figure 2.4 Automated experimental setup

In another work, Pohl et al. [27] employed Impedance Spectroscopy as a tool for the NDE of smart CFRP structures. They managed to detect damage (delamination) due to low-velocity impact by monitoring changes in the magnitude of the impedance over a wide frequency range Figure 2.5

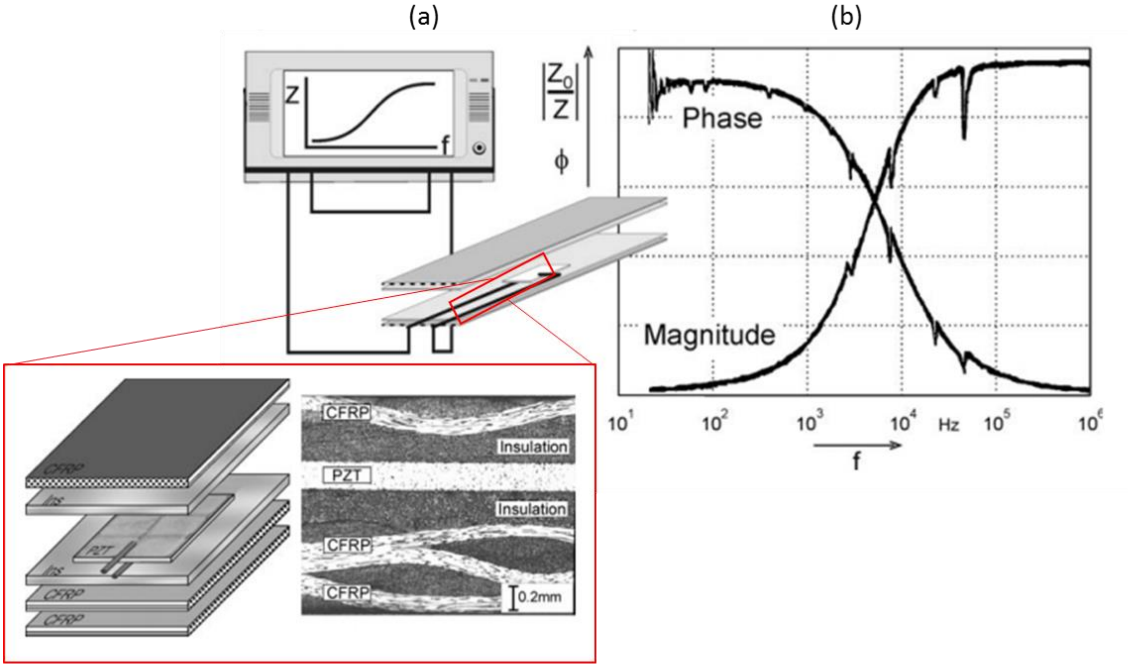

Figure 2.5 (a) Experimental setup and (b) measured magnitude and phase of impedance

Shimamura and coworkers [28], studied the influence of moisture absorption on the electrical impedance of CFRPs. of the Moisture content monitoring was achieved by attaching electrodes on the surface of the composite. They showed that the electrical impedance of the composite increased with moisture absorption, and that the electrical impedance change in the fiber direction was much larger than that due to tensile strain corresponding to swelling. An interesting application of IS was presented by Peairs and et al. [29]. In their study, they showed that impedance-based techniques are capable of *in situ* NDE of a space shuttle ground structure Figure 2.6. They focused on the optimization of the sensor frequency range in order to ensure maximum sensitivity for correlation with the integrity of the interrogated structure.

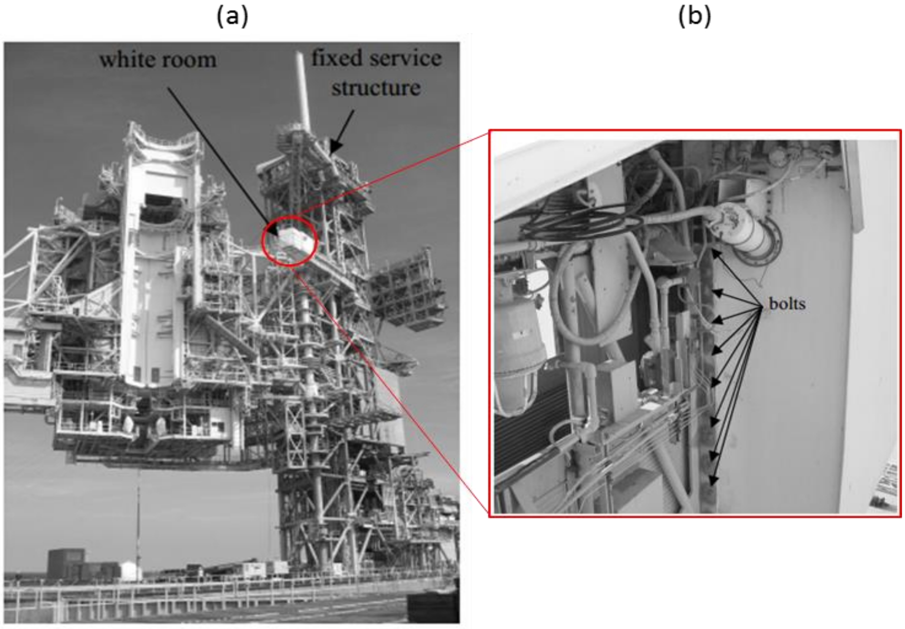

Figure 2.6 (a) White room attached to fixed service, (b) bolts connecting white room to fixed service

However, little research effort has been devoted to the study of the impedance properties of composites containing non-conductive reinforcing fibers [30,31]. The use of a non-conductive reinforcing phase (i.e. glass) in a polymeric matrix results to a composite material with dielectric characteristics. Therefore, a material response to an alternating field, takes place towards low frequencies of the dielectric spectrum where the effect of Electrode Polarization (EP) plays an important role in the IS measurements [32,33] . This effect, arises from the accumulation of ions at the interface between the metallic electrodes and the composite's surface forming a space-charge region. The EP effect may mask the material's behavior, and as a result lower the signal-to-noise ratio in the lower frequency region of the dielectric spectrum. As can be seen in Figure 2.7 this effect impedes the estimation of dielectric parameters of the composite [34].

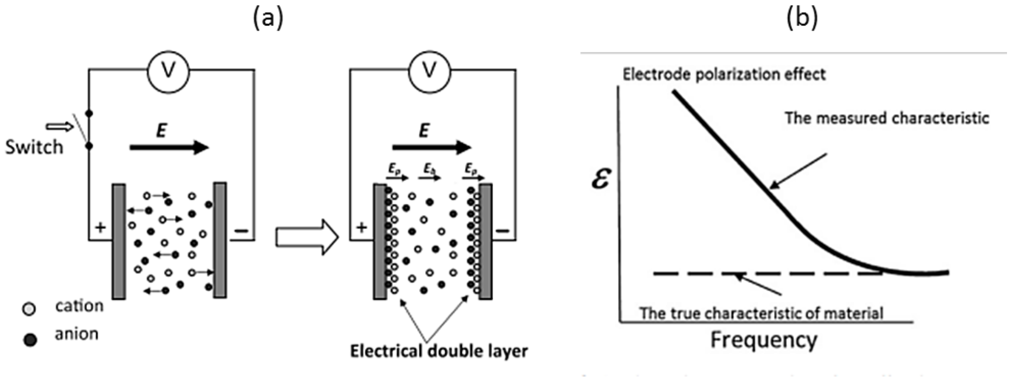

Figure 2.7 (a) A schematic representing the formation of ionic double layers at the electrode/sample interfaces, (b) A schematic representation of EP effect in a measured signal.

Possible solutions to overcome the EP effect include specialized modifications of the IS techniques [34,35] and/or modeling the electrode effects using an equivalent electrical circuit [36–39]. In a different approach, Fazzino et al. [40] have successfully characterized progressive damage initiation and progression in thin woven glass/epoxy composites due to fatigue loading, by monitoring changes in the impedance spectra. Samples were soaked in 5M conductive solution and a correlation between solution uptake and micro-cracks formulation was achieved through the analysis of the impedance data. Changes in the dielectric profile were attributed to the phenomenon of micro-crack creation which resulted in increased solution uptake and thus creating more conductive pathways through the material.

A non-invasive, in-operando technique to study changes in dielectric properties during progressive damage accumulation in composite materials subjected to mechanical loading, was presented by R. Raihan and his co-workers [41] . It was determined that the size, shape and orientation of microdamage as well as the dielectric character of the defect volume and the interfaces created are all distinguished by the method. Observed changes were not monotonic, and were specific to the dominant damage mode as a function of load level Figure 2.8.

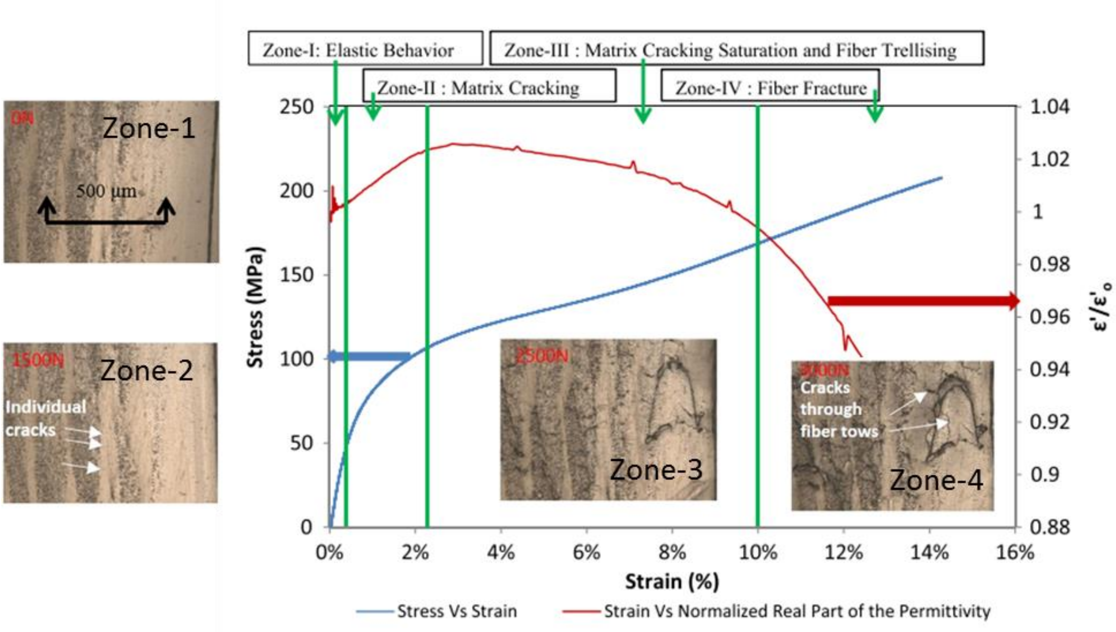

Figure 2.8 Response of the dielectric property in different zones of damage progression. **Insert:** Edge replica at different load.

Bekas et al [42] studied the effect of damage on the hysteretic electrical behavior of carbon nanotube reinforced epoxy composites by measuring phase delays at several frequencies for different levels of cyclic thermal shock damage. This study showed that there is a direct correlation between the degradation of the material and the impedance data, which proved extremely sensitive to the changes invoked in the material microstructure due to thermal shock. The embedment of CNTs within the polymeric matrix forced the electrical response of the material to AC towards higher frequencies where the effect of EP longer exists (Figure 2.9).

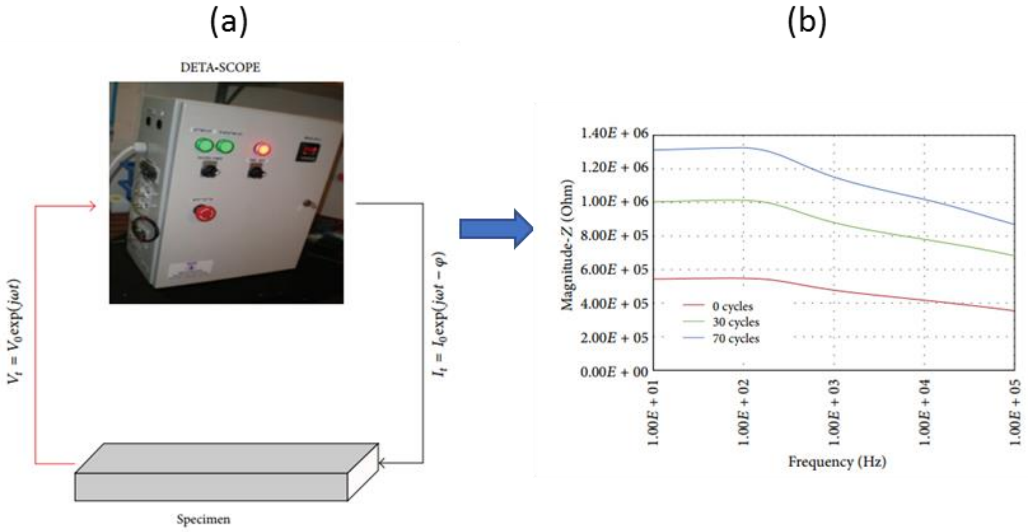

Figure 2.9 (a) Experimental setup for the IS measurements. (b) Bode plot-impedance magnitude versus frequency

Under the aforementioned considerations, it is evident that there is still room for improvement in damage detection and prevention of non-conductive composite materials using IS.

The purpose of the present work is unfolding in three axes: First to enhance the resolving ability of the electrical based methodologies via the employment of AC configurations. For this purpose, IS has been utilized in order to monitor changes in the dielectric profile of nano-composites that are subjected to water absorption tests and hybrid multiscale composites that are subjected to mechanical loading and unloading. Second, to tailor the electrical response of the composites to higher frequencies of the impedance spectra (avoiding the EP effect) through the incorporation of multi-walled carbon nanotubes (MWCNTs) as a modulating phase within the polymeric matrix. Third, to study the effect of damage (level and type) on the dielectric properties of the material. This involves the simulation of induced damage with a typical RC circuit in parallel which simulates both resistivity changes at the material level and structural damage at the coupon manifested via the creation of interfaces which contribute to the capacitive behaviour of the structure. In addition, Optical Microscopy was utilized in order to verify the damages sequence that occurred in quasi-isotropic laminates during the mechanical testing.

2.2. Theoretical considerations

Impedance Spectroscopy is a well-developed branch of AC based methodologies that monitors the response of a system to an alternating current or voltage as a function of frequency. It may be used to investigate the dynamics of bound or mobile charge in the bulk or interfacial regions of any kind of solid or liquid material: ionic, semiconducting, mixed electronic–ionic, and even insulators (dielectrics). Typically, IS involves the application of a monochromatic voltage to the material under test while phase delay and amplitude of the resulting current are measured at that frequency using fast Fourier transform (FFT) analysis of the response. A spectrum is generated by sweeping in a range of frequencies and measuring the impedance at each point. [43].

The sinusoidal electric potential that is applied to the material and involves the single frequency $v=\omega/2\pi$ can be expressed by

$$V(t) = V_o \sin(\omega t) \tag{2.1}$$

where the V(t) is the external potential at time t, V_0 is the amplitude of the waveform and ω is the radial frequency. The resulting steady state current is governed by

$$\mathrm{I(t)} = \mathrm{I_o \sin(\omega t + \varphi)} \tag{2.2}$$

where I(t) is the current at time t, I_0 is the amplitude of the outbound signal and φ is the phase difference between the voltage and the current; it is zero for purely resistive behavior. This technique works by first polarizing the material under test at a fixed voltage and then applying a small additional voltage (or occasionally, a current) to perturb the system. The perturbing input oscillates harmonically in time to create an alternating current, as shown in Figure 2.10.

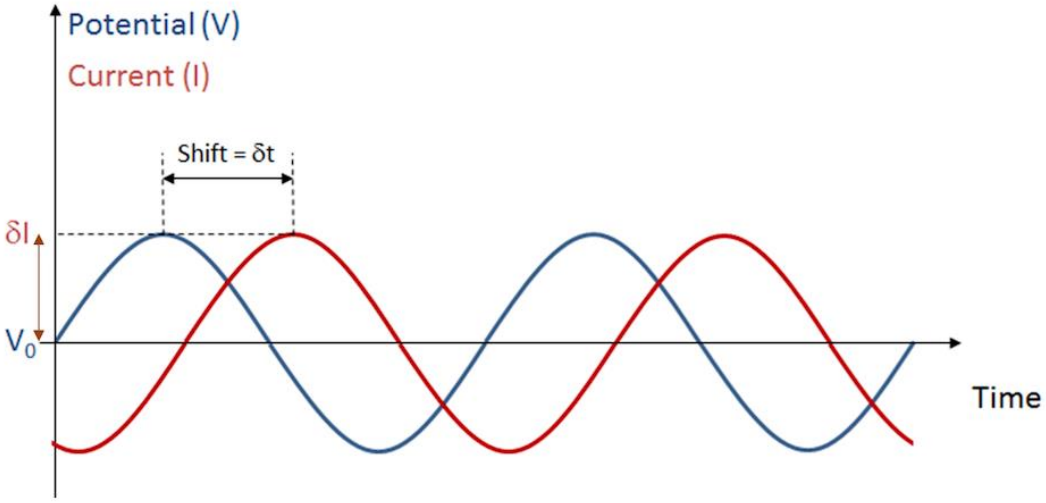

Figure 2.10 External potential and resulting steady state current signals

The total impedance of the system can be calculated using voltage/current relations that can be rearranged to a form similar to Ohm’s law for DC current:

$$\mathrm{Z = \frac{V(t)}{I(t)} = \frac{V_0 \sin(\omega t)}{I_0 \sin(\omega t + \varphi)} = Z_0 \frac{\sin(\omega t)}{\sin(\omega t - \varphi)} = Z_0 \exp(i\varphi) = Z_0(\cos\varphi + i\sin\varphi)}$$
$$\mathrm{= Z' + iZ''} \tag{2.3}$$

where Z is the total impedance of the system. The impedance is then represented as a complex number with a real and an imaginary part:

with

$$Z' = |Z| * \cos(\varphi) \qquad (2.4)$$
$$Z'' = |Z| * \sin(\varphi)$$

where Z' and Z'' is the real and the imaginary parts of the complex impedance respectively and $|Z|$ is the magnitude of the total impedance. It is evident that impedance is real when φ=0 and thus $Z = Z'$ denoting a frequency independent or completely resistive behavior. Overall, impedance spectroscopy is expected to increase the dimensionality of the electrical methodology by introducing both the real and the imaginary part of the resistance, providing thus more information on the accumulating damage. This is critical for the accurate solution of the inverse problem, where the formulation of governing equations based on observation and/ or experiment about any physical problem or system is required. By measuring the frequency depending behavior of materials and materials systems, beneath electrical properties, structural properties may be extracted as well. Figure 2.11 depicts the characterization of a material system using IS.

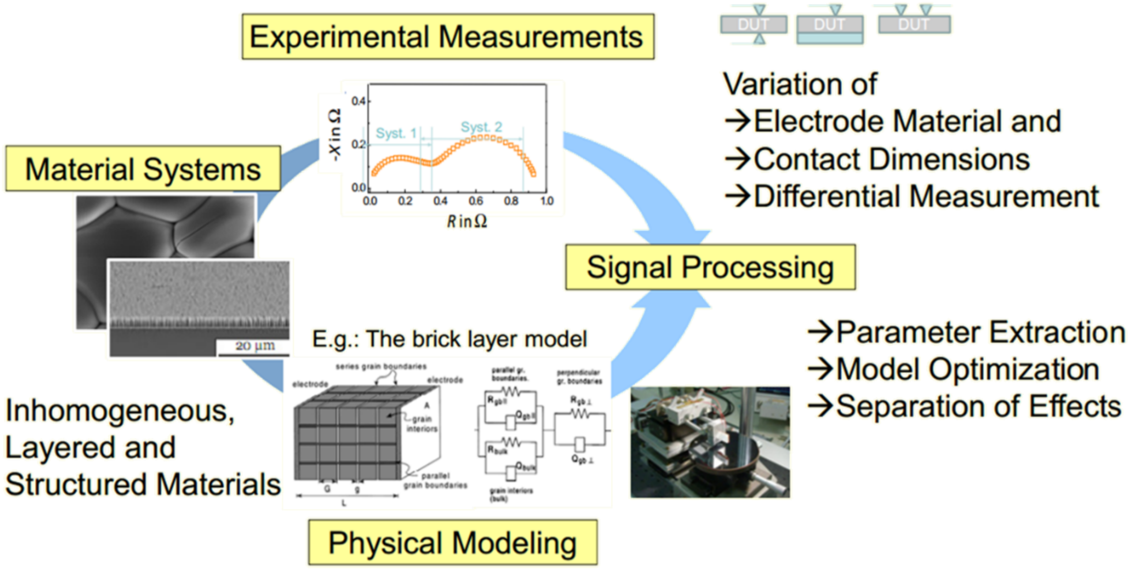

Figure 2.11 Materials characterization route via Impedance spectroscopy

A common method of presenting impedance data is the Nyquist plots. If the real part is plotted on the X-axis and the imaginary part is plotted on the Y-axis of a chart, we get a "Nyquist Plot" (Figure 2.12a). Notice that in this plot the Y-axis is negative and that each point on the Nyquist Plot is the impedance at one frequency. Figure 2.12a has been annotated to show that low frequency data are on the right side of the plot and higher frequencies are on the left. On the Nyquist Plot the impedance can be represented as a vector (arrow) of length |Z|. The angle between this vector and the X-axis, commonly called the “phase angle”, is f (=arg Z). The Nyquist Plot in Figure 2.12a results from the electrical circuit of Figure 2.12c. The semicircle is characteristic of a single "time constant". Impedance plots often contain several semicircles. Often only a portion of a semicircle can be observed. Another way to present IS results is the Bode plot where the impedance is plotted with log frequency on the X-axis and both the absolute values of the impedance ($|Z|=Z_0$) and the phase-shift on the Y-axis. The Bode Plot for the electric circuit of Figure 2.12c is shown in Figure 2.12a. It should be pointed out that unlike the Nyquist Plot, the Bode Plot does show frequency information.

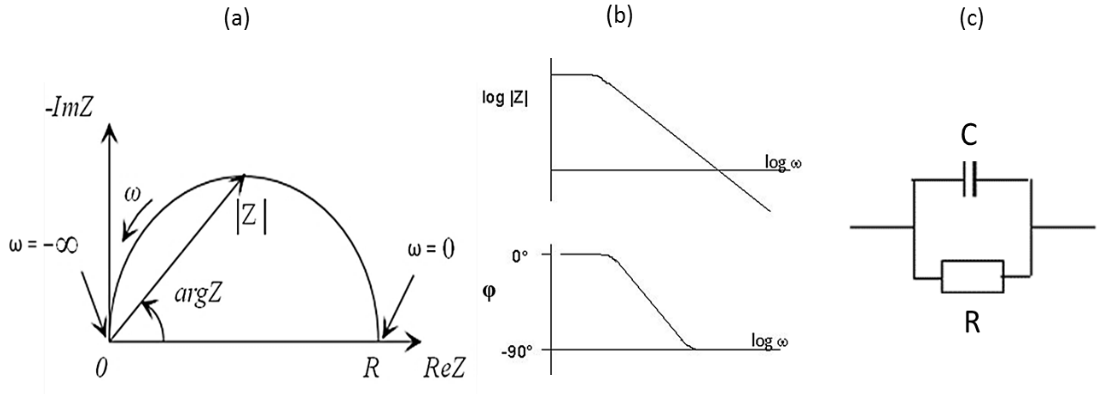
(a) (b) (c)

Figure 2.12 (a) Nyquist and (b) Bode plots, (c) simple electrical circuit

and the Nyquist plot i.e. the imaginary part vs real part of the impedance. The aforementioned methods have been adopted in the present study along with the Bode plot of the phase delay vs frequency.

2.3. Materials and methods

2.3.1. Materials

The Graphistrength Multi Wall CNTs supplied by ARKEMA, France were used in this study. They were synthesized by Catalyzed Chemical Vapor Deposition (CCVD); the tube diameter ranged from 10 to 15 nm and the tube length was more than 500 nm. The epoxy matrix used was the Araldite LY 5052/ Aradur 5052 by Huntsman International LLC (Switzerland). For the 16 plies Glass Fiber Reinforced Polymers (GFRPs) quasi isotropic laminates, interglas 92145 E-glass unidirectional and E-glass biaxial fabrics supplied by R&G, Germany were employed as reinforcement.

2.3.2. Specimen preparation

Dispersion of 0.5 % w/w MWCNTs in the host resin took place in a laboratory dissolver (Dispermat AE, VMA-GETZMANN GMBH, Germany) (Figure 2.13). The temperature during the dispersion was kept at 25 ± 1^0C, so as to avoid overheating of the polymer resin and introduction of defects on the CNTs surface, by using a cooling bath manufactured by Grant, UK. The dispersion lasted for 2 h at 2000 rpm under vacuum. At the end of the dispersion process the hardener was added, and the MWCNTs-epoxy resin mixture was degassed in vacuum oven at 23^0C in order to remove trapped air. Subsequently, the mixture was cast to silicon rubber molds and cured at 25 ^{0}C for 24 h (Figure 2.13) to manufacture square plates of approximately $150 \times 150 \times 4$ mm^3. Finally, the plates were removed from the mold and postured at 100 ^{0}C for 4 h.

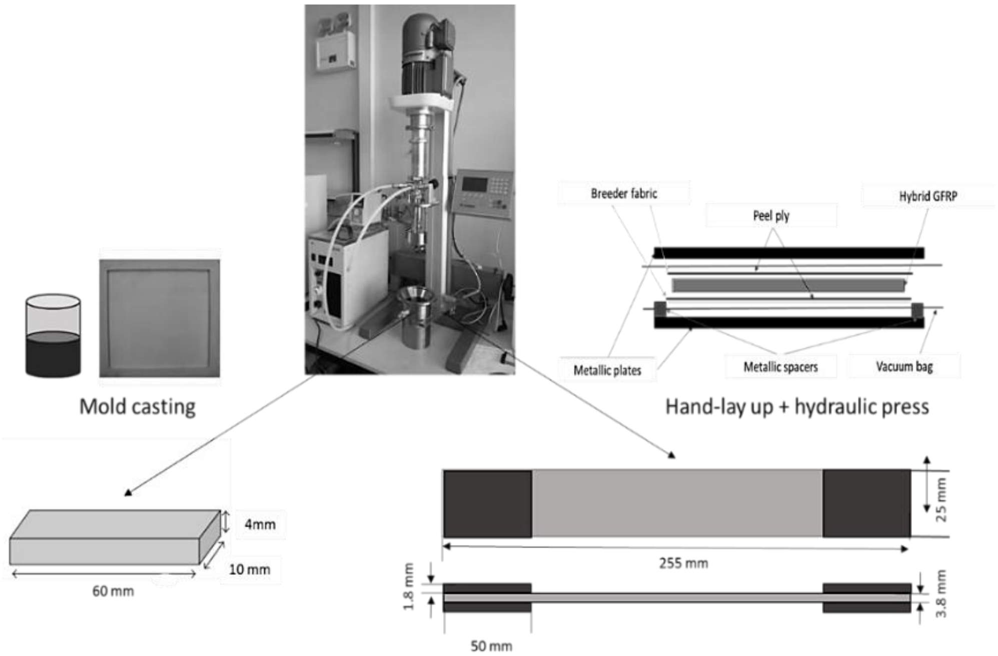

Figure 2.13 Manufacturing procedure of the nanocomposites and the hybrid GFRPs

Prismatic specimens of 60 × 100 × 4 mm^3 were cut from the plates using a water lubricated table diamond saw (Fig. 1). Finally, specimens were lightly sanded in order to (i) remove defects from the manufacturing process and (ii) prepare the side surface for the application of the measuring electrodes.

The CNT modified epoxy resin was also employed as matrix for the manufacturing of 16 plies quasi isotropic laminates GFRPs, $[0/\pm45/90]_{s2}$. The hybrid GFRPs were manufactured with the hand layup method and pressed in a heated hydraulic press under the pressure of 10^7 Pa at 25 ^{0}C for 24 h. Post curing took place at 100 ^{0}C for 4 hours (Fig.1). Specimens were cut in the desired dimensions according to ASTM-STP3039 while the ends of the specimens were reinforced with end tabs made of cross-ply laminate with the fibers at ±45° to the specimen axis. The tab thickness was 1.8 mm.

2.3.3. Water absorption

An initial conditioning protocol for all nanocomposites was followed before the hygrothermal exposure, i.e. 5h at 40 °C. Hygrothermal exposure of the specimens involved immersing the nano-composites into hot distilled water (80 °C) (Figure 2.14). For that purpose, a water bath with temperature control was used and the interrogated specimens were divided into four groups. The first group remained undamaged and worked as reference. The total exposure of the second, third and fourth groups of specimens was 5, 10 and 15 days respectively. At the end of each testing, specimens were removed from the water bath and placed in an oven for 5 min at 40 ^{0}C so as to remove the moisture within the polymeric matrix which would affect the IS measurements.

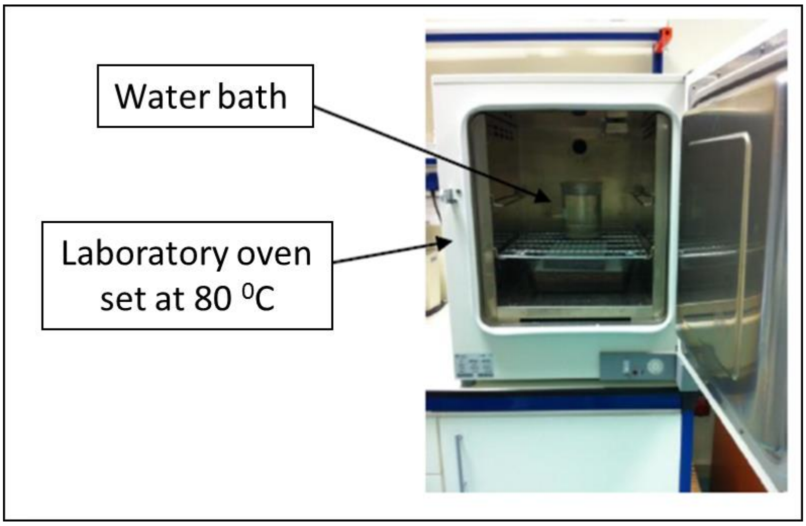

Figure 2.14 Experimental set-up for the hygrothermal exposure test

2.3.4. *Step-loading*

Loading-unloading tests were performed using an Instron 5850 universal testing machine equipped with 35 kN load cell. The loading sequenced involved incremental loading steps at extension control mode with constant loading rate of 2 mm/min. In order to determine the ultimate tensile strength (UTS) of the composites, five specimens were subjected to tensile loading until fracture according to ASTM-STP3039. The rest of the specimens subjected to tensile step-loading of 20%, 40%, 60%, 80% and finally 100% of their UTS. The experimental set-up for the step-loading tats is illustrated in Figure 2.15.

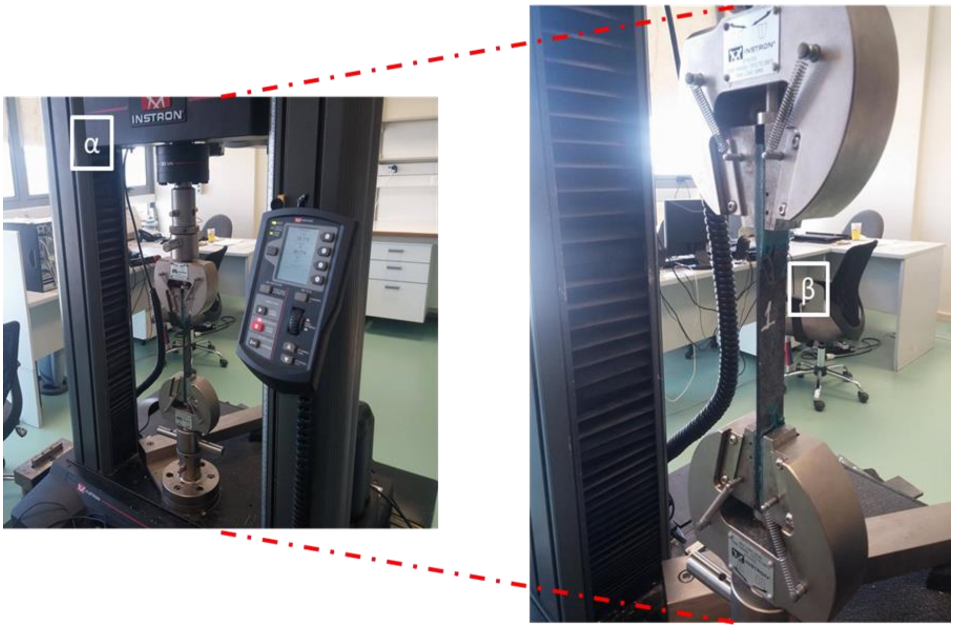

Figure 2.15 Experimental set-up for the step-loading test, (a) Instron 5850 universal testing machine, (b) GFRP

2.3.5. Impedance Spectroscopy-IS

Impedance spectroscopy was performed, in both cases, using a dielectric spectrometer-frequency spectrum analyzer (DETA SCOPE L1 provided by Advise Ltd.). For the purposes of the electrical measurements of the nano-composites that were subjected to water absorption tests, electrodes were attached at the side surfaces (left and right surface, as seen in Figure 2.16) of the prismatic specimens using silver conductive paste so as to minimize contact resistance and achieve good electrical coupling. The spectrometer applied a sinusoidal electrical excitation waveform of varying frequency while the induced current waveform was recorded. The excitation frequency ranged from 10 Hz to 0.5 MHz.

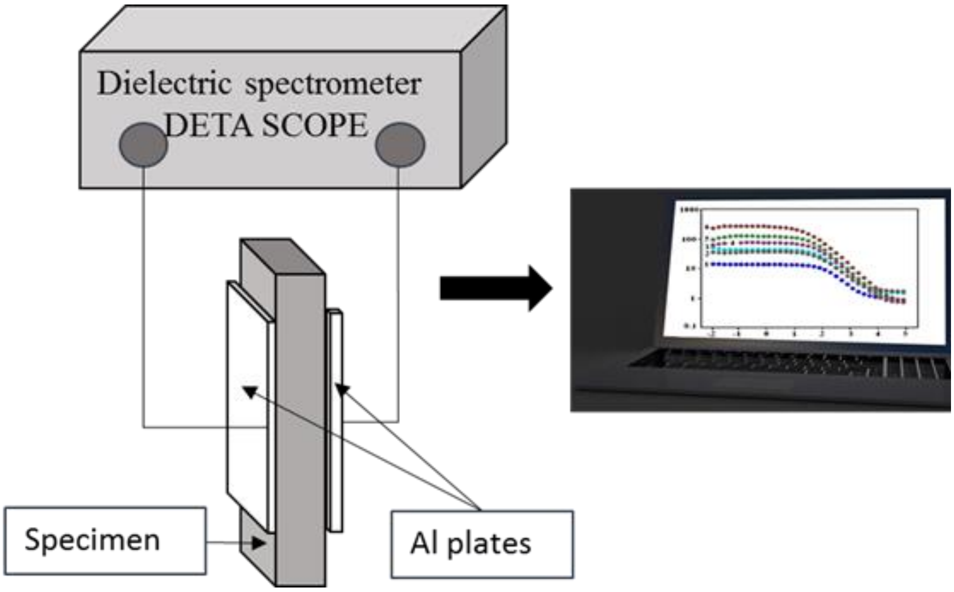

Figure 2.16 Experimental set-up for the IS measurements of the nanocomposites

For the case of hybrid GFRPs that were subjected to mechanical step-loading protocols, IS was employed in every step of the mechanical test, in order to achieve a correlation between the loading histories, IS data and the local material state changes associated with the irreversible damage that were accumulated during the tensile loading. The specimens were placed between two aluminum plates so that the plates completely covered the sides of the specimens. The aluminum plates were held on the specimen's sides using mechanical grips (Figure 2.17).

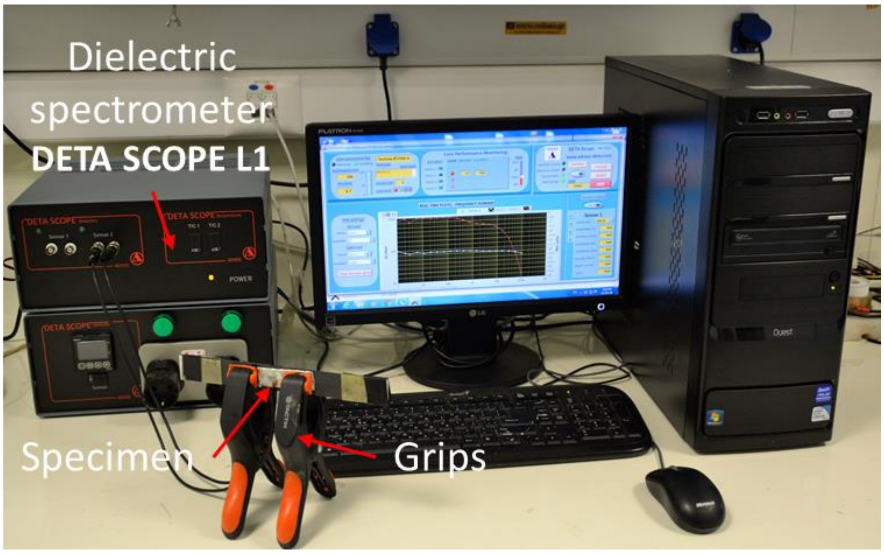

Figure 2.17 Experimental set-up for the IS measurements of the hybrid GFRPs

2.3.6. Optical Microscopy

Parallel to the IS study an extensive optical microscopic campaign was employed in order to trace and verify the typical sequence of damage processes encountered in quasi-isotropic laminates. These damage modes are expected to lead to the global change in the dielectric behaviour of the composite mirrored in its impedance profile. Optical Microscopy (OM) examinations were employed in between step loading from the polished edge of purposely prepared composite coupons using a Leica optical Microscope.

2.4. Results and Discussion

2.4.1. Nano-composites – IS analysis

When a material is subjected to an external alternating field, its dipoles are forced to orient to the direction of the field. As frequency of the field increases, these dipoles are unable to simultaneously follow the variations of the external filed due to inertia effects. Therefore, hysteretic phenomena are induced manifesting a phase delay between excitation and response signals.

On the other hand, moisture absorption in epoxy based composites may lead to swelling, plasticization and in some cases softening of the matrix [44–46]. These defects disrupt the conductive CNT network within the polymeric matrix and as a result the dielectric response of the material to an alternating field is highly affected.

The Bode plots i.e. magnitude of impedance and phase delay versus frequency for the nano-composites that were subjected to water absorption can be seen in Figure 2.18a and Figure 2.18b respectively.

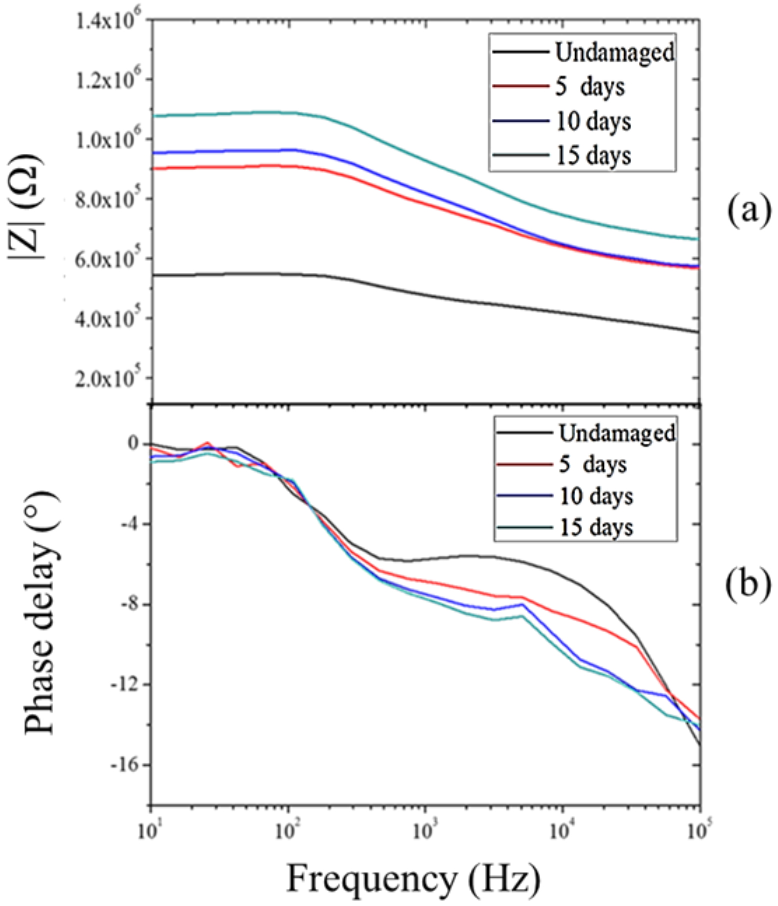

Figure 2.18 Bode plot of (a) Impedance magnitude vs. frequency, (b) phase delay vs. frequency for the four nanocomposites

As can be clearly observed, the magnitude of the impedance at low frequency increases with increasing hygrothermal exposure time. In all cases the transition from Ohmic (linear, phase delay ≈ 0) to non-Ohmic behavior (non-linear, phase delay < 0) takes place at approximately 250 Hz (Figure 2.18a). This behavior is in agreement with DC resistance measurements, where the resistance is monotonically increasing as the micro-cracks which are created due to mechanical loading, disrupt the conductive CNT network in the nano-composite [19]. It is evident that the magnitude of the impedance is highly affected by the presence of internal damage, almost doubling its initial value, after 5 days of hygrothermal exposure, indicating that is a highly sensitive damage index. It should be mentioned that another important feature of the recorded impedance data is the absence of the EP effect at low frequencies followed by a high signal-to-noise ratio.

Variations can also be seen in the case of phase delay values between frequencies of 800 Hz and 20 kHz (Figure 2.18b). These differences can be attributed to plasticization effects and physical degradation of the polymer chains [45] . In all cases, there is an initial part where phase oscillates around zero, denoting an initial DC behaviour which is followed by a reduction in the values of the phase delay which are indicative of a completely capacitive behaviour [43].

In Figure 2.19a, the Nyquist plot of the imaginary and real part of the impedance, as they are calculated from Eq. 4, is depicted. The experimental Nyquist plot is different from that of a typical Cole-Cole plot (RC circuit in parallel) [43], which is a semicircle and possesses a single time constant (Figure 2.19b), however is indicative of a strong capacitance element which is scaled according to the level of damage. It can be observed that the hygrothermal exposure, led to an increase in the real part of the impedance. This is attributed to the fact that the induced microcracks act as discontinuities in the conductive network, created by the dispersed conductive nanophase in the composite. The imaginary part of the impedance is altered as the developed microcracks may be regarded as nanocapacitors which cumulatively contribute to the increase of the reactance of the system at approximately half order of magnitude (Figure 2.19a).

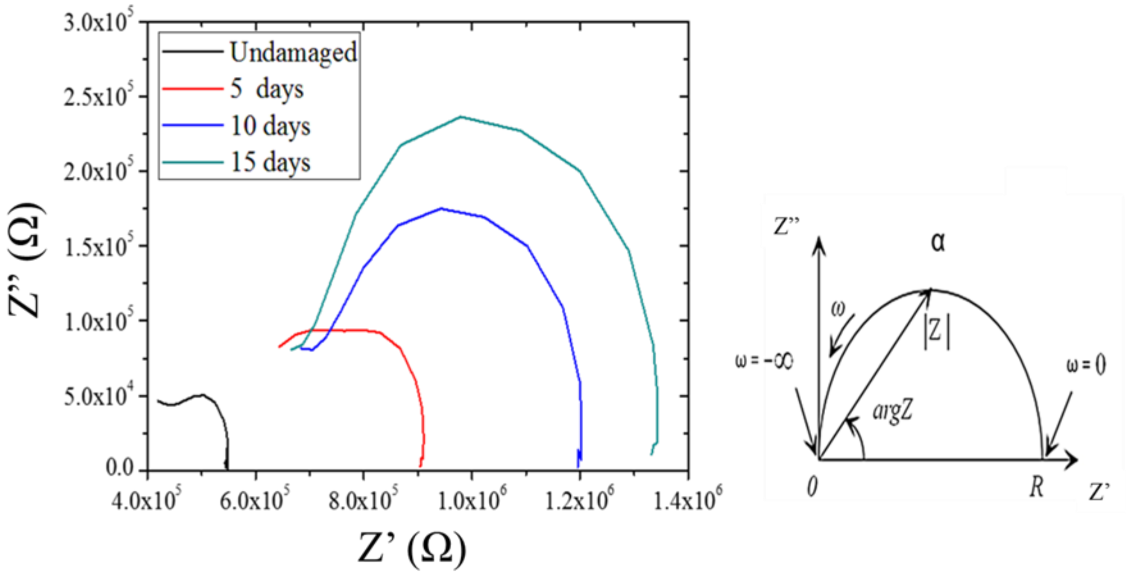

(a) (b)

Figure 2.19 Nyquist plot for the four nanocomposites and (b) typical Cole-Cole of a single time constant

The imaginary part of the impedance or reactance, represents the energy storage part of the system and is related to capacitance and inductance properties of the interrogated element when seen as a typical electrical circuit. Reactance is expressed by

$$\mathrm{X} = \mathrm{X_L} - \mathrm{X_C} = \omega\mathrm{L} - \frac{1}{\omega\mathrm{C}} \tag{2.5}$$

where X is the total reactance, X_L is s the inductive reactance, X_C is the capacitive reactance ω is the radial frequency, L is the inductance and C the capacitance. In all observed systems, the negative values of the imaginary part of the impedance -or that current leads the voltage – that have been recorded indicate the presence of a capacitive behaviour. The total capacitance of the system can be expressed by

$$\mathrm{C} = -\frac{1}{\omega\mathrm{X_C}} \tag{2.6}$$

In detail, the total capacitance of the system can be calculated by

$$\mathrm{C} = \varepsilon_0\varepsilon_\mathrm{r}\mathrm{A}/\mathrm{d} \tag{2.7}$$

where ε_0 is s the permittivity of free space, ε_r is the relative permittivity of the material, A is the area of overlap of the two electrodes (in the case of the GFRPs, Al plates) and d is the separation between the electrodes.

The introduction of defects (microcracks) lowers the conductivity of the system; therefore, the relative permittivity of the material is changing. The total capacitance of the nano-composite is then represented by

$$\mathrm{C} = \varepsilon_0(\varepsilon_\mathrm{r}(1-\mathrm{V}) + \mathrm{V}\varepsilon_\mathrm{A})\mathrm{A}/\mathrm{d} \tag{2.8}$$

where ε_A is the relative permittivity of the air and V is the concentration of the air (voids) within the polymeric matrix. It must be pointed out that the relative permittivity of the air (ε_A) has lower values than the relative permittivity of the composite (ε_r). Thus, the total capacitance of the system is decreasing as the level of damage increases.

In an effort to simulate the induced damage as a function of the capacitance and/or the resistance, a typical RC circuit in parallel has been utilized. The simulation was carried out using the LEVMW Complex Nonlinear Least Squares software (Copyright: James Ross Macdonald). The results can be seen in Figure 2.20 where the capacitance and the resistance versus the exposure time is depicted. As can be observed, there exists an inverse relationship between capacitance and resistance of the system where the resistance of the material is monotonically increasing whereas the capacitance of the system is decreasing significantly with increasing exposure time.

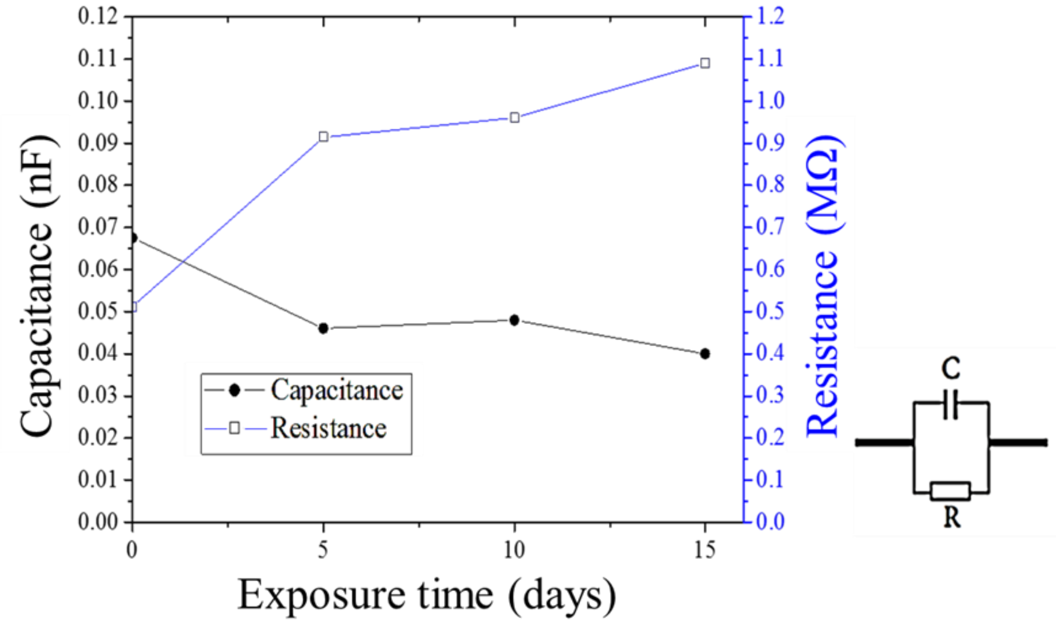

Figure 2.20 Equivalent RC circuit: R and C vs. exposure time

2.4.2. *Hybrid GFRP - Mechanical analysis*

Figure 2.21a presents the stress vs strain curves for all the steps of the mechanical tensile step-loading while Figure 2.21b depicts the normalized Young’s modulus (E/E_0) as a function of applied load. The calculation of the Young’s modulus values was performed according to ASTM D 3039. It can be seen that the relative stiffness is decreasing with increasing level of applied stress (Figure 2.21b). All specimens exhibited a typical brittle behavior with a UTS of 200 ±1 MPa. As loading increases, damage initiation, accumulation and propagation occur progressively with the interaction of known failure mechanisms (i.e. matrix-cracking, fiber–matrix debonding, delamination, fiber – cracking) [47]. Stress vs strain curves could be divided into four major regions depending on the dominant failure mechanism that takes place throughout the mechanical testing [48]. The first region (up to 31 MPa) concerns the elastic behaviour of the composite where only reversible changes occur, followed by the next region where damage initiation manifested via transverse matrix failure modes i.e. matrix – microcracking etc.

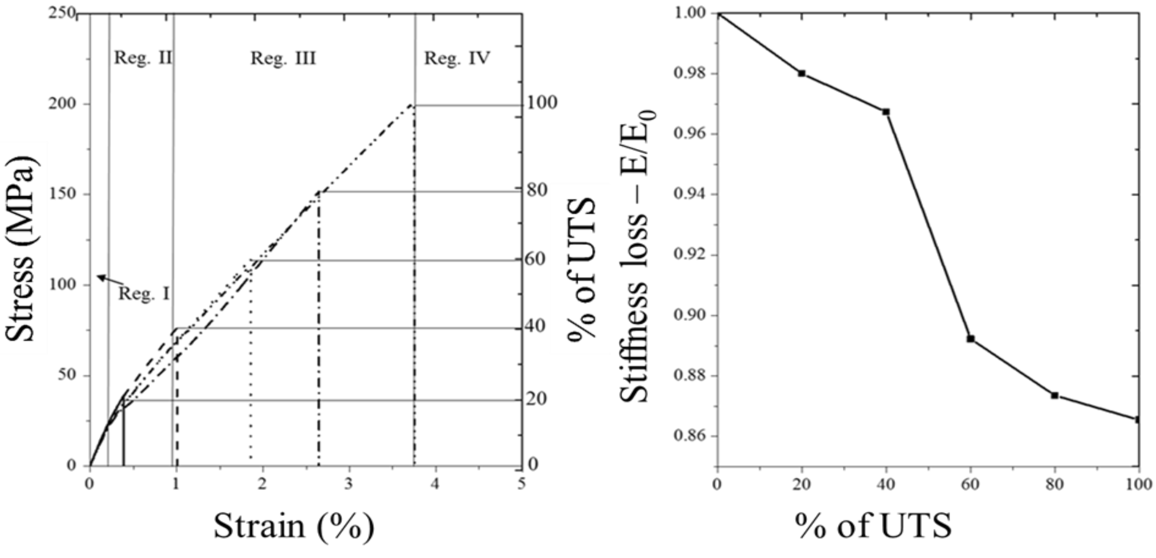

(a) (b)

Figure 2.21 a) Stress vs. strain curves and (b) stiffness loss vs. applied load curve for the hybrid GFRPs

At higher levels of applied load, saturation of matrix cracking with concurrent stretching of the fibers is observed (region III) while the region IV refers to fiber fracture (specimen failure). It must be pointed out that deterioration is evident even from the first step of the applied loading protocol (20% of UTS) which enters region II, denoting irreversible damage to the matrix material.

2.4.3. Hybrid GFRP IS analysis

Fiber reinforced composite materials are universally dielectric. They are poor and imperfect conductors that trap charge at interfaces and micro-boundaries, defects, and micro-cracks, and they typically conduct with several mechanisms. Heterogeneous material systems have many micro-nano interfaces and when they degrade, new “phases” are created. Thus, materials of different electrical properties contact each other, and with degradation, the nature of the contact changes. In such a material system, polarization is typically an interfacial effect that is due to the build-up of charge on the interfaces. The dielectric relaxation due to interfacial polarization provides information about the heterogeneous structure and the electrical properties of the constituent components. The number of dielectric relaxations expected in heterogeneous systems depends not only on the number of different interfaces but also on the shape of the inclusions and their orientation relative to the vector direction of the applied field. In practice, however, all relaxations predicted are not observed because of the limited frequency range and sensitivity of measurements.

Figure 2.22a and Figure 2.22b depict the Bode plot of the magnitude of the impedance and phase delay versus frequency respectively. Similar to the previous case, the magnitude of impedance is highly affected by the presence of damage within the composite material showing an increase of two orders of magnitude to its initial values after the first step of the mechanical loading (Figure 2.22a). This abrupt increase is followed by a relative stabilization of the magnitude's values while a second significant increase can be observed in the case of the fractured specimen caused by the large amount of air within the discontinuities caused by the failure of the specimen.

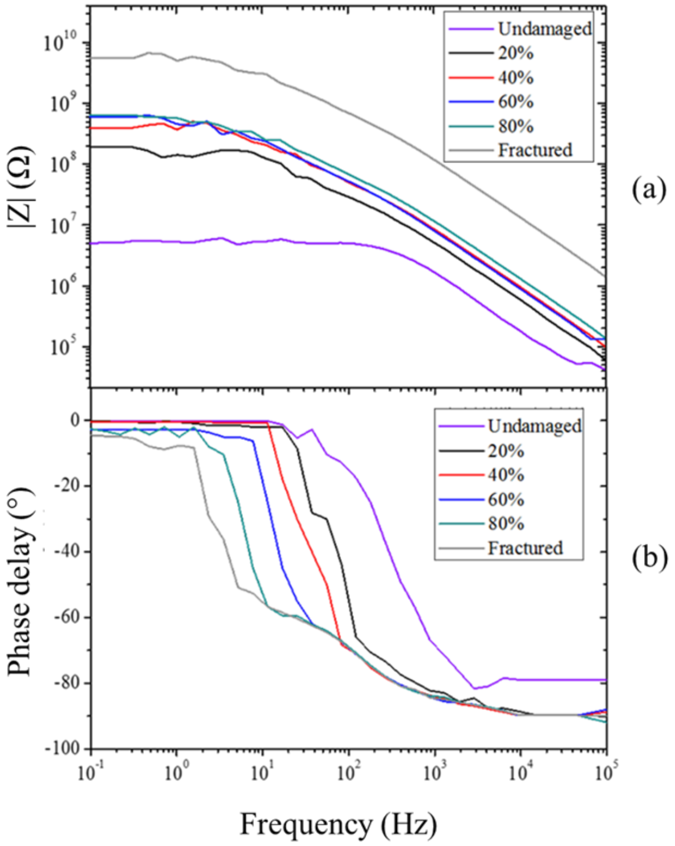

Figure 2.22 Bode plot of (a) impedance magnitude versus frequency, (b) phase delay vs. frequency for the hybrid GFRP

Micro-cracking of the matrix material induces a third phase which is trapped air (voids) to the composite material that disrupts the conductive CNT network and inevitably enhances the effect of interfacial polarization. A polarization mechanism that, as stated, occurs due to accumulation of charges between regions with different electrical conductivity is reflected in the phase delay versus frequency curves by the reduction of the transition frequency from Ohmic to non-Ohmic behaviour (Figure 2.22b).

Along with the Bode plots, significant changes can be spotted in the case of Nyquist plot of the imaginary versus real part of the impedance (Figure 2.23).

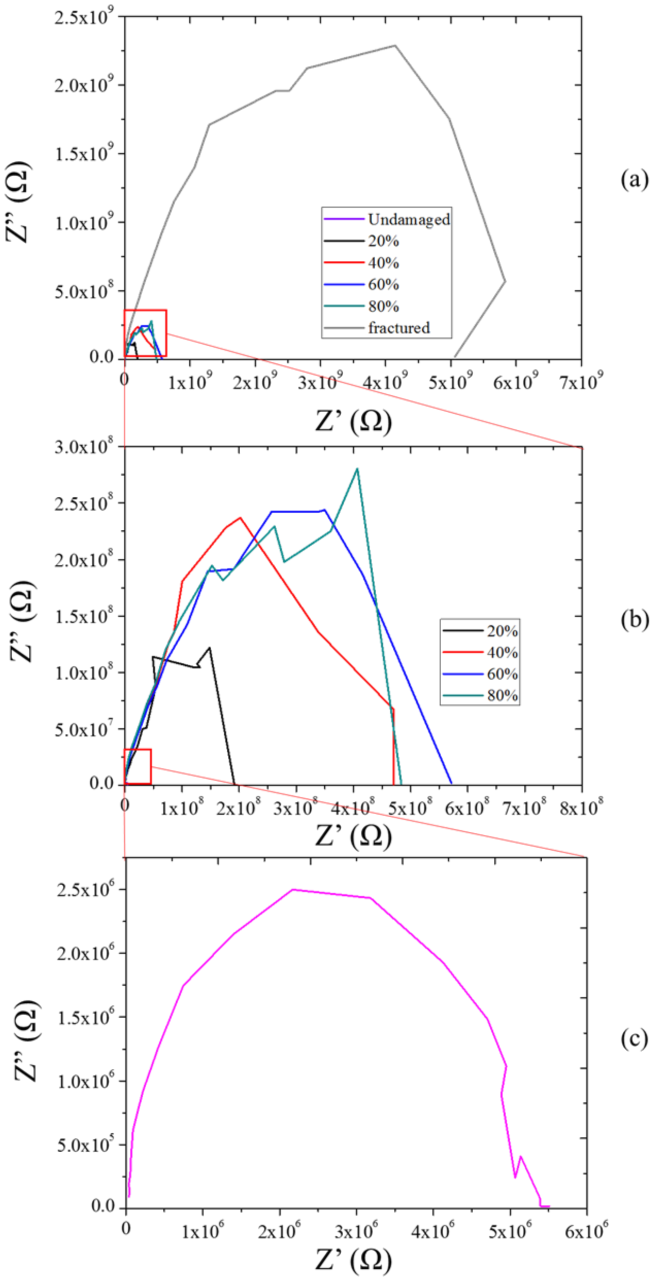

Figure 2.23 Nyquist plot for (a) all cases, (b) intermediate cases and (c) the undamaged specimen

As can be seen in Figure 2.23, the experimental Nyquist plot is that of a typical RC circuit in parallel, which is a semicircle and possesses a single time constant, and is indicative of a strong capacitance element which is scaled according to the level of damage. Both real and imaginary parts of the impedance show major differences as the level of damage increases.

The real part of the impedance is affected by the disruption of the CNT network, exhibiting an increase of two orders of magnitude compared to its initial values after the first step of the mechanical loading (20 % of UTS). On the other hand, the imaginary part of the impedance shows a significant increase to its initial values. This behaviour can be attributed to the increased effect of interfacial polarization at the boundaries of the introduced microcracks.

Based on the analysis descripted in previous section., as the level of damage increases the total capacitance of the system is decreasing (Eq. 7). This can be clearly observed if we simulate the induced damage as a function of the capacitance and resistance using a typical RC circuit in parallel.

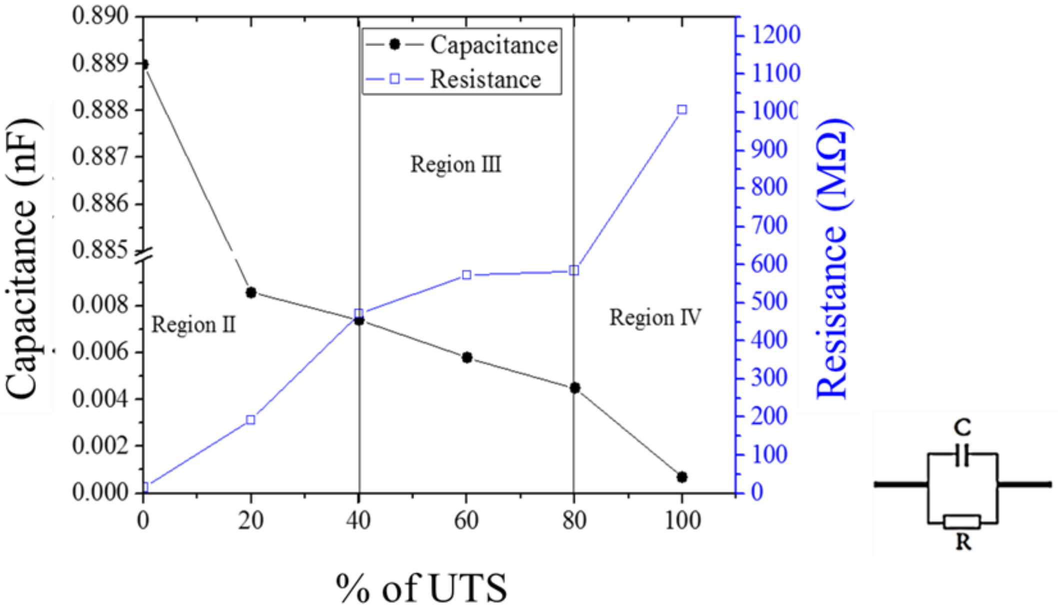

Figure 2.24 Equivalent RC circuit: R and C vs. applied load (% of UTS)

In Figure 2.24, the equivalent capacitance and resistance versus loading level curves are presented. As can be seen, these curves can be divided into three regions which correspond to levels of mechanical damage, as described in section 2.4.2. The first IS measurement was performed at 20% of UTS which is well above region I i.e. the elastic region, so it is not directly represented in Figure 2.24. In region II, both capacitance and resistance values show abrupt changes that can be attributed to the initiation and evolution of a failure mechanism that of matrix cracking. As stated, induced microcracks (voids) destroy the conductive CNT network and as a result the total resistance of the system is increasing while the capacitance moves towards lower values. On the other hand, as tensile loading increases, saturation of matrix cracking occurs. Thus, no major differences in the aforementioned equivalent values are observed (Region III). In region IV a second and even more pronounced change in both capacitance and resistance values is noticed.

2.4.4. Hybrid GFRP - Optical Microscopy

Figure 2.25-d depict the micrographs of the loading sequence applied on the coupon. Typically, damage sequence in quasi-isotropic laminates involves the transverse cracking at 90 ° followed by shear failure of the ±45 ° and crack initiation leading to extensive interply delamination between the 90° plies and the ±45° interface. At the final stage, the failure of the 0° ply leads to the global failure of the coupon [49].

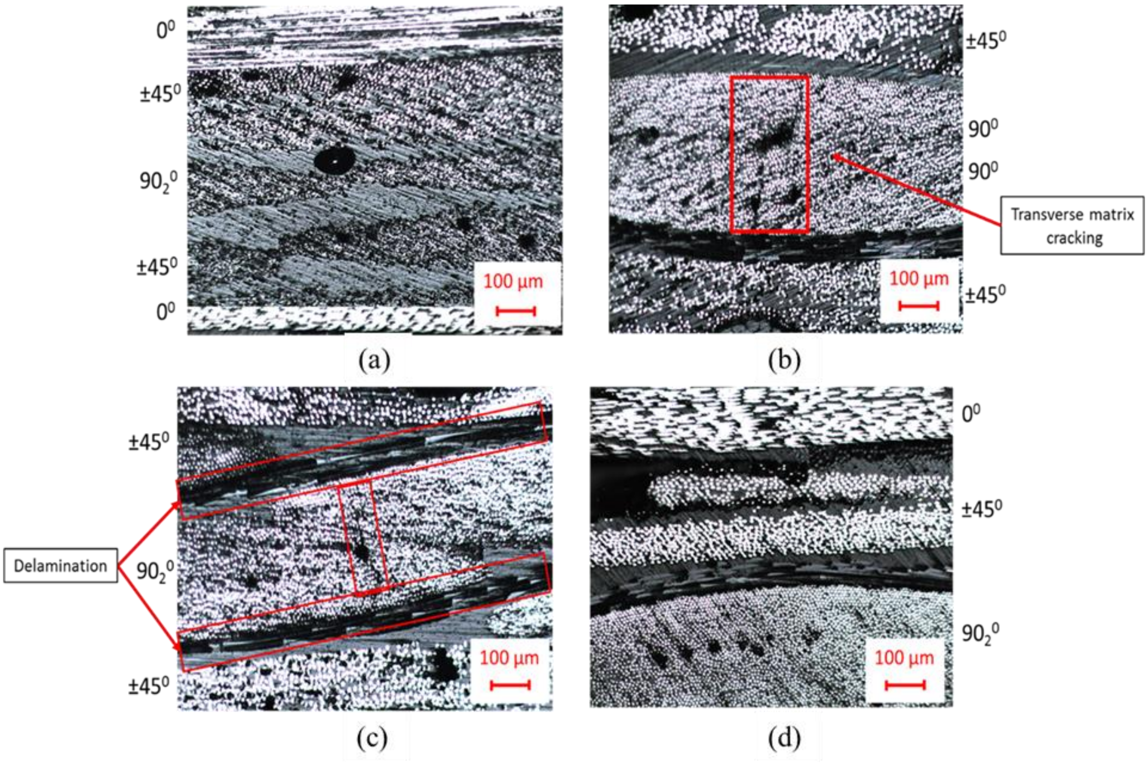

Figure 2.25 Optical micrographs from the edge of the GFRP coupon (a) undamaged specimen, (b) 40% of UTS, (c) 80% of UTS and (d) post failure

As seen in Figure 2.25, this damage sequence was indeed verified by micrographs taken in between step loading from the polished edge of the coupons. In the case of the undamaged coupon (Figure 2.25a), resin rich regions and void nuclei (entrapped gas bubbles) during the manufacturing process can be seen. As is well known, these sites may act as crack initiation sites in the absence of reinforcement. At the early stages of the mechanical testing (up to 74MPa), the dominant damage mechanism is manifested as transverse matrix cracking (region II, Figure 2.25b). At this point the magnitude of impedance exhibits the first significant increase to its values (Figure 2.22a). Incremental increase in tensile stress up to 151 MPa, resulted in an increase of the transverse crack density until saturation of matrix cracking is achieved (region III, Figure 2.25c). Figure 2.25d depicts the specimen after failure near the failure site, where large scale delaminations can be seen (region IV).

2.5. Conclusions

The scope of this work was the study of the effect of damage on the electrical hysteretic behaviour of CNT-reinforced epoxy nanocomposites. The dielectric profile of the composites was monitored using Impedance Spectroscopy (IS) over a wide frequency spectrum. IS measurements were performed employing a simple two-electrode technique. Results indicate that there is a direct correlation between the degradation of the material and the impedance data. In all examined cases, the magnitude of impedance was the most sensitive damage metric showing significant changes to its initial values at the early stages of materials degradation. It should be pointed out the incorporation of the CNTs within the insulating polymeric matrix tailored the material’s electrical response towards higher frequencies of the dielectric spectra where the estimation of dielectric parameters of the composite was not affected by the presence of electrode polarization effects.

As was shown, the electrical behaviour of the induced defects has been successfully simulated with an equivalent electrical RC circuit in parallel. The disruption of the conductive CNT network resulted in an increased total resistance while the capacitance of the system exhibited a significant decrease to its values. In the case of hybrid GFRPs, IS provided useful information about dominant damage modes that took place at specific load levels, as verified by optical microscopy.

References

[1] V. Kostopoulos, A. Vavouliotis, P. Karapappas, P. Tsotra, A. Paipetis, Damage Monitoring of Carbon Fiber Reinforced Laminates Using Resistance Measurements. Improving Sensitivity Using Carbon Nanotube Doped Epoxy Matrix System, J. Intell. Mater. Syst. Struct. 20 (2009) 1025–1034. doi:10.1177/1045389X08099993.

[2] A. Vavouliotis, A. Paipetis, V. Kostopoulos, On the fatigue life prediction of CFRP laminates using the Electrical Resistance Change method, Compos. Sci. Technol. 71 (2011) 630–642. doi:10.1016/j.compscitech.2011.01.003.

[3] D. Bekas, S. a Grammatikos, C. Kouimtzi, a S. Paipetis, Linear and non-linear electrical dependency of carbon nanotube reinforced composites to internal damage, IOP Conf. Ser. Mater. Sci. Eng. 74 (2015) 12002. doi:10.1088/1757-899X/74/1/012002.

[4] J.K.W. Sandler, J.E. Kirk, I.A. Kinloch, M.S.P. Shaffer, A.H. Windle, Ultra-low electrical percolation threshold in carbon-nanotube-epoxy composites, Polymer (Guildf). 44 (2003) 5893–5899. doi:10.1016/S0032-3861(03)00539-1.

[5] W. Zheng, S. Wong, Electrical conductivity and dielectric properties of PMMA / expanded graphite composites, 63 (2003) 225–235.

[6] Y. Huang, N. Li, Y. Ma, F. Du, F. Li, X. He, X. Lin, H. Gao, Y. Chen, The influence of single-walled carbon nanotube structure on the electromagnetic interference shielding efficiency of its epoxy composites, Carbon N. Y. 45 (2007) 1614–1621. doi:10.1016/j.carbon.2007.04.016.

[7] J. Sandler, M.S.. Shaffer, T. Prasse, W. Bauhofer, K. Schulte, a. . Windle, Development of a dispersion process for carbon nanotubes in an epoxy matrix and the resulting electrical properties, Polymer (Guildf). 40 (1999) 5967–5971. doi:10.1016/S0032-3861(99)00166-4.

[8] A. Moisala, Q. Li, I.A. Kinloch, A.H. Windle, Thermal and electrical conductivity of single- and multi-walled carbon nanotube-epoxy composites, Compos. Sci. Technol. 66 (2006) 1285–1288. doi:10.1016/j.compscitech.2005.10.016.

[9] A. Allaoui, S. Bai, H.M. Cheng, J.B. Bai, Mechanical and electrical properties of a MWNT/epoxy composite, Compos. Sci. Technol. 62 (2002) 1993–1998. doi:10.1016/S0266-3538(02)00129-X.

[10] W. Bauhofer, J.Z. Kovacs, A review and analysis of electrical percolation in carbon nanotube polymer composites, Compos. Sci. Technol. 69 (2009) 1486–1498. doi:10.1016/j.compscitech.2008.06.018.

[11] P.R. Bandaru, Electrical Properties and Applications of Carbon Nanotube Structures, J. Nanosci. Nanotechnol. 7 (2007) 1239–1267. doi:10.1166/jnn.2007.307.

[12] L. Gao, E.T. Thostenson, Z. Zhang…, Sensing of Damage Mechanisms in Fiber-Reinforced Composites under Cyclic Loading using Carbon Nanotubes, Adv. Funct. …. 19 (2009) 123–130. doi:10.1002/adfm.200800865.

[13] J.M. Park, D.S. Kim, S.J. Kim, P.G. Kim, D.J. Yoon, K.L. DeVries, Inherent sensing and interfacial evaluation of carbon nanofiber and nanotube/epoxy composites using electrical resistance measurement and micromechanical technique, Compos. Part B Eng. 38 (2007) 847–861. doi:10.1016/j.compositesb.2006.12.004.

[14] Y. Shindo, Y. Kuronuma, T. Takeda, F. Narita, S.Y. Fu, Electrical resistance change and crack behavior in carbon nanotube/polymer composites under tensile loading, Compos. Part B Eng. 43 (2012) 39–43. doi:10.1016/j.compositesb.2011.04.028.

[15] A. Todoroki, D. Haruyama, Y. Mizutani, Y. Suzuki, T. Yasuoka, Electrical Resistance Change of Carbon / Epoxy Composite Laminates under Cyclic Loading under Damage Initiation Limit, Open J. Compos. Mater. 2014 (2014) 22–31.

[16] R. Schueler, S.P. Joshi, K. Schulte, Damage detection in CFRP by electrical conductivity mapping, Compos. Sci. Technol. 61 (2001) 921–930. doi:10.1016/S0266-3538(00)00178-0.

[17] E.T. Thostenson, T.W. Chou, Carbon nanotube networks: Sensing of distributed strain and damage for life prediction and self healing, Adv. Mater. 18 (2006) 2837–2841. doi:10.1002/adma.200600977.

[18] T. Takeda, F. Narita, Fracture behavior and crack sensing capability of bonded carbon fiber composite joints with carbon nanotube-based polymer adhesive layer under Mode I loading, Compos. Sci. Technol. 146 (2017) 26–33. doi:10.1016/j.compscitech.2017.04.014.

[19] S.A. Grammatikos, A.S. Paipetis, On the electrical properties of multi scale

reinforced composites for damage accumulation monitoring, Compos. Part B Eng. 43 (2012) 2687–2696. doi:10.1016/j.compositesb.2012.01.077.

[20] A. Baltopoulos, N. Polydorides, L. Pambaguian, A. Vavouliotis, V. Kostopoulos, Exploiting carbon nanotube networks for damage assessment of fiber reinforced composites, Compos. Part B Eng. 76 (2015) 149–158. doi:10.1016/j.compositesb.2015.02.022.

[21] S.A. Grammatikos, M.-E. Kouli, G. Gkikas, A.S. Paipetis, Structural health monitoring of aerospace materials used in industry using electrical potential mapping methods, 8346 (2012) 83461K–83461K–7. doi:10.1117/12.915492.

[22] R.C. Glass, S.R. Taylor, G.L. Cahen, G.E. Stoner, Electrochemical impedance spectroscopy as a method to nondestructively monitor simulated in-service damage in a carbon fiber reinforced plastic, J. Nondestruct. Eval. 6 (1987) 181–188. doi:10.1007/BF00566846.

[23] M. Kupke, K. Schulte, R. Schüler, Non-destructive testing of FRP by d.c. and a.c. electrical methods, Compos. Sci. Technol. 61 (2001) 837–847. doi:10.1016/S0266-3538(00)00180-9.

[24] J.C. Abry, Y.K. Choi, A. Chateauminois, B. Dalloz, G. Giraud, M. Salvia, In-situ monitoring of damage in CFRP laminates by means of AC and DC measurements, Compos. Sci. Technol. 61 (2001) 855–864. doi:10.1016/S0266-3538(00)00181-0.

[25] D. a Pavlacky, V. Johnston, C. a Ulven, The Use of Electrochemical Impedance Spectroscopy to Monitor Delaminations in Polymer Matrix Composites : A Review, Int. J. Mater. Sci. 1 (2011) 23–29.

[26] G.A. Slipher, R.A. Haynes, J.C. Riddick, Mechanics of Composite and Multi-functional Materials, Volume 7: Proceedings of the 2015 Annual Conference on Experimental and Applied Mechanics, in: C. Ralph, M. Silberstein, R.P. Thakre, R. Singh (Eds.), Springer International Publishing, Cham, 2016: pp. 41–48. doi:10.1007/978-3-319-21762-8_5.

[27] F.M. Jurgen Pohl, Sven Herold, Gerhard Mook, Damage detection in smart CFRP J urgen, SMARTMATERIALS Struct. 10 (2001) 834–842.

[28] Y. Shimamura, T. Urabe, A. Todoroki, H. Kobayashi, Electrical impedance change method for moisture absorption of CFRP, Adv. Compos. Mater. 13 (2004) 297–310.

[29] D.M. Peairs, B. Grisso, D.J. Inman, K.R. Page, R. Athman, R.N. Margasahayam, Proof-of-Concept Application of Impedance Based Health Monitoring on Space Shuttle Ground Structures, (2003) 2–10. http://ntrs.nasa.gov/archive/nasa/casi.ntrs.nasa.gov/20040016326.pdf.

[30] P.D. Fazzino, K.L. Reifsnider, P. Majumdar, Impedance spectroscopy for progressive damage analysis in woven composites, Compos. Sci. Technol. 69 (2009) 2008–2014. doi:10.1016/j.compscitech.2009.05.007.

[31] P. Fazzino, K. Reifsnider, Electrochemical impedance spectroscopy detection of damage in out of plane fatigued fiber reinforced composite materials, Appl. Compos. Mater. 15 (2008) 127–138. doi:10.1007/s10443-008-9062-6.

[32] F. Kremer, A. Schönhals, Broadband Dielectric Spectroscopy, 2002.

[33] P. Ben Ishai, M.S. Talary, A. Caduff, E. Levy, Y. Feldman, Electrode polarization in dielectric measurements: a review, Meas. Sci. Technol. 24 (2013) 102001. doi:10.1088/0957-0233/24/10/102001.

[34] S. Emmert, M. Wolf, R. Gulich, S. Krohns, S. Kastner, P. Lunkenheimer, A. Loidl, Electrode polarization effects in broadband dielectric spectroscopy, Eur. Phys. J. B. 83 (2011) 157–165. doi:10.1140/epjb/e2011-20439-8.

[35] B.A. Mazzeo, A.J. Flewitt, Two- and four-electrode, wide-bandwidth, dielectric spectrometer for conductive liquids: Theory, limitations, and experiment, J. Appl. Phys. 102 (2007). doi:10.1063/1.2815666.

[36] J.C. Dyre, P. Maass, B. Roling, D.L. Sidebottom, Fundamental questions relating to ion conduction in disordered solids, Reports Prog. Phys. 72 (2009) 46501. doi:10.1088/0034-4885/72/4/046501.

[37] R.J. Klein, S. Zhang, S. Dou, B.H. Jones, R.H. Colby, J. Runt, Modeling electrode polarization in dielectric spectroscopy: Ion mobility and mobile ion concentration of single-ion polymer electrolytes, J. Chem. Phys. 124 (2006) 1–8. doi:10.1063/1.2186638.

[38] W. Scheider, Theory of the frequency dispersion of electrode polarization. Topology of networks with fractional power frequency dependence, J. Phys. Chem. 79 (1975) 127–136. doi:10.1021/j100569a008.

[39] A. Serghei, M. Tress, J.R. Sangoro, F. Kremer, Electrode polarization and charge transport at solid interfaces, Phys. Rev. B - Condens. Matter Mater. Phys. 80 (2009)

1–5. doi:10.1103/PhysRevB.80.184301.

[40] P.D. Fazzino, K.L. Reifsnider, P. Majumdar, Impedance spectroscopy for progressive damage analysis in woven composites, Compos. Sci. Technol. 69 (2009) 2008–2014. doi:10.1016/j.compscitech.2009.05.007.

[41] R. Raihan, J.M. Adkins, J. Baker, F. Rabbi, K. Reifsnider, Relationship of dielectric property change to composite material state degradation, Compos. Sci. Technol. 105 (2014) 160–165. doi:10.1016/j.compscitech.2014.09.017.

[42] D.G. Bekas, A.S. Paipetis, Study of the Effect of Damage on the Electrical Impedance of Carbon Nanotube Reinforced Epoxy Nanocomposites, J. Sensors. 2015 (2015).

[43] E. Barsoukov, J.R. Macdonald, Impedance Spectroscopy Theory, Experiment, and Applications, 2005.

[44] R. Selzer, K. Friedrich, Mechanical properties and failure behaviour of carbon fibre-reinforced polymer composites under the influence of moisture, Compos. Part A Appl. Sci. Manuf. 28 (1997) 595–604. doi:10.1016/S1359-835X(96)00154-6.

[45] G. Gkikas, D. Douka, N. Barkoula, A.S. Paipetis, Composites : Part B Nano-enhanced composite materials under thermal shock and environmental degradation : A durability study, Compos. Part B. 70 (2015) 206–214. doi:10.1016/j.compositesb.2014.11.008.

[46] G.Z. Xiao, M.E.R. Shanahan, Water Absorption and Desorption in an Epoxy Resin, J. Polym. Sci. Part B. 35 (1997) 2659–2670.

[47] M.E. Tuttle, Structural Analysis of Polymetric Composite Materials, 2004.

[48] P.K. Mallick, Fiber-reinforced composites: materials, manufacturing, and design, 2008. doi:10.1016/0010-4361(89)90651-4.

[49] D. Tsamtsakis, M. Wevers, P. De Meester, Damage Monitoring during Monotonic Tensile Loading of Quasi-Isotropic Carbon Epoxy Laminates, Mater. Sci. Forum. 210–213 (1996) 125–132. doi:10.4028/www.scientific.net/MSF.210-213.125.

CHAPTER 3

Carbon Nanotubes reinforced polymeric healing agents for vascular self-repairing composites

3.1. Introduction

Similar to blood vessels in biology, vascular self-healing systems incorporate healing agents into a polymer matrix through micro-channels. As can be seen in Figure 3.1 the design cycle for vascular networks takes into account several important issues regarding to mechanical characterization, the triggering mechanism and the healing performance

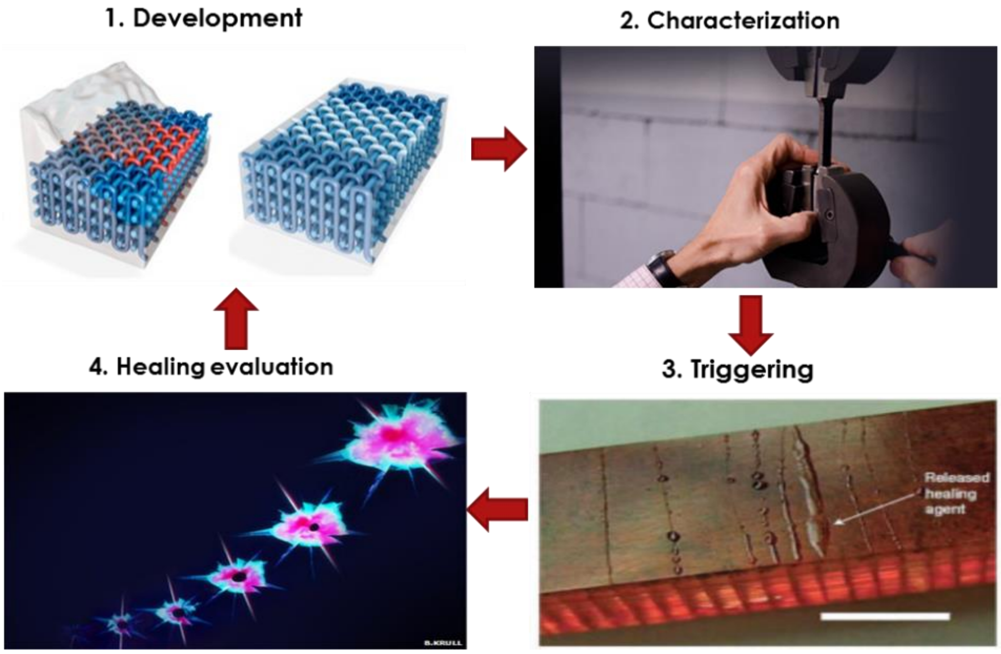

Figure 3.1 The design cycle for vascular self-healing materials

The original idea as proposed by Toohey et. al. [1], concerned the incorporation of a microchannel network containing dicyclopentadiene (DCPD) in the material that is capable of delivering DCPD to an epoxy surface coating containing Grubbs' catalyst Figure 3.2. Over the last years, the bio-mimetic vascular self-healing Fiber Reinforced Polymers, have been extensively studied due to the variety of healing agents that can be employed and the large scale of damage that can be healed, spanning from matrix cracks to large scale delamination.

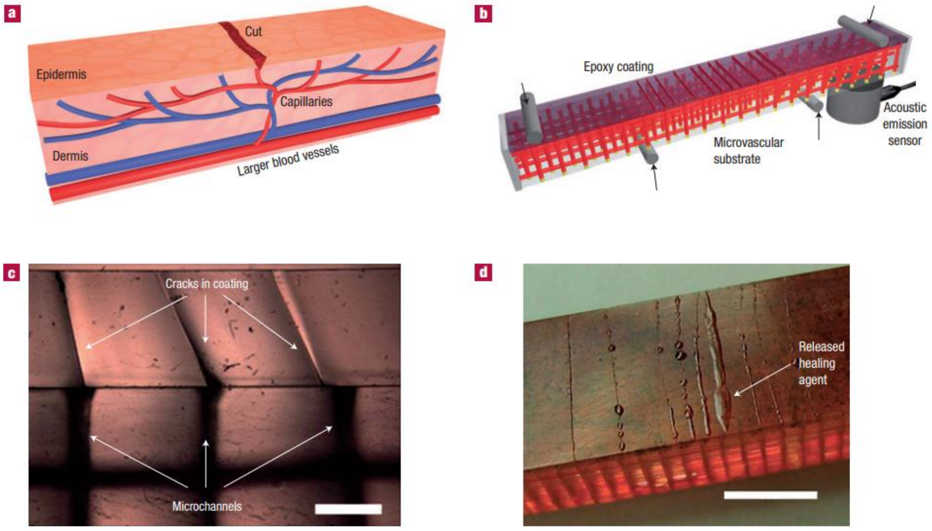

Figure 3.2 Self-healing materials with 3D microvascular networks. a, Schematic diagram of a capillary network in the dermis layer of skin with a cut in the epidermis layer. b, Schematic diagram of the self-healing structure composed of a microvascular substrate and a brittle epoxy coating containing embedded catalyst in a four-point ending configuration monitored with an acoustic-emission sensor. c, High-magnification cross-sectional image of the coating showing that cracks, (scale bar = 0.5 mm). d, Optical image of self-healing structure after cracks are formed in the coating (with 2.5 wt% catalyst), revealing the presence of excess healing fluid on the coating surface (scale bar = 5 mm) [1].

Patrick et. al. [2] demonstrated that in situ self-healing can be achieved in structural fiber-composites via microvascular delivery of isolated, reactive healing reactants. Diglycidyl ether of bisphenol A (DGEBA) based epoxy resin (EPON 8132) and aliphatic triethylenetetramine (TETA) based hardener (EPIKURE 3046) were used as healing agents due to their reaction kinetics and their post-polymerized mechanical properties. In order to create the microvascular network, pre-vascularized composite textile reinforcement was produced by stitching catalyst-infusion, in a precise pattern of aerospace-grade woven fabric. The fiber composite preform was then consolidated into a structural laminate via vacuum assisted resin transfer molding (VARTM) of a thermoset epoxy matrix. It is worth mentioning that after the final thermal PLA evacuation step (three-dimensional (3D) microvasculature), no significant change to fracture properties was observed. They have also shown that vascular architectures not only provide efficient and repetitive delivery of healing agents, but they also contribute to increased resistance to delamination initiation and propagation. The two variations of 3D vascular architectures that were fabricated in this work are depicted in Figure 3.3.

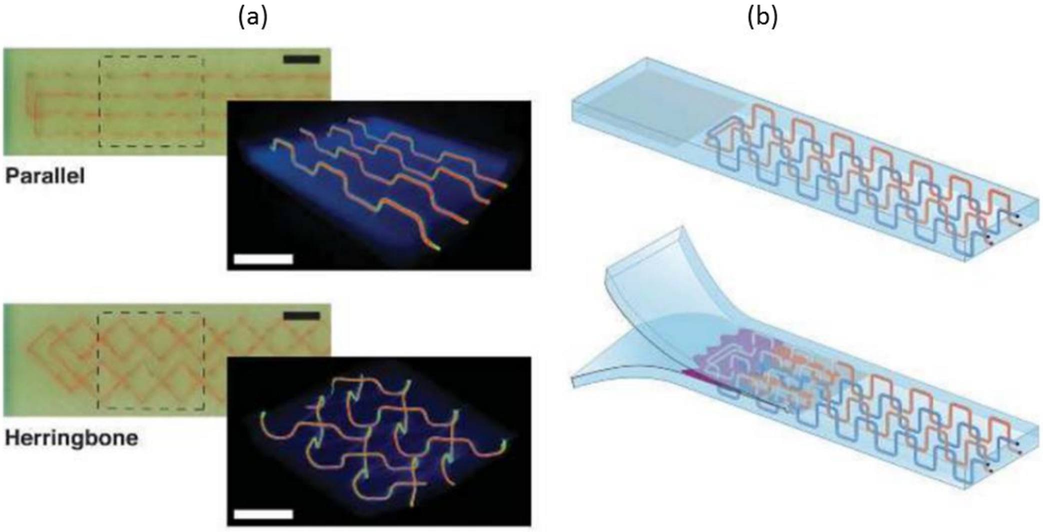

Figure 3.3 (a) Pre-vascularized, fiber-reinforced composite laminate samples showing sacrificial PLA stitching patterns (scale bars = 10 mm) and post-vascularized, X-ray computed microtomographic reconstructions of vascular networks filled with eutectic gallium-indium alloy for radiocontrast (scale bars = 5 mm). b) Schematic of microvascular double cantilever beam (DCB) fracture specimen with dual channel (red/blue) vascular network where fracture triggers release of liquid healing agents from ruptured microchannels [2].

In another study by Norris et al [3], a vascular network was fabricated which combined damage sensing and healing capabilities within an advanced FRP composite. When these vascules were ruptured, due to a low-velocity impact event, the damage was detected using pressure sensors triggering the delivery of a low-viscosity epoxy healing agent from an external reservoir, to the damage site.

In a similar work R.S Trask and co-workers [4] presented the construction of a combined sensing and healing vascular network within an advanced FRP composite. Poly(tetrafluoroethylene) (PTFE)-coated steel wires used in order to create the microvascular network inside a fiber reinforced polymer composite. A low-pressure sensor was directly connected within the perceived damage zone, while the output signal of the sensor was monitored via open-source microprocessors. The laminates were subjected to a 10-J energy impact and the healing agent was delivered through a pump from an external reservoir Figure 3.4. Two different healing chemistries were tested, a commercial system ResinTech RT151 and the well-known epoxy based system of DGEBA, ethyl phenylacetate (EPA) and diethylenetriamine (DETA) resulting to a recovery of 91% and 94% in post-impact compression strength, respectively.

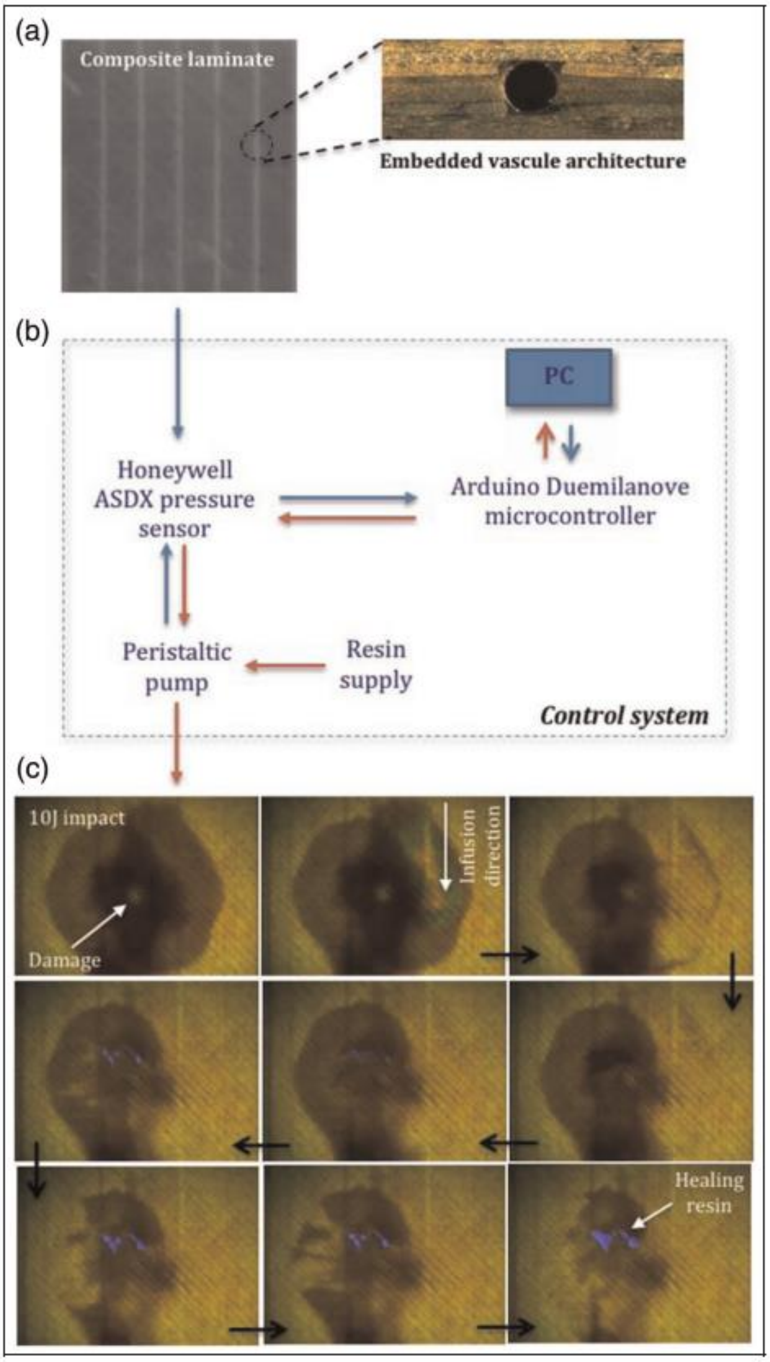

Figure 3.4 Damage sensing and healing agent delivery system in fibre-reinforced composites: (a) schematic illustration of coordinated damage detection and autonomous self-healing, (b) schematic illustration of the electronic control system and (c) healing agent infusion sequence from a single point of entry (the pigmented RT151 healing resin is observed to migrate through the laminate cracking and ’pool’ on the surface, as indicated by the arrow in the last photograph) [4].

In another work, the effect of microvascular channels on the in-plane tensile properties and damage propagation in a 3D orthogonally woven/glass epoxy has been successfully described by Coppola et al. [5]. Using Vaporization of Sacrificial Components (VoSC) process they managed to produce composites consisted of two-part epoxy matrix with straight and wave shaped channels (Figure 3.5). Sacrificial fibers (SF) were prepared using poly(lactic acid) (PLA) monofilament fibers treated with tin(II) oxalate (SnOx) catalyst so as to decrease their thermal degradation temperature. SF removed during the post-curing process leading to an insignificant alteration on the tensile properties, strength and modulus of the composite material.

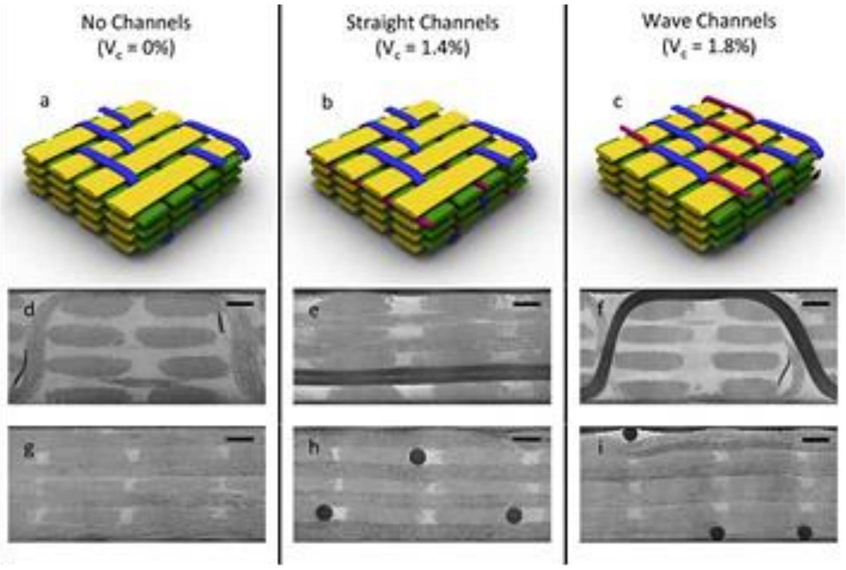

Figure 3.5 (a–c) Schematics of the unit cell of the preforms. Optical micrographs show surfaces (d– f) normal to the warp direction and sur faces (g – i) normal to the weft direction. Scale bars represent 1 mm [5].

A. R. Hamilton et al. [6] reported the use of active pumps that can deliver a two-part healing system (Epon 8132/Epikure 3046) inside a material through microvascular networks. This technique allowed a small vascular system to deliver large volumes of healing agent to the damaged area. Moreover, dynamic pumping resulted to an enhancement of components mixing in the target region, improving with that way the self-healing efficiency.

The construction of self-healing materials with embedded ternary interpenetrating microvascular networks by direct-write assembly of fugitive inks has been reported by Hansen and his team [7]. The matrix material consisted of a two-part epoxy system DGEBA (EPON 8132) and an aliphatic amidoamine (Epikure 3046) as hardener. It is noteworthy that they managed to accelerate the recovery of mechanical properties of the resin by exploring the effect of temperature on the healing reaction kinetics of the healing agent. They have managed to reduce the healing times by over an order of magnitude.

The use of Hollow Glass Fibers (HGFs) filled with a single component epoxy resin (Envirez 70301) in e-glass/epoxy composites has been reported by S. Zainuddin et al.

[8]. The matrix consisted of a two-part epoxy system. Part-A was a blend of DGEBA, aliphatic deglycidylether and epoxy terminated polyether polyol. The curing agent (Part-B) was a mixture of 70– 90% cycloaliphatic amine and 10–30% polyoxylalkylamine. A commercially available woven fabric oriented in two directions (warp at 0^o and fill at 90^o) was used as reinforcement. Figure 3.6 depicts the fabrication of composite embedded with HGFs. Using this methodology the managed to achieve significant regaining of the mechanical properties after multiple Low Velocity Impact (LVI).

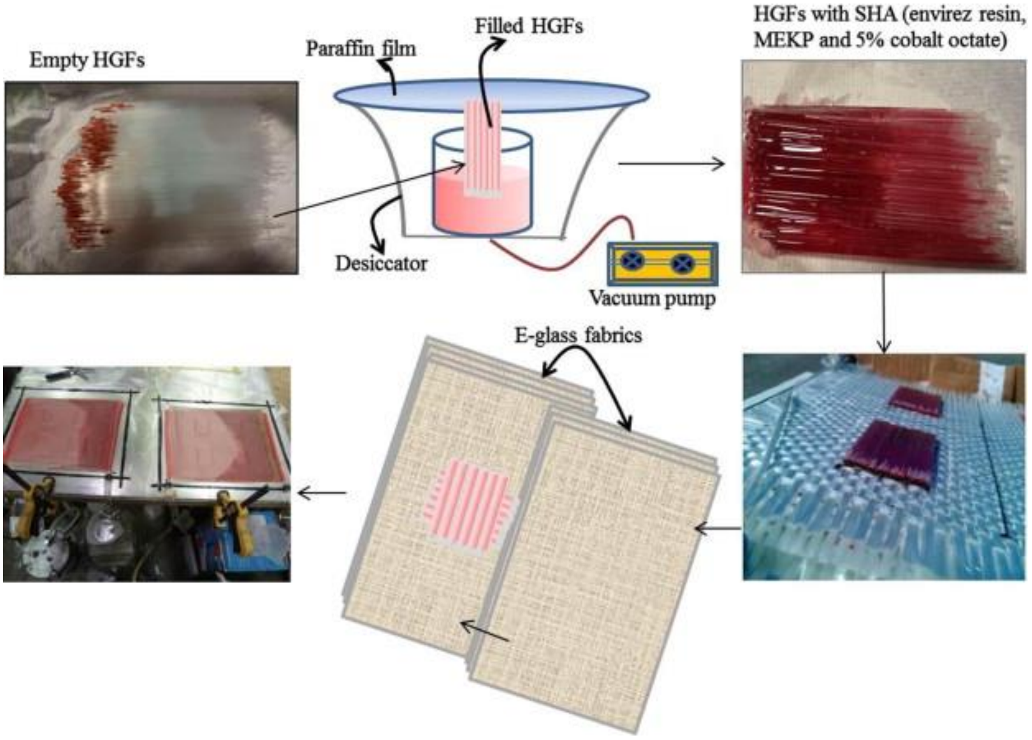

Figure 3.6 Filling of HGFs and fabrication of e-glass/epoxy composite [8].

In a step closer to industrial application of vascular self-healing composites, R. Luterbacher and his co-worker [9], explored the potential of using a vascular approach in a simplified strap-lap specimen to heal delaminations initiating at the tip of the flange and to transfer this knowledge and understanding to a large panel “stringer run-out” specimen. In their work, they demonstrate that both composites structures were able to fully recover the disbond at the tip of the stringer run-out configuration. A schematic representation of the vascular composite structures is depicted in Figure 3.7.

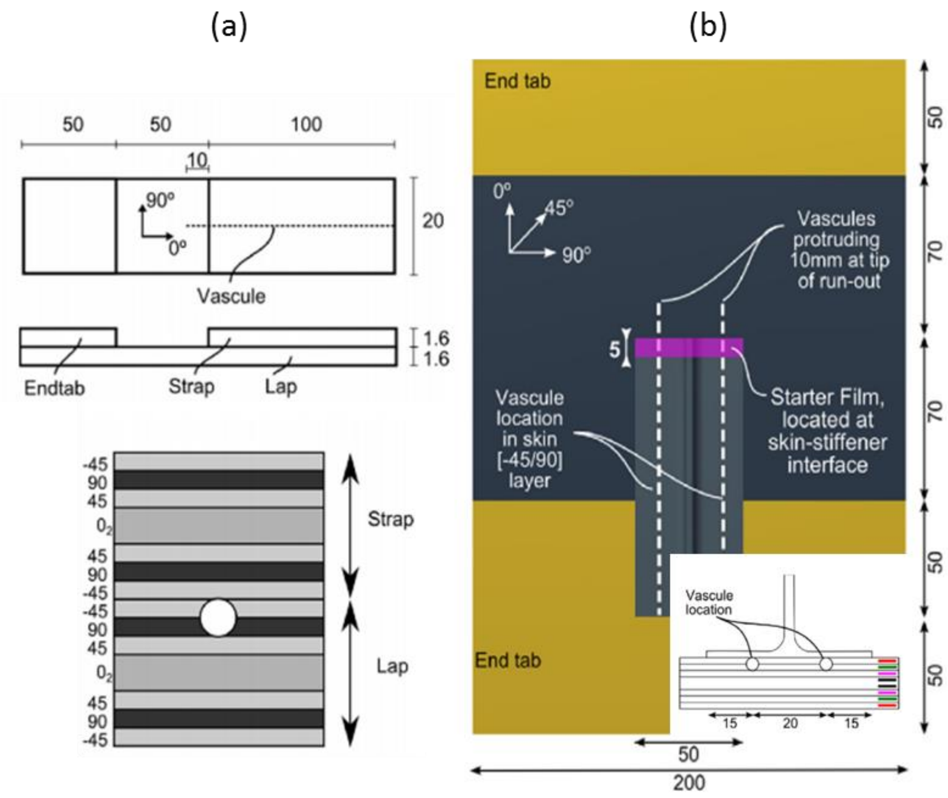

Figure 3.7 Schematic representation of (a)la-strap and (b) Stringer run-out specimen [9]

In a recent study, Coope et al [10] presented a vascular self-healing FRP composite, capable of recovering its initial fracture toughness after Mode I crack opening displacement, by employing a Lewis acid-catalyzed epoxy self-healing agent. The viscosity of the epoxy was adjusted using ethyl phenylacetate (EPA) solvent, while the vascular network was created parallel to the fiber direction using poly(tetrafluoroethylene) (PTFE)-coated steel wires Figure 3.8.

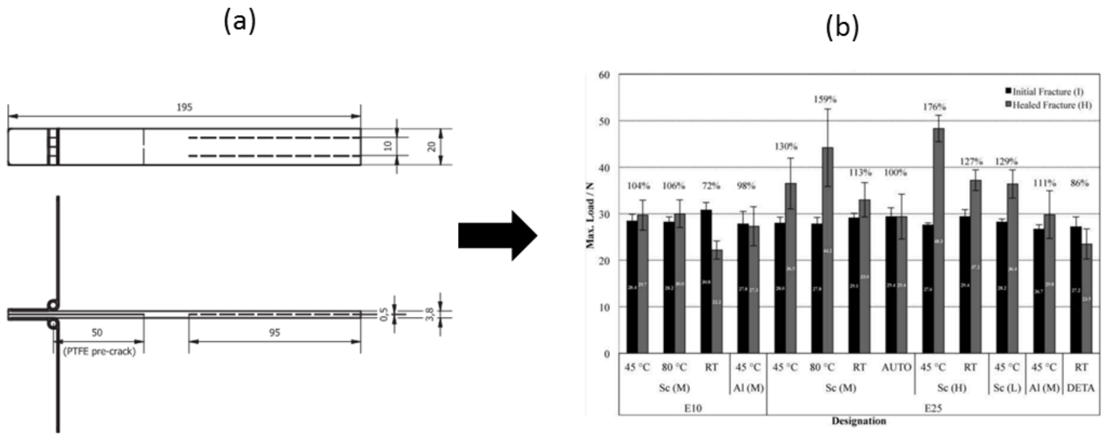

Figure 3.8 (a) Double cantilever beam (DCB) Mode I specimen geometry, (b) Healing performance for maximum load [10]

It is evident that one of the most critical aspects that affect the development of a smart and efficient vascular self-repairing composite structure is the selection of a proper healing agent. The delivery mechanism, as well as the physical and chemical properties (i.e. viscosity, curing time etc.) of the healing agents, are fundamental to the repairing process as well as to the restoration of the mechanical properties of the composite.

An unwanted side effect of the healing process in vascular FRPs is that the damaged area (i.e. delamination) inevitably becomes a resin rich region which may act as a crack initiation site due to the absence of primary fiber reinforcement. A reliable route towards eliminating this effect, may be that of the nano-reinforcement of the infused healing agent through the incorporation of nanoscaled fillers such as carbon nanotubes (CNTs) [11]. Possessing exceptional mechanical properties, low mass density and high surface-to-volume ratio, CNTs have been proved as excellent candidates for reinforcing epoxy resins and hybrid FRP composites [12–17]. However, the addition of CNTs within an epoxy resin leads to a significant viscosity increase of the polymer system due to their high surface-to-volume ratio [18–20], a property that plays an decisive role to the effectiveness of a vascular self-healing system.

Summarizing, the scope of this work is the nano-reinforcement of a low viscosity epoxy resin via the incorporation of multi wall CNTs (MWCNTs) and the employment of this nanocomposite as a healing agent in vascular glass fiber reinforced polymer composites (GFRPs). As the rheological behavior of the healing agent is a crucial parameter in the development of an efficient self-repairing system, the viscosity of the nanomodified healing agents, has been monitored and adjusted using EPA as a solvent. The vascularized GFRPs were subjected to quasi-static mode I interlaminar fracture toughness tests, using the double cantilever beam (DCB) coupon specimen geometry, so as to examine and evaluate the effect of MWCNTs to the interlaminar fracture toughness and consequently to the healing efficiency of the system [21]. A comparative scanning electron microscopy (SEM) study on the fractured surfaces of the healed specimens was also conducted in order to gain an insight on the morphology of the laminates fracture process.

3.2. Experimental

3.2.1. Materials

A two-part low viscosity epoxy resin system, i.e. the Araldite LY 5052 and Aradur 5052, supplied by Huntsman Advanced Materials, Switzerland at a mix ratio of 100:38 by weight, was used both as the GFRP matrix material as well as the healing agent. This epoxy resin-polyamines hardener system was selected due to its low viscosity and easy impregnation of reinforcement fabrics. As a healing agent, it was modified using MWCNTs supplied by ARKEMA, France with typical diameters and lengths ranging from 10 to 15 nm and 1 to 10 μm, respectively. MWCNTs were produced via Catalyzed chemical vapor deposition (CVD). Unidirectional GFRPs were manufactured using E-glass unidirectional fabric supplied by R&G, Germany while EPA solvent was purchased from Sigma–Aldrich.

3.2.2. Specimen preparation

Initially, the influence of tube diameter in the final mechanical properties of the composite was investigated. For that purpose, two vascular laminates were manufactured and tested using two different Nylon strings with dimeters of 0.6 and 0.8 mm. After the selection of the optimized Nylon string diameter, four laminates were manufactured for each healing agent scenario (i.e. neat, doped 0.1-0.3 and 0.5+EPA), using 16-plies of unidirectional glass fabric with areal density 220gr/m^2 and lamina thickness of 0.242mm. The hand lay-up method was selected as the manufacturing process, with a curing cycle at 25 ^{0}C for 24 h and applied pressure of 10^{7}Pa while post curing took place at 100^{0}C for 4 hours under the same pressure. Spacers were used in order to achieve uniform laminate thickness of 3.9mm. As stated the vascular network within the composites was created using nylon strings (0.6 mm diameter), placed at the mid-plane of the laminate parallel to the fibers direction. An 18-μm-thick teflon release film (PTFE) was placed in the mid-thickness plane of the laminate to act as initial pre-crack according to ASTM- 5528 [21]. Figure 3.9 illustrates the manufacturing process of the GFRP laminates.

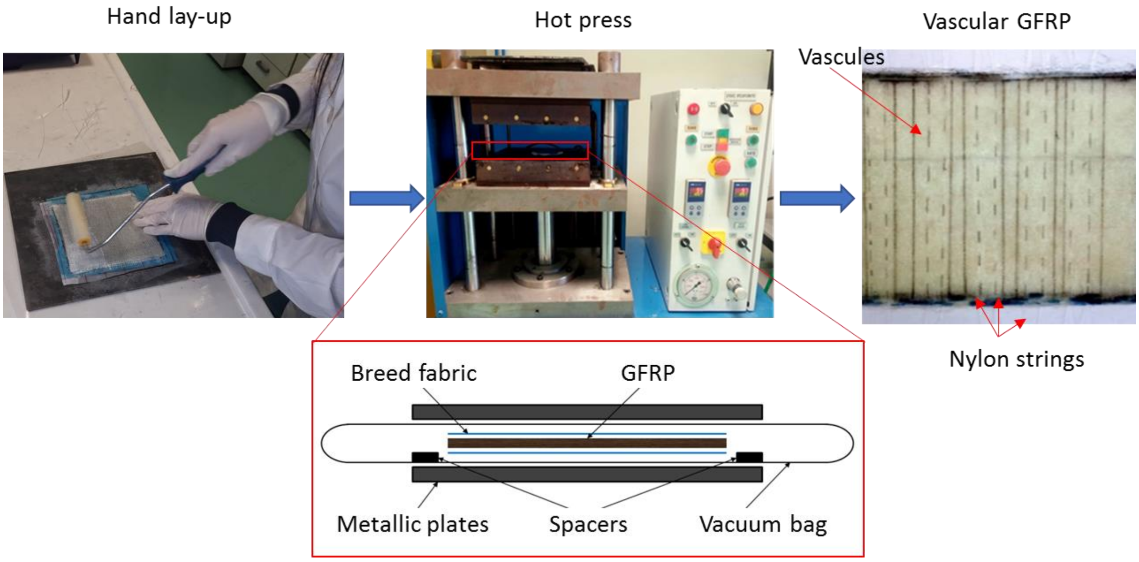

Figure 3.9 Manufacturing process

At the end of the curing process, the nylon strings were manually pulled out and the GFRP plates were cut to DCB specimen geometry. A two-part epoxy adhesive namely Epocast 52 A/Epibond 1590 was used to glue pairs of piano hinge tabs at the end of each specimen as shown in Figure 3.10. Prior to the bonding process of the end tabs, the surfaces of the laminate were roughened using sandpaper (200 grit) and cleaned with acetone.

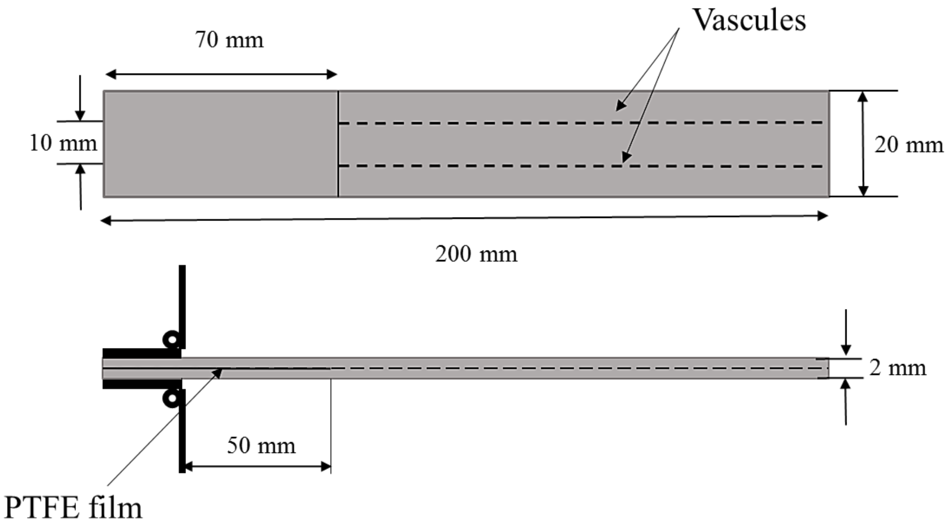

Figure 3.10 Double Cantilever Beam (DCB) coupon specimen geometry

For the modification of the epoxy healing agent, three different MWCNT contents i.e. 0.1, 0.3 and 0.5 % w.w. were selected. Dispersion of the nanofillers within the polymeric healing agent was achieved using a laboratory dissolver, i.e. Dispermat AE, VMA-GETZMANN GMBH, Germany equipped with a double-walled dispersion container

Figure 3.11. All dispersions were conducted at 2000rpm for a duration of 2 hours. In order to avoid overheating of the mixtures and avoid introduction of defects on the MWCNTs surface, the temperature during the dispersion was kept at 25 ± 1 °C using a cooling bath manufactured by Grant, UK connected to the dispersion container.

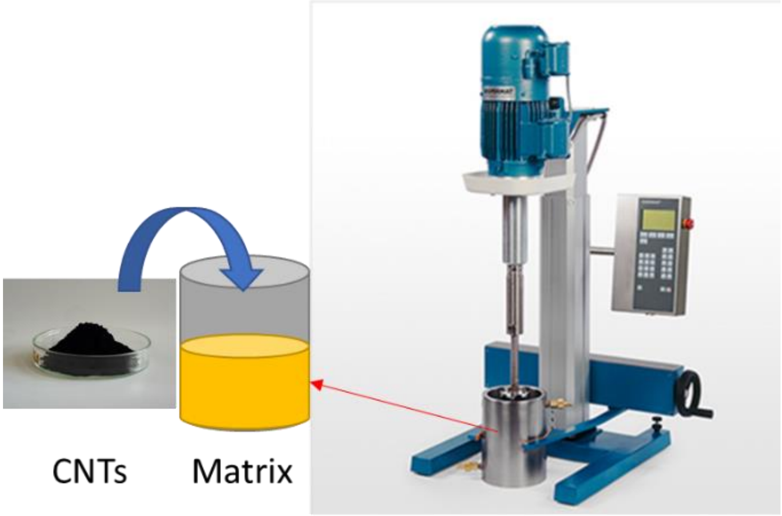

Figure 3.11 Dispersion process

Hereafter, unmodified healing agents and MWCNT modified healing agents will be denoted as neat epoxy (plain epoxy), doped-0.1 (0.1% w.w.), doped-0.3 (0.3% w.w.) and doped-0.5 (0.5% w.w.) respectively.

3.2.3. Viscosity measurements

As stated, a very important factor that affects the efficiency of a healing system is the viscosity of the selected healing agent. Therefore, it was crucial to study and adjust the viscosity of the nanomodified mixtures after the incorporation of the MWCNTs. Apparent dynamic viscosity measurements were conducted using a digital rotary viscometer NDJ-8S Figure 3.12 at 25 ^{0}C in a range of shear rates with the same spindle for all the systems so as to investigate any shear rate dependent phenomena. Each shear rate was applied for approximately 2 min in order to achieve pseudo-equilibrium and ensure data accuracy.

Figure 3.12 Viscometer NDJ-8S

3.2.4. *Differential Scanning Calorimetry (DSC)*

DSC measurements were conducted on all employed healing agents so as to examine the effect of the CNTs inclusion on glass transition temperature (Tg). All measurements were conducted in the range between 20 and 200 ^{0}C under N_2 atmosphere with a heating rate of 3^0C/min.

3.2.5. *Interlaminar Fracture Toughness Test*

Mode I crack opening displacement tests were performed using a WDW-100 Jinan universal testing machine equipped with a 100 kN load shell. All specimens were loaded at 2 mm/min while load, point displacement, and crack length were recorded. The critical mode-1 strain energy release rate, G_{IC}, was calculated using the modified beam theory (MBT) method according to ASTM- 5528 [33]. Assuming that during the mechanical testing the composite beam is not perfectly built-in, a correction factor ‘Δ’ was added to the conventional expression of the G_{IC} resulting in a slightly longer delamination length. Δ was calculated experimentally by generating a least squares plot of the cube root of compliance, $C^{1/3}$, as a function of delamination length. G_{IC} was calculated using Eq. 3.1:

$$G_{IC} = \frac{3L\delta}{2b(\alpha+|\Delta|)} \qquad (3.1)$$

where L is the applied load (N), d is the width of specimen (mm), a is the delamination length (mm), δ is the displacement (mm) and Δ is the correction factor.

3.2.6. Healing process and healing efficiency of the hybrid GFRPs

At the end of the mechanical testing, neat and doped healing agents were injected through the microvascular tubes to the fractured area using a Braun Prefusor fm syringe pump set to 0.1 ml/min steady mass flow and commercially available syringes 0.46 mm in diameter Figure 3.13.

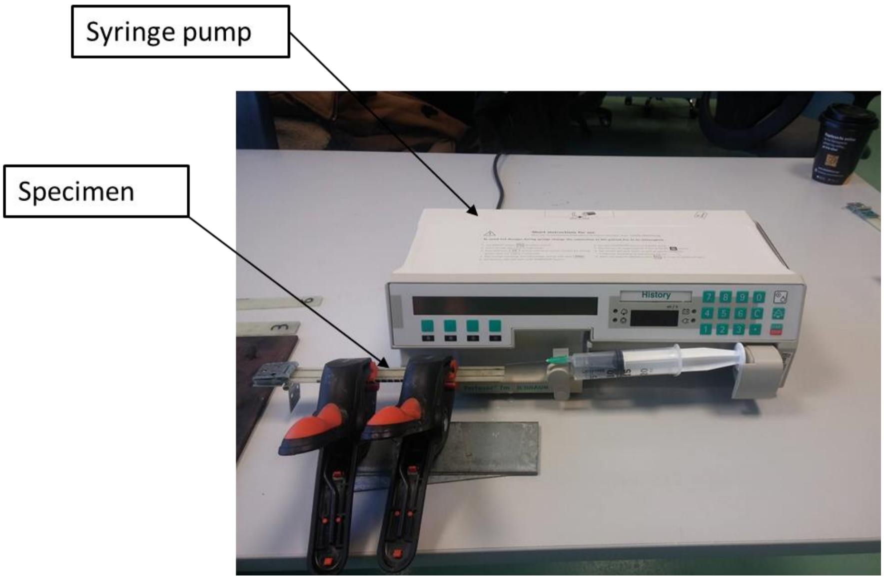

Figure 3.13 Infusion process

Prior to the injection, appropriate amount of hardener was added to the epoxy resin and the mixture was placed in a vacuum oven at 25 °C under low vacuum in order to remove any trapped air. Approximately a quantity of 0.3-0.4 mL healing agent was used to fully wet both of the crack surfaces. A high intensity commercial lamp was used to illuminate the bottom side of the specimen during the injection process in order to ensure full wettability. As can be seen in Figure 3.14 a thin nylon sheet (16μm) was placed at the mid-plane of the laminate in order to prevent wetting of the pre-crack area. During the infusion process, the composites were brought into contact using mechanical grips with negligible pressure so as to ensure that the thickness of the injected composites remained unaltered. Curing of the healed specimens was achieved by placing the laminates in an oven at 25 °C for 24h. Post curing was not applied so as to avoid any degradation in the GFRP virgin specimens.

The healed composites were then retested under the same loading conditions while the healing efficiencies of the systems were calculated based on the maximum bearing load, L_{max} (Eq.3.2) and the strain energy release rate, G_{Ic} (Eq.3.3):

$$n_L = L_{healed}/L_{virgin} \tag{3.2}$$

$$n_{G_{IC}} = {G_{IC}}_{healed}/{G_{IC}}_{virgin} \tag{3.3}$$

$G_{Icvirgin}$ corresponds to a global average obtained from virgin specimens from all 4 manufactured laminates.

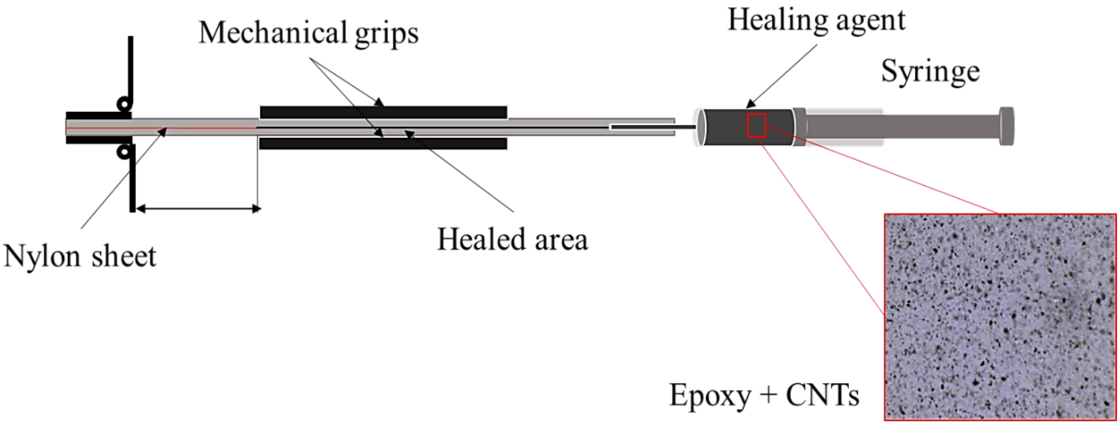

Figure 3.14 Schematic representation of the self-healing process

3.2.7. *Scanning Electron Microscopy*

SEM photographs were obtained from the DCB vascular specimens, so as to examine the effect of the manufacturing process on the tubes diameter. Afterwards were obtained were employed in order to study the fracture surfaces of healed specimens in all configurations, i.e. neat and doped healing agents, using a JEOL JSM 6510LV, Oxford Instruments scanning electron microscope. The opposite sides of the fractured surfaces, corresponding to plies 8 and 9, were cut in coupons 50x25mm and subsequently were scanned under SEM.

3.3. Results and Discussion

3.3.1. *Viscosity measurements*

In Figure 3.15, apparent dynamic viscosity vs shear rate log-log scaled diagrams for the neat and the MWCNTs modified epoxy mixtures are depicted. As can be seen, the neat epoxy resin exhibited a typical Newtonian fluid behavior with the viscosity remaining unaltered for all the measured shear rates, while the obtained value (1.52 Pa s) is in complete agreement with the one provided by the resin manufacturer. The inclusion of small weight content of MWCNTs (0.1%w.w.) increased slightly the low shear rate apparent viscosity of the solution at 1.66 Pa s but did not significantly affected the rheological behavior of the modified epoxy. Further increase in MWCNTs concentration enhanced the interactions between MWNTs and the low shear rate viscosity increased to 3.00 and 8.00 Pa s for 0.3 and 0.5 % w.w. respectively. The rheological behavior of the solutions was altered for the two latter mixtures, exhibiting shear thinning at low shear rates [22].

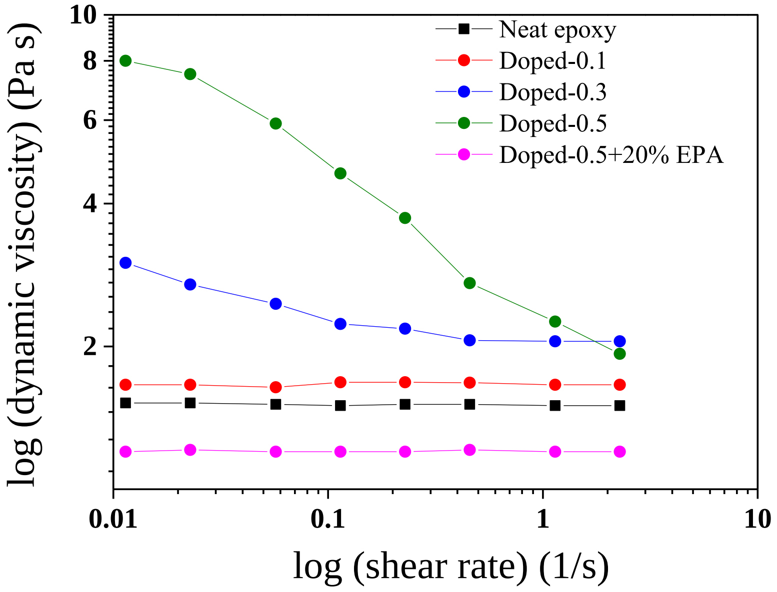

Figure 3.15 Log-log scaled diagrams of apparent dynamic viscosity versus shear rate for all the studied healing agents

As is well known when CNTs are dispersed in a polymer matrix, they gradually form an interconnected 3-D network. With increasing dispersion duration, the various sizes of CNTs aggregates are broken down until an ideal network is formed, comprised of fully disentangled CNTs. However, all relevant literature on CNTs/epoxy composites, indicate that in reality the formed network is in between these two states as CNTs are never fully disentangled. Thus, the formed network is comprised of CNTs aggregates of various sizes and individual CNTs [23].

In such a network, with increasing concentration, individual CNTs and CNTs aggregates are found to occupy the same volume which results to increased interconnections. The increased interconnections, induce a polymer chain mobility reduction due to Van Der Waals forces [24]. At higher shear rates, the viscosity increase is less prominent due to shear thinning which is attributed to the loss of these interactions between CNTs and CNTs aggregates [26].

It is interesting to note that at higher shear rates, the apparent viscosity plateaus on values close to that of the neat epoxy resin (Figure 3.15). At 0.5% w.w. filler content, the viscosity of the mixture showed a drastic increase making the aforementioned mixture an unsuitable self-healing agent in a vascular self-repairing composite. In order to decrease the viscosity of the doped-0.5 mixture and inherently assist the infusion of the healing agent via the vascular network, EPA (20% w.w.) was added to the doped-0.5 system, resulting in a mixture with a low shear rate apparent viscosity of 1.2 Pa s, characterized by a Newtonian behavior similar to that of the neat epoxy resin. This reduction in apparent dynamic viscosity, as expected, facilitated the infusion of the modified healing agent to the vascular network.

3.3.2. Differential Scanning Calorimetry.

In a parallel study, the Tg of the neat and nanomodified healing agents were measured using DSC measurements. The Tg of all systems is shown in Table 3-1 T_g values for all employed healing agent systems.

Healing agent	**T_g (^{0}c)**
Neat epoxy	49.8
Doped 0.1	54
Doped 0.3	54.9
Doped 0.5+EPA	45

As can be seen, the inclusion of the CNTs led to a marginal increase of the Tg, a phenomenon that has been extensively reported in the literature [25,26], although CNTs may also have detrimental effects to the resin properties [27]. The inclusion of the EPA led to an approximately 10% decrease of the Tg in relation to the neat epoxy. This may be attributed to the plasticization of the epoxy due to the inclusion of the solvent, which impedes the crosslinking process. This plasticization is expected to positively affect the toughness of the resin and consecutively the composite, as plasticizing agents are well known to improve the toughness of brittle matrix systems [28–30].

However, it may be assumed that as the solvent evaporates, the resin attains the properties of the neat system asymptotically. This process is rapidly evolving, as the Tg already reached 90% of its original value after 24h. Thus, the effect of the remaining EPA in the healing agent may be regarded as marginal or even negligible in relation to the G_{IC} toughness of the composite. Thus, all the employed healing agents can be considered stable at room temperature.

3.3.3. Interlaminar Fracture Toughness

Knock down effect

As stated, an initial work was conducted in order to study the effect of tube diameter to the fracture toughness of the final vascular GFRP. In Figure 3.16 representative load versus extension curves for the pristine (no vascules) and the vascular DCB specimens with tube diameter 0.6 mm and 0.8 mm are presented.

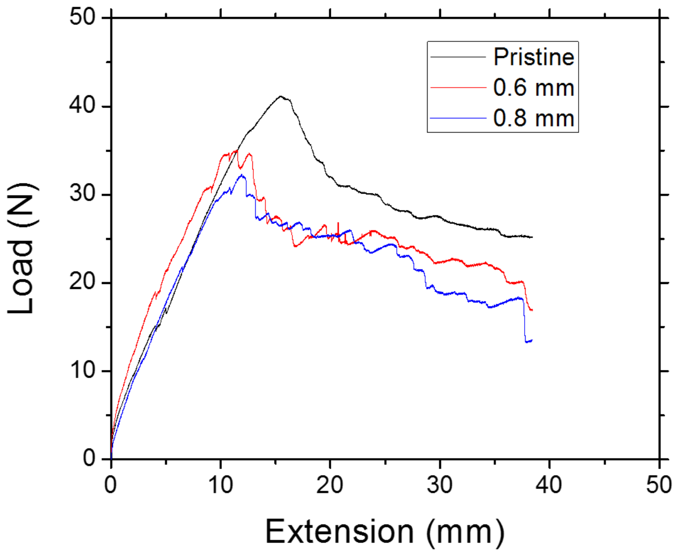

Figure 3.16 Load vs extension curves for all configurations

As can be seen, the pristine specimen has a maximum load of 41.21 N. In the case of vascular DCB specimens with tube diameter of 0.6 mm and 0.8 mm the maximum load decreases to 35.06 N and 32.33 N respectively. Therefore, the introduction of the vascular network within the GFRP, results in a knockdown effect of 14.9 % and 21.5% for the two studied tube diameters. In terms of strain energy release rate (G_{Ic}), a total reduction of 10% and 13% was observed after the introduction of 0.6 mm and 0.8 mm tube diameter respectively. In detail, the strain energy release rate of the pristine GFRP composite was calculated at 480 J/m^2 while for the case of vascular composites with tube diameter of 0.6 mm and 0.8 mm, the G_{Ic} was calculated at 435 J/m^2 and 420 J/m^2 respectively Figure 3.17.

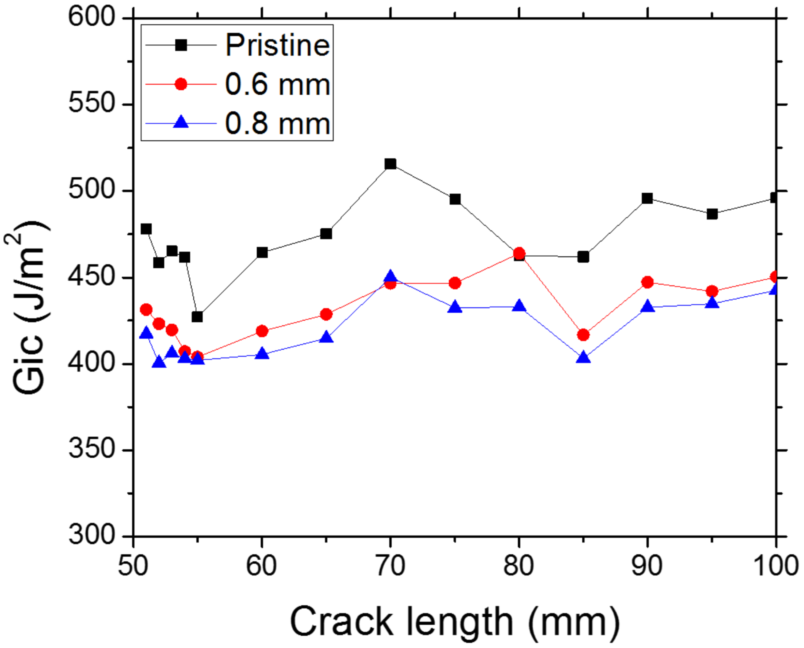

Figure 3.17 Evolution of the strain energy release rate (GIc) with increased crack length for all the studied configurations

3.3.4. Evaluation of the healing process

Figure 3.18 depicts the evolution of the strain energy release rate (G_{Ic}) with increasing crack length for all the studied self-healing composites. “Virgin” specimens were not subjected to any healing process, “Healed: Neat” specimens were healed with plain epoxy healing agent, while “Healed: Doped -0.1, -0.3 and -0.5+EPA” specimens were healed using nano-reinforced healing agents with 0.1, 0.3 and 0.5 %w.w. MWCNTs weight content, respectively. In all cases the mode-1 fracture toughness of the healed specimens was characterized by a resistive (R-curve) behavior that included an initial value of Gic followed by a region of increasing toughness until a quasi-steady-state was achieved. As can be observed, the doped-0.3 and doped-0.5+20% EPA curves exhibited a higher initiation value and a more abrupt toughening region when compared with the neat epoxy and doped-0.1 curves. In order to examine the significance of the observed differences between the fracture toughness of the neat and the modified epoxy systems, the experimental data were statistically analyzed and represented in terms of the confidence level, based on student’s t- test and the hypothesis that the examined property of the studied material equals the property of the reference material. If the confidence level is found above 99% or 95%, the measured property of the studied composite, i.e. fracture toughness, is considered significantly different than that of the reference one at the respective confidence level.

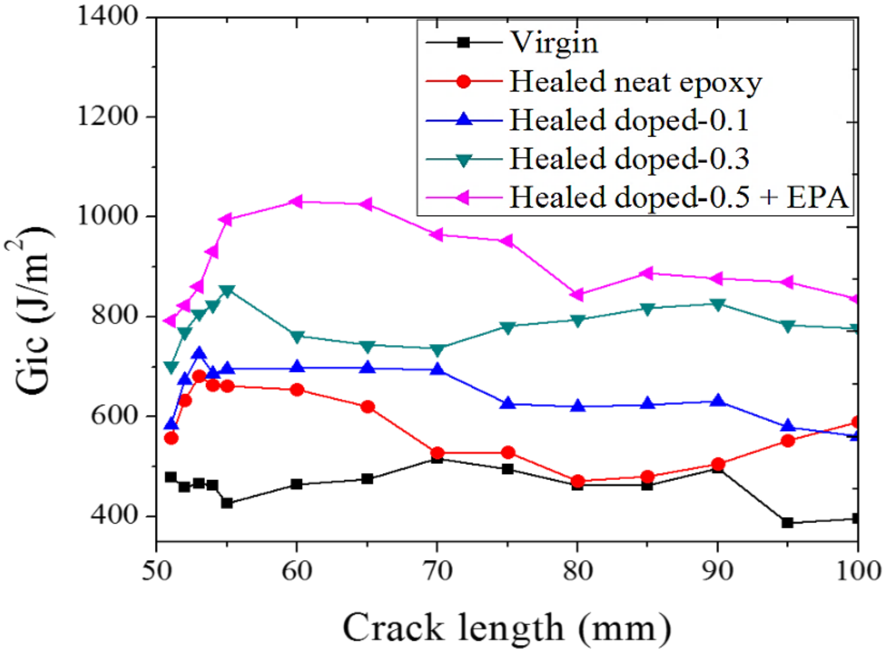

Figure 3.18 Evolution of the strain energy release rate (GIc) with increased crack length for all the studied self-healing composites

The experimental values of the fracture toughness (G_{Ic}) along with the healing efficiency values as they were calculated based on the recovery of the energy release rate, are summarized in Table 3-2. The relative difference, in terms of G_{Ic}, was calculated with respect to the virgin composite.

Table 3-2 Experimental values of the fracture toughness and the calculated healing efficiency

G_{IC} virgin (J/m^2)	**Healing agent**	**G_{IC} healed (J/m^2)**	**Healing efficiency n_{GIC} (%)**
459±28	Neat Epoxy	580 ± 108	126
	Doped-0.1	625 ± 125	136
	Doped-0.3	777 ± 101	169
	Doped-0.5 + 20% EPA	883 ± 146	192

For the case of the healed doped-0.1 composite, the relative increase in fracture toughness was 7.7 %, while the recovery of the initial fracture toughness was 136%. An increase that is not significantly different at 99% or 95% confidence level compared to that of the healed neat ($n_{G_{IC}} = 126\ \%$). On the other hand, the relative increase in toughness in the cases of healed doped-0.3 and doped-0.5 systems, was found significantly different at 99 % confidence level. In detail, the fracture toughness of the healed doped 0.3 and 0.5 composites was increased by 33.8% and 52.0% in comparison with the healed neat composite, resulting in a remarkable healing efficiency of 169% and 192% respectively. The aforementioned increase can be associated with the CNTs effect on the curing process of the epoxy and specifically on the cross-link density [31]. It has been shown that the fracture toughness of an unmodified resin, is inversely proportional to the polymer cross-link density [32], while the incorporation of CNTs within an epoxy results in reduced cross linked density [33]. Therefore, the resulted nanomodified polymers were characterized by a greater energy consumption capability.

Significant improvements, in terms of maximum load recovery, were also found for the healed doped 0.3 and 0.5 composites. Figure 3.19 depicts the maximum bearing loads for the virgin and all healed specimens. A total healing efficiency of 126 % was calculated for the healed neat composites while in the cases of healed doped-0.1-0.3 and 0.5 composites, the healing efficiencies were calculated at 136, 169 and 192 %, respectively. It must be pointed out that the doped-0.3 and doped-0.5 composites, exhibited significant increase in terms of maximum load recovery (99 % confidence level) compared with the healed neat composites.

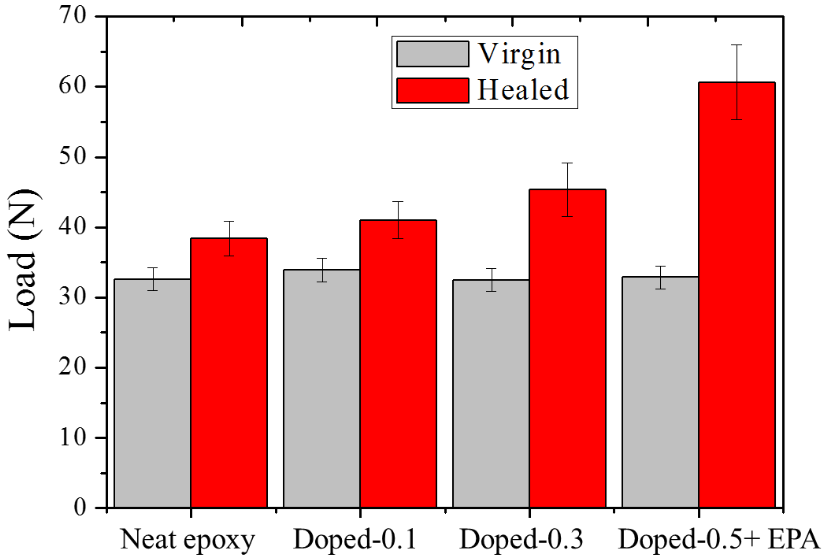

Figure 3.19 Maximum loads for the virgins and the healed vascular GFRPs.

As stated, the inclusion of the MWCNTs in the healing agents, leads to an increase in healing efficiency up to 192% in relation to the virgin specimen. Figure 3.20 reveals that η_{Gic} is a linear function of CNT ww% content.

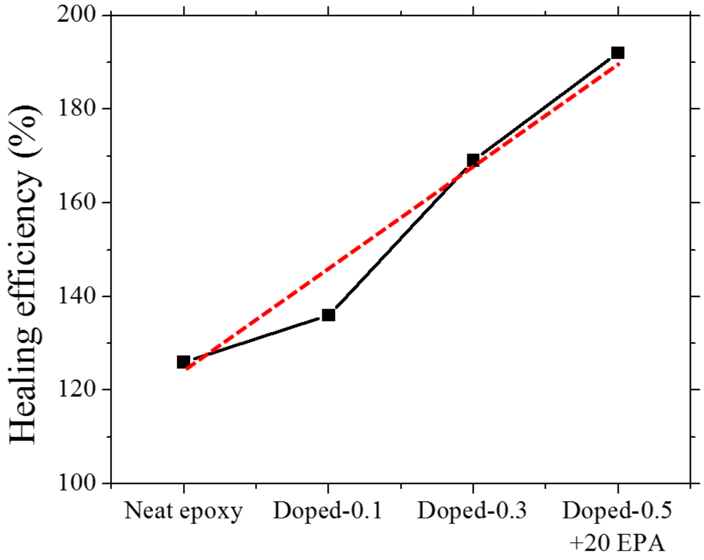

Figure 3.20. Healing efficiency vs healing agent system. Healing efficiencies were calculated in relation to the virgin specimen.

However, this dependence is technically limited by the increased viscosity which was overcome by the usage of solvent i.e. EPA in this study. The selected EPA quantity in this study (20%w.w.), resulted in the required reduced viscosity but also resulted to a marginally reduced Tg. As is indicated in similar studies, further increase in EPA weight content, could deteriorate the resulting matrix system [10].

3.3.5. SEM fractography

Figure 3.21 depicts SEM photographs obtained from the DCB vascular specimens with different tube diameter.

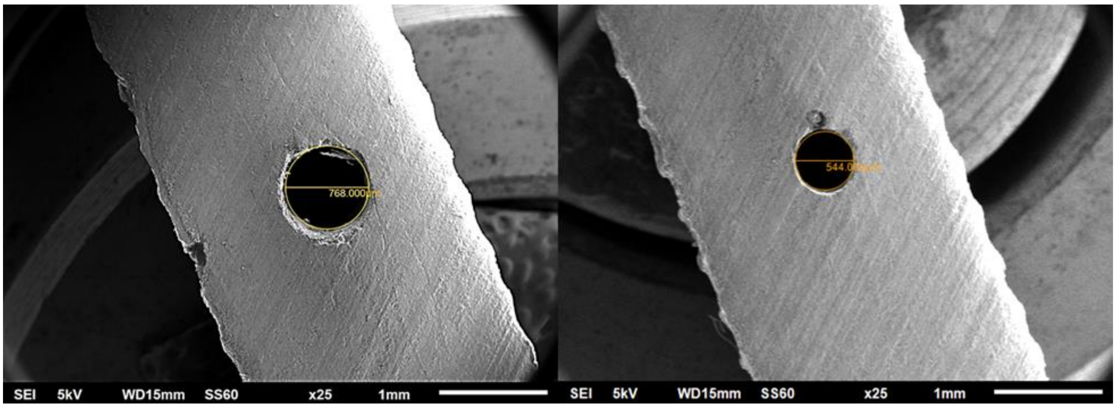

Figure 3.21 SEM photographs obtained from the DCB vascular specimens for the case of 0.8mm (left) and 0.6mm (right) diameter

A slight reduction in the diameter was observed in both cases. This reduction can be possibly attributed to the pressure applied in the manufacturing process in combination with the increase in the temperature during the post-curing process.

Figure 3.22a presents SEM micrographs obtained from fractured healed neat and doped composites. Both sides of the healed neat fractured surface in low magnification (x25) are presented in the middle section of Figure 3.22(a), while selected areas at higher magnification (x150) are presented in the left and right inserts. As can be observed, the healed neat composite failed at an adhesive manner at the glassy epoxy interface created by plies 8 and 9. On one side (left insert) of the fracture surface, only bare glass fibers can be seen while the opposite side (right insert) is essentially the imprint of the glass fibers onto the epoxy matrix. The exposed glass fibers possess smooth surfaces with no significant residues of epoxy matrix while a small amount of fractured fibers appear at the stitching direction (green arrow). The observed adhesive failure is indicative of a relatively weak epoxy/glass fiber interface. As can be seen in Figure 3.22(b-d) the fracture surfaces of the healed doped 0.1 and 0.3 specimens, revealed a completely different morphology. The healed doped-0.1 (Figure 3.22b) and healed doped-0.3 (Figure 3.22c) specimens seem to have failed in a cohesive manner at the middle of the epoxy matrix. Healed doped-0.5 specimen failed in a cohesive manner as well, while small areas of adhesive failure are present (Figure 3.22d).

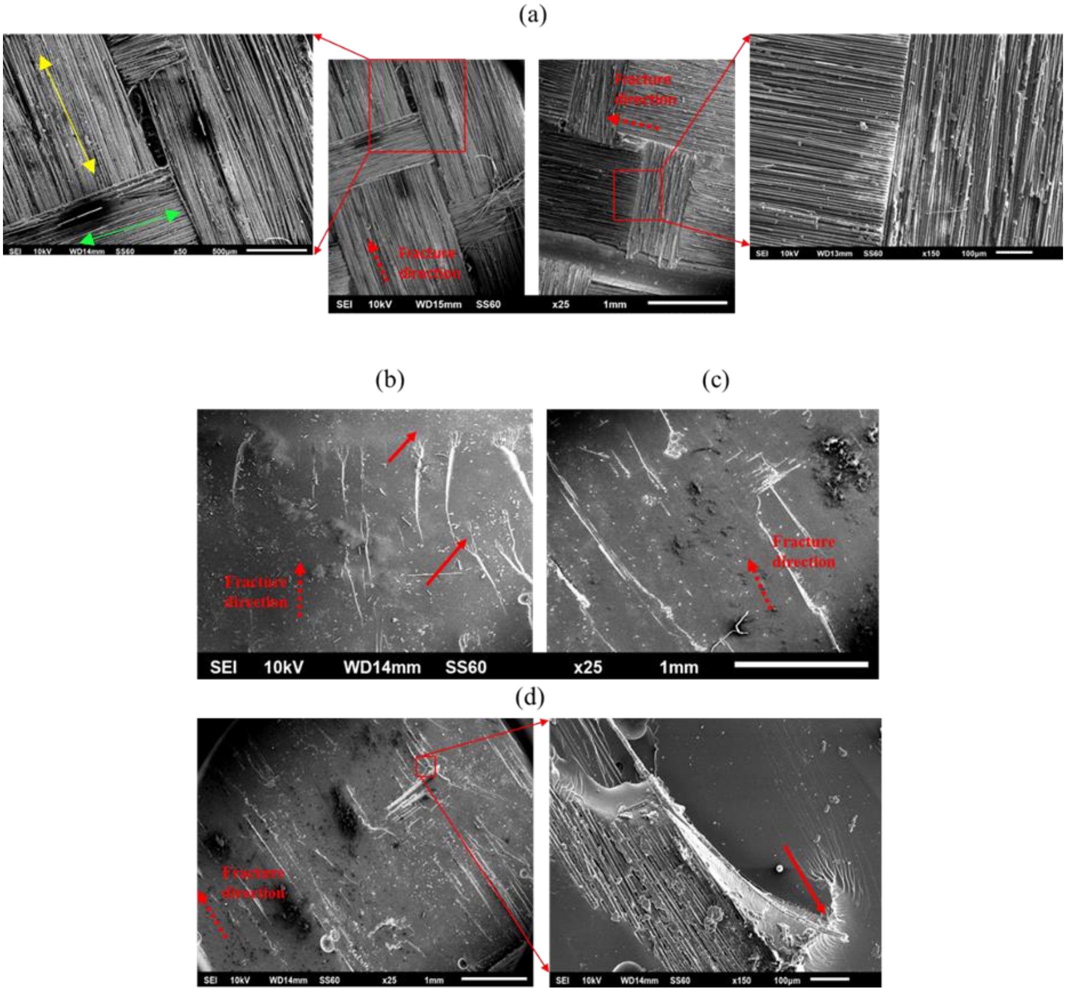

Figure 3.22 Fractured surfaces from specimens healed with (a) unmodified healing agent and modified with (b) 0.1%, (c) 0.3% and (d) 0.5% w.w. CNTs. Red arrows indicate sites of (b) crack bifurcation and (d) fiber pullout. The yellow arrow indicates the glass fiber primary reinforcement orientation while the green arrow indicates the perpendicular supporting stitching orientation of the UD fabric.

It is interesting to note that, the exposed fibers on the healed doped-0.5 specimen, were partially protected with nanomodified epoxy matrix. This behavior is a clear indication of a stronger adhesive bonding between the nanoenhanced healing agents and the virgin fractured surface due to the fact that the MWCNTs affect the epoxy and sizing coating of fibers interface, resulting in increased interfacial bond [34]. It is evident that the incorporation of the MWCNTs within the polymeric healing agent enabled different energy absorption mechanisms i.e. crack deflection and/or bifurcation that delay or hinder the crack initiation and propagation [35,36]. The additional presence of fiber pull-out and breakage phenomena in the case of healed doped-0.5 system, justified the observed increase in the fracture toughness and self-healing efficiency while simultaneously proving the effectiveness of the novel nano-reinforced self-healing system. In addition, the dissolution of the healed doped-0.5 system using 20% of EPA as a solvent, increased the plasticity of the epoxy mixture, resulting in a higher ductile failure mechanism.

3.4. Conclusions

In the present work, the employment of a MWCNT-reinforced low-viscosity epoxy as a healing agent in vascular self-healing GRFP composites, was evaluated. The effectiveness of the novel nano-modified healing agent was assessed via rheological, mechanical and scanning electron microscopy studies. The main findings of this work are:

1. The study of the rheological behavior of the healing agents (neat and doped) showed that the incorporation of small MWCNTs weight content resulted in a slight increase to the dynamic viscosity of the mixture but did not affect the rheological behavior of the epoxy. However, in the cases of 0.3 and 0.5 % w.w. MWCNTs, a significant increase to the low shear rate dynamic viscosity, up to 3.00 and 8.00 Pa s, was observed, respectively. The viscosity of the doped-0.5 mixture was adjusted using 20% of EPA as solvent, resulting in a Newtonian mixture with reduced apparent dynamic viscosity of 1.2 Pa s.
2. Results obtained from the DCB mode-1 interlaminar fracture toughness tests, indicated that in the cases of doped-0.3 and doped-0.5 systems, the relative increase in terms of fracture toughness was 33.8% and 52.0% resulting in healing efficiencies of 169% and 192%, respectively. A healing recovery that is significantly different when compared with that of the healed neat composite ($n_{G_{IC}} = 126$ %), indicating the great effectiveness of the nano-reinforced systems as healing agents for vascular self-repairing FRP composites.
3. SEM images revealed that the nanoreinforced healing agents enabled additional energy consumption mechanisms (e.g., crack bifurcation). The observed transition from adhesive to cohesive failure, indicated an enhancement of the

adhesive strength between the nanomodified healing agents and the virgin fractured surface due to the beneficiary effect of MWCNTs on the epoxy/sizing coating of fibers interfacial strength. In the case of the doped-0.5 system, the addition of the EPA solvent increased the plasticity of the epoxy mixture, resulting in a higher ductile failure mechanism.

Based on the findings of this study, the nano-reinforcement of the epoxy healing agent proved to be a highly effective route towards the recovery of the initial structural integrity of a vascular FRP composite. The best performing system was that of the healed doped 0.5 composite, where the polymer was modified via the incorporation 0.5% w.w. CNTs.

References

[1] K.S. Toohey, N.R. Sottos, J. a Lewis, J.S. Moore, S.R. White, Self-healing materials with microvascular networks., Nat. Mater. 6 (2007) 581–5. doi:10.1038/nmat1934.

[2] J.F. Patrick, K.R. Hart, B.P. Krull, C.E. Diesendruck, J.S. Moore, S.R. White, N.R. Sottos, Continuous Self-Healing Life Cycle in Vascularized Structural Composites., Adv. Mater. (2014) 1–7. doi:10.1002/adma.201400248.

[3] C.J. Norris, J.A.P. White, G. McCombe, P. Chatterjee, I.P. Bond, R.S. Trask, Autonomous stimulus triggered self-healing in smart structural composites, Smart Mater. Struct. 21 (2012) 94027. doi:10.1088/0964-1726/21/9/094027.

[4] R.S. Trask, C.J. Norris, I.P. Bond, Stimuli-triggered self-healing functionality in advanced fibre-reinforced composites, 25 (2014) 87–97. doi:10.1177/1045389X13505006.

[5] A.M. Coppola, P.R. Thakre, N.R. Sottos, S.R. White, Tensile properties and damage evolution in vascular 3D woven glass/epoxy composites, Compos. Part A Appl. Sci. Manuf. 59 (2014) 9–17. doi:10.1016/j.compositesa.2013.12.006.

[6] A.R. Hamilton, N.R. Sottos, S.R. White, Pressurized vascular systems for self-healing materials, (2011).

[7] C.J. Hansen, S.R. White, N.R. Sottos, J. a. Lewis, Accelerated Self-Healing Via Ternary Interpenetrating Microvascular Networks, Adv. Funct. Mater. 21 (2011) 4320–4326. doi:10.1002/adfm.201101553.

[8] S. Zainuddin, T. Arefin, A. Fahim, M. V Hosur, J.D. Tyson, A. Kumar, J. Trovillion, S. Jeelani, Recovery and improvement in low-velocity impact properties of e-glass / epoxy composites through novel self-healing technique, Compos. Struct. 108 (2014) 277–286. doi:10.1016/j.compstruct.2013.09.023.

[9] R. Luterbacher, T.S. Coope, R.S. Trask, I.P. Bond, Vascular self-healing within carbon fibre reinforced polymer stringer run-out configurations, 136 (2016). doi:10.1016/j.compscitech.2016.10.007.

[10] T.S. Coope, D.F. Wass, R.S. Trask, I.P. Bond, Metal triflates as catalytic curing agents in self-healing fibre reinforced polymer composite materials, Macromol.

Mater. Eng. 299 (2014) 208–218. doi:10.1002/mame.201300026.

[11] N. Domun, H. Hadavinia, T. Zhang, T. Sainsbury, G.H. Liaghat, S. Vahid, Improving the fracture toughness and the strength of epoxy using nanomaterials – a review of the current status, Nanoscale. 7 (2015) 10294–10329. doi:10.1039/C5NR01354B.

[12] B.G. Falzon, S.C. Hawkins, C.P. Huynh, R. Radjef, C. Brown, An investigation of Mode I and Mode II fracture toughness enhancement using aligned carbon nanotubes forests at the crack interface, Compos. Struct. 106 (2013) 65–73. doi:10.1016/j.compstruct.2013.05.051.

[13] L. Liu, L. Shen, Y. Zhou, Improving the interlaminar fracture toughness of carbon/epoxy laminates by directly incorporating with porous carbon nanotube buckypaper, J. Reinf. Plast. Compos. 35 (2016) 165–176. doi:10.1177/0731684415610919.

[14] P. Karapappas, A. Vavouliotis, P. Tsotra, V. Kostopoulos, A. Paipetis, Enhanced Fracture Properties of Carbon Reinforced Composites by the Addition of Multi-Wall Carbon Nanotubes, J. Compos. Mater. 43 (2009) 977–985. doi:10.1177/0021998308097735.

[15] G. Gkikas, A.S. Paipetis, Optimisation and analysis of the reinforcement effect of carbon nanotubes in a typical matrix system, Meccanica. 50 (2014) 461–478. doi:10.1007/s11012-014-9915-z.

[16] V. Kostopoulos, A. Baltopoulos, P. Karapappas, A. Vavouliotis, A. Paipetis, Impact and after-impact properties of carbon fibre reinforced composites enhanced with multi-wall carbon nanotubes, Compos. Sci. Technol. 70 (2010) 553–563. doi:10.1016/j.compscitech.2009.11.023.

[17] Z. Spitalsky, D. Tasis, K. Papagelis, C. Galiotis, Carbon nanotube-polymer composites: Chemistry, processing, mechanical and electrical properties, Prog. Polym. Sci. 35 (2010) 357–401. doi:10.1016/j.progpolymsci.2009.09.003.

[18] E.E. Uren, M.J. Kayatin, V.A. Davis, Dispersion and Rheology of Multiwalled Carbon Nanotubes in Unsaturated Polyester Resin, Macromolecules. 46 (2013) 1642–1650.

[19] S.S. Rahatekar, K.K.K. Koziol, S. a. Butler, J. a. Elliott, M.S.P. Shaffer, M.R.

Mackley, a. H. Windle, Optical microstructure and viscosity enhancement for an epoxy resin matrix containing multiwall carbon nanotubes, J. Rheol. (N. Y. N. Y). 50 (2006) 599. doi:10.1122/1.2221699.

[20] Z. Fan, S.G. Advani, Rheology of multiwall carbon nanotube suspensions, J. Rheol. (N. Y. N. Y). 51 (2007) 585. doi:10.1122/1.2736424.

[21] F.P.M. Composites, Standard Test Method for Mode I Interlaminar Fracture Toughness of Unidirectional, 1 (2013) 1–12. doi:10.1520/D5528-01R07E03.2.

[22] a. Allaoui, N.E. Bounia, Rheological and Electrical Transitions in Carbon Nanotube/Epoxy Suspensions, Curr. Nanosci. 6 (2010) 158–162. doi:10.2174/157341310790945669.

[23] Z. Fan, S.G. Advani, Rheology of multiwall carbon nanotube suspensions, J. Rheol. (N. Y. N. Y). 51 (2007) 585–604. doi:10.1063/1.2711176.

[24] S.S. Rahatekar, K.K.K. Koziol, S.A. Butler, J.A. Elliott, M.S.P. Shaffer, M.R. Mackley, A.H. Windle, Optical microstructure and viscosity enhancement for an epoxy resin matrix containing multiwall carbon nanotubes, J. Rheol. (N. Y. N. Y). 50 (2006) 599. doi:10.1122/1.2221699.

[25] Y. Zhou, F. Pervin, L. Lewis, S. Jeelani, Experimental study on the thermal and mechanical properties of multi-walled carbon nanotube-reinforced epoxy, Mater. Sci. Eng. A. 452–453 (2007) 657–664. doi:10.1016/j.msea.2006.11.066.

[26] A. Allaoui, N. El Bounia, How carbon nanotubes affect the cure kinetics and glass transition temperature of their epoxy composites? - A review, Express Polym. Lett. 3 (2009) 588–594. doi:10.3144/expresspolymlett.2009.73.

[27] K. Lau, M. Lu, Chun-ki Lam, H. Cheung, F.-L. Sheng, H.-L. Li, Thermal and mechanical properties of single-walled carbon nanotube bundle-reinforced epoxy nanocomposites: the role of solvent for nanotube dispersion, Compos. Sci. Technol. 65 (2005) 719–725. doi:10.1016/j.compscitech.2004.10.005.

[28] C. Guo, L. Zhou, J. Lv, Effects of expandable graphite and modified ammonium polyphosphate on the flame-retardant and mechanical properties of wood flour-polypropylene composites, Polym. Polym. Compos. 21 (2013) 449–456. doi:10.1002/app.

[29] S.J. Park, F.L. Jin, J.R. Lee, Thermal and mechanical properties of tetrafunctional

epoxy resin toughened with epoxidized soybean oil, Mater. Sci. Eng. A. 374 (2004) 109–114. doi:10.1016/j.msea.2004.01.002.

[30] M. Bakar, F. Djaider, Effect of Plasticizers Content on the Mechanical Properties of Unsaturated Polyester Resin, J. Thermoplast. Compos. Mater. 20 (2007) 53–64. doi:http://dx.doi.org/10.1177/0892705707068820.

[31] J. Karger-Kocsis, J. Gremmels, Use of Hygrothermal Decomposed Polyester – Urethane, J. Appl. Polym. Sci. 78 (2000) 1139–1151.

[32] G. Levita, S. Petris, a. Marchetti, a. Lazzeri, Crosslink density and fracture toughness of epoxy resins, J. Mater. Sci. 26 (1991) 2348–2352. doi:10.1007/BF01130180.

[33] M. Li, Z. Wang, Q. Liu, S. Wang, Y. Gu, Y. Li, Z. Zhang, Carbon Nanotube Film / Epoxy Composites With High Strength and Toughness, (2015). doi:10.1002/pc.

[34] E. Borowski, E. Soliman, U. Kandil, M. Taha, Interlaminar Fracture Toughness of CFRP Laminates Incorporating Multi-Walled Carbon Nanotubes, Polymers (Basel). 7 (2015) 1020–1045. doi:10.3390/polym7061020.

[35] A. Godara, L. Mezzo, F. Luizi, A. Warrier, S. V. Lomov, A.W. van Vuure, L. Gorbatikh, P. Moldenaers, I. Verpoest, Influence of carbon nanotube reinforcement on the processing and the mechanical behaviour of carbon fiber/epoxy composites, Carbon N. Y. 47 (2009) 2914–2923. doi:10.1016/j.carbon.2009.06.039.

[36] F.H. Gojny, M.H.G. Wichmann, U. Köpke, B. Fiedler, K. Schulte, Carbon nanotube-reinforced epoxy-composites: Enhanced stiffness and fracture toughness at low nanotube content, Compos. Sci. Technol. 64 (2004) 2363–2371. doi:10.1016/j.compscitech.2004.04.002.

***C*HAPTER 4**

Synthesis, characterization and evaluation of poly(urea-formaldehyde) microcapsules

4.1. Introduction

An alternative approach to achieve self-repairing polymeric materials is the incorporation of capsules within the polymer. Inside these microcapsules lies the healing agent which will be delivered to the damaged area upon rupture of the capsule. In self-healing approaches using microencapsulated healing agents, at least one component of the healing agent must be of low viscosity and capable of being stored in the microcapsules. In addition, the capsules should be easily breakable upon cracking of the matrix, thereby releasing the healing agent to the target areas via capillary effects. Subsequently, the cracked portions are repaired through chemical and/or physical interactions with the healing system. The first capsule-based self-healing concept was proposed by White et al. [1]. They embedded microcapsules containing healing agent and catalyst particles into a matrix material achieving a very promising self-healing efficiency. Since then, microcapsules were extensively studied by many researchers due to their ease of applicability and their potential for mass production. The design cycle for capsule-based self-healing materials is composed of (1) development of encapsulation technique(s), (2) integration strategies into the bulk material, (3) characterization of mechanical properties, (4) validation of damage triggering and release of healing agents, and (5) evaluation of healing performance (Figure 4.1).

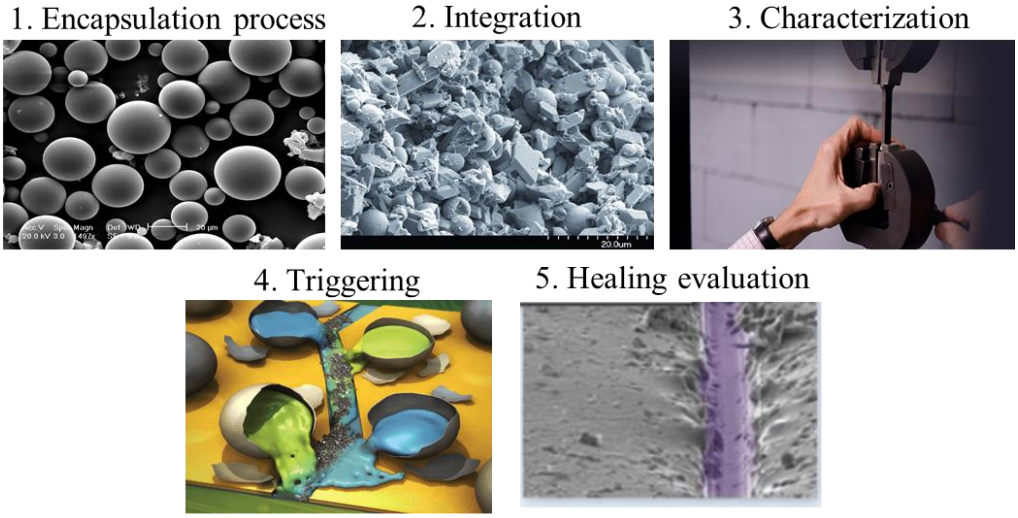

Figure 4.1 The design cycle for capsule-based self-healing materials

Among the different classes of microencapsulated healing agent systems, five types of healing systems have proven efficient (Figure 4.2).

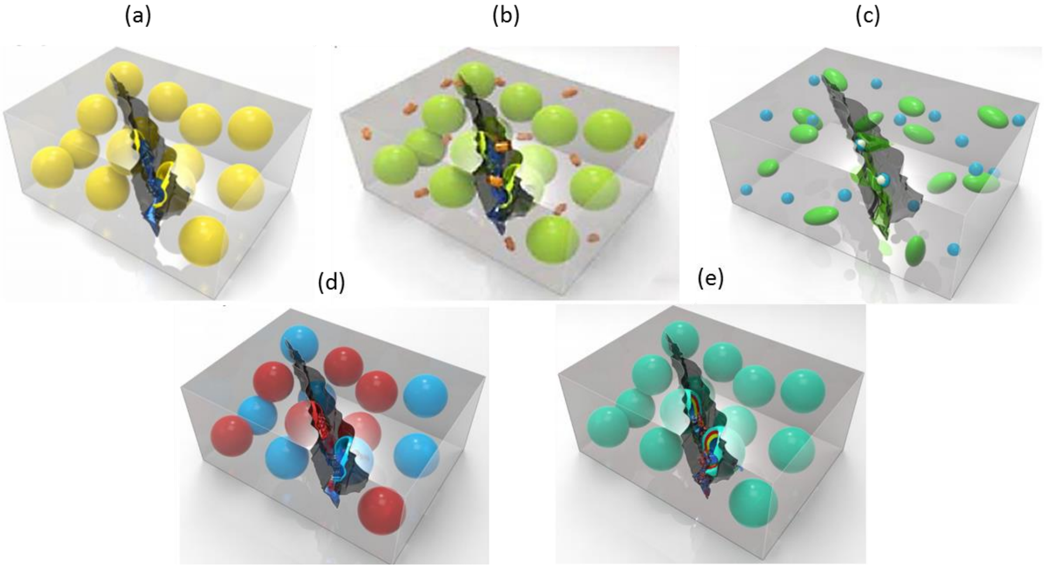

Figure 4.2 5 different types of healing systems, (a) Single capsules, (b) Capsule/dispersed catalyst, (c) Phase-separated droplet/capsules, (d) Double-capsule and (e) all-in-one microcapsules [2]

The single-capsule system consists of one type of encapsulated healing agent. The healing agent can be a reactive chemical, a solvent, or a low-melting point metal. The release of the agent initiates reactions with the functional groups of the polymer matrix like polymerization induced by the surrounding moisture environment or light, chain entanglement across the fractured surfaces, or conductive bridging. The second type of capsule-based self-healing materials that of capsule/dispersed catalyst system concerns the encapsulation of the monomer within brittle capsules and the dispersion of the catalyst within the matrix. After breakage of the microcapsules in the matrix, the released monomer and catalyst come in contact and polymerization takes place. In the third capsule-based approach (phase separation), either the healing agent or the polymerizer is phase-separated in the matrix material. These two fluids react with each other upon release. The double-capsule system is concerned with the encapsulation of one or more reactive liquid healing agents while the all-in-one microcapsules system is entirely self-contained. Both monomer and catalyst/initiator are either sequester in the core and shell wall of the same capsule and isolated from each other by layers (thus generating a multilayer microcapsule) or are encapsulated in separate smaller spheres that are stored within a larger sphere (thus generating a capsule-in-capsule). Upon rupture, the released healing agent comes in contact with the catalyst and is subsequently healing with the damaged area [3,4].

Several epoxy monomers have been easily encapsulated using various methods [5–9]. Capsule synthesis can proceed via a number of methods including layer-by-layer assembly, coacervation, internal phase separation and emulsification polymerization (Figure 4.3). In order to determine which microencapsulation technique and shell material should be adopted, the following parameters must be taken into account: properties of the core material (viscosity, Tg, etc.), capsule size, permeability of the shell, encapsulation efficiency, difference in the toughness properties and interfacial interactions between the microcapsule and polymer matrix, and processing parameters of the self-healing composite system.

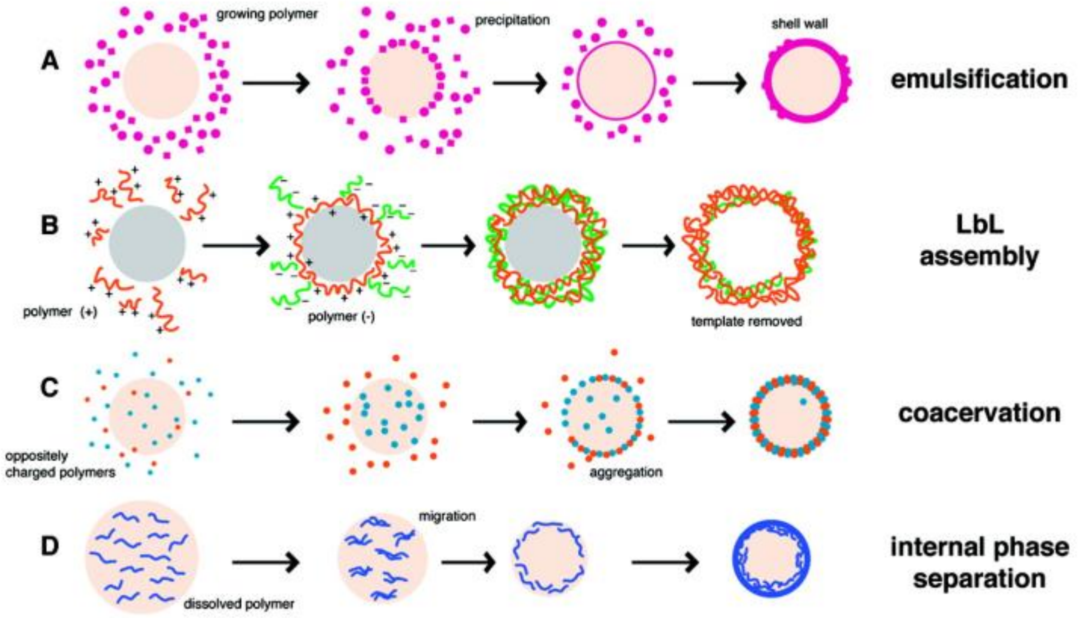

Figure 4.3 Methods for the dynamic self-assembly of nano- and microcapsules. (a) emulsification [2]

Li Yuan et al. [10] demonstrated the self-healing ability of a cyanate ester (CE) resin by the addition of microcapsules within the volume of the material. The capsules consisted of a poly(urea-formaldehyde) shell filled with an bishenol A epoxy (EP) as curing agent. Diaminodiphenylsulfone (DDS) catalyst was also used in the CE formulation to decrease the polymerization reaction temperature. Specimens exhibited an 85% self-healing efficiency proving the effectiveness of the microcapsule approach for the development of self-healing polymer materials, as well as for fiber-reinforced CE composites. Henghua Jin et al. [11] demonstrated a self-healing epoxy adhesive suitable for bonding steel substrates using DCPD filled microcapsules and Grubbs' first generation catalyst. It was noteworthy that the addition of both components to the neat resin epoxy (EPON 828) increased the virgin fracture toughness by 26% and a recovery of 56% of fracture toughness was reported.

Another possible application of capsule based self-healing is that of self-healing coatings. Capsule-based self-healing coatings have been studied by many researchers over the last three years to due to the increased importance of maintaining the potential of protection of the underlying substrate [12–16]. In detail, X. Liu et al. [17] prepared a smart self-healing coating consisted of an epoxy resin Diglycidyl Ether of Bisphenol-A (DGEBA) as matrix and microcapsules filled with the same polymer as curing agent. Capsules were synthesized by interfacial polymerization of epoxy droplets with ethylenediamine (EDA). These microcapsules exhibited high shell strength but able to rupture under external force, releasing the healing agent to the damaged area. It should be noted that the complete absence of catalyst along with the high level of healing efficiency, make epoxy-capsule loaded polymers excellent candidates for the development of self-healing films. In another study, E. Manfredi and co-workers [18] produced glass fiber reinforced polymer (CFRP) containing a solvent (ethyl phenylacetate –EPA) capsule-based healing system using vacuum assisted resin infusion molding technique. Capsules were manually dispersed into the composite and the maximum pressure threshold, in order to avoid premature capsule rupture was calculated at 0.3 bar. Optical images of the capsule-functionalised ply after undergoing different vacuum pressure differences are depicted in Figure 4.4.

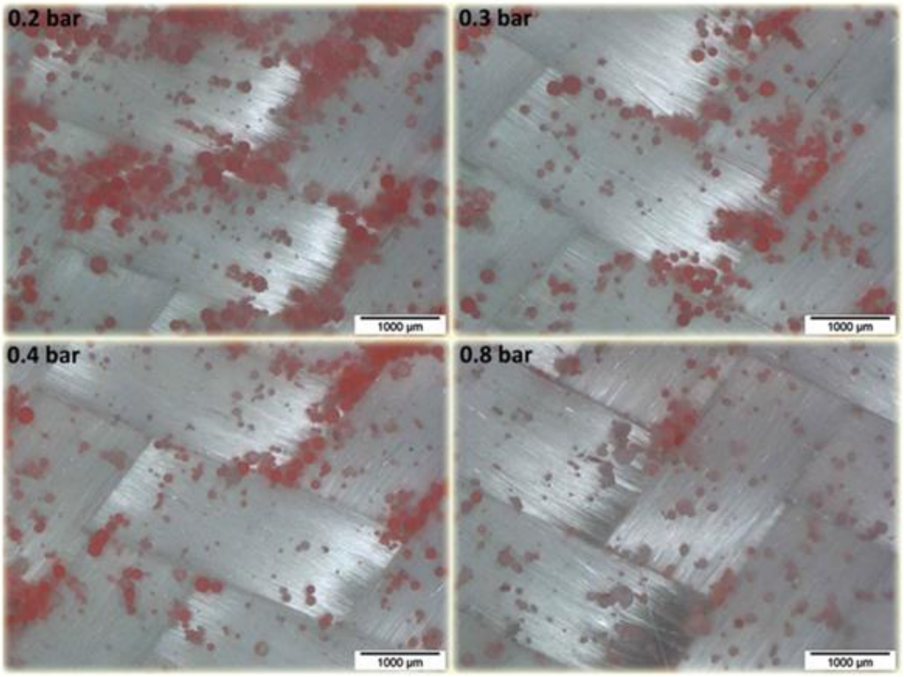

Figure 4.4 Compaction test under vacuum: optical images of the capsule-functionalised ply after undergoing different vacuum pressure [18]

It must be pointed out that the healing process is based on the swelling mechanism of the polymeric matrix (Epon 828/DETA) in the presence of EPA solvent which results in filling the defects that have been created due to static loading in Mode I and II. Using a single capsule, resin-solvent self-healing chemistry, Jones and co-workers [19] managed to obtain a full recovery of interfacial shear strength (IFSS) for a glass/epoxy composite. Microcapsules contained EPON 862 (diglycidyl ether of bisphenol-F) dissolved in EPA while the shell material consisted of poly(urea-formaldehyde) - pUF. Moreover, several parameters that can affect the healing efficiency of the system, like the resin-solvent ratio, the capsule coverage and the capsules size were also examined. Results indicated that the critical resin-solvent ratio in order to obtain submicron capsules (0.6 lm diameter) was 30:70 in which a total of 83% recovery of IFSS was reported. Figure 4.5 depicts SEM images of fibers with varying capsule coverage that have been used for the IFSS experiment.

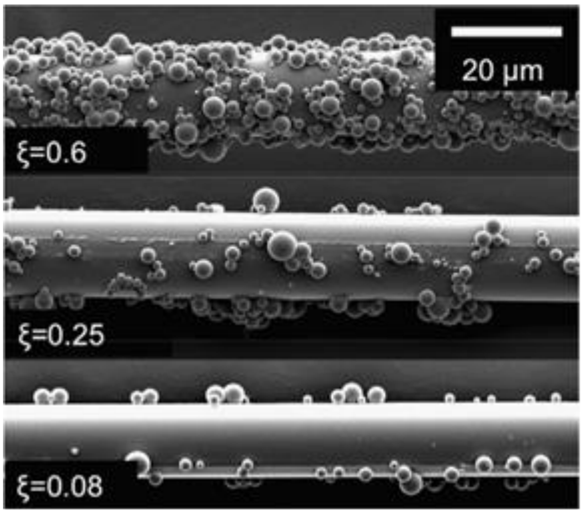

Figure 4.5 SEM micrographs of glass fibers with varying capsule loadings [19].

Dual-component microcapsules also drew the attention of the research community. As stated, the approach lies in fabricating a self-healing epoxy composite by embedding a healing agent consisting of epoxy and its hardener inside separate capsules. H. Zhang and co-worker [20] created two types of healing agent carriers, i.e. microcapsules containing epoxy solution (Epolam 5015 and hardener 5015) and etched hollow glass bubbles (HGBs) loaded with amine solution (diethylenetriamine and ethyl phenyl acetate) which they incorporated in self-healing epoxy system (Epolam 5015 and hardener 5015) (Figure 4.6).

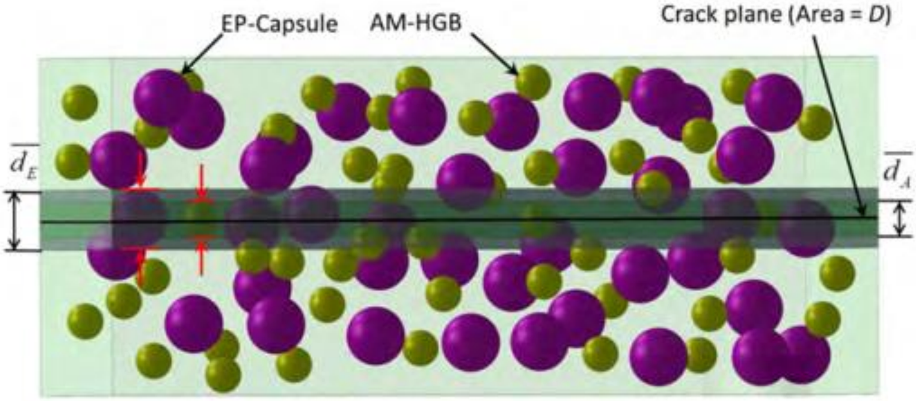

Figure 4.6 Scheme of capsules and HGBs randomly distributed in the epoxy matrix [20].

Using TGA, SEM and optical microscopy they managed to characterize both capsules and bubbles. The results indicate that the amine in the etched HGBs shows high thermal stability during the curing stage. A mathematical model has been also formulated in order to calculate the available healants and the diffusion distance on the crack plane of a two-part epoxy- amine. Based on the simple cubic array model, the diffusion distance of the released healing agent was calculated to be inversely proportional to the cubic root of the concentration of the healing agent carrier. In a more recent study, Jin and his team [21] focused on the encapsulation of epoxy and amine reactants in separate polymeric microcapsules. In the case of the epoxy resin, a polyurethane (PU)-poly(urea-formaldehyde) (PUF) double shell wall was used. The core consisted of Bisphenol-A epoxy resin diluted with a low viscosity reactive diluent (o-cresyl glycidyl ether). As for the amine capsules, they were produced following a method of vacuum infiltration of polyoxypropylenetriamine (POPTA) into polymeric hollow (PUF walled) microcapsules, demonstrating thus a simple approach for the encapsulation of a highly reactive core material. Both epoxy and amine microcapsules can be seen in Figure 4.7. Afterwards, capsules were embedded into an epoxy matrix system (Araldite/Aradur 8615) while taking into account the required stoichiometry. Maintaining the total capsule concentration at 10 wt% while varying the ratio of epoxy to amine capsules, which was at an equal mass ratio of amine:epoxy capsules (5:5), they managed to obtain the highest average healing efficiency. It was demonstrated, that higher exposure temperature caused more loss of core contents for both types of capsules leading to a poor mixing of the reactants in the damaged area.

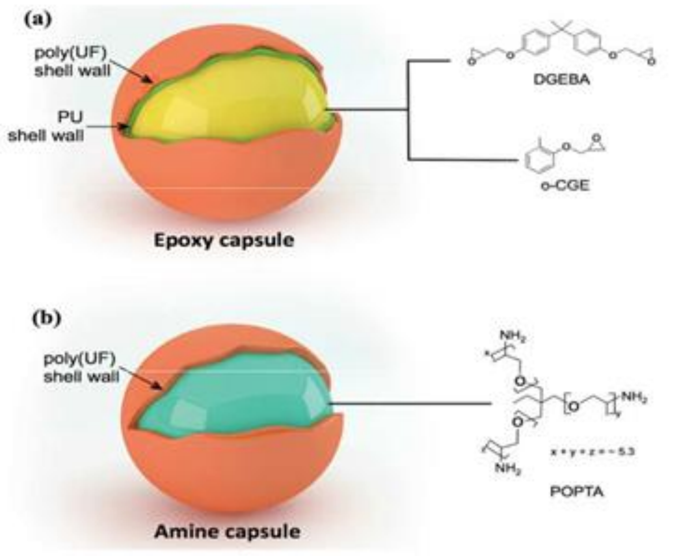

Figure 4.7 a) Epoxy capsules consist of a polyurethane – poly (UF) double shell wall and a DGEBA/o-CGE core. (b) Amine capsules contain a poly(UF) shell wall and a POPTA core [21].

Apart from the well-known poly(urea-formaldehyde)-shell microcapsules, a generalized silica coating scheme was developed by Jackson et al. [22]. In order to functionalize and protect sub-micron and micron size dicyclopentadiene monomer-filled capsules and Grubbs' catalyst particles Fluoride-catalyzed silica condensation chemistry was used for the construction of the protective and functional silica coatings resulting to an improvement of the dispersion of the capsules and catalyst particles inside the epoxy matrix. Unlike many other studies, a successful incorporation of both capsules into the epoxy was achieved without significant loss of healing agent. In Figure 4.8, a TEM image of a silica coated DCPD-filled capsule is presented.

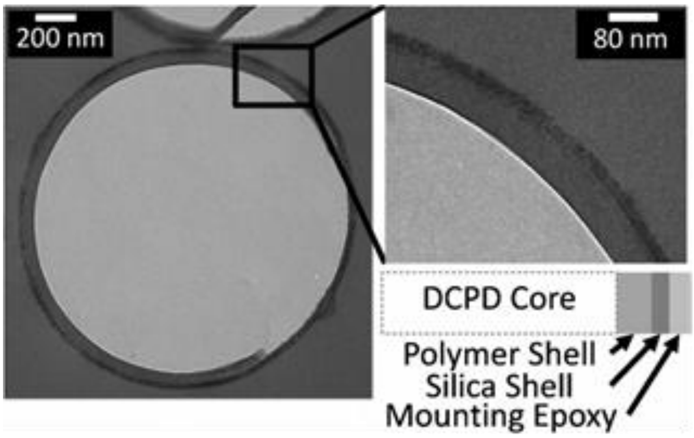

Figure 4.8 A representative TEM image of a microtomed cross - section of a silica coated DCPD -filled capsule . The DCPD core is removed during the microtoming process [22].

In an effort to improve the self-healing efficiency of epoxy resin, Qi Li and his co-workers [23] prepared a dual-component microcapsule of DGEBA and polyether amine (hardener) using a water-in-oil-in-water emulsion solvent evaporation technique with polymethyl methacrylate (PMMA) as shell material. They have shown that the healing efficiency of epoxy was affected by the content and ratio of the dual-component microcapsules. Self-healing was carried out successfully at room temperature, but, as was indicated, an increase in temperature led to higher levels of the self-healing efficiency.

A very interesting concept developed by Dong Yu Zhu and his team [24], constitutes the construction and development of a multilayered microcapsules used for self-healing thermoplastics (Figure 4.9). By optimizing the synthesis conditions, robust poly(melamine-formaldehyde) (PMF)-walled microcapsules containing fluidic glycidyl methacrylate (GMA) monomer with proper size and core content were produced. Second and third (outer/protective) layers consisted of living poly(methyl methacrylate) (PMMA -Br) and wax respectively. Results concerning the performance and stability (thermal and chemical) indicate that the multilayered microcapsules might be applicable for manufacturing not only self-healing thermoplastics but also self-healing thermosets.

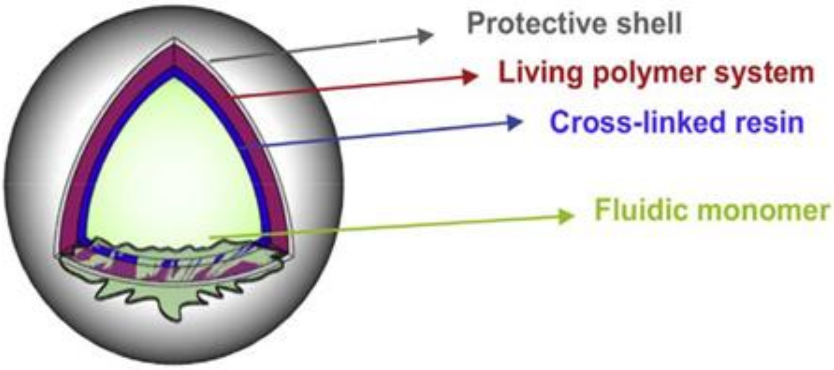

Figure 4.9 Profile of multilayered microcapsule [24].

A novel approach that concerned the implementation of a Lewis acid-catalysed self-healing system into epoxy-based fibre reinforced polymer (FRP) composite materials was investigated by Coope and his co-workers [25]. In their work, self-healing performance was quantified using a TDCB test specimen and the effects of several parameters such as the capsule content and healing temperature and time are also instigated. The Lewis acid-catalyzed self-healing epoxy resin exhibited good compatibility and adhesion between the healing agent and the host matrix, while a recovery value of greater than 80% fracture strength was reported.

In a recent study conducted by L. Hia et al. [24], alginate multi-cored microcapsules were developed and embedded into epoxy matrix to produce a capsule-based self-healing composite system. The micro capsules were produced via the electrospraying method while two different epoxy resins (EPIKOTE 828 and ARALDITE 506) were employed as core material. The produced self-healing systems were tested via fracture (TDCB geometry) and impact tests. Figure 4.10 illustrates the synthesis of the multi-core microcapsules. Results obtained from impact tests showed multiple healing events up to 3 cycles due to the controlled release of multi-core capsules system, while in the case of the TDCB specimens showed only a single healing cycle which was attributed to the slow and steady crack propagation of the test.

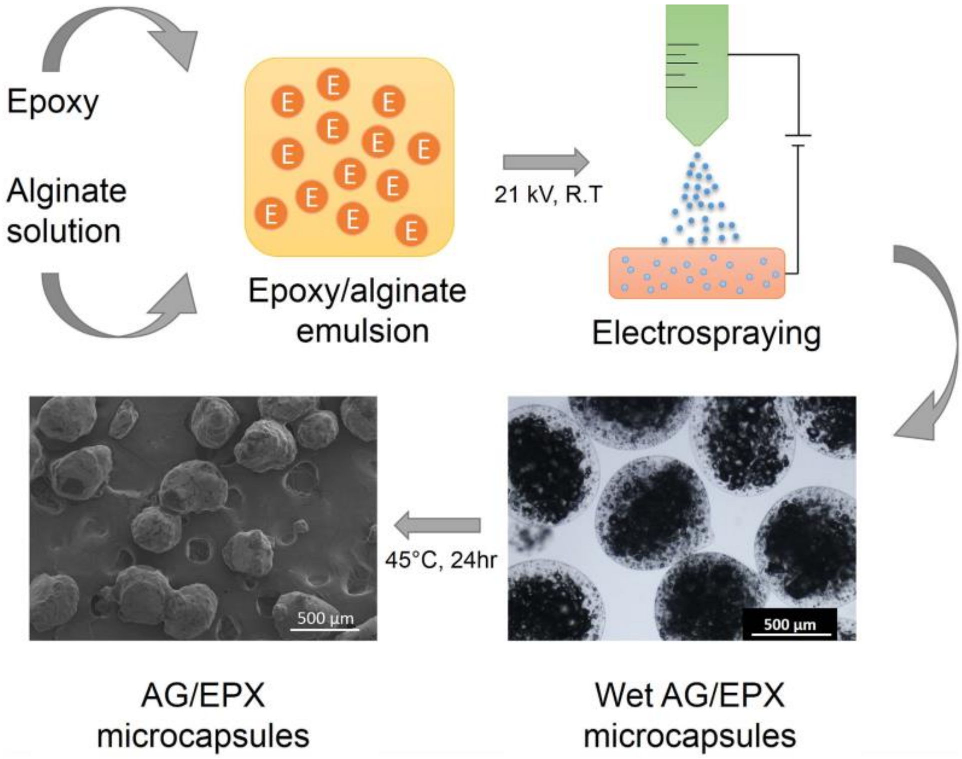

Figure 4.10 Schematic illustration of multi-core microcapsules synthesis process [24].

It is evident that capsule-based self-healing materials are more likely to be commercialized in the near future because there are no changes in the molecular structure of the host polymers, the microencapsulation has matured as a technology since its emergence in the 1950s [24] and loaded microcapsules can be easily incorporated into the polymer matrix using existing blending techniques. Therefore, continuous efforts should be devoted to this research area to facilitate large-scale application of self-healing composites.

The work related to this chapter concerns the synthesis and characterization of p(Urea-Formaldehyde) microcapsules containing DGEBA resin as core material. UF microcapsules were prepared by in situ polymerization in an oil-in-water emulsion. Characterization of the UF capsules was achieved using SEM, TGA, DSC and Raman spectroscopy. The produced capsules were then incorporated in a polymeric matrix and the evaluation of the healing efficiency was investigated using several testing configurations and geometries at (i) matrix/polymer level (Tapered double cantilever beam), (ii) composite level (mode-II fracture toughness test) and finally (ii) model composite structure level (lap strap geometry).

4.2. Experimental

4.2.1. Materials

4.1.1.1 Microcapsule materials

The solvent Ethyl phenylacetate (EPA), the wall materials urea (NH_2CONH_2), formalin (37 wt% in H_2O) the surfactant poly(ethylene-alt-maleic anhydride), (EMA, M_w 500,000), the stabilizers resorcinol (C_6H_4-1,3-$(OH)_2$) and ammonium chloride (NH_4Cl) and sodium hydroxide (NaOH) were purchased from Sigma-Aldrich and used as received. The core material or the healing agent EPON 828 was purchased from Polysciences. Inc.

4.1.1.2 TDCB specimen

EPON 828 resin, supplied from Polysciences. Inc, cured with diethylenetriamine (DETA) purchased from Sigma-Aldrich, was selected as the matrix system for the manufacturing of Tapered Double Cantilever Beam specimens. The catalyst aluminum(III) triflate ($Al(OTf)_3$) was also supplied from Sigma-Aldrich.

4.1.1.3 Glass Fiber reinforced composites – GFRP

A two-part epoxy resin system, i.e. the EPON 828 and EPIKURE 541, supplied by Huntsman Advanced Materials, Switzerland at a mix ratio of 100:50 by weight, was used both as the GFRP matrix material as well as the healing agent. E-glass unidirectional and biaxial fabric supplied by R&G, Germany as primary reinforcements.

4.2.2. Preparation of microcapsules

Although there are several microencapsulation techniques, they are not necessarily appropriate to self-healing applications, and the encapsulation method is often suited for specific types of core materials. The emulsification polymerisation method benefits from high strength capsule shell walls, large scale synthesis, thick shell wall and a narrow size distribution. ([2]). Therefore, when considering possible commercial exploitation this is the preferred method for scale-up synthesis. The principle of in situ microencapsulation oil-in-water emulsion polymerisation synthesis, as employed by self-healing material researchers, is based on the methodology employed by Brown et al. (2003) [26]. By using this setup, capsule size can be altered simply by changing the agitation rate or by introducing a sonication step during the initial synthesis. [27].

Figure 4.11depicts an outline of the in-situ polymerization in an oil-in-water emulsion that was adopted in this work for the synthesis of the UF microcapsules.

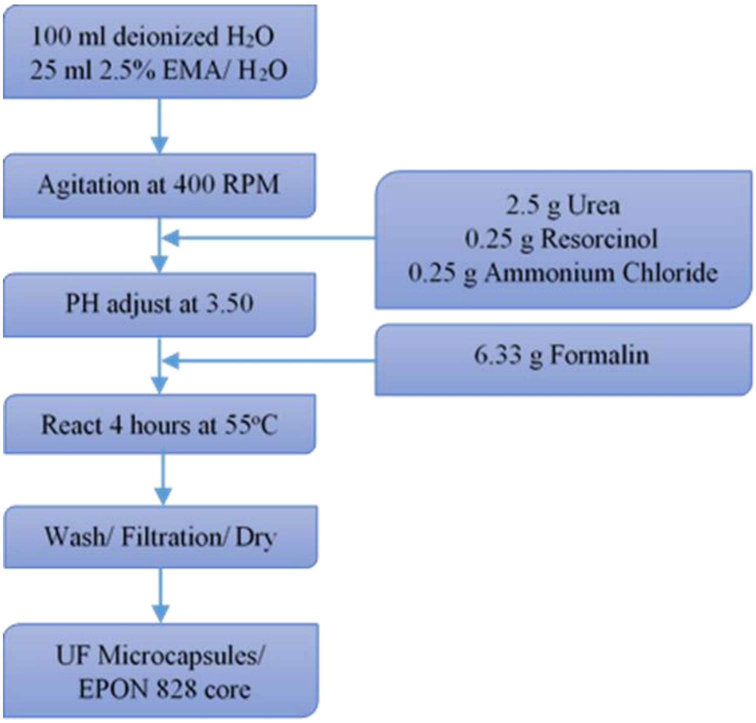

Figure 4.11 Microencapsulation of EPON 828 utilizing in situ polymerization of urea with formaldehyde to form capsule wall

In detail, 2.5 gr EMA powder was mixed overnight with 100 ml of deionized water, in a warm bath in order to achieve a 2.5% (w/v) aqueous surfactant solution (Figure 4.12).

Figure 4.12 Aqueous surfactant solution of EMA

Before the encapsulation process, the resin was diluted with a non-toxic solvent (ethyl-phenylacetate EPA) so as to decrease the viscosity of the healing agent. For the encapsulation process, 100 mL of deionized H_2O was placed in a high shear stirrer (Dispermat D-51580) with 25 mL of 2.5% (w/v) EMA aqueous surfactant solution at room temperature. The experimental set-up for the synthesis of the microcapsules is depicted in Figure 4.13.

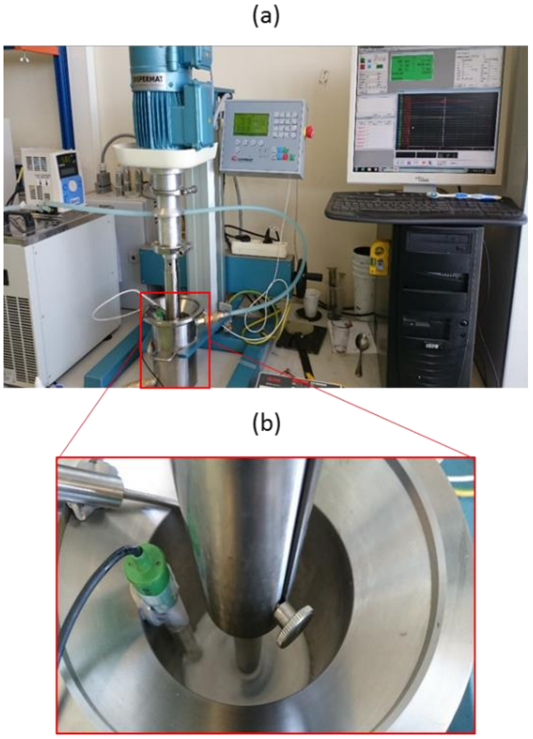

Figure 4.13 (a) experimental set-up for the UF microcapsule synthesis, (b) aqueous solution

Under continuous agitation, 2.5 g urea, 0.25 g ammonium chloride, and 0.25 g resorcinol were dissolved in the solution. After the addition of those chemicals, the pH was adjusted from approximately 2.7 to 3.5 by drop-wise addition of sodium hydroxide (NaOH). 60 mL of the core was then dispersed (epoxy resin – solvent, 15% dilution), in the mixture and the agitation continued at 400 RPM for 10 min. 6.33 g of formalin solution was then added, and the temperature was increased to 55 ^{o}C with a rate of 10 ^{o}C/min. The reaction proceeded under continuous agitation with the temperature at 55 ^{o}C for 4 h. Once cooled to ambient temperature, the suspension of microcapsules was recovered by filtration using a Buchner funnel (Figure 4.14a) The microcapsules after several ablutions were placed in an oven at 25 ^{o}C for drying (Figure 4.14b).

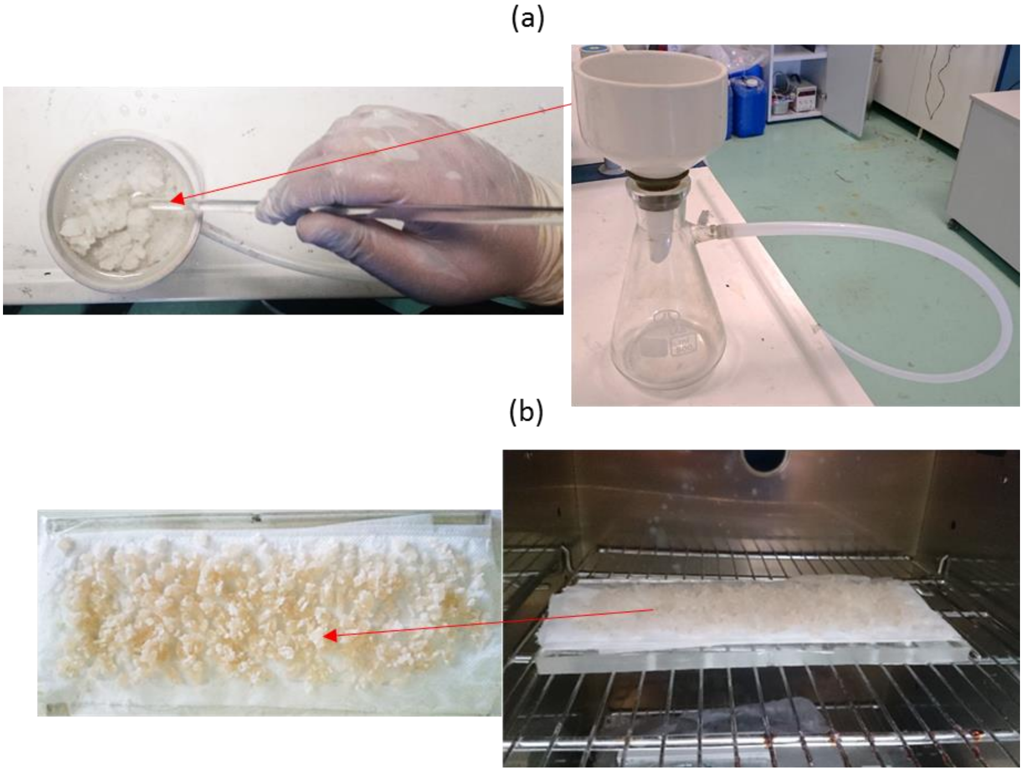

Figure 4.14 (a) filtration and (b) drying of the microcapsules

4.2.3. Microcapsule characterization

4.2.3.1 Scanning Electron Microscopy- SEM

Microcapsule size analysis and surface morphology was performed using a JEOL JSM 6510LV, Oxford Instruments scanning electron microscope. Microcapsule samples were prepared on glass slides, dried in a vacuum oven, and sputter coated with gold. The accelerating voltage for the SEM measurements was selected at 5.0 kV. Mean diameter and standard deviation were determined from data sets of at least 200 measurements.

4.2.3.2 Differential Scanning Calorimetry-DSC

The presence of EPA and EPON 828 within the produced microcapsules was confirmed DSC measurements using a DSC 404 C Pegasus Thermal analyzer Netzsch-Gerätebau GmbH, Germany. The temperature range was selected at 25-400^{0}C and the heating rate was 10 ^{0}C/min.

4.2.3.3 Thermogravimetric analysis -TGA

An important parameter that affects the healing efficiency of a system is the thermal stability of the microcapsules at elevated temperatures. For that purpose, two independent studies were conducted. In the first case, TGA scans were performed on a DSC 404 C Pegasus Thermal analyzer (Netzsch-Gerätebau GmbH, Germany) under nitrogen flow and a heating rate of 10 ^{0}C/min in order to investigate the thermal stability of the UF capsules. Prior to testing Capsule samples were dried at 80 ^{0}C for 2 h before thermal testing in order to remove residual water. In a parallel study, the mass loss of a capsule system was measured during 2 h isotherm at given temperature, in order to investigate the thermal stability of the UF microcapsules for a time period. Isothermal experiments were performed at 180 and 210 ^{0}C.

4.2.3.4 Raman Spectroscopy

Raman spectroscopy was employed in order to confirm the structure of the produced capsules by discriminating between the Raman signatures of the encapsulated chemicals (resin and solvent) and the UF wall. Initially, characteristic Raman profiles of each utilized substance were recorded. Subsequently, a single capsule was selected for a depth profile study. In more detail, spectra were acquired with the laser focused initially on the capsule wall and then moving in steps of 5 μm towards the center of the capsule (80 μm). This study was conducted twice in order to ensure repeatability of the results. A Labram HR - Horiba scientific system was used for the Raman measurements. The 784 nm line of an NIR laser operating at 45mW at the focal plane was employed for the Raman excitation. An optical micro- scope served as the collector of the Raman scattering equipped with a 50x long working distance objective. Raman spectra in the range of 1000–2000 cm^{-1} were collected. Spectral treatment included a quadratic baseline subtraction, normalization to the band with the highest intensity and then fitting with an adequate number of Lorentzian distributions.

4.2.4. Manufacturing process

4.2.4.1 TDCB specimen

As stated, the healing evaluation of the microcapsules at the matrix/polymer level was achieved via fracture tests using a modified TDCB geometry, which ensures controlled crack growth along the grooved central trench of the brittle specimen [28,29]. For the grooved central trench, 20 wt.% of UF microcapsules were initially dispersed within the host matrix (EPON 828) using shear mixing for 10 min. At the end of the dispersion process, hardener DETA and aluminum triflate (catalyst) were added to the mixture. The mix ratio for the host system was 12 parts curing agent DETA for 100 parts EPON 828 while the concentration of the Lewis-acid catalyst was at 3 wt%. Mixture was then degassed and casted into closed silicon molds and left to cure for 24 hours at room temperature. The main body of all the TDCB samples was manufactured consisted of the epoxy system EPON 828/DETA epoxy system. Figure 4.15 illustrates the TDCB geometry adopted in this study.

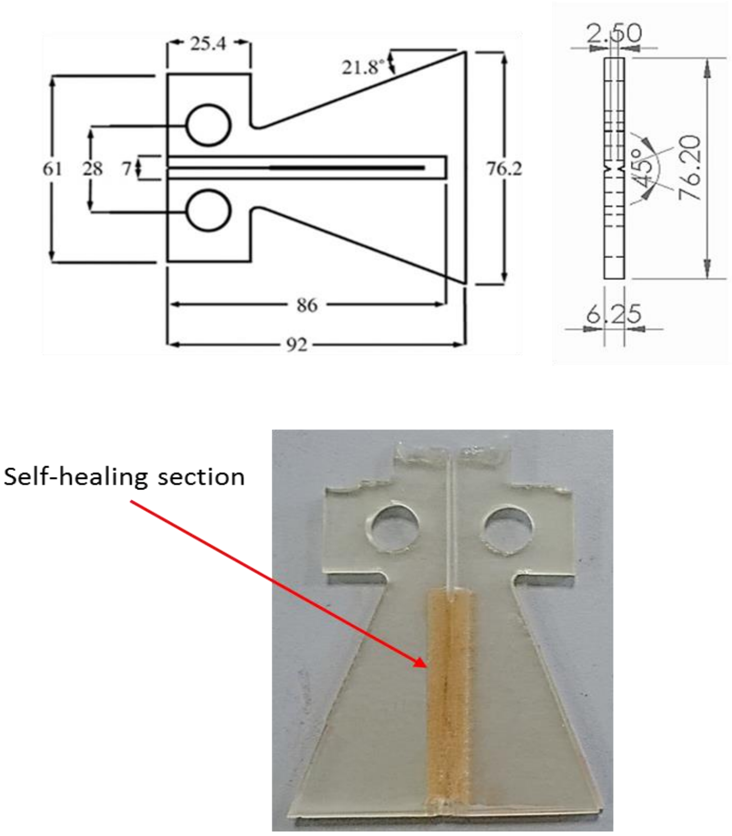

Figure 4.15 TDCB specimen geometry

4.2.4.2 GFRP coupons

GFRP specimens were manufactured using 18-plies of unidirectional glass fabric with areal density 220gr/m^2 and lamina thickness of 0.242mm. The hand lay-up method was selected as the manufacturing process, with a curing cycle at 25 ^{0}C for 24 h under vacuum. A modified epoxy resin system (EPON 828/DETA) containing 20 wt% of UF capsules and 3 wt% of aluminum triflate was employed to impregnate plies 8 and 9. As matrix materials for the host composite, the epoxy system EPON 828/DETA was employed. During the manufacturing process, an artificial crack starter was created in the mid-place using a 15 μm thick sheets of polytetrafluoroethylene (PTFE). One GFRP laminate was manufactured without incorporating UF capsules at the mid-plane and worked as reference in order to study the effect of capsule incorporation of the fracture toughness. At the end of the manufacturing process, specimens were cut to the desired dimensions according to the ASTM 1.0006 standard [30] for mode II interlaminar fracture toughness tests. 5 specimens were created for each case. The capsule-based self-healing GFRP composite is depicted in Figure 4.16.

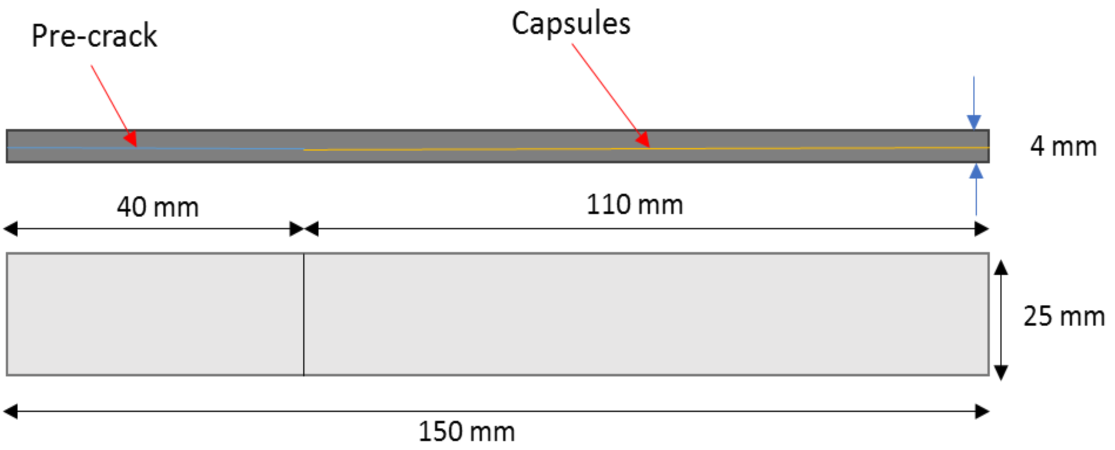

Figure 4.16 Capsule-based self-healing GFRP coupon

4.2.4.3 Lap strap specimens

In an effort to scale-up the use of capsules in composites structures, an epoxy resin was modified using the UF microcapsules and employed as an adhesive between two composite laminates with a lap strap geometry in order to simulate the stiffening of a composite panel. The aforementioned geometry was proposed by R. Luterbacher and his co-workers [31] who explored the potential of using a vascular approach in a simplified strap-lap specimen to heal delaminations initiating at the tip of the flange and to transfer this knowledge and understanding to a large panel “stringer run-out” specimen. In our work, both lap and strap consisted of quazi isotropic ($[-45/90/45/0]_S$) GFRPs. The GFRPs were manufactured with the hand layup method and pressed in a heated hydraulic press under the pressure of 10^7 Pa at 25 ^{0}C for 24 h. Post curing took place at 100 ^{0}C for 4 h. For the modification of the adhesive, 20wt. % of UF capsules and 3wt.% of aluminum triflate were dispersed in a two-part epoxy systems EPON 828/DETA as described in the previous section. Specimens were then cut in the desired dimensions while the ends of the specimens were reinforced with end tabs made of cross-ply laminate. The lap-strap specimen is depicted in Figure 4.17.

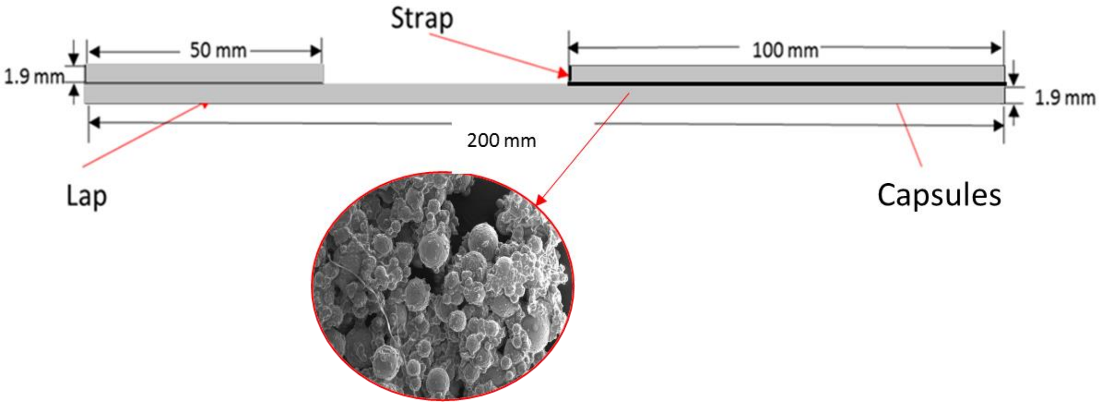

Figure 4.17 Capsule-based self-healing Lap strap geometry

4.2.5. *Mechanical characterization*

In all cases (matrix, composite and composite structure level) a comparative study between unmodified (reference) and capsule-modified (virgin) materials have been conducted in order to investigate the knock-down effect of introducing a self-healing functionality to a polymer or a polymer composite.

4.2.5.1 *TDCB fracture test – matrix level*

Before testing, a pre-crack was created by tapping a fresh razor blade into the front part of the grooved central trench of the TDCB specimens. Afterwards, specimens were pin-loaded on an in-house mini-testing machine (Figure 4.18). Testing was conducted at ambient temperature until the crack was fully propagated through the groove while the displacement rate was selected at 1 mm/min.

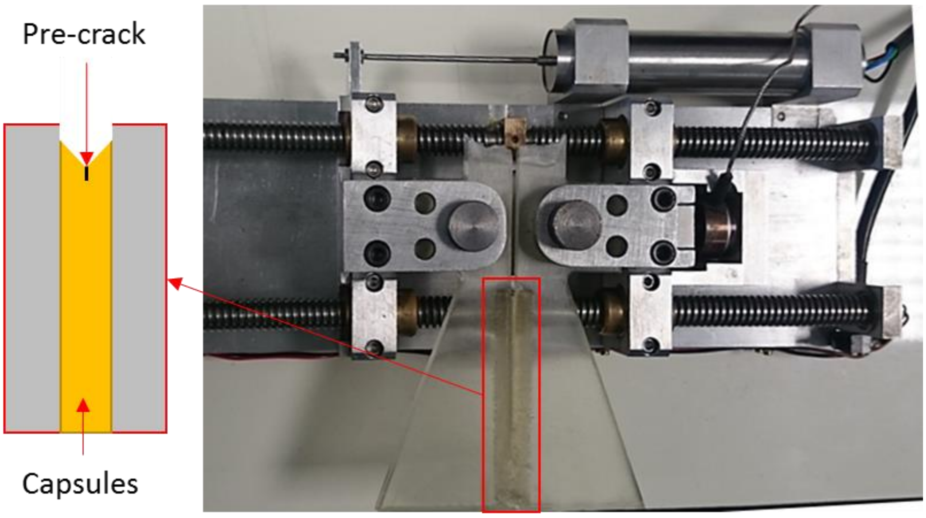

Figure 4.18 TDC fracture test set-up

4.2.5.2 *Mode II interlaminar fracture toughness tests of GFRP – composite level*

Mode II crack opening displacement tests were performed using a WDW-100 Jinan universal testing machine equipped with a 100 kN load shell. Five specimens were tested for each case scenario. The fracture of the interface occurring during this test is an in-plane shear fracture. All specimens were loaded at 1 mm/min while load, point displacement, and crack length were recorded. Following Szekreneyes [32] the critical mode-II strain energy release rate, G_{IIC}, was calculated using Eq 4.1:

$$G_{IIC} = \frac{9Fua^2}{2b(\frac{1}{4}L^3+3a^2)} \tag{4.1}$$

where G_{IIC} (J/mm^2) is the mode -II fracture toughness energy, F is the critical load to start the crack, u is the displacement at the onset of the delamination, a is the initial crack length, b is the width of the specimen and L is the span length. The experimental set-up for the mode II interlaminar fracture toughness tests can be seen in Figure 4.19. It must be noted that the mechanical testing stopped when delamination at the mid-plane was evident.

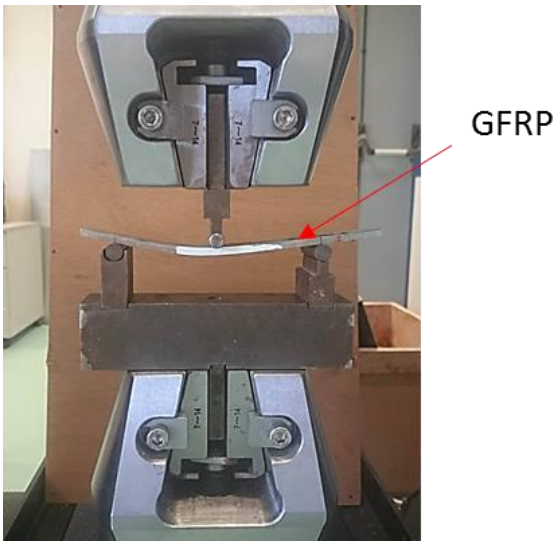

Figure 4.19 mode II interlaminar fracture toughness tests

4.2.5.3 Lap strap specimen testing protocol – model composite structure

Lap strap specimens were tested under tensile loading using a WDW-100 Jinan universal testing machine equipped with a 100 kN load shell. Tests were performed at ambient temperature and the displacement rate was selected at 1 mm/min. The stresses were calculated using the cross-section of the skin. The specimens were gripped 50 mm at either end leaving an initial grip-to-grip separation of 100 mm while tests were stopped upon delamination of the strap. As explained in [31], during tensile loading the specimen deforms through the thickness causing through thickness stresses at the tip of the flange, due to the offset between the loading axis and the neutral axis. This causes delamination at the tip of the flange. It should be mentioned that failure in this case is manifested in a mixed mode. At the early stages of the tensile test, the adhesive layer between lap and strap, fails in mode II followed by mode-I failure at higher stress levels. This behavior is depicted in Figure 4.20, where displacements are exaggerated for illustration purposes.

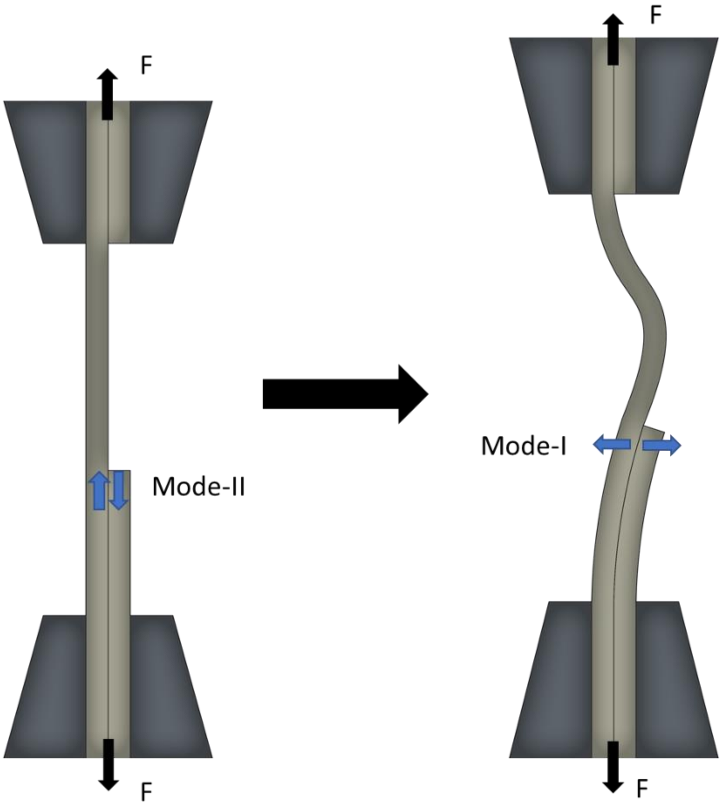

Figure 4.20 Initial stages of the mechanical testing (left), out of plane deformation of the lap strap specimen (right).

4.2.6. Assessment of the healing efficiency

4.2.6.1 TDCB specimen

At the end of the mechanical testing, healing was performed by holding the two sides of the fractured TDCB specimen in place using duct tape. Specimens were then placed in a laboratory oven and healing took place for 48 h at 80 ^{0}C. At the end of the healing process, specimens were left to cool down for 4 hours until they were retested under the same loading conditions. From Eq 4.2 it can be seen that, the TDCB fracture geometry, as it proposed by Mostovoy et al. [33], provides a crack length independent measure of fracture toughness.

$$K_{Ic} = 2P_c \frac{\sqrt{m}}{\beta} \tag{4.2}$$

where P_c is the critical fracture load and m and β are geometric terms. In detail, β depends on the specimen and crack widths b and b_n, respectively. The value of can be calculated theoretically:

$$\mathrm{m} = \frac{3\mathrm{a}^2}{\mathrm{h(a)}^3} + \frac{1}{\mathrm{h(a)}} \tag{4.3}$$

or experimentally:

$$\mathrm{m} = \frac{\mathrm{Eb}}{8}\frac{\mathrm{dC}}{\mathrm{da}} \tag{4.4}$$

where a is the crack length from the line of loading and h(a) is the specimen height profile, E is the Young's modulus and C is the compliance. Based on the above equations, the evaluation of healing efficiency, η, can be defined as the ratio of fracture toughness of healed specimen, K_{IC}^{h} to the virgin specimen, K_{IC}^{v}, which is then scaled to the ratio of peak loads at fracture:

$$\mathrm{n} = \frac{\mathrm{K}_{\mathrm{Ic}}^{\mathrm{h}}}{\mathrm{K}_{\mathrm{Ic}}^{\mathrm{v}}} = \frac{\mathrm{P}_{\mathrm{c}}^{\mathrm{h}}}{\mathrm{P}_{\mathrm{c}}^{\mathrm{v}}} \tag{4.5}$$

4.2.6.2 GFRP coupons

For the case of the fractured GFRP specimens, healing was achieved using a hot press at a temperature of 80 ^{0}C during the entire process while no external pressure was applied on the composites. A thin nylon sheet (16μm) was also placed at the mid-plane of the laminate in order to prevent wetting of the pre-crack area while the pre-cracked area of the coupons was outside the hot press Figure 4.21.

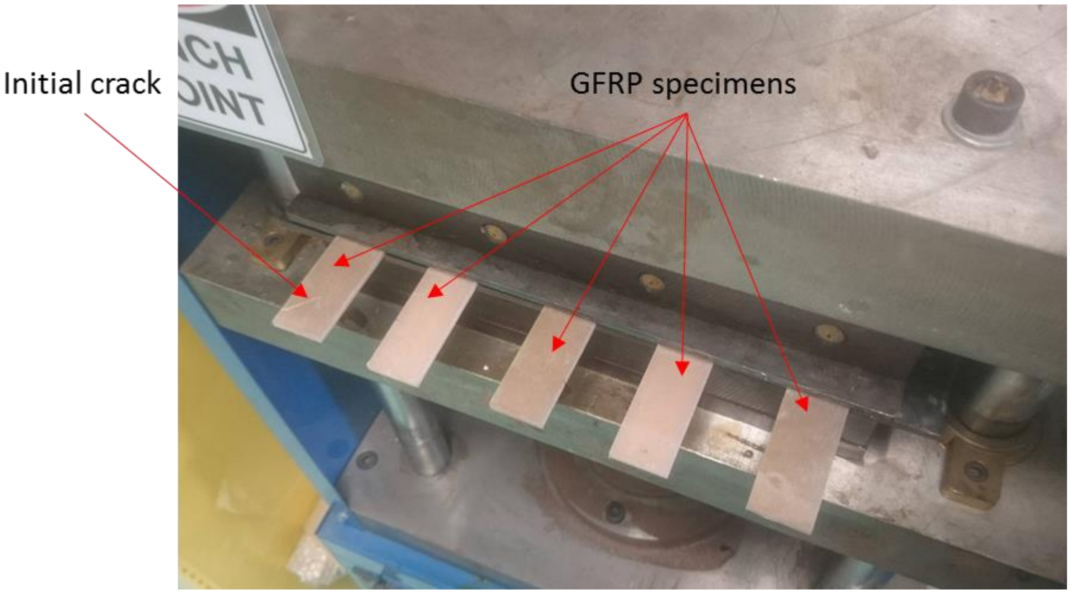

Figure 4.21 Healing process of the GFRP specimens

At the end of the healing process composites were left to cool down and retested under the same loading conditions. Healing efficiency was then calculated in terms of peak load (P_c) and mode-II interlaminar fracture toughness energy (G_{IIC}) recovery:

$$n_p = \frac{P_c^h}{P_c^v} \tag{4.6}$$

$$n_G = \frac{G_{IIc}^h}{G_{IIc}^v} \tag{4.7}$$

where P_c^h and P_c^v are the peak load of the healed and the virgin coupons, respectively, while the G_{IIc}^h and G_{IIc}^v represent the mode-II interlaminar fracture toughness energies, respectively.

4.2.6.3 Lap strap specimen

The healing protocol that was adopted for the restoration of the initial mechanical properties of the lap strap specimens was the one described in the previous section (GFRP coupons). The healing efficiencies in this case were related to: (i) the efficiency in the recovery of stiffness n_E and (ii) the recovery of the initial delamination strength n_σ:

$$n_E = \frac{E^h - E^d}{E^v - E^d} \tag{4.8}$$

and

$$n_\sigma = \frac{\sigma_I^h}{\sigma_I^v} \tag{4.9}$$

where E^h, E^d and E^v represent the stiffness of the healed, damaged and pristine state. σ_I^v and σ_I^h correspond to the stress level at which the delamination initiated at the tip of the strap of the virgin and the healed specimen, respectively. The apparent stiffness was calculated using the linear part of the resulted stress-strain curve between 50 and 150 MPa. The strain level was calculated using the initial grip-to-grip distance and the stress level refers to the lap thickness while the damaged stiffness E^d was calculated during a second loading performed after delamination initiation.

4.3. Results and discussion

4.3.1. Microcapsule characterization

4.3.1.1 SEM analysis

Figure 4.22 shows two SEM images of EPON 828/EPA filled microcapsules obtained at two levels of magnification (i.e. x30 and x65). As can be seen, the SEM images revealed that the capsules were spherical in shape, and had rough exterior shell walls. It is evident that capsules tend to agglomerate after drying and sieving. This effect can be attributed to the low concentration of EMA surfactant [27]. The rough porous morphology of the outer surface results to an enhanced mechanical interlocking between the capsules and the host polymer matrix. This is a crucial parameter, since the efficiency of a capsule-based self-healing system is highly affected by the capsules facture.

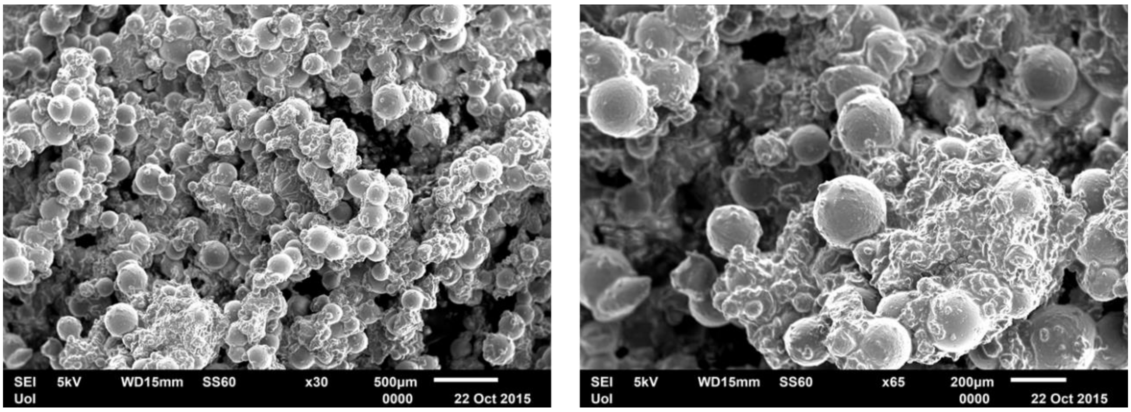

Figure 4.22 SEM images obtained at different levels of magnification

Capsule mean diameter was determined at 200 μm from data sets of at least 200 measurements while the standard deviation was calculated at 36 μm. Figure 4.23a depicts the dimensional analysis conducted using the SEM software while Figure 4.23b illustrates the microcapsules size distribution.

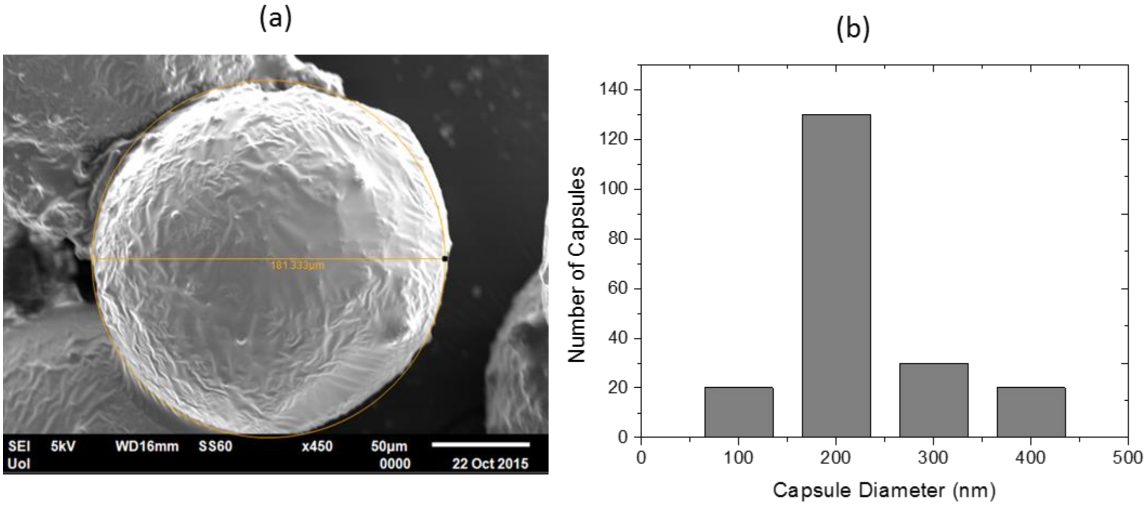

Figure 4.23 Microcapsules (a) Dimensional analysis and (b) size distribution

4.3.1.2 *Differential Scanning Calorimetry - DSC*

As stated, DSC analysis was performed in order to confirm the presence of both components within the UF microcapsules. Figure 4.24 depicts the DSC spectra obtained from the core solution of dried UF microcapsules. Two distinct transitions which are characteristic of the healing agent (epoxy) and the EPA (solvent) in the core of the microcapsules.

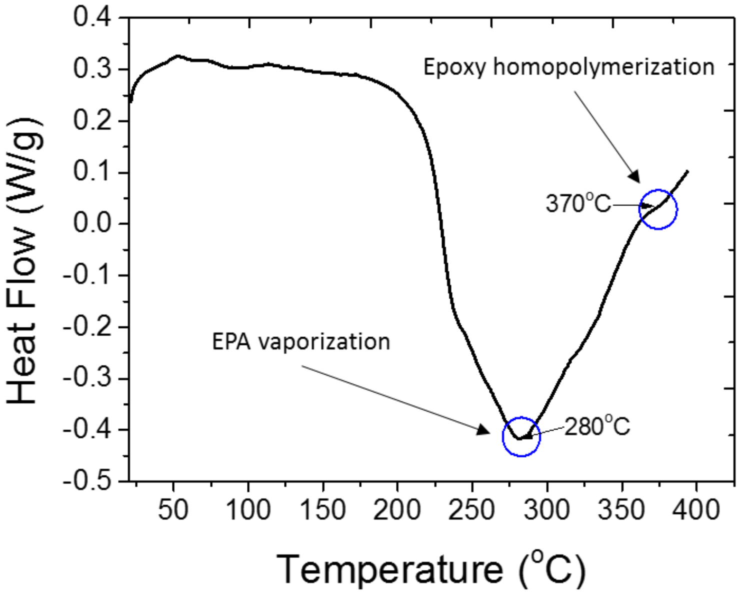

Figure 4.24 DSC curves obtained from UF microcapsules

In detail, the DSC curves presented in Figure 4.24 exhibit an endothermic peak that is representative of the evaporation of EPA (minimum ca. 240 ^{0}C) and an exothermic peak that corresponds to the homopolymerization of the healing agent EPON 828 [34].

4.3.1.3 Thermogravimetric analysis - TGA

Thermal stability and overall quality of the produced capsules were investigated using Thermogravimetric analysis (TGA). Figure 4.25 illustrates representative TGA curves for the UF microcapsules over the selected temperature spectrum. Microcapsules exhibited an initial minor mass loss of 5-7% from 150 – 200 ^{0}C that can be attributed to the thermal decomposition of the shell polymer. Behavior that is in accordance with the results obtained from separated UF shell wall material [35]. The second onset of mass loss at 220-240 ^{0}C is associated with the boiling point of encapsulated EPA. This point indicates that capsules were stable up to the rupture and release of the vaporized healing agent. At elevated temperatures and specifically over 350 ^{0}C, the third onset of mass loss is an indication that the encapsulated EPON 828 was partially polymerized.

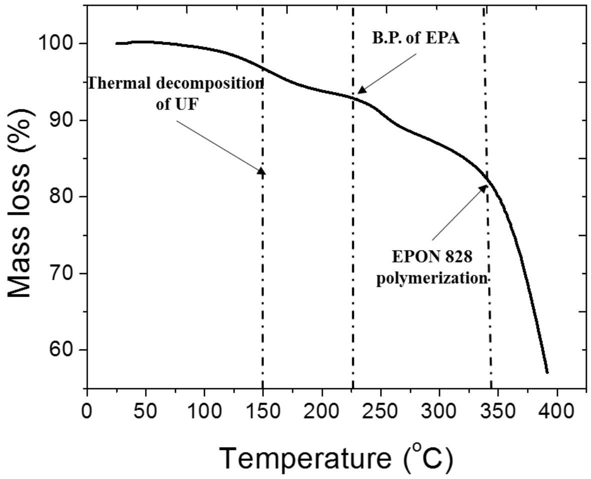

Figure 4.25 Representative TGA curves for the UF microcapsules

To further investigate the thermal stability of microcapsules, isothermal experiments were performed at 180 and 210 ^{0}C for 2 h. Representative TGA curves for the isothermal scans at 180 and 210 ^{0}C are depicted in Figure 4.26a and Figure 4.26b, respectively.

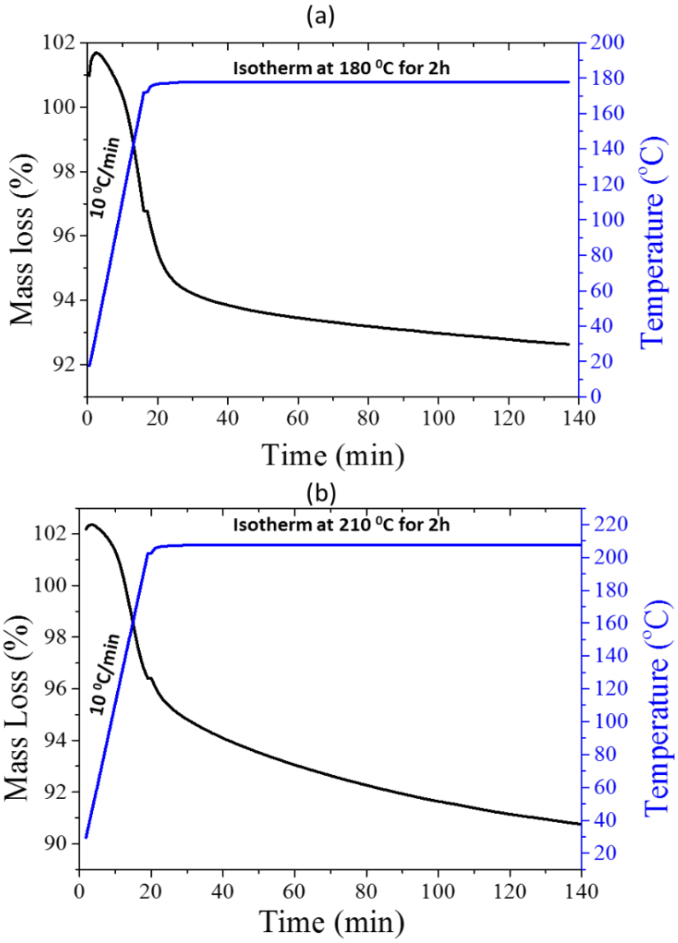

Figure 4.26 Representative mass loss of microcapsules during a 2 h isotherm at (a) 180 ^{0}C and (b) 210 ^{0}C

As can be observed, the produced UF microcapsules exhibited a satisfying thermal stability at elevated temperatures. In detail, a total mass loss of 8% was recorded after maintaining the microcapsules at 180 ^{0}C for 2h. The aforementioned loss was increased after 2h at 210 ^{0}C, reaching at approximately 10%. In both cases, the recorded mass loss can be attributed to the removal of either residual water or/and unencapsulated EPA solvent.

4.3.1.4 Raman Spectroscopy

Characteristic Raman spectra of the chemicals (wall: urea and formaldehyde, healing agent: EPON 828 and EPA, stabilizers: EMA, NH_4Cl and Resorcinol) used for the preparation of the UF capsules are presented in Figure 4.27,Figure 4.28,Figure 4.29, along with a schematic representation of their molecular structure. The red circles indicate the most prominent bands for each material. These spectra were used as a reference for the identification and assignment of the Raman bands found in the final spectra to specific molecular vibrations. A complete peak assignment, not presented here, was conducted. Further details about the molecular frequencies of interest for this study are summarized in Table 4-1 below.

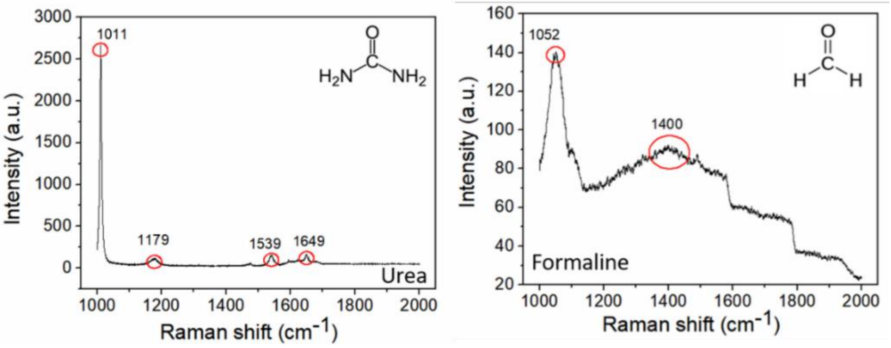

Figure 4.27: Raman spectra and schematic representations of molecular structures of Urea (left) and Formaline (right).(*Note: Formaline is diluted formaldehyde.)

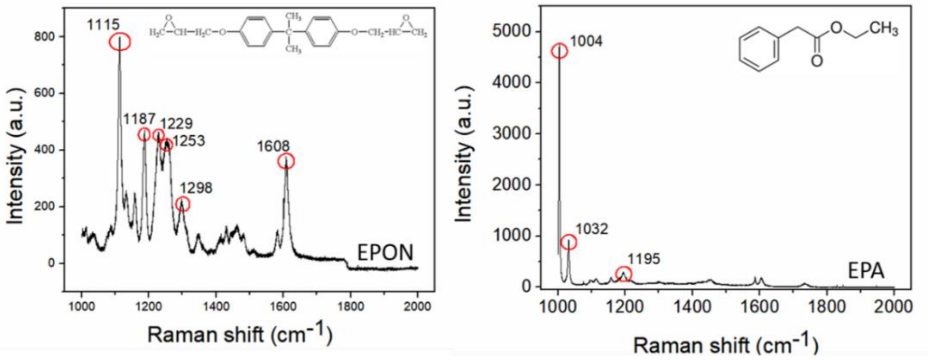

Figure 4.28: Raman spectra and schematic representations of molecular structures of EPON828 (left) and EPA (right).

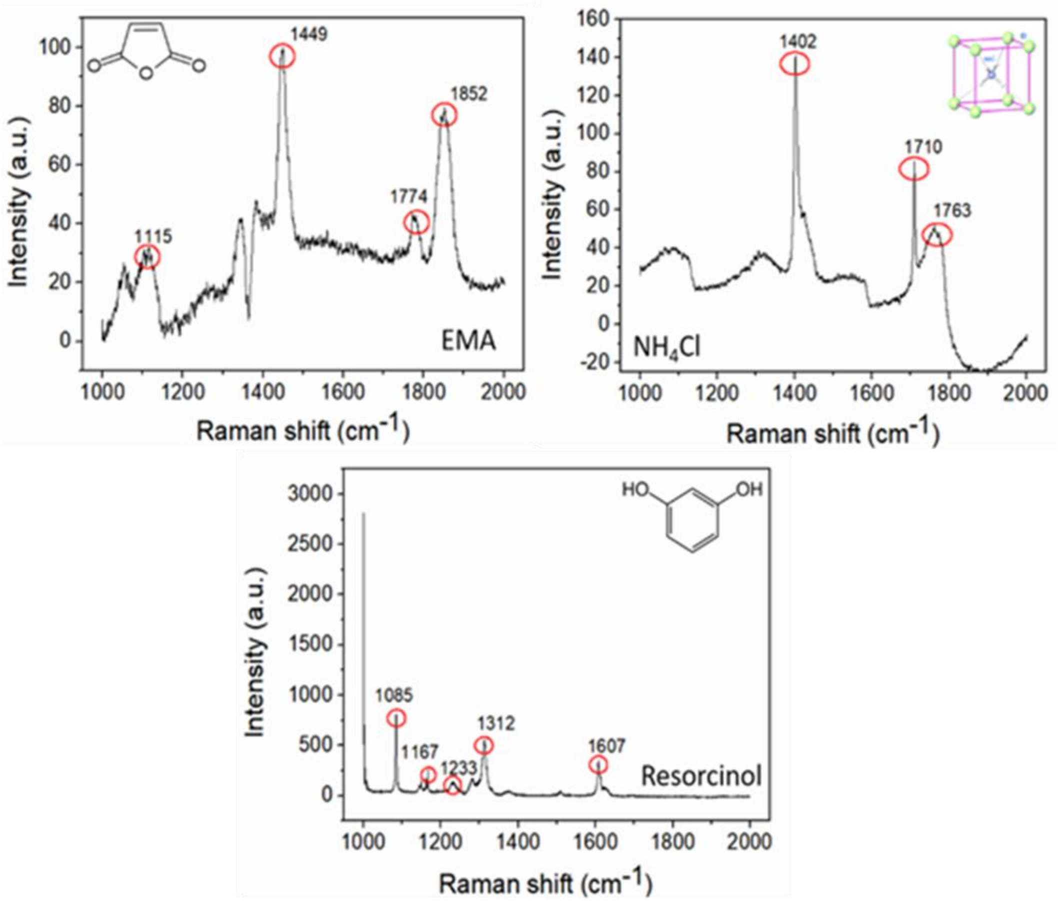

Figure 4.29: Raman spectra and schematic representations of molecular structures of EMA (left), ammonium chloride (right) and resorcinol (down).

The depth profile study using Confocal Raman Microscopy of a UF capsule is presented in Figure 4.30 (up). This plot reflects a 3D map of the molecular vibrations of the capsules, from their surface and up to 80 μm into their core, for 1000 – 2000 frequency range. Several overlapping bands were found in the spectra of the capsules due to their complex chemical nature and the resulting various molecular vibrations. Some of these bands were selected for the confirmation of the capsule wall and core materials, as summarized in Table 4-1. The selection of these bands was based on the aforementioned assignment, taking into consideration typical displacements caused to the bands due to molecular interactions.

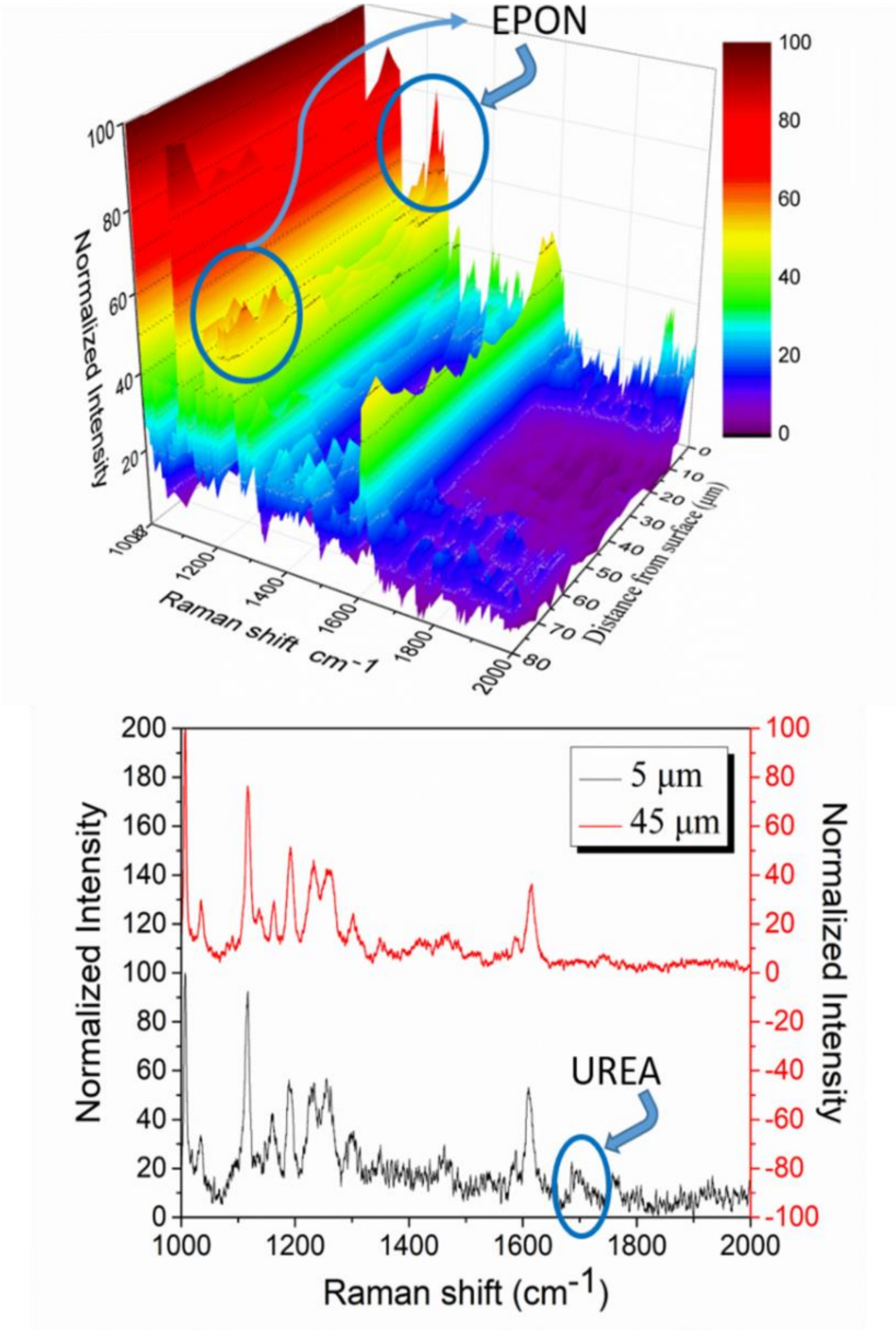

Figure 4.30: Raman depth profile (3D map) of the UF microcapsules (up), selected Raman spectra of the wall and the inner part of the capsule for comparison (down).

As can be seen in Figure 4.30(up) the normalized intensities of a triplet of bands situated at 1230, 1246 and 1297 cm^{-1} were increased in the spectrum corresponding to the surface of the capsule possibly due to EPON resin from some other ruptured capsules covering the studied surface. Then the respective intensities decreased while penetrating from the surface inside the capsule wall and finally increased again at ~ 40 μm from the surface and onwards, demonstrating the increased concentration of EPON inside the capsule core. Additionally, a lower intensity band representing the stretching vibration of the carbonyl group in urea (the capsule wall material) appeared only in the spectra acquired at the first 15 μm from the capsule surface and then vanished as we moved to the capsule core. The aforementioned statements were proven by the spectra corresponding to depths of 5 and 45 μm from the surface of the capsule as presented in Figure 4.30(down).

Table 4-1 Molecular frequencies of interest

Experimental band frequency (cm^{-1})	Assignment by comparing to the spectra of constituent material	Assignment by comparing to literature values
1006	EPA - Urea	Ring deformation (EPA) [36] / C-N symmetric stretching in urea [37]
1230	EPON - Resorcinol	In plane molecular deformation in EPON [38] / OH deformation in resorcinol [39]
1246	EPON	Epoxy ring deformation [38]
1297	EPON	C-O and C-C stretching [38]
1620	EPON / Resorcinol (1608 cm^{-1})	C=C symmetric stretching in EPON [38] / CC intermolecular stretching in resorcinol [39]
1697	Urea (1649cm^{-1})	Stretching of carbonyl group [40]

4.3.2. TDCB specimen – matrix level

4.3.2.1 Mechanical characterization

Figure 4.31 depicts representative load-extension curves obtained from the reference (no capsules), virgin (embedded UF-capsules) and healed TDCB specimens. The average critical loads were determined from the first failure event (i.e. peak loads). As can be seen, the incorporation of the microcapsules within the polymeric matrix induced a marginal toughening effect. In detail, the peak load of the virgin TDCB specimen was recorded at 93 ± 25 N while for the case of the reference TDCB specimen was at 81 ± 15 N showing an increase of approximately 14%. The aforementioned enhancement can be attributed to several operative toughening mechanisms (energy consumption mechanisms) i.e. capsules rapture, crack pinning, crack deflection caused from the incorporation of the microcapsules within the polymer [25,41]

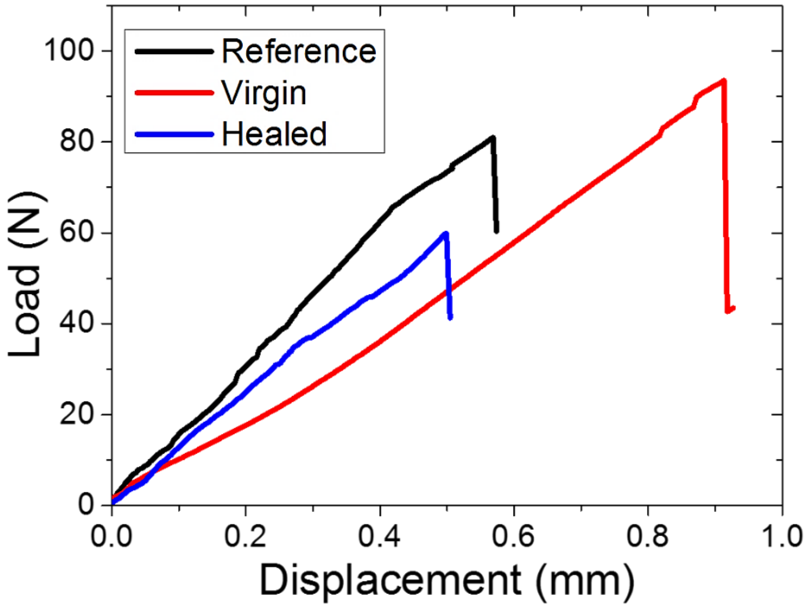

Figure 4.31 Load versus displacement curves for all the reference, virgin and healed specimen.

The healing efficiency of the TDCB specimens was calculated according to Eq 4.6. After the healing process, the total recovery of the fracture toughness was calculated at approximately 72 % showing the ability of the capsule-based system to effectively regain a sufficient percentage of its initial fracture toughness. According to other studies, the calculated healing efficiency is considered very satisfying for a capsule-based self-healing system and provides evidence that there was a good adhesion between the new polymer and the host matrix [25,41,34,42]. Table 4-2 summarizes the peak load along with the calculated healing efficiency for the investigated system.

Table 4-2 Peak load and healing efficiency values for the TDC specimens

Specimen	Peak Load - P_{max} (N)	Healing efficiency - n (%)
Reference	81.04 ± 15	-
Virgin	93.10 ± 25	-
Healed	59.92 ± 32	72

4.3.2.2 SEM analysis

In order to gain an insight on the quality of the healing process, a comparative scanning electron microscopy (SEM) study on the fractured surfaces of the healed TDCB specimens was conducted (Figure 4.32). SEM photographs of the healed fractured surfaces revealed that the healed polymer failed in a cohesive manner indicating a strong interface between the reacted healing agent and the host polymer.

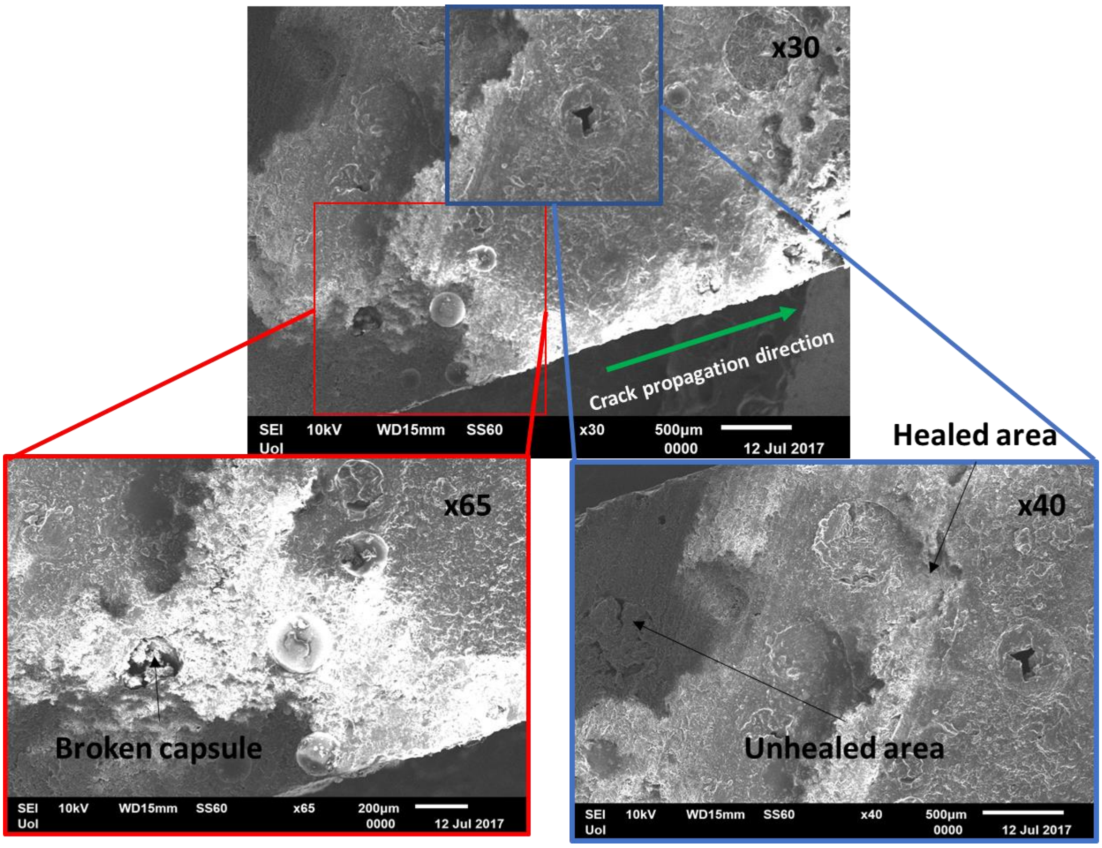

Figure 4.32 SEM images of the fracture surface of the healed TDCB specimen.

As stated, upon rupture the resin–solvent mixture (healing agent) that was encapsulated is delivered to the crack plane. However, as can be seen there are small areas that were not properly healed, thus undermining the total healing efficiency of the system. This behavior can be attributed to (i) the absence of microcapsules due to insufficient dispersion (ii) capsule pull-out phenomena and (iii) crack deviation phenomena around the capsules.

4.3.3. *GFRP – composite level*

4.3.3.1 Mechanical characterization

Representative load versus displacement curves obtained from the mode II interlaminar fracture toughness tests of the reference virgin and healed capsule-based self-healing GFRPs are depicted in Figure 4.33. As can be seen, the load curves exhibited a linear increase followed by a deviation from linearity. At the final stages of the experiment a load drop at crack propagation onset was recorded. This was an expected trend and is common in brittle composites [43,44]. It should be noted, that the inclusion of UF microcapsules within the polymer matrix at the midplane of the GFRP composite had a detrimental effect on the mode II fracture toughness energy (G_{IIc}) values while the P_{max} did not significantly changed. In detail, the P_{max} and the G_{IIc} in the case of the reference GFRPs were 568 ± 20 N and 2.84 ± 0.15 kJ/m^2, respectively. In the case of the virgin GFRPs the aforementioned values exhibited an increase reaching at 654 ± 38 N and 2.10 ± 0.4 kJ/m^2 for P_{max} and the G_{IIc}, respectively. This reduction may be attributed to the increased diameter of the microcapsules which may lead to crack initiation sites.

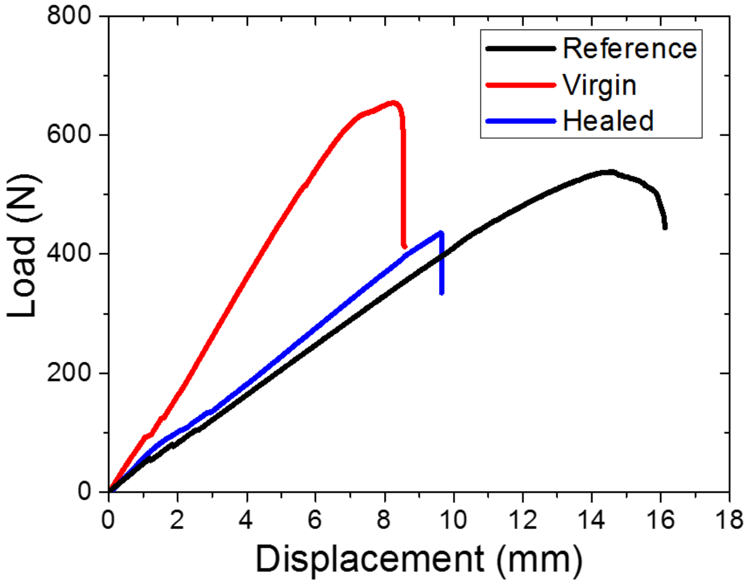

Figure 4.33 Load vs cross-head displacement curves for the reference, virgin and healed GFRPs

Table 4-1 summarizes the calculated healing efficiency values in terms of P_{max} (Eq. #) and G_{IIc} (Eq.#). After, the healing process the GFRP regained its initial maximum load at 66.5% and the mode II fracture toughness energy at 77.84%. Although failure in this case occurred predominantly in the matrix phase (matrix dominant), the fracture toughness recovery was reduced compared with the TDCB specimens. This behavior indicates that healing of large scale damages (i.e. delaminations) using capsule-based approaches remains a challenge. However, it should be pointed out that the calculated healing efficiencies found to be similar or even higher compared to those reported in the literature [45].

Table 4-3 Mode II Fracture toughness energy under (G_{IIC}), peak load (P_{max}) and healing efficiency values

Specimen	**P_{max} (N)**	**G_{IIC} (kJ/m^2)**	**Knockdown Effect (%)**	**n_P (%)**	**n_G (%)**
Reference	568 ± 20	2.84 ± 0.15	-	-	-
Virgin	654 ± 38	2.10 ± 0.4	-26	-	-
Healed	435 ± 79	1.63	-	66.5	77.84

4.3.3.2 SEM analysis

SEM photographs were obtained from the fractured area of the healed GFRPs in order to assess the quality of the healing process. As can be seen in Figure 4.34a, failure occurred in a mixed mode manner (both adhesively and cohesively). In several areas, the polymerized healing agent can easily be observed, indicating a strong interface between the reacted healing agent and the host polymer. However, there are areas that were not properly healed and thus do not contribute to the recovery of the materials fracture toughness (Figure 4.34b).

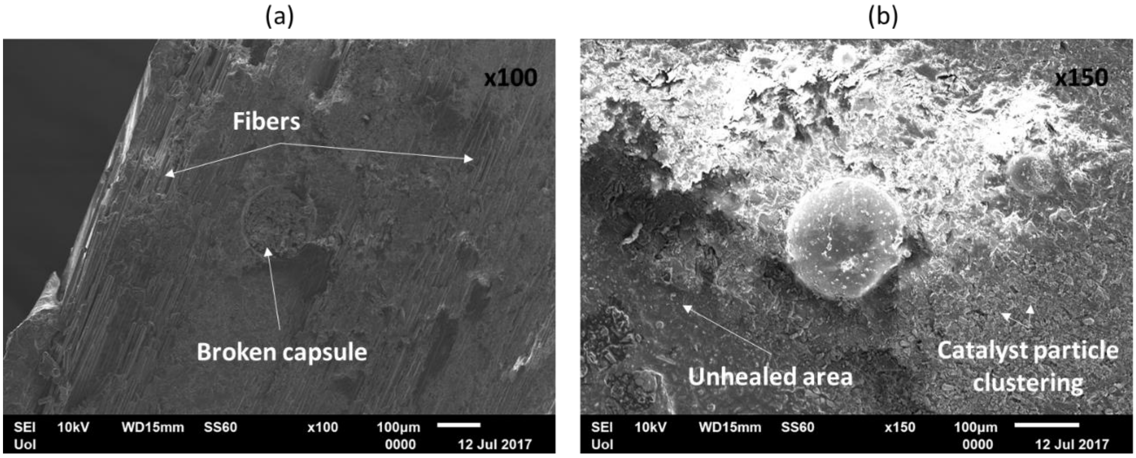

Figure 4.34 SEM photographs from the fractured areas of the healed GFRPs at different magnifications

This behavior can be either attributed to (i) broken capsules during the manufacturing process, (ii) capsule pull-out phenomena and/or (iii) crack deviation phenomena around the capsule. In addition, the catalyst clusters are visible on the fracture plane may lead to unstable crack propagation in the virgin loading cycle (knock-down effect) and to poor recovery of the initial fracture toughness during the healed loading cycle [45].

4.3.4. Lap strap specimen – composite structure level

4.3.4.1 Mechanical characterization

Figure 4.35 illustrates representative stress-strain curves from the reference, virgin and healed lap strap specimens. The apparent stiffness was calculated using the linear part of the resulted stress-strain curve between 50 and 150 MPa. The strain level was calculated using the initial grip-to-grip distance and the stress level refers to the lap thickness while the damaged stiffness E^d was calculated during a second loading performed after delamination initiation. In all cases a brittle failure of the adhesive layer is evident and is manifested by a small drop in the stress strain curve. As can be seen the incorporation of the UF microcapsules within the adhesive polymer, did not significantly affect the initiation load of the delamination, which showed a reduction of 4% reaching from 269.31 ± 22 N (reference) to 261.73 ± 35 N (virgin) while the Young's modulus increased from 10.17 ± 1.2 N to 11.55 ± 1.7 N.

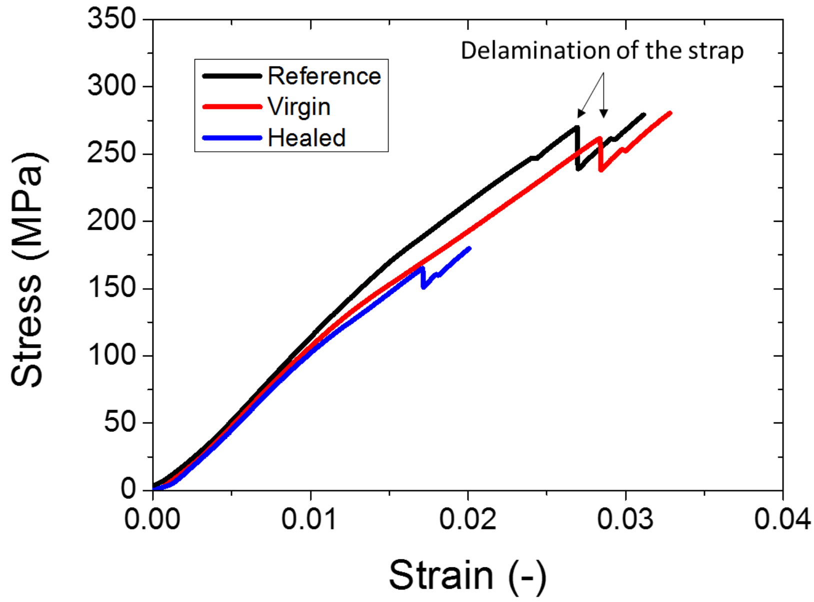

Figure 4.35 Representative stress-displacement curves for the reference, virgin and healed specimen

After the healing process, the stress-displacement response was similar to that of the virgin specimen demonstrating a successful recovery in performance. Healing efficiencies based on the recovery of the stress at the delamination of the strap (n_σ) and the Young's modulus (n_E) were calculated using Eq. 4.8 and Eq. 4.9, respectively. Table 4-4 presents the critical stress, the Young's modulus and the calculated healing efficiencies for the lap strap specimens.

Table 4-4 Critical stress, Young's modulus and the calculated healing efficiencies for the lap strap specimens

Specimen	E_{max} (MPa)	σ_c (MPa)	n_E (%)	n_σ (%)
Reference	10.17 ± 1.2	269.31 ± 22	-	-
Virgin	11.55 ± 1.7	261.73 ± 35	-	-
Healed	10.93 ± 2.0	165.23± 38	70.19	63.13

As can be observed, the stiffness of the composite structure was recovered at 70.19 % (from 11.55 ± 1.7 MPa to 10.93 ± 2.0) and the delamination stress level of the strap, was decreased from 261.73 ± 35MPa to 165.23± 38MPa, resulting in a healing efficiency, n_σ = 63.13%. The calculated healing efficiency values along with the negligible knock-down effect constitute encouraging factors for up-scaling the employment of capsule-based approaches to model composite structures.

4.4. Conclusions

Poly(urea–formaldehyde) microcapsules filled with EPON 828/EPA mixture were prepared via in situ microencapsulation oil-in-water emulsion polymerization. The produced capsules were characterized via SEM TGA DSC and Raman spectroscopy and then incorporated into a thermoset matrix in order to assess the healing efficiency of the system at (i) matrix, (ii) composite and (iii) model composite level. Obtained results indicated that the capsules were thermally stable at elevated temperature while the rough external wall material enhanced the interlocking between the capsules and the host matrix. At matrix level, the capsule-based self-healing polymer was able to restore its initial fracture toughness at 72% while in the case of GFRP specimens, the healing efficiency was almost the same reaching at 77.84%. However, the incorporation of capsules at the midplane of a GFRP composite had a detrimental effect on the fracture toughness, thus showing that the employment of capsule-based methodologies remains a challenge.

Finally, it has been proved that the modification of a polymeric adhesive using UF microcapsules, could be a reliable route towards up-scaling the employment of capsule-based self-healing methodologies to more complicated composite structures.

References

[1] S.R. White, N.R. Sottos, P.H. Geubelle, J.S. Moore, M.R. Kessler, S.R. Sriram, E.N. Brown, S. Viswanathan, Autonomic healing of polymer composites, Nature. 409 (2001) 794–797. doi:10.1038/35057232.

[2] D.Y. Zhu, M.Z. Rong, M.Q. Zhang, Self-healing polymeric materials based on microencapsulated healing agents: From design to preparation, Prog. Polym. Sci. 49–50 (2015) 175–220. doi:10.1016/j.progpolymsci.2015.07.002.

[3] D.G. Bekas, K. Tsirka, D. Baltzis, A.S. Paipetis, Self-healing materials: A review of advances in materials, evaluation, characterization and monitoring techniques, Compos. Part B Eng. 87 (2016) 92–119. doi:10.1016/j.compositesb.2015.09.057.

[4] S.R. White, B.J. Blaiszik, S.L.B. Kramer, S.C. Olugebefola, J.S. Moore, N.R. Sottos, Self-healing polymers and composites, Am. Sci. 99 (2011) 392–399. doi:10.1146/annurev-matsci-070909-104532.

[5] P.R. Hondred, L. Salat, J. Mangler, M.R. Kessler, Tung oil-based thermosetting polymers for self-healing applications, J. Appl. Polym. Sci. 131 (2014) 1–9. doi:10.1002/app.40406.

[6] J.L. Moll, H. Jin, C.L. Mangun, S.R. White, N.R. Sottos, Self-sealing of mechanical damage in a fully cured structural composite, Compos. Sci. Technol. 79 (2013) 15–20. doi:10.1016/j.compscitech.2013.02.006.

[7] M.F. Haase, D.O. Grigoriev, H. Möhwald, D.G. Shchukin, Development of nanoparticle stabilized polymer nanocontainers with high content of the encapsulated active agent and their application in water-borne anticorrosive coatings, Adv. Mater. 24 (2012) 2429–2435. doi:10.1002/adma.201104687.

[8] H.Y. Li, R.G. Wang, W.B. Liu, Preparation and self-healing performance of epoxy composites with microcapsules and tungsten (VI) chloride catalyst, J. Reinf. Plast. Compos. 31 (2012) 924–932. doi:Doi 10.1177/0731684412442990.

[9] A.C. Jackson, J. a. Bartelt, P. V. Braun, Transparent Self-Healing Polymers Based on Encapsulated Plasticizers in a Thermoplastic Matrix, Adv. Funct. Mater. 21 (2011) 4705–4711. doi:10.1002/adfm.201101574.

[10] L. Yuan, S. Huang, A. Gu, G. Liang, F. Chen, Y. Hu, S. Nutt, A cyanate ester/microcapsule system with low cure temperature and self-healing capacity, Compos. Sci. Technol. 87 (2013) 111–117.

doi:10.1016/j.compscitech.2013.08.005.

[11] H. Jin, G.M. Miller, N.R. Sottos, S.R. White, Fracture and fatigue response of a self-healing epoxy adhesive, Polymer (Guildf). 52 (2011) 1628–1634. doi:10.1016/j.polymer.2011.02.011.

[12] Y. González-García, S.J. García, A.E. Hughes, J.M.C. Mol, A combined redox-competition and negative-feedback SECM study of self-healing anticorrosive coatings, Electrochem. Commun. 13 (2011) 1094–1097. doi:10.1016/j.elecom.2011.07.009.

[13] S.J. García, H.R. Fischer, P.A. White, J. Mardel, Y. González-García, J.M.C. Mol, A.E. Hughes, Self-healing anticorrosive organic coating based on an encapsulated water reactive silyl ester: Synthesis and proof of concept, Prog. Org. Coatings. 70 (2011) 142–149. doi:10.1016/j.porgcoat.2010.11.021.

[14] M.J. Hollamby, D. Fix, I. Dönch, D. Borisova, H. Möhwald, D. Shchukin, Hybrid polyester coating incorporating functionalized mesoporous carriers for the holistic protection of steel surfaces., Adv. Mater. 23 (2011) 1361–5. doi:10.1002/adma.201003035.

[15] M. Huang, J. Yang, Long-term performance of 1H, 1H′, 2H, 2H ′-perfluorooctyl triethoxysilane (POTS) microcapsule-based self-healing anticorrosive coatings, J. Intell. Mater. Syst. Struct. 25 (2014) 98–106. doi:10.1177/1045389X13505785.

[16] T. Nesterova, K. Dam-Johansen, S. Kiil, Synthesis of durable microcapsules for self-healing anticorrosive coatings: A comparison of selected methods, Prog. Org. Coatings. 70 (2011) 342–352. doi:10.1016/j.porgcoat.2010.09.032.

[17] X. Liu, H. Zhang, J. Wang, Z. Wang, S. Wang, Preparation of epoxy microcapsule based self-healing coatings and their behavior, Surf. Coatings Technol. 206 (2012) 4976–4980. doi:10.1016/j.surfcoat.2012.05.133.

[18] E. Manfredi, A. Cohades, I. Richard, V. Michaud, Assessment of solvent capsule-based healing for woven E-glass fibre-reinforced polymers, Smart Mater. Struct. 24 (2015) 15019. doi:10.1088/0964-1726/24/1/015019.

[19] A.R. Jones, B.J. Blaiszik, S.R. White, N.R. Sottos, Full recovery of fiber/matrix interfacial bond strength using a microencapsulated solvent-based healing system, Compos. Sci. Technol. 79 (2013) 1–7. doi:10.1016/j.compscitech.2013.02.007.

[20] H. Zhang, J. Yang, Development of self-healing polymers via amine–epoxy

chemistry: I. Properties of healing agent carriers and the modelling of a two-part self-healing system, Smart Mater. Struct. 23 (2014) 65003. doi:10.1088/0964-1726/23/6/065003.

[21] H. Jin, C.L. Mangun, A.S. Griffin, J.S. Moore, N.R. Sottos, S.R. White, Thermally stable autonomic healing in epoxy using a dual-microcapsule system., Adv. Mater. 26 (2014) 282–7. doi:10.1002/adma.201303179.

[22] A.C. Jackson, J. a Bartelt, K. Marczewski, N.R. Sottos, P. V Braun, Silica-protected micron and sub-micron capsules and particles for self-healing at the microscale., Macromol. Rapid Commun. 32 (2011) 82–7. doi:10.1002/marc.201000468.

[23] Q. Li, N.H. Kim, D. Hui, J.H. Lee, Effects of dual component microcapsules of resin and curing agent on the self-healing efficiency of epoxy, Compos. Part B Eng. 55 (2013) 79–85. doi:10.1016/j.compositesb.2013.06.006.

[24] D.Y. Zhu, M.Z. Rong, M.Q. Zhang, Preparation and characterization of multilayered microcapsule-like microreactor for self-healing polymers, Polym. (United Kingdom). 54 (2013) 4227–4236. doi:10.1016/j.polymer.2013.06.014.

[25] T.S. Coope, U.F.J. Mayer, D.F. Wass, R.S. Trask, I.P. Bond, Self-healing of an epoxy resin using scandium(III) triflate as a catalytic curing agent, Adv. Funct. Mater. 21 (2011) 4624–4631. doi:10.1002/adfm.201101660.

[26] E.N. Brown, M.R. Kessler, N.R. Sottos, S.R. White, In situ poly(urea-formaldehyde) microencapsulation of dicyclopentadiene., J. Microencapsul. 20 (2003) 719–30. doi:10.1080/0265204031000154160.

[27] B.J. Blaiszik, N.R. Sottos, S.R. White, Nanocapsules for self-healing materials, Compos. Sci. Technol. 68 (2008) 978–986. doi:10.1016/j.compscitech.2007.07.021.

[28] J.D. Rule, N.R. Sottos, S.R. White, Effect of microcapsule size on the performance of self-healing polymers, Polymer (Guildf). 48 (2007) 3520–3529. doi:10.1016/j.polymer.2007.04.008.

[29] E.N. Brown, N.. Sottos, S.R. White, Fracture Testing of a Self-Healing Polymer Composite, Exp. Mech. 42 (2002) 372–379. doi:10.1177/001448502321548193.

[30] E. Directorate, DocMaster : Uncontrolled copy when printed, (2006) 1–8.

[31] R. Luterbacher, T.S. Coope, R.S. Trask, I.P. Bond, Vascular self-healing within

carbon fibre reinforced polymer stringer run-out configurations, Compos. Sci. Technol. 136 (2016) 67–75. doi:10.1016/j.compscitech.2016.10.007.

[32] a Szekrényes, Overview on the experimental investigations of the fracture toughness in composite materials, Hungarian Electron. J. Sci. Http//hej. …. (2002) 1–19. http://hej.sze.hu/MET/MET-020507-A/met020507a.pdf.

[33] S. Mostovoy, Crosley, P.B., E.J. Ripling, Use of Crack-Line Loaded Specimens for measuring Plain-Strain Fracture Toughness, J. Mater. Sci. 2 (1967) 661–681.

[34] B.J. Blaiszik, M.M. Caruso, D.A. McIlroy, J.S. Moore, S.R. White, N.R. Sottos, Microcapsules filled with reactive solutions for self-healing materials, Polymer (Guildf). 50 (2009) 990–997. doi:10.1016/j.polymer.2008.12.040.

[35] P.A. Bolimowski, I.P. Bond, D.F. Wass, Robust synthesis of epoxy resin-filled microcapsules for application to self-healing materials Subject Areas : Author for correspondence :, Philos. Trans. R. Soc. a-Mathematical Phys. Eng. Sci. 374 (2016). doi:10.1098/rsta.2015.0083.

[36] M. Baranska, H. Schulz, S. Reitzenstein, U. Uhlemann, M.A. Strehle, H. Krüger, R. Quilitzsch, W. Foley, J. Popp, Vibrational spectroscopic studies to acquire a quality control method of eucalyptus essential oils, Biopolymers. 78 (2005) 237–248. doi:10.1002/bip.20284.

[37] J. Jehlicka, H.G.M. Edwards, A. Culka, Using portable Raman spectrometers for the identification of organic compounds at low temperatures and high altitudes: exobiological applications, Philos. Trans. R. Soc. A Math. Phys. Eng. Sci. 368 (2010) 3109–3125. doi:10.1098/rsta.2010.0075.

[38] L.Y. T., K.J. L., DEVELOPMENTS IN REINFORCED PLASTICS-4 CONTENTS OF VOLUMES 1 TO 3 Volume 1, Elsevier Applied Science Publishers LTD, 1984. doi:10.1007/978-94-009-5620-9.

[39] G.N.R. Tripathi, Crystal spectra and vibrational assignments in α-resorcinol, J. Chem. Phys. 74 (1981) 250. doi:10.1063/1.440881.

[40] G. Socrates, Infrared and Raman characteristic group frequencies, 2004. doi:10.1002/jrs.1238.

[41] E.N. Brown, S.R. White, N.R. Sottos, Microcapsule induced toughening in a self healing polymer composite, J. Mater. Sci. Vol. 39 (2004) 1703–1710. doi:10.1023/B:JMSC.0000016173.73733.dc.

[42] H. Jin, C.L. Mangun, D.S. Stradley, J.S. Moore, N.R. Sottos, S.R. White, Self-healing thermoset using encapsulated epoxy-amine healing chemistry, Polymer (Guildf). 53 (2012) 581–587. doi:10.1016/j.polymer.2011.12.005.

[43] T. Ebeling, A. Hiltner, E. Baer, Delamination Failure of a Woven Glass Fiber Composite, J. Compos. Mater. 31 (1997) 1318–1333. doi:10.1177/002199839703101304.

[44] Y. Hirai, H. Hamada, Determination of interfacial material constants in plain glass woven fabric composites using finite element analysis, Compos. Interfaces. 5 (1997) 69–86. doi:10.1163/156855497X00316.

[45] M.R. Kessler, N.R. Sottos, S.R. White, Self-healing structural composite materials, Compos. Part A Appl. Sci. Manuf. 34 (2003) 743–753. doi:10.1016/S1359-835X(03)00138-6.

CHAPTER 5

Modification of an epoxy resin towards the development of intrinsic self-healing polymer

5.1. Introduction

Due to their sophisticated molecular architecture, polymers and polymeric materials constitute ideal candidates that can be “transformed” into self-healing materials by programming or designing their functionalities at the molecular level. These polymers constitute one of the most important categories of self-healing materials, that of the intrinsic or remendable healing polymers. In this case, repair is achieved through the inherent reversibility of bonding in the matrix phase, which acts as a healing agent. The first intrinsic self-healing strategy relied on the ability of the polymeric chains to increase their mobility upon heating. Thus, chain entanglements in the damaged area were able to reform and subsequently heal the damage [1]. Two important limitations of this concept lie: (i) in the slow formation of interfacial entanglements due to the high melt viscosities of the polymer and (ii) that this approach can be only applied for thermoplastic polymers.

Despite the good healing performance that was achieved in a first-generation intrinsic self-healing epoxy systems [2], the incorporation of dicyclopentadiene (DCPD)/Grubbs’ catalyst within the matrix -an expensive and unstable substrate in the hostile environment Grubbs’ catalyst- limits its applications [3]. Within the aim of the research community is to maximize the healing efficiency and minimize the cost. In an effort to address the self-healing functionality to different classes of polymers, several concepts based on ionomers [4], disulphide bridges [5,6], Diels-Alder reaction [7–9] and supramolecular chemistry [10–14] have been developed to meet the application requirements.

Takahiro Kakuta et al. [15] used the host-guest interaction to produce self-healing materials that can recover their initial strength even after being sectioned in the middle. The aforementioned self-healable supramolecular materials were consisted of cyclodextrins (CD) - guest gel crosslinked between poly(acrylamide) chains with inclusion complexes. The obtained CD–guest gels exhibit a self-standing property without chemical crosslinking reagents, indicating that the newly formed host − guest interactions between the CD and the guest units stabilize the conformation of the CD–guest gels. In another study [16], a promising non-covalent thermal-switchable self-healing hydrogel was developed by mixing hydrophobically modified chitosan (hm-chitosan) with thermal-responsive vesicle composed of 5-methyl salicylic acid (5mS) and dodecyltrimethylammonium bromide (DTAB). By tuning the temperature, the hydrogel can be switched from sol to gel state (Figure 5.1). These transitions can be reversibly performed for several cycles in a similar way to a supramolecular gel. The gelation temperature in particular, can be easily controlled by varying the ratio of DTAB to 5mS.

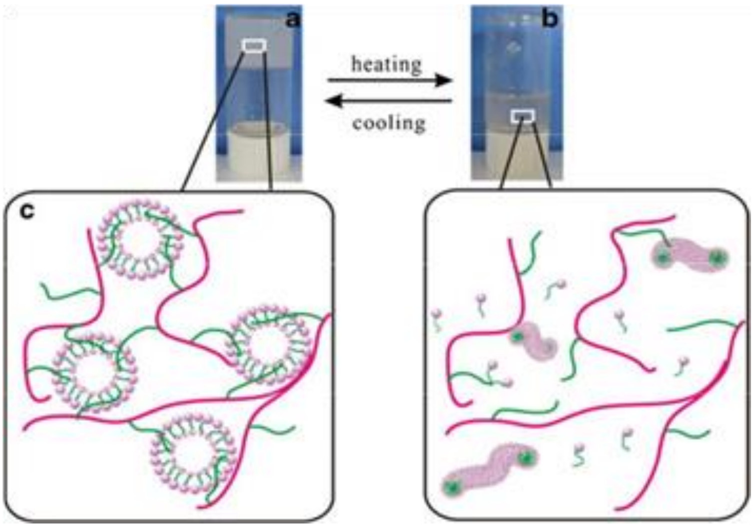

Figure 5.1 Thermal-switching of the vesicle-based gel. Photographs of a sample in aqueous solution: (a) before and (b) after heating. (c) Schematic illustration of the sol–gel transition [16]

In a more recent work, Lafont and his team [17], created a multifunctional self-healing composite capable of multiple healing by mixing an uncured thermoset rubber with reversible disulphide bonds, loading it with inert, thermally conductive graphite and hexagonal boron nitride (hBN) as fillers. They proved that the higher the healing temperature the better was the cohesion recovery even for highly loaded composites. A very promising concept that combines reversible covalent linkages through imine bond formation with non-covalent interactions through hydrogen bonds between urea-type groups inside the same polymer structure was presented by Nabarun Roy and his team [18]. Through polycondensation reaction between siloxane-based dialdehyde and carbohydrazide they managed to address reversibility to carbinol (hydroxyl) - terminated polydimethylsiloxane (PDMS) via the formation of bis-iminourea type subunits. Acylhydrazone units and lateral hydrogen bonding interactions impart to the polymer structure reversible covalent and non-covalent linkages respectively, resulting to a soft dynamic polymer film capable of autonomous healing. In addition, alterations to the mechanical properties of the polymer can be achieved by modifying the length of the siloxane spacer units. In another study, So Young An et al. [19] reported a novel dual sulfide–disulfide crosslinked networks which exhibited a rapid (30 s to 30 min) and effective self-healing ability at room temperature without external stimuli. The method that has been used for the synthesis of dual-sulfide–disulfide crosslinked network, produced a sufficient density of disulfide crosslinkages which was necessary for the completion of the self-healing process at room temperature. In a recent study, healing functionality was successfully incorporated in a polyurethane (PU) elastomer by crosslinking the tri-functional homopolymer of hexamethylene diisocyanate (tri-HDI) and polyethylene glycol (PEG) with alkoxyamine-based diol. It was shown that the design of the polyurethane molecules can be used to optimize not only the mechanical properties but also the healing performance. As can be seen in Figure 5.2 the healing process was completed only by a single step dynamic equilibrium of C-ON bonding [19].

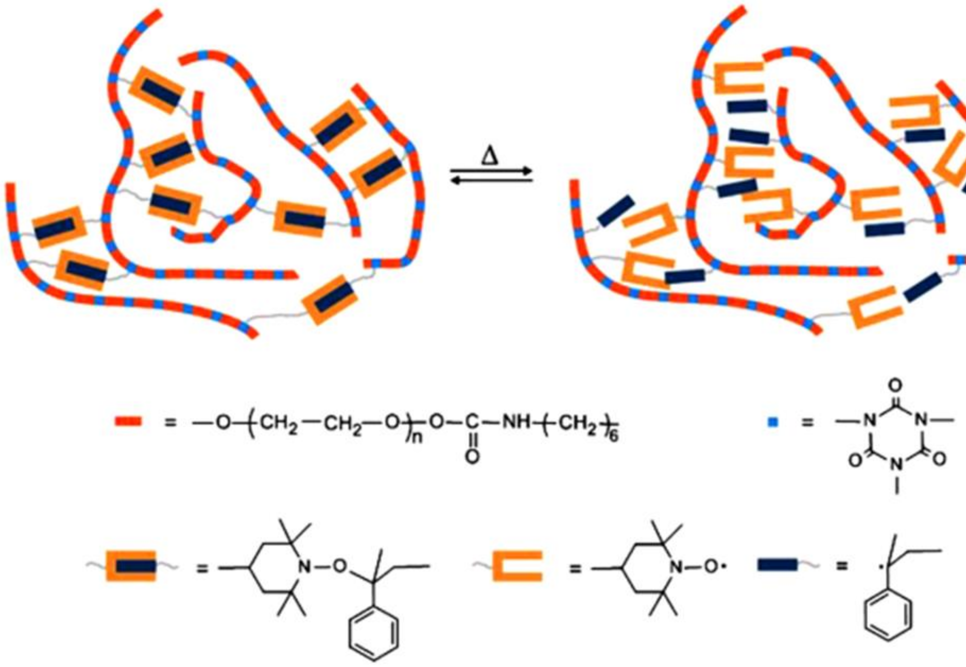

Figure 5.2 Healing mechanism of polyurethane crosslinked by alkoxyamines [19].

Thermally reversible reactions, especially the Diels-Alder (DA) reaction, for cross-linking linear polymers have been extensively studied by many researchers. The Diels–Alder reaction is an organic chemical reaction ([4+2] cycloaddition) between a conjugated diene and a substituted alkene, commonly termed the dienophile, to form a substituted cyclohexene system and can be reversible under certain conditions; the reverse reaction is known as the retro-Diels–Alder reaction (Figure 5.4). Their main advantage is the theoretically infinite number of repetitions of the healing process without any further addition of chemical or healing agents [20–23].

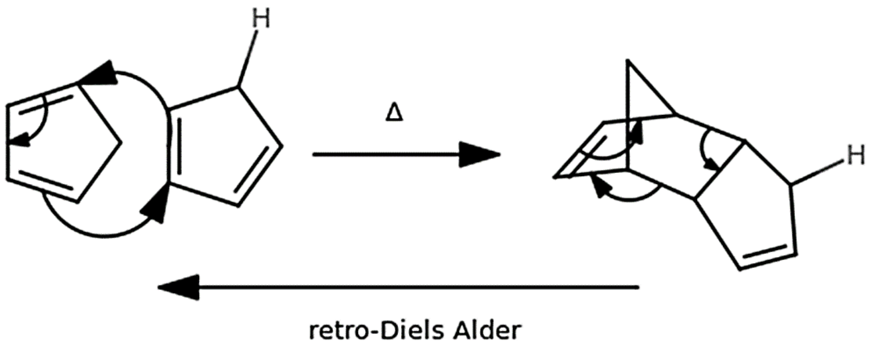

Figure 5.3 Diels-Alder and retroDiels-Alder reactions

Hermosilla et al. [24] presented a novel reversible thermoset polymer based on chemical modification of aliphatic polyaketones into the corresponding derivatives containing furan and/or amine groups along the backbone (Figure 5.4).

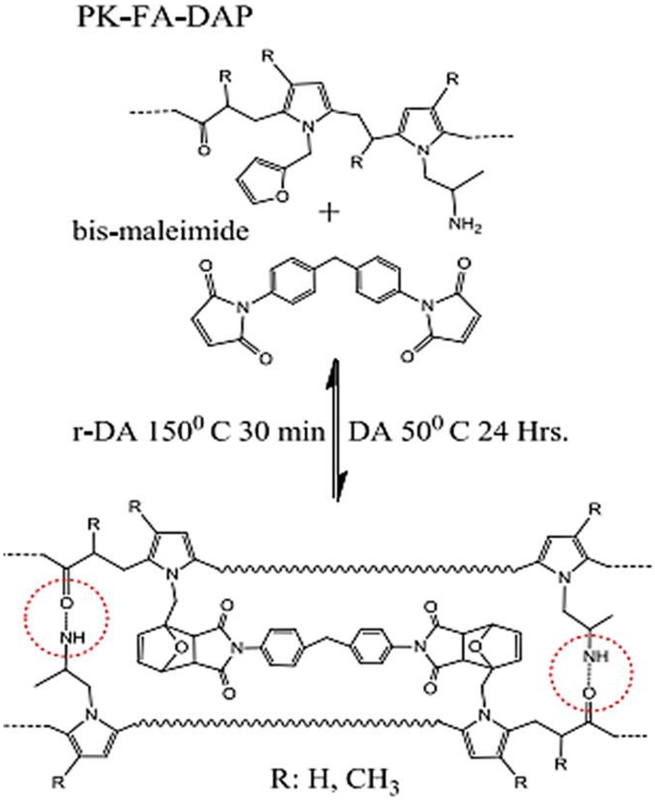

Figure 5.4 Reversible polymer networks containing covalent and hydrogen bonding interactions [24].

The furan moieties allow for the thermal setting of the polymer by the Diels–Alder (DA) and retro-DA sequence (bis-maleimide), while amine moieties allow for the tuning of the hydrogen bonding density. This new class of polymer material showed improved Tg values with respect to the respective counterparts containing only furan groups. Via this modification, these materials recovered their mechanical properties after three thermal cycles. In another study, Joost Brancart et al. [25] investigated the ability of furan-maleimide building blocks to create reversible covenant networks in an epoxy based coating. Furan-fictionalized precursors were synthesized via reaction of amines with furfuryl glycidyl ether (FGE). The reversible cross-linking of the furan- precursors with a bis-maleimide was achieved in a two-step procedure. Thermal analysis of these composites showed that modification of the polymer network structure allows for the tailoring of the temperature for the self-healing process while Atomic Force Microscopy was employed so as to study the self-healing behavior of coatings at the microscopic level (Figure 5.5).

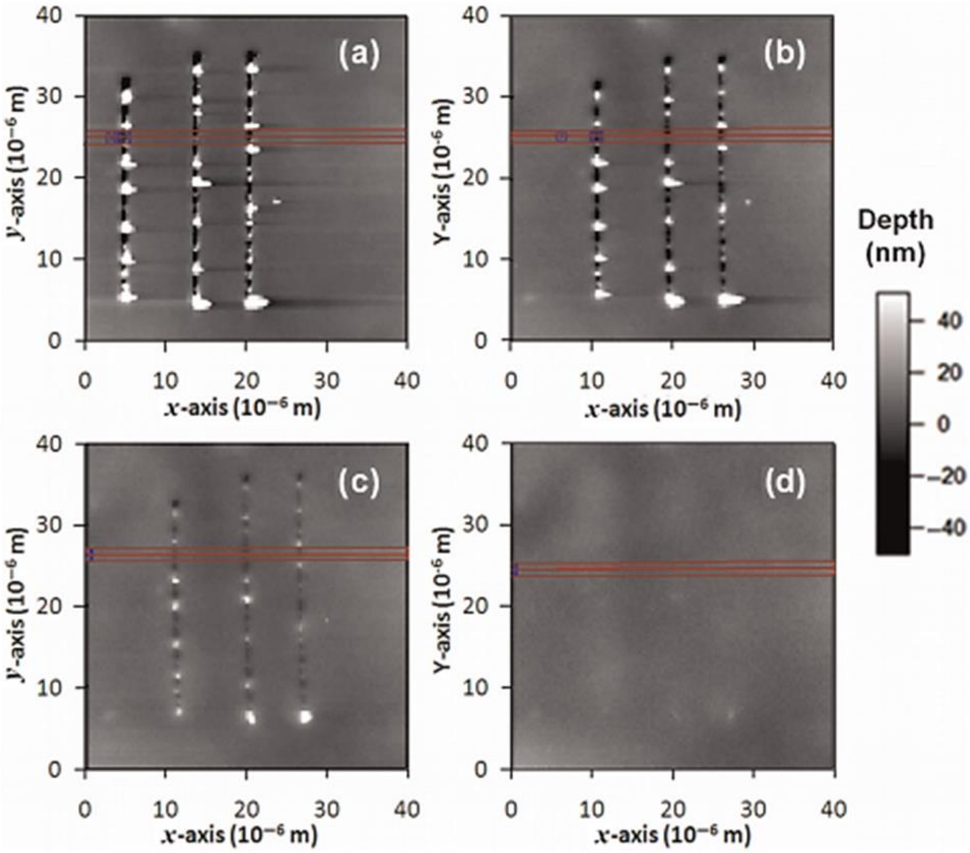

Figure 5.5 Atomic force microscopy-based study of self-healing coatings based on reversible polymer network systems [25]

Jenifer Ax and Gerhard Wenz [26] created a processable, remendable and highly oriented polymeric material with pending furane substituents, esterifying hydroxyethylcellulose with both furoylchloride and acetic anhydride (Figure 5.6). In order to achieve crosslinking (DA reaction), 1,6-bis(N-maleimido) hexane was used. They have shown that both constituents can be mixed without premature formation of gels due to the low rate DA reaction under 70 ^{o}C.

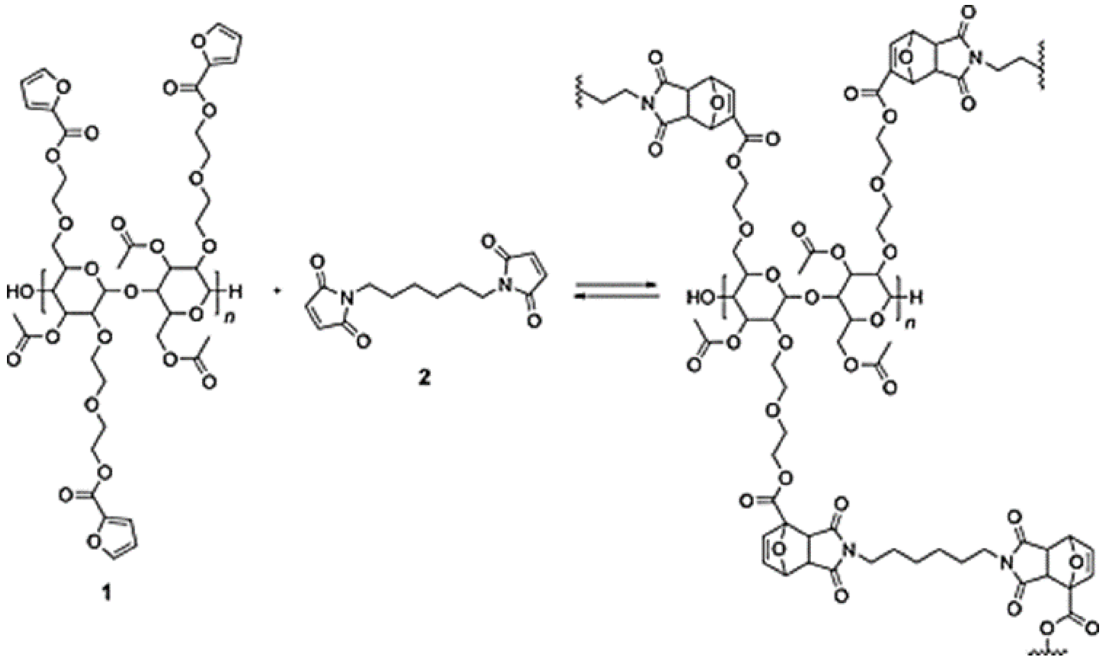

Figure 5.6 Thermoreversible Diels–Alder reaction of hydroxyethylcellulose furoate acetate **1** with bismaleimide **2** [26].

Amamoto Y. et al. [27] have successfully produced a cross-linked polymer based on reshuffling of thiuram disulfide (TDS) units. Stimulation of the self-healing process occurred under ambient conditions (visible light, air, room temperature) in the absence of a solvent. To carry out the self-healing reaction in a bulk material at room temperature, the reactive TDS units, capable of re-shuffling, were incorporated in the main chain of a low T_g polyurethane. The produced self-healing polymer managed to regain its initial mechanical properties after a 24h healing process. Figure 5.7 illustrates representative photographs of TDS cross-linked polymer along with stress strain curves at different healing times.

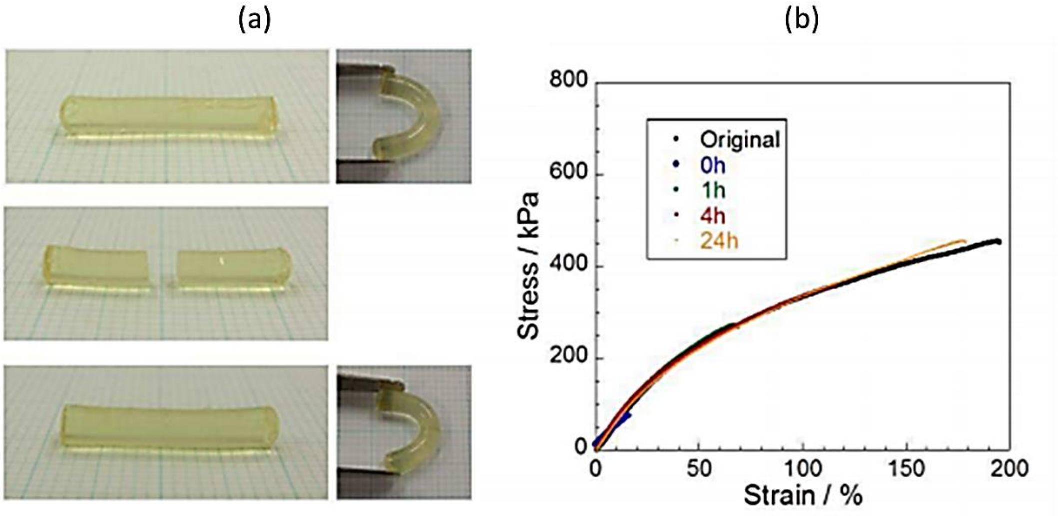

Figure 5.7 Photographs of TDS cross-linked polymer in self-healing reaction. (a) Before self-healing reaction, after cutting cross-linked polymer, and after self-healing reaction for 24 h. (d) Stress-strain curve of cross-linked polymer after irradiation of visible light at room temperature over time [27].

In a more recent work, Claudio Toncelli and co-workers [28] presented the successful synthesis and crosslinking of functionalized (varying amounts of furan groups) polyketones with (methylene-di-p-phenylene)bis-maleimide. In addition, they managed to modify thermal and mechanical properties of the material by controlling the furan reactions. This self-healable polymer exhibited an almost full recovery of thermal and mechanical properties for seven consecutive self-healing cycles, independently of the furan intake. Guadalupe Rivero et al. [29] managed to produce polyurethane networks with healing capability, based on PCL and furan-maleimide chemistry, at mild temperature conditions via one-pot synthesis. A combination of a quick shape memory effect (contact of the free furan and maleimide moieties) followed by a progressive Diels – Alder reaction (reformation of the covenant bonds) allows the remendable process to take place at 50 ^{0}C, resulting in a complete recovery of the structural integrity without complete melting of the polymer. A schematic representation of the Diels−Alder based shape memory assisted self-healing process is depicted in Figure 5.8.

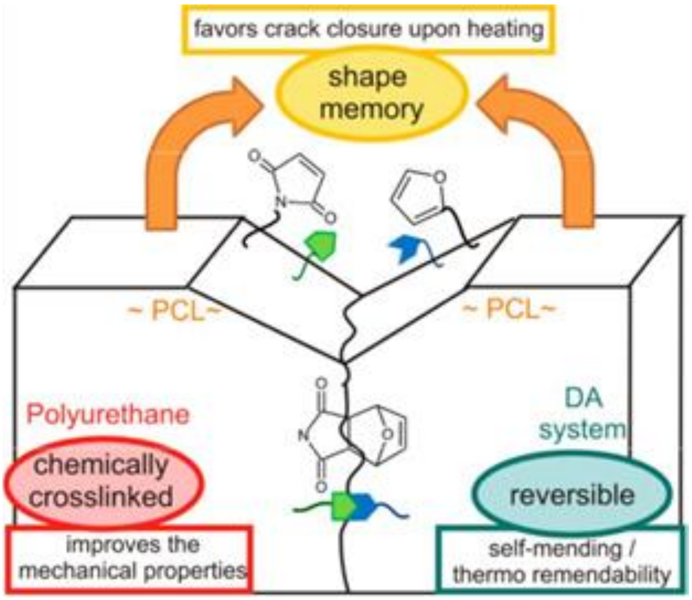

Figure 5.8 Schematic depiction of the Diels−Alder based shape [29]

The use of surface-functionalized silica nanoparticles as cross-linking agents in thermally triggered self-healing nanocomposites based on Diels-Alder chemistry of poly (butyl methacrylates) and structurally varied polysiloxanes was proposed by Sandra Schafer and Guido Kickelbick [29]. It has been observed that the healing properties of the nanocomposite are highly affected by the molecular structure of the crosslinker (spacer length), the length of the polymeric chain but also by the type of the polymer. DA reaction seemed to be favored by the use of modified polymers (high mobility) and by the presence of particles that have long spacer groups along with lower molar amount of coupling agent.

The DA mechanism has been also incorporated into polymers using a wide variety of traditional polymerization methods to obtain epoxies that combine the self-healing functionality with the advantages of a thermoset polymer [30–32]. However, during the synthesis and/or the healing process of these self-healing polymers, several side reactions may take place that could undermine the total healing efficiency of the system [33–35]. The side reaction could involve maleimide groups reacting with excess amine units (Michael addition) [36] and/or exposed maleimides reacting together (homopolymerization). The main parameter that favors the aforementioned reactions is the process time period at elevated temperatures. In detail, if the polymer is held at an elevated temperature for a long period of time, the possibility of side reaction to take place increases dramatically and the polymer is no longer thermally reversible.

In an effort to avoid the unwanted side reactions, D.H. Turkenburg and H.R. Fischer [37] modified a conventional epoxy system with Diels-Alder-based thermo-reversible crosslinks using a two-step process consisting of a bulk polymerization reaction followed by a network formation step using 1,1’- (methylenedi-4,1-phenylene) bismaleimide (BMI).The self-healing epoxy system was then used as a matrix material for the fabrication of Glass Fiber Reinforced Composites that were capable to heal cracked and delaminated areas.

To date, most previous works focused on optimizing the processing conditions during the synthesis of thermally reversible cross-linked polymers. Within the scope of this work is to investigate the effects of three different thermo-reversible cross-linking agents on the thermal and mechanical properties of the resulted self-healing epoxy systems. For this purpose, 3 different bismaleimide oligomers were introduced as cross-linking agants via a two-step process in a diglycidyl ether of bisphenol A (DGEBA) resin. Prior to the synthesis of the reversible polymers, size exclusion chromatography (SEC) was employed in order to study the average molecular weights and the polydispersities of the three oligomers. The thermal properties of the produced self-healing polymers were investigated using Differential Scanning Calorimetry while the healing efficiency was assessed using two different testing configurations at composite (mode-II fracture toughness test) and model composite (lap strap geometry) levels. GFRP coupons, have been also studied using Acoustic Emission (AE) in order to monitor the fracture process of the GFRP coupons and build an understanding on the damage behavior of materials under stress while the failure mechanisms of the virgin GFRPs have been studied using optical microscopy.

5.2. Experimental

5.2.1. Materials

Epoxy resin Diglycidyl ether of bisphenol A (DGEBA) was obtained from Polysciences Inc., USA and furfuryl amine (FA) was obtained from Sigma-Aldrich. The cross-linkers, bismaleimide oligomers BMI-1500 (viscous liquid), BMI-1700 (viscous liquid) and BMI-3000 (light yellow powder) were kindly provided by Designer Molecules Inc. It should be pointed out that the number in the BMI name denotes the average Molecular Weight of the oligomer in daltons. Figure 5.9 depicts the molecular structures of the BMIs used in this study. According to the material datasheets, the average value of n lies between 1-10 for the case of BMI-1700 and BMI-3000, while for the case of BMI-1500 is 1.3.

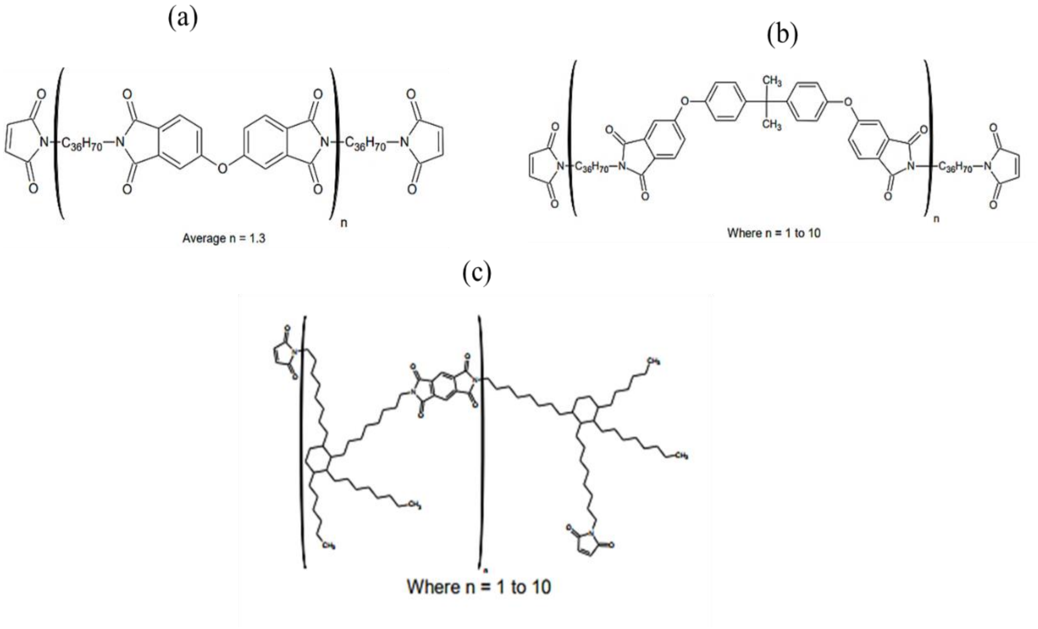

Figure 5.9 Molecular structure of (a) BMI-1500, (b) BMI-1700 and (c) BMI-3000

5.2.1.1 Glass Fiber reinforced composites – GFRP

The materials that have been employed for the manufacturing of the Glass Fiber Reinforced Polymers were described in detail in Section 4.1.1.3 of Chapter 4 (Capsules). In this case, a catalyst was not used, since the material itself acts as the healing agent and is capable of healing defects.

5.2.2. Synthesis of the reversible polymers

5.2.2.1 Prepolymerization of DGEBA/FA polymer

For the prepolymerization of the DGEBA, a similar approach as described in [37,38], was followed. This step induced a substantial degree of (irreversible) polymerization to the host material that is required to secure a sufficient mechanical strength which the most favorable characteristic of a thermoset polymer. DGEBA and FA were mixed in a metallic container at a 5:2 ratio in order to ensure that each amine group will react twice (once as primary amine and once as secondary amine) with an epoxy group, making them inactive and thus ensuring the reduction of the unwanted side reactions with the maleimide. In order to avoid evaporation of FA in the early stages of polymerization, the mixture was gradually heated up to 130 ^{0}C for 40 mins under continuous stirring. With the progress of the polymerization the viscosity of the system was dramatically increased and the stirring was stopped. Prepolymerization took place at 130 ^{0}C for 2 h and the final prepolymer was left to cool down at room temperature. At the end of the process, the final product was grinded using a laboratory grinder mill (Figure 5.10).

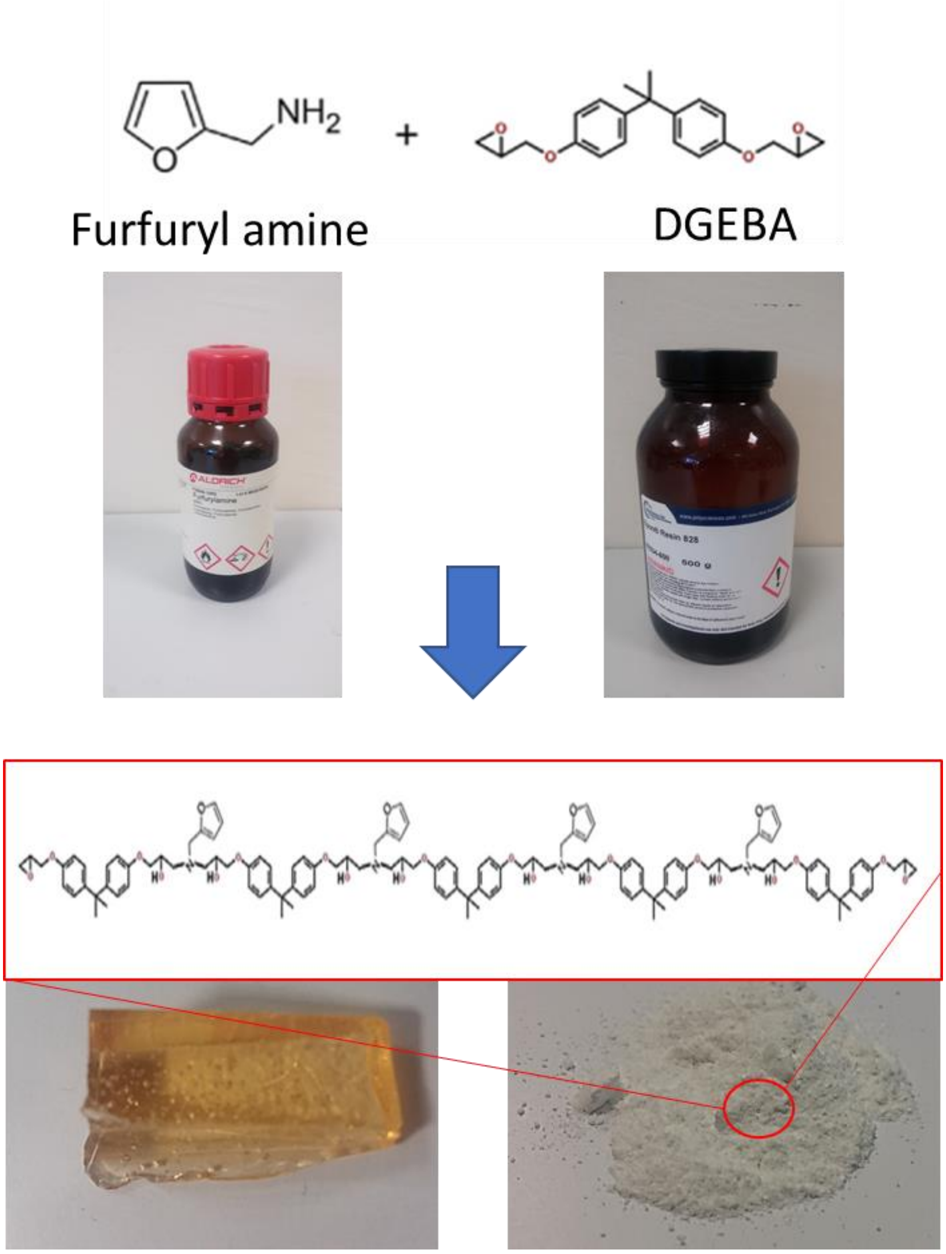

Figure 5.10 Prepolymerization of the DGEBA resin

5.2.2.2 Reversible cross-linking process

Cross-linking of the DGEBA resin occurred by adding a stoichiometric amount of BMI to the prepolymer solution. The reaction between the BMI and the furfuryl groups was performed in a ceramic container under continuous stirring. In order to avoid unwanted side reactions that take place at elevated temperatures after a long period of time, the prepolymer/BMI mixture was rapidly heated up to 150 ^{0}C ($\Delta t < 3$ min). The BMI was completely dissolved into the prepolymer after 5 min and the final polymer left to cool down to room temperature. At this stage, the reversible crosslinks between the polymeric chains of the prepolymer were formed resulting in an intrinsic self-healing epoxy resin. Due to the different molecular weight of the three cross-linkers, the average distance (d) between 2 polymeric chains is different in each of the produced polymers. Hereafter, the produced self-healing polymers will be denoted as BMI-1500, BMI-1500 and BMI-3000 with an average chain distance of d_1, d_2 and d_3, respectively ($d_3 > d_2 \geq d_1$). Figure 5.11 depicts a schematic representation of the cross-linking process along with the produced self-healing polymers.

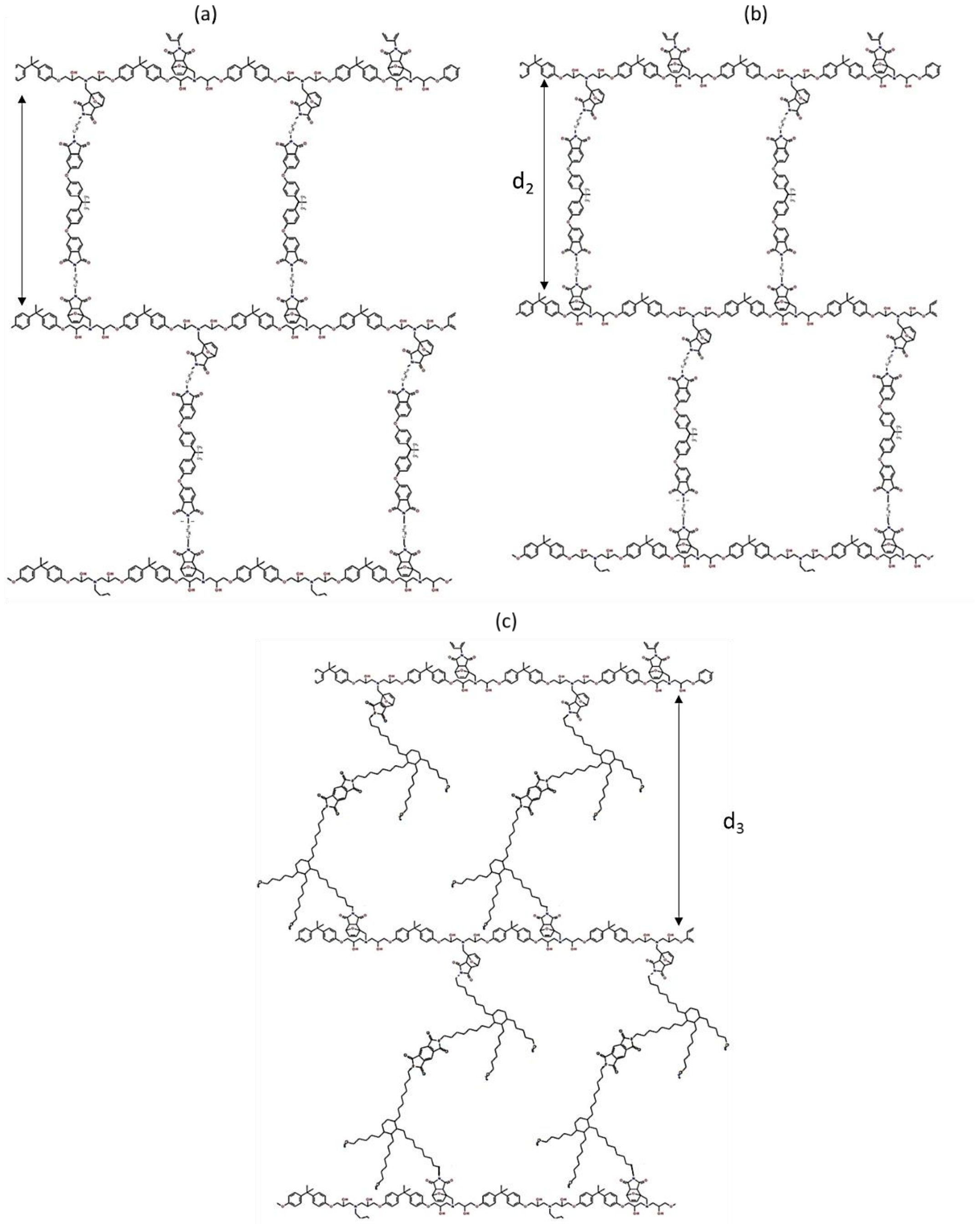

Figure 5.11 Molecular structure of (a) BMI-1500, (b) BMI-1700 and (c) BMI-3000

5.2.3. Characterization Methods of reversible polymers

5.2.3.1 Size exclusion chromatography (SEC)

Average molecular weights and polydispersities of all samples were determined by size exclusion chromatography (SEC). A size exclusion chromatograph, equipped with an isocratic pump (Spectra System P1000), column oven (Lab Alliance) heated at 30 ^{o}C, three columns in series (PL gel 5 mm Mixed-C, 300 x 7.5 mm), refractive index (RI, Shodex RI-101) and two-angle laser light scattering detectors, and tetrahydrofuran (THF) as the eluent, was calibrated with eight PS standards (M_p: 1,200–3,000,000 g/mol).

5.2.3.2 Raman Spectroscopy

The successful incorporation of the self-healing agents into the structure of the DGEBA resin was confirmed by Raman spectroscopy measurements. The 784 nm line of an NIR laser operating at 2mW at the focal plane was employed for the Raman excitation. An optical microscope served as the collector of the Raman scattering equipped with a 50x long working distance objective. Raman spectra in the range of 500–2000 cm^{-1} were recorded using a Labram HR - Horiba scientific system. Spectral treatment included a quadratic baseline subtraction, and a subsequent normalization to the band with the highest intensity.

5.2.3.3 Differential Scanning Calorimetry -DSC

To investigate the thermal behavior of the produced self-healing epoxies from 30 to 200 ^{0}C, Differential Scanning Calorimetry was employed for four subsequent heating- cooling cycles (heating with 10ºC/min, cooling with 5º/min) using a DSC 404 C Pegasus Thermal analyzer Netzsch-Gerätebau GmbH, Germany. This study provided useful information about the optimized temperature for the synthesis and the healing process of the reversible epoxy systems.

5.2.4. Manufacturing process

5.2.4.1 Glass Fiber reinforced composites – GFRP

GFRP coupons manufacturing process was described in Chapter 4, Section 4.2.4.2 (Capsules). At the midplane of the GFRP coupon, 170 g/m^2 of melted reversible polymer was employed to impregnate plies 9 and 10 of the GFRP coupons. Figure 5.12 illustrates a schematic representation of the manufactured GFRP coupons that have been subjected to mode-II interlaminar fracture toughness test.

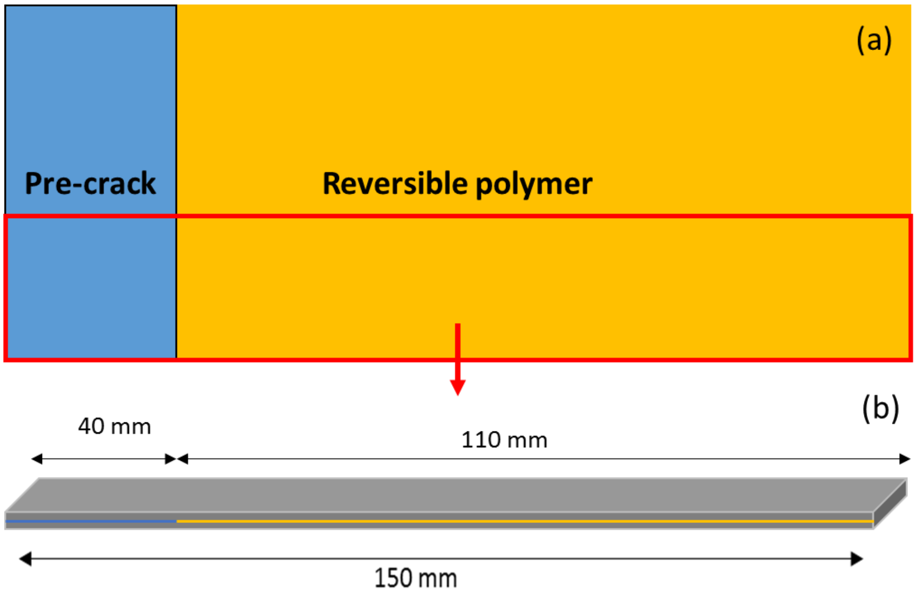

Figure 5.12 Intrinsic healing GFRP composite

5.2.4.2 Lap strap specimen

The manufacturing process of the lap strap specimens was described in detail in Chapter 4, Section 4.2.4.3. BMI-1500, BMI-1700, and BMI-3000 were employed as adhesives between the lap and the strap, in order to assess the efficiency of these three reversible epoxy systems to heal damages in composite structures. The thermo-reversible polymers were introduced between the lap and the strap using a hot press. Bonding took place at 140 ^{0}C for the cases of BMI-1500 and BMI-1700 and at 110 ^{0}C for the case of BMI-3000 while the process duration was selected at 3 min in order to avoid/reduce the unwanted side reactions. Processing temperatures (bonding and healing) were selected based on the results obtained from the DSC experiment which will be presented in the following section (Results and Discussion). At the end of the process, the manufactured lap strap specimens left to cool down for 10 h at ambient temperature.

5.2.5. Mechanical characterization

The testing protocols that have been adopted for the mechanical characterization of the GFRP coupons and the lap strap specimens was described in detail in Chapter 4 , Section 4.2.5.2. Mechanical testing was performed on unhealed and after 4 healing events specimens. Hereafter, specimens before healing will be denoted as virgin specimens while healed 1, healed 2, healed 3 and healed 4 will be referred to specimens that have been subjected to 1,2,3 and 4 healing cycles, respectively. In the case of GFRP coupons a comparative study between unmodified (reference) and intrinsic (virgin) composite materials have been conducted in order to investigate the knock-down effect of introducing a self-healing functionality to a polymeric matrix.

5.2.6. *Acoustic Emission – AE*

AE has been employed in order to monitor the fracture process of structural materials and build an understanding on the damage behavior of materials under stress. The AE activity was recorded on-line using a wide band AE sensor (R-15-ALPHA, Physical Acoustics Corp., PAC) that was attached on the upper side of the specimen. A layer of medical ultrasonic gel was applied between the sensors and the specimen to provide acoustic coupling. Due to the specific sensors sensitivity to frequencies from 100 up to 600 kHz, it can capture a wide range of different sources. The pre-amplifier gain was set to 40 dB. After performing a pilot test, the threshold was also set to 40 dB in order to avoid the possibility of electronic/environmental noise. The signals were recorded in a two-channel monitoring board PCI-2, PAC with a sampling rate of 5 MHz.

5.2.7. *Optical microscopy*

Optical Microscopy (OM) was employed on the fractured surfaces of the GFRP specimens in order to gain an insight on the morphology of the laminates fracture characteristics. At the end of the mechanical testing, the opposite sides of the fractured surfaces, corresponding to plies 8 and 9, were cut in coupons 50x25mm and subsequently were optically scanned using a Leica DM-4000M optical microscope with up to 1000x magnification.

5.2.8. *Assessment of the healing efficiency*

After mechanical testing, healing of the GFRP coupons and lap strap specimens was achieved using a hot press. In the case of composites containing BMI-1500 and BMI-1700 polymers, healing was performed at 140 ^{0}C, while for the BMI-3000 modified composites, the selected healing temperature was 110 ^{0}C. The entire healing process lasted 5 mins while no external pressure was applied on the composites in order to avoid material loss due to resin leakage and maintain the virgin specimen thickness**.** Healed specimens were left to cool down for 3 h and were retested under the same loading conditions. At this point the second reaction that is required for the self-healing process, that of DA was completed. For both testing configurations, a total of 4 healing cycles were performed. Healing efficiency for the case of GFRP coupons was calculated in terms of peak load (P_C) and mode-II interlaminar fracture toughness energy (G_{IIC}) recovery using Eq. 4.6 and 4.7, respectively. The efficiency of the lap strap specimens to regain their initial mechanical properties was quantified using Eq 4.8 and 4.9. These two quantities are related to: (i) stiffness recovery n_E and (ii) initial delamination strength recovery n_σ.

5.3. Results and discussion

5.3.1. *Reversible polymers*

5.3.1.1 Size exclusion chromatography (SEC)

The SEC was calibrated with polystyrene standards varying from 10^3 up to $3x10^6$. Since the standards have a different chemical structure from the initial materials that have been used, only qualitative results have been obtained from the SEC method. For comparison reasons, all the chromatographs of the three different materials are illustrated in a single graph (Figure 5.13).

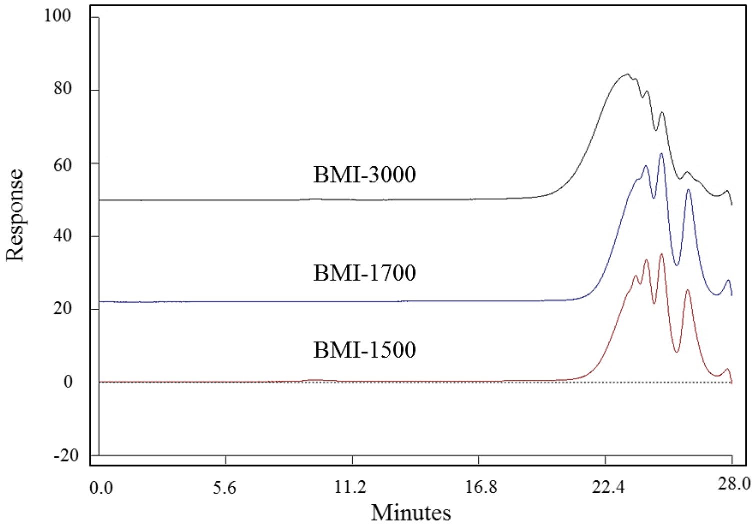

Figure 5.13 Chromatographs obtained from the three oligomers.

As can be observed, the BMI-1500 and BMI-1700 exhibited similar results, whereas BMI-3000 showed a completely different behavior. For the case of BMI-1700, the obtained n value seamed to vary from 1 up to 4 and not from 1 up to 10 as indicated in the datasheet. A different n value of that indicated in the datasheet (n=1.3) was also obtained for the oligomer BMI-1500 where the average “n” value seemed to vary from 1 – 3.5. However, in the case of BMI-3000 the GPC results are in a good agreement with those given in the datasheet where the n value lied between 1 and 8 instead of 1 to 10.

5.3.1.2 Raman Spectroscopy

Figure 5.14 shows the basic vibrational modes of FA, DGEBA and the resulting prepolymer. The most prominent bands in the spectrum of FA were the C-N stretching vibration of primary amines at about 1074 cm^{-1} and the furan ring vibration appearing at 1504 cm^{-1} [39]. The more complex structure of DGEBA resin was reflected in its spectrum by a multitude of different peaks. However, only the band placed around 1250 cm^{-1} and representing the C-O stretching motions of the epoxide groups was of interest in the current analysis [40].

As already shown in Figure 5.10 an opening of the epoxide group takes place during the prepolymerization of DGEBA with FA. As is evident in the prepolymer spectrum of Figure 5.14 this characteristic vibrational mode was still present, denoting a remaining amount of unreacted epoxide groups, but its shape became sharper in comparison to the DGEBA spectrum showing a notable decrease in the amount of epoxide groups. An additional evidence of the successful formation of the prepolymer was given by the presence of the C-N stretching vibration at 1067 cm^{-1}. This vibration was downshifted by ~7 cm^{-1} as a result of the incorporation of the amine group in the polymeric chain of the host resin.

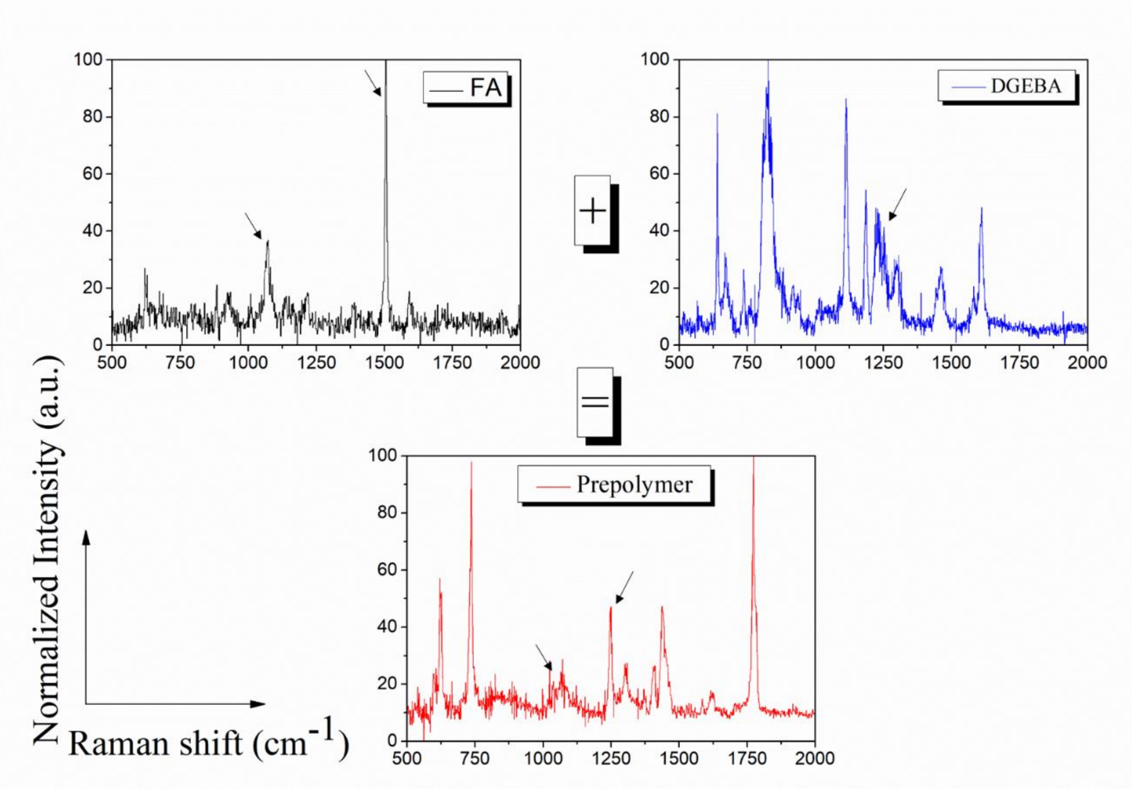

Figure 5.14: Normalized Raman spectra of FA, DGEBA and the resulting prepolymer.

A comparison of the spectra of the three BMIs with that of the prepolymer can be seen in Figure 5.15. The black arrows indicate the peaks of interest for the current analysis. In general, the three BMIs presented the same number of Raman bands with the main differences among them being exhibited in the peaks' characteristics (shape, intensity and position). More specifically, in all BMI cases some new peaks arose after the addition of the maleimide to the prepolymer. These bands were, i) The maleimide out-of-plane C-H bending vibration found at 820 cm^{-1}, 831 cm^{-1} and 827 cm^{-1} for the BMI-1500, BMI-1700 and BMI-3000 [41] , respectively and ii) the furan ring vibration [39] placed at 1500-1505 cm^{-1} for all the three BMIs.

A differentiation among the BMIs was evidenced as a decrease in the intensity of the maleimide out-of-plane C-H bending vibration for the case of the lengthy BMI-3000 precursor. BMI-3000 also presented a significantly higher amount of epoxide groups (Raman band positioned at about 1250 cm^{-1}) in comparison to BMI-1500 and BMI-1700. Based on the aforementioned evidence we postulate that although BMI-1500 and BMI-1700 have very similar spectral profiles or equally structures, BMI-3000 differs substantially possibly due to its decreased ability to be inserted into the prepolymer's polymeric chains.

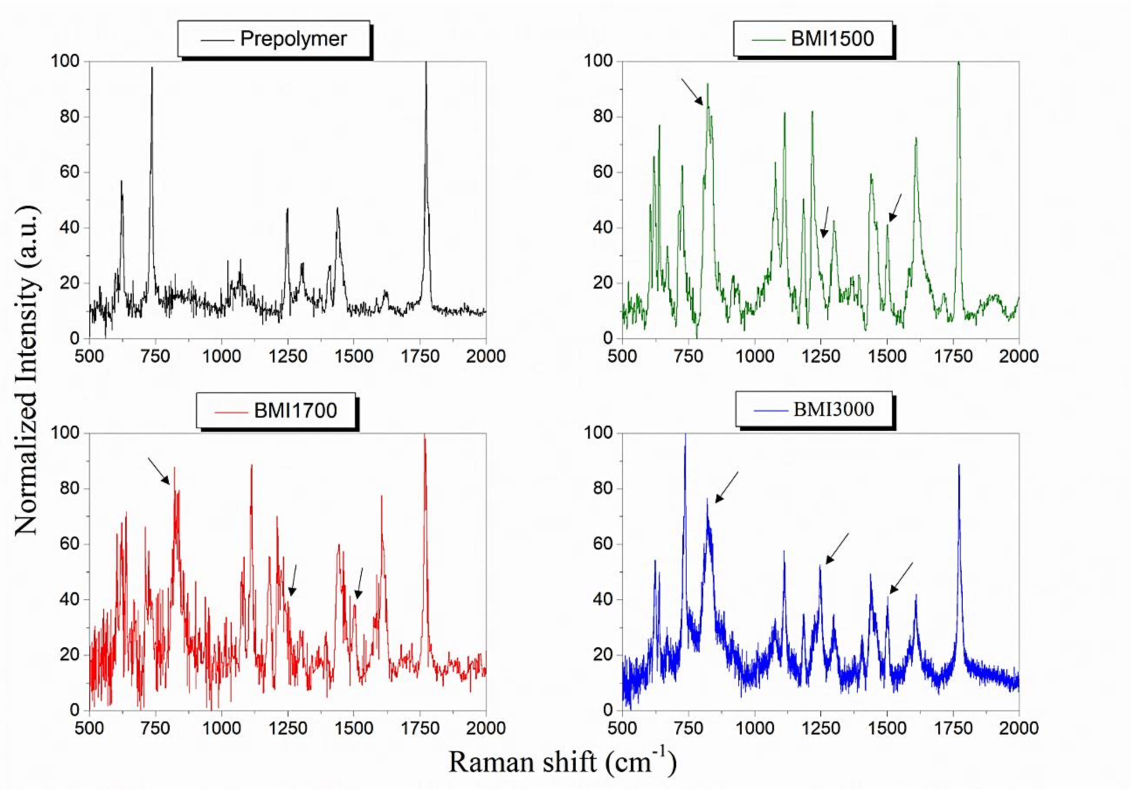

Figure 5.15 Normalized Raman spectra of the prepolymer and the three BMIs.

5.3.1.3 *Differential Scanning Calorimetry*

Figure 5.16a illustrates the DSC curves obtained from the virgin BMI-1500 polymer and the same polymer after 4 consecutive healing cycles. The glass transition temperature (Tg) of the virgin self-healing polymer was manifested as an endothermic peak and was calculated at 50.1 ^{0}C. This value exhibited a minor decrease at 48.6 ^{0}C after 4 healing cycles showing that the healing process had a minor impact on the glass transition temperature of the polymer. It should be mentioned that the duration of all the healing cycles was kept as short as possible to avoid unwanted side reactions.

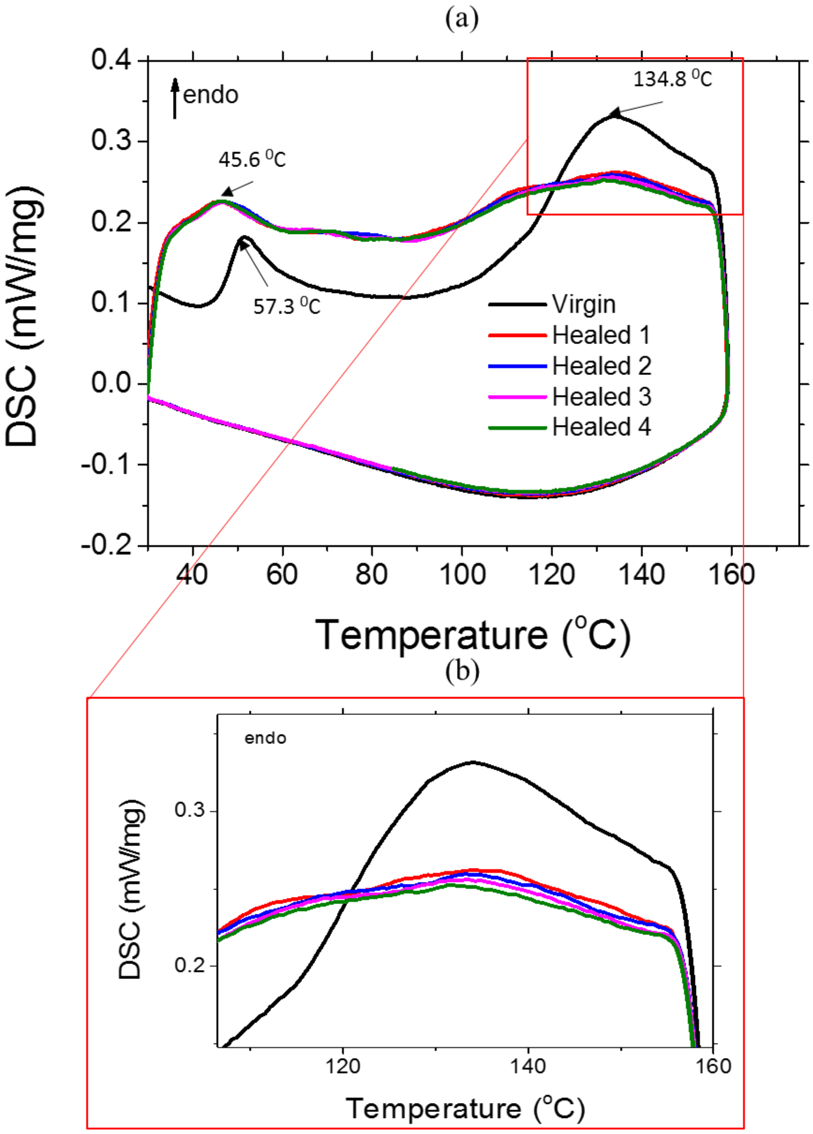

Figure 5.16 (a) DSC curves for the BMI-1500 for 5 subsequent heating- cooling cycles and (b) zoomed temperature window of the reversible rDA reaction.

The second endothermic peak for the virgin BMI-1500 was evident at approximately 134.8 ^{0}C and was attributed to the thermo-reversible reaction of retroDiels-Alder (Figure 5.16b). As is well know the area under a peak of a DSC curve, represents the total amount of energy that is required for the completion of a reaction. In this case, the area under the peak that represents the rDA reaction showed a reduction after the first healing cycle and remained unaltered for the rest of the heating-cooling cycles. This behavior can be attributed to the radical polymerization of the unreacted BMI-1500 precursor that did not participate to the formation of the thermo-reversible cross-link network. The aforementioned process is irreversible, thus cannot be spotted in the rest heating cycles of the DSC measurement. During cooling, a wide exothermic peak can be observed and is attributed to the second thermo-reversible reaction that participates to the healing process, that of Diels-Alder.

The DSC curves obtained from the polymer BMI-1700 after 5 heating-cooling cycles are depicted in Figure 5.17a

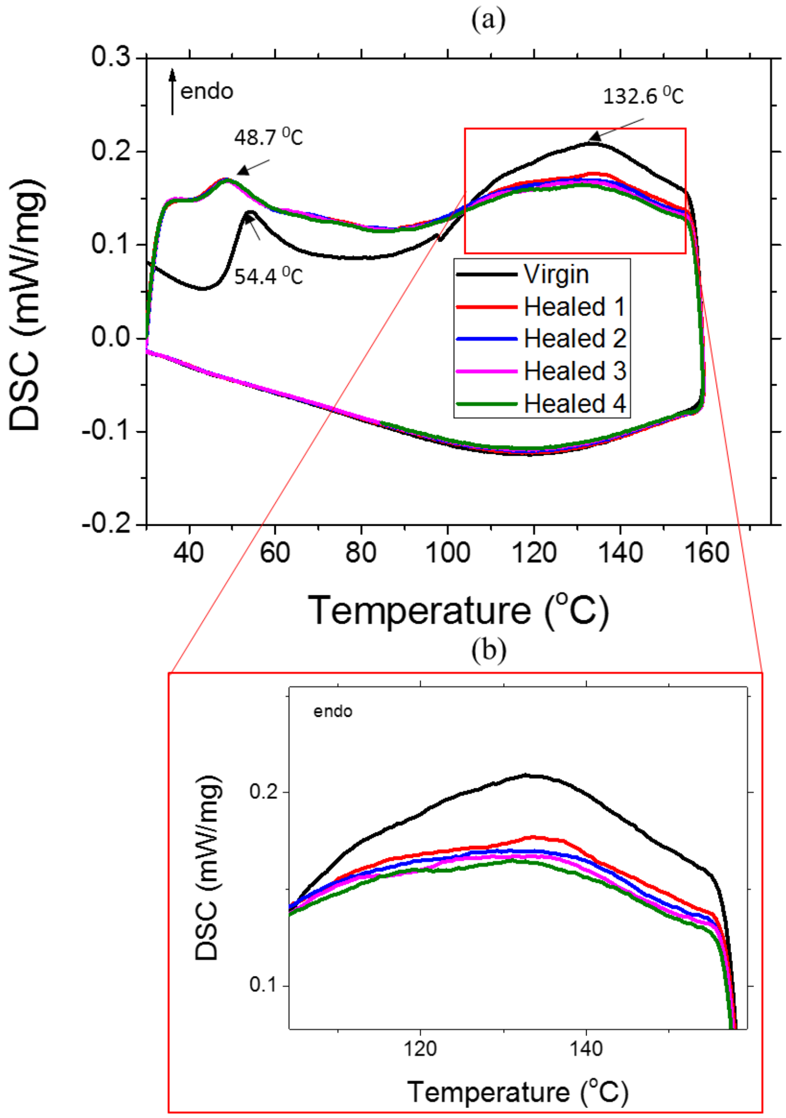

Figure 5.17 (a) DSC curves for the BMI-1700 for 5 subsequent heating- cooling cycles and (b) zoomed temperature window of the reversible rDA reaction.

As can be seen the BMI-1700 exhibited a similar thermal behavior compared with the BMI-1500. In detail, the glass transitions temperature was determined at 48.0 ^{0}C for the case of the virgin polymer while after 4 healing cycles, the Tg decreased marginally at 46.2 ^{0}C, showing that the heating-cooling process did not affect the glass transition temperature of the polymer. However, the second endothermic peak at 132.6 ^{0}C that corresponds to the rDA reaction, appeared wider than that of the BMI-1500 indicating a more gradual transition from the solid to the liquid state (healing process). In addition, the reduction in the area under the second endothermic curve after a healing event is approximately the same compared to BMI-1500 (Figure 5.17b). Thus, it can be postulated that the amount of unreacted BMI precursor during the formation of the reversible network is almost the same for both cases.

As can be observed in Figure 5.18a, the thermal behavior of the BMI-3000 is significantly different compared to the other two reversible polymers. The Tg was determined at 46.2 ^{0}C for the virgin reversible polymer while it remained unaltered after 5 heating-cooling cycles.

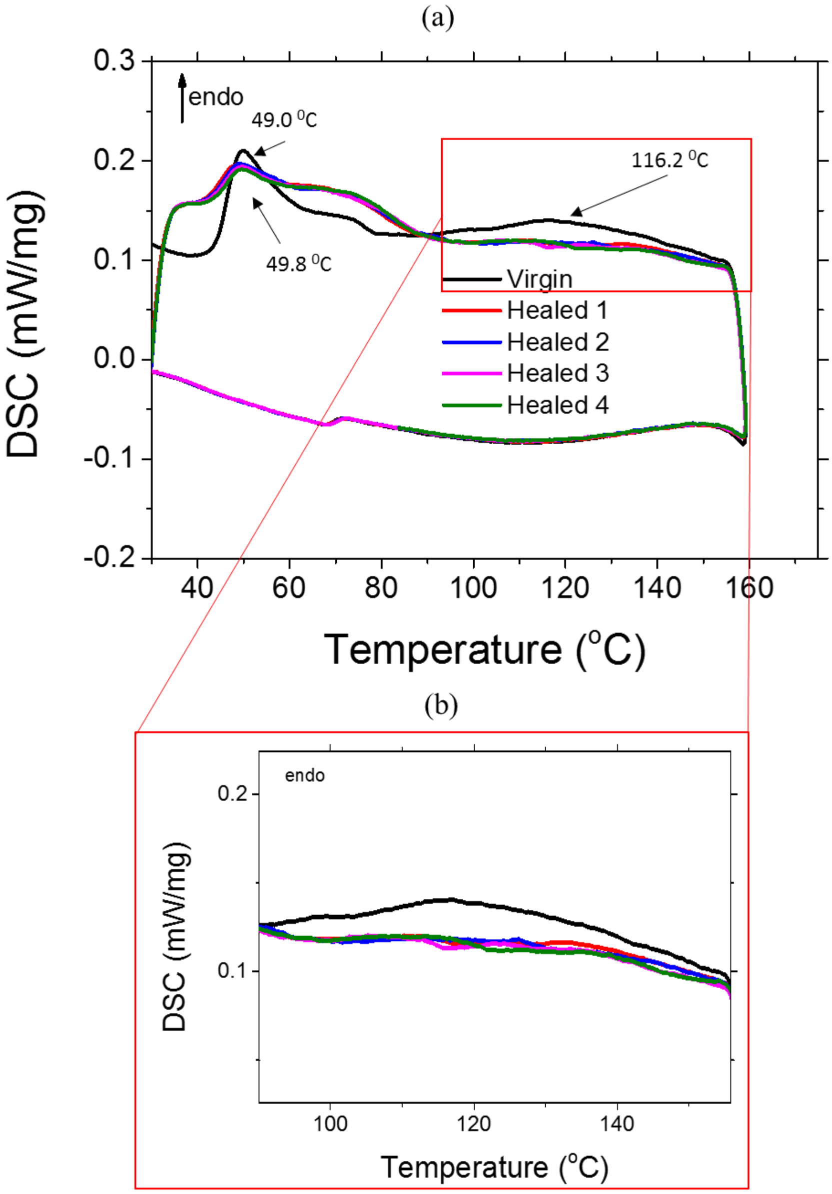
(a)

(b)

Figure 5.18 (a) DSC curves for the BMI-1700 for 5 subsequent heating- cooling cycles and (b) zoomed temperature window of the reversible rDA reaction.

The second rDA reaction in this case took place at approximately 110 ^{0}C (Figure 5.18b). This shift of the healing temperature towards lower values can be attributed to the increased length of the BMI-3000 precursor that enhanced the occurrence of the rDA reaction at lower temperatures. In addition, the reduction of the energy required for the completion of the rDA reaction was significantly increased after a single healing cycle, showing that the lengthy, BMI-3000 precursor was not sufficiently inserted between the polymeric chains and thus remained unreacted. This enhancement in the irreversible radical polymerization of the BMI is expected to have a detrimental effect on the self-healing performance of the BMI-3000. Table 5-1 summarizes the obtained glass transition temperatures for 5 heating-cooling cycles for all the interrogated systems.

Table 5-1 Tg values or all the interrogated systems

Specimen	**Cycle**	**Tg (^{0}C)**	**Specimen**	**Cycle**	**Tg (^{0}C)**	**Specimen**	**Cycle**	**Tg (^{0}C)**
BMI-1500	1	50.1	BMI-1700	1	48.0	BMI-3000	1	46.2
	2	48.7		2	45.6		2	45.1
	3	48.7		3	47.2		3	45.8
	4	48.6		4	46.3		4	46.0
	5	48.6		5	46.2		5	46.2

5.3.2. GFRP coupons

5.3.2.1 Mechanical characterization

Representative load versus displacement curves obtained from the mode II interlaminar fracture toughness tests of the reference, virgin and healed (4 healing cycles) BMI-1500 GFRPs are depicted in Figure 5.19. As can be seen, by modifying the epoxy resin into a reversible polymer, did not significantly affected neither the peak load (P_{max}) nor the mode II fracture toughness energy (G_{IIc}) values Table 5-2. In detail, the P_{max} and the G_{IIc} in the case of the reference GFRPs were calculated at 608 ± 20 N and 2.84 ± 0.15 kJ/m^2, respectively. In the case of the virgin BMI-1500 GFRP the aforementioned P_{max} values exhibited a minor increase reaching at 559 ± 25 N while the G_{IIc} remained unaltered at 2.85 ± 0.3 kJ/m^2.

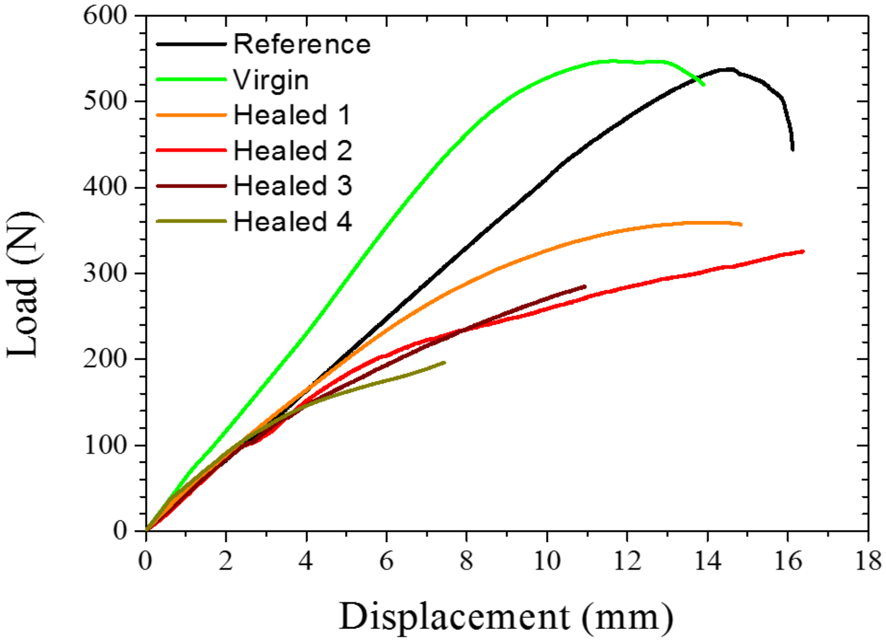

Figure 5.19 Load vs cross-head displacement curves for the reference, virgin and healed BMI-1500 GFRPs

After, the first healing event the GFRP regained its initial maximum load at 64.40% and the mode II fracture toughness energy at 66.30% while after the second healing cycle the aforementioned healing efficiency values were calculated at 53.8% and 56.14% (Table 5-2).

Table 5-2 Mode II Fracture toughness energy under (G_{IIC}), peak load (P_{max}) and healing efficiency values for the BMI-1500 composite

Specimen	**P_{max} (N)**	**G_{iic} (kJ/m2)**	**n_P (%)**	**n_G (%)**
Reference	538 ± 20	2.84 ± 0.15	-	-
Virgin	559 ± 25	2.85 ± 0.20	-	-
Healed 1	360 ± 20	1.89 ± 0.32	64.4	66.31
Healed 2	301 ± 31	1.6 ± 0.35	53.84	56.14
Healed 3	220 ± 18	0.62 ± 0.22	39.35	21.75
Healed 4	148 ± 17	0.25 ± 0.14	26.47	8.77

After the fourth healing process, the reversible polymer was unable to effectively regain its initial properties (n_p = 26.40% and n_G = 8.77%). This behavior can be attributed to the increased cumulative duration of the healing process that enhanced the side reactions at elevated temperatures. Even though an intrinsic self-healing polymer is theoretically capable of regaining its initial properties/functionalities for an infinite number of repetitions, in practice there is a limit to this reversible character and its associated with the side reactions [30,34]. Figure 5.20 presents a schematic representation of the irreversible side reactions occurring after an increased process time at elevating temperature.

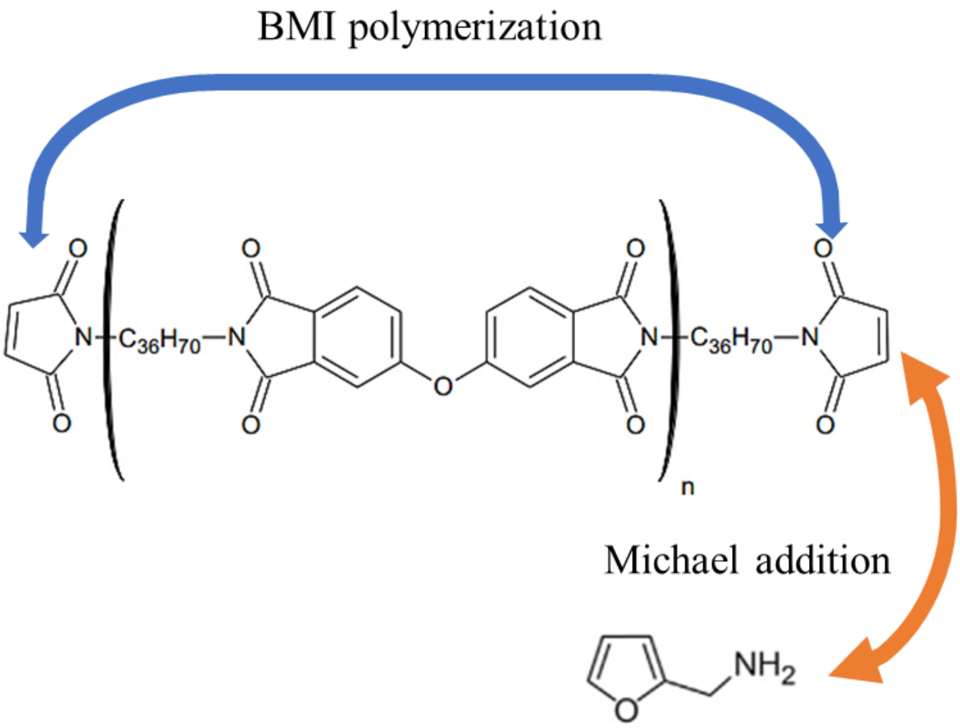

Figure 5.20 Unwanted side reactions

Figure 5.21 illustrates representative load extension curves obtained from the mode II interlaminar fracture toughness tests of the reference, virgin and healed (4 healing cycles) BMI-1700 GFRPs while Table 5-3 summarizes the calculated healing efficiency values in terms of P_{max} (Eq. 4.6) and the G_{IIc} (Eq.4.7).

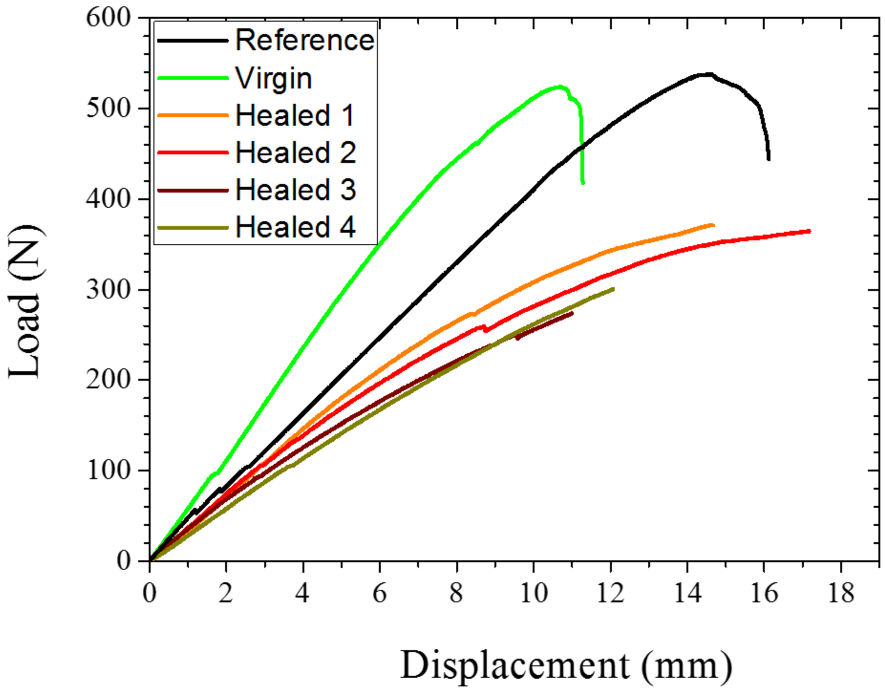

Figure 5.21 Load vs cross-head displacement curves for the reference, virgin and healed BMI-1500 GFRPs

In this case, a similar behavior with the composites containing BMI-1500 as interlayer can be observed. However, it is evident that the introduction of the reversible polymer BMI-1700 at the composite midplane had a detrimental effect on the fracture toughness. In detail, the P_{max} and G_{IIC} values of the virgin specimens showed a decrease of 3% and 20%, respectively. After the first healing event, the recovery of P_{max} reached at 67.93% and the healing efficiency in terms of G_{IIC} was calculated at 77.63%. The aforementioned healing efficiency values remained the same even after two healing cycles (n_p = 65.83%, n_G = 79.38%) while after the fourth healing, a satisfying recovery in both quantities was calculated (n_p = 43.89%, n_G = 32.89%).

Table 5-3 Mode II Fracture toughness energy under (G_{IIC}), peak load (Pmax) and healing efficiency values for the BMI-1700 composite

Specimen	**P_{max} (N)**	**G_{iic} (kJ/m2)**	**n_P (%)**	**n_G (%)**
Reference	538 ± 20	2.84 ± 0.15	-	-
Virgin	524 ± 18	2.28 ± 0.12	-	-
Healed 1	356 ± 21	1.77 ± 0.32	67.93	77.63

Healed 2	345 ± 23	1.81± 0.35	65.83	79.38
Healed 3	254 ± 17	0.92 ± 0.22	48.47	40.35
Healed 4	230 ± 27	0.75 ± 0.14	43.89	32.89

Representative load versus displacement curves obtained from the mode-II interlaminar fracture toughness tests of the reference virgin and healed GFRPs containing BMI-3000 at the midplane are depicted in Figure 5.22.

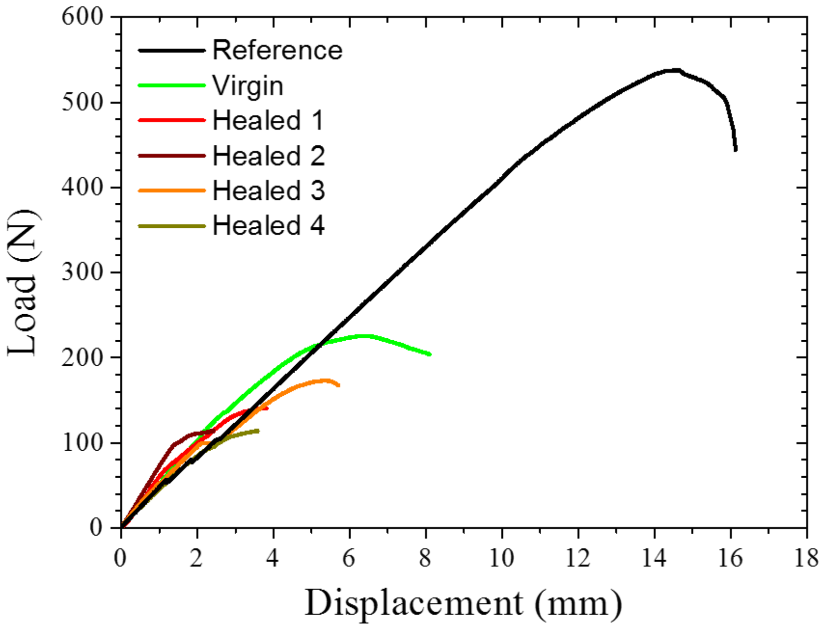

Figure 5.22 Load vs cross-head displacement curves for the reference, virgin and healed BMI-1500 GFRPs

It is evident, that the incorporation of the BMI-3000 as interlayer at the GFRP midplane, highly decreased the fracture toughness of the composite. As can be seen in Table 5-4 both the P_{max} and G_{IIC} values exhibited a dramatic decrease reaching at 225 ± 18 N and 0.57 ± 0.12 kJ/m^2, respectively. Regarding the healing efficiency of the system, after the first healing event the reversible polymer managed to regain its initial peak load at 76.44% and the G_{IIC} values at 56.14% while after the second healing cycle the aforementioned percentages reached at 62.22% and 31.57%, respectively. This behavior is a clear indication that the BMI-3000 is not a suitable candidate for the modification of an epoxy system towards the development of a reversible polymeric matrix.

Table 5-4 Mode II Fracture toughness energy under (GIIC), peak load (Pmax) and healing efficiency values for the BMI-1700 composite

Specimen	**P_{max} (N)**	**G_{iic} (kJ/m^2)**	**n_P (%)**	**n_G (%)**
Reference	538 ± 20	2.84 ± 0.15	-	-
Virgin	225 ± 18	0.57 ± 0.12	-	-
Healed 1	172 ± 21	0.32 ± 0.32	76.44	56.14
Healed 2	140 ± 23	0.18 ± 0.35	62.22	31.57
Healed 3	113 ± 17	0.09 ± 0.22	50.22	15.78
Healed 4	110 ± 27	0.14 ± 0.14	48.89	24.56

5.3.2.2 Acoustic Emission

Figure 5.23 summarizes the AE profile of the virgin BMI-1500, BMI-1700 and BMI-3000 GFRP coupons during the mode-II fracture toughness tests. As can be seen, in all cases the cumulative AE activity of the virgin specimens indicated a typical brittle crack initiation. For almost the entire duration of the mechanical testing, AE activity, exhibited a plateau on the respective graphs followed by an abrupt increase just before the crack initiation. However, it should be noted that the AE activity in the case of BMI-3000 is significantly lower than the other two reversible systems. This behavior can be possible attributed to the weak interfacial bonding between the polymer and the glass fibers. A postulation that can be supported by the decreased fracture toughness reported in the case of BMI-3000 and from the results obtained from the OM study that will be presented in the next section.

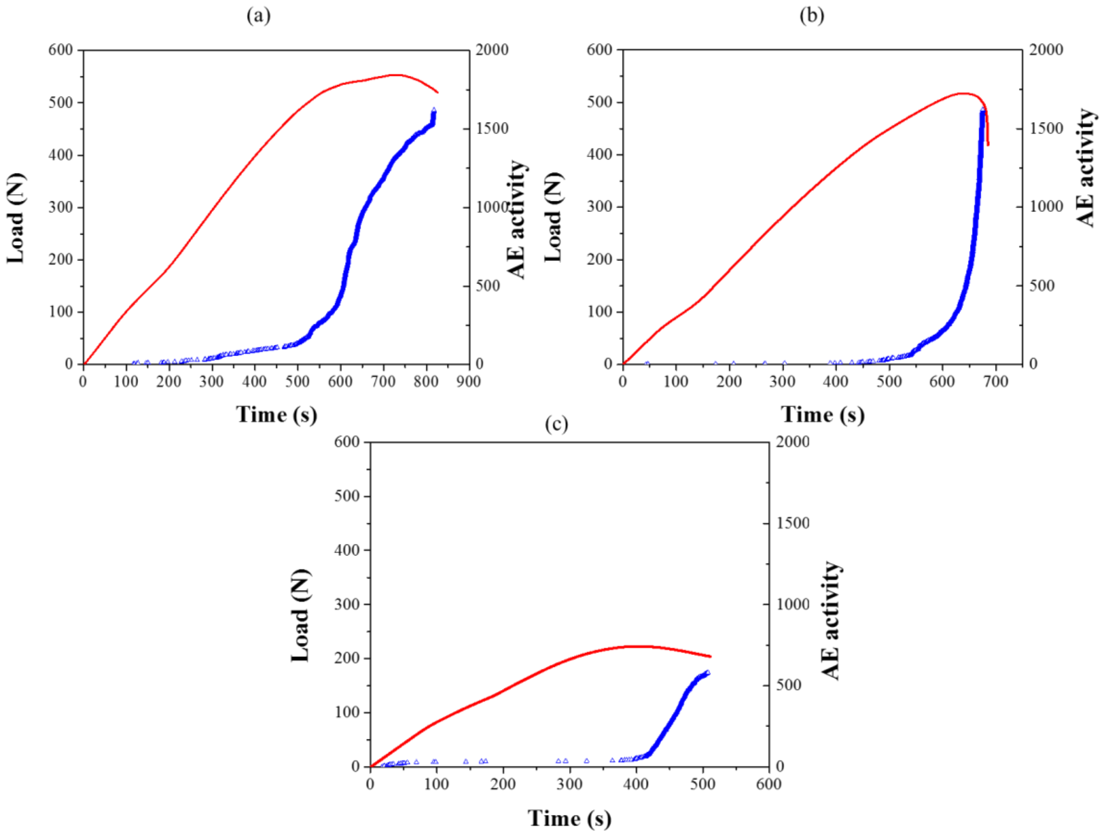

Figure 5.23 AE activity of the virgin (a) BMI-1500, (b) BMI-1700 and (c) BMI-3000.

Figure 5.24 depicts how the healing processes affected the cumulative AE activity of the interrogated GFRP coupons.

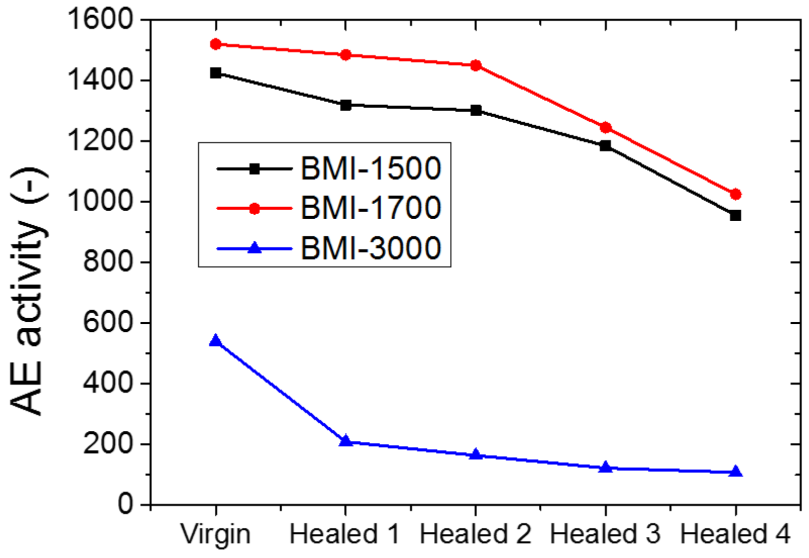

Figure 5.24 AE activity versus healing cycles for all the studied systems

As it was expected, the AE activity decreased because the healing functionality of the material is well known to decrease with successive healing cycles and is not in reality a reversible process [42]. In all cases, a reduction in AE activity with increasing healing cycles is evident since the material after healing is not capable of full repairing all the damaged sites. It is well known that the initiation and propagation of cracks within a material under stress invokes stress waves that propagate within the material known as AE [43,44]. Thus, the number of produced AE events was decreasing with increasing healing events.

5.3.2.3 Optical microscopy - OM

In order to examine the failure mechanisms after the mode-II fracture toughness tests, the fractured surfaces of the virgin GFRP coupons were studied via optical microscopy. The following figures illustrate the OM micrographs obtained from the opposite sides of the fractured surfaces of the three GFRP coupons. As can be observed the failure mechanisms differ with the BMI-3000 exhibiting a completely different behavior. In more detail, in the case of BMI-1500 a cohesive failure mechanism is evident since both surfaces of the composite are completely covered by the reversible polymer and there is no evidence of exposed fibers. (Figure 5.25). This failure mechanism indicates a strong interphase between the BMI-1500 and the glass fibers. It should be noted, that these results are in agreement with those obtained from the mechanical characterization of the BMI-1500.

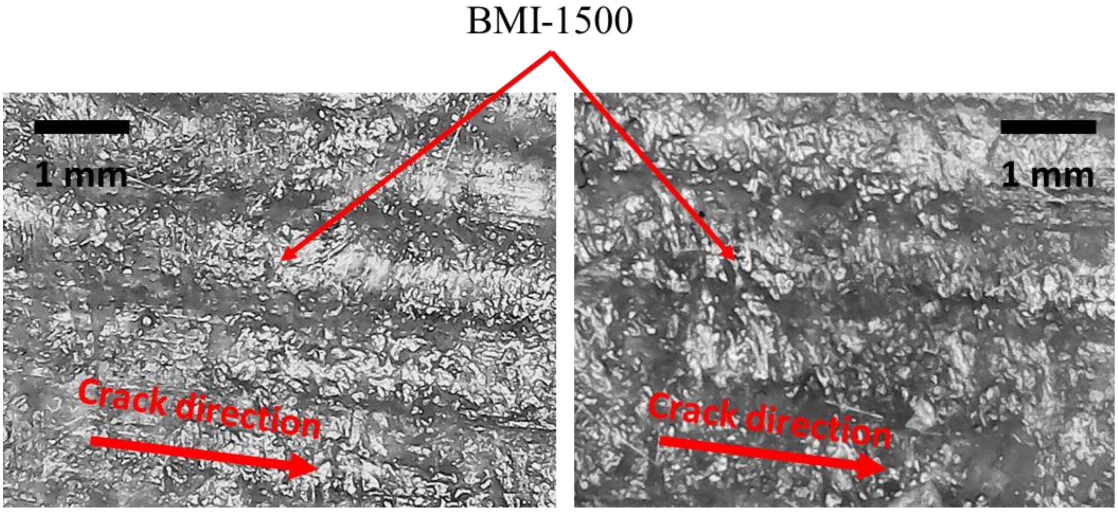

Figure 5.25 Fractured surfaces of the GFRP coupon containing BMI-1500 as interlayer

As can be seen in Figure 5.26 the fracture in the case of GFPR coupons that contained BMI-1700 interlayer occurred both adhesively and cohesively. Unlike BMI-1500, there are exposed glass fibers in both fractured surfaces, indicating a relatively weaker glass fiber/BMI-1700 interface.

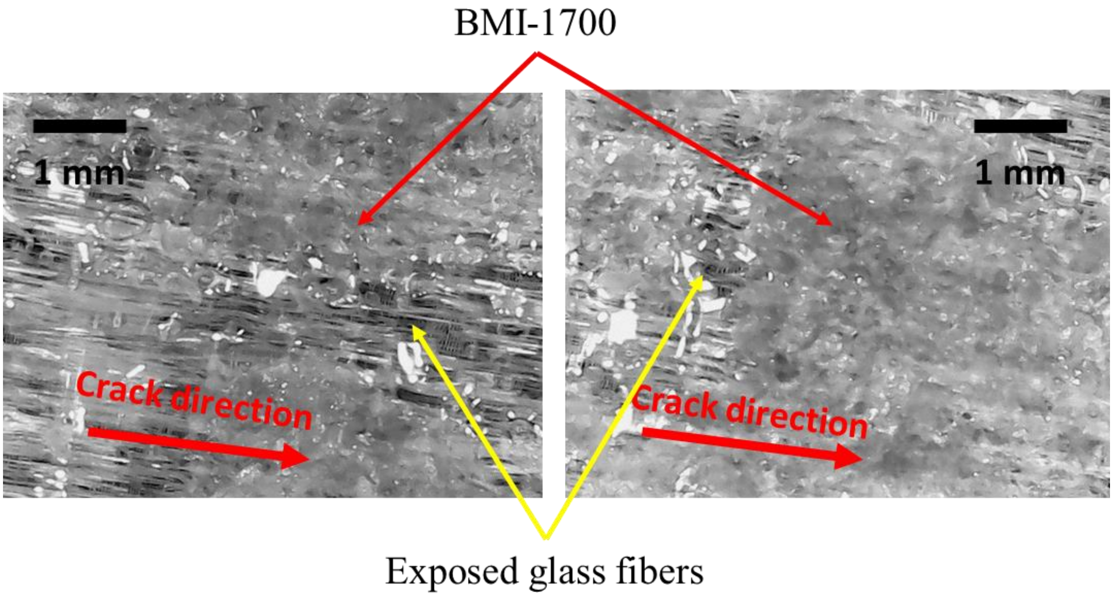

Figure 5.26 Fractured surfaces of the GFRP coupon containing BMI-1700 as interlayer

The OM photographs obtained in the case of BMI-3000 confirmed what was postulated after the mechanical characterization of the BMI-3000 GFRP coupons. As can be seen in Figure 5.27, the composite in this case failed in an adhesive manner, indicating an even weaker interface glass fibers/BMI-3000 interface. As stated, these results are in agreement with the significantly decreased fracture toughness that was observed from the mode-II fracture toughness test.

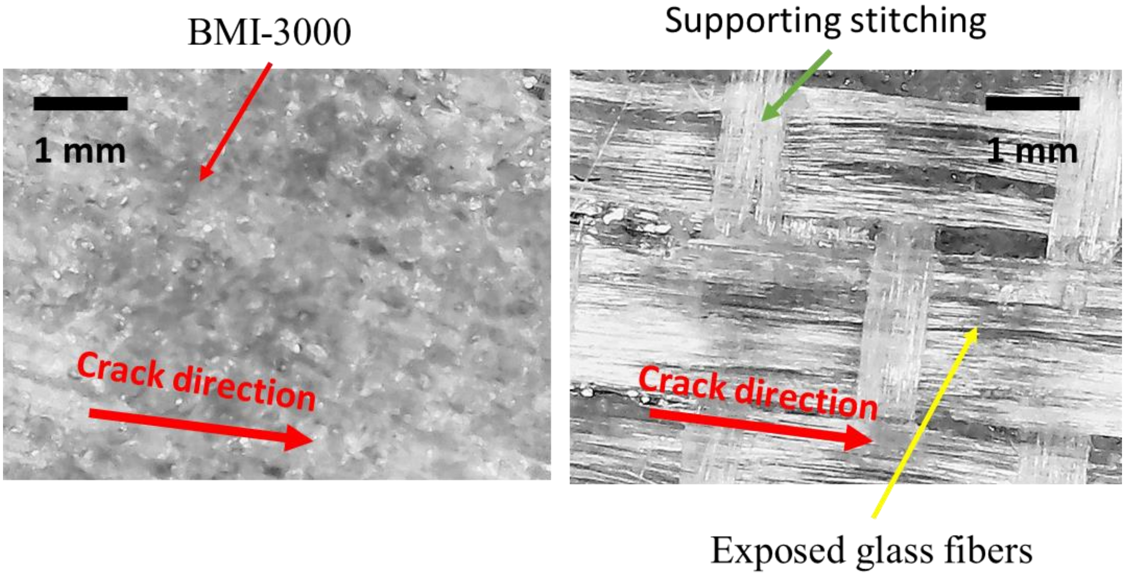

Figure 5.27 Fractured surfaces of the GFRP coupon containing BMI-3000 as interlayer

5.3.3. Lap strap specimens

5.3.2.4 Mechanical Characterization

The following figures illustrate representative stress-strain curves from the reference, virgin and healed BMI-1500, BMI-1700 and BMI-300 lap strap specimens. In all cases, the apparent stiffness was calculated using the linear part of the resulted stress-strain curve between 50 and 150 MPa. The strain level was calculated using the initial grip-to-grip distance and the stress level refers to the lap thickness. The damaged stiffness E^d was calculated during a second loading performed after delamination initiation. In almost all cases a brittle failure of the adhesive layer is evident and manifested by a small drop in the stress strain curve. However, it should be noted that in the case of BMI-3000 healed-4, failure of the adhesive layer occurred in a more ductile manner. Thus, the maximum stress was calculated at the point where the slope of the stress-strain curve changed (Figure 5.28).

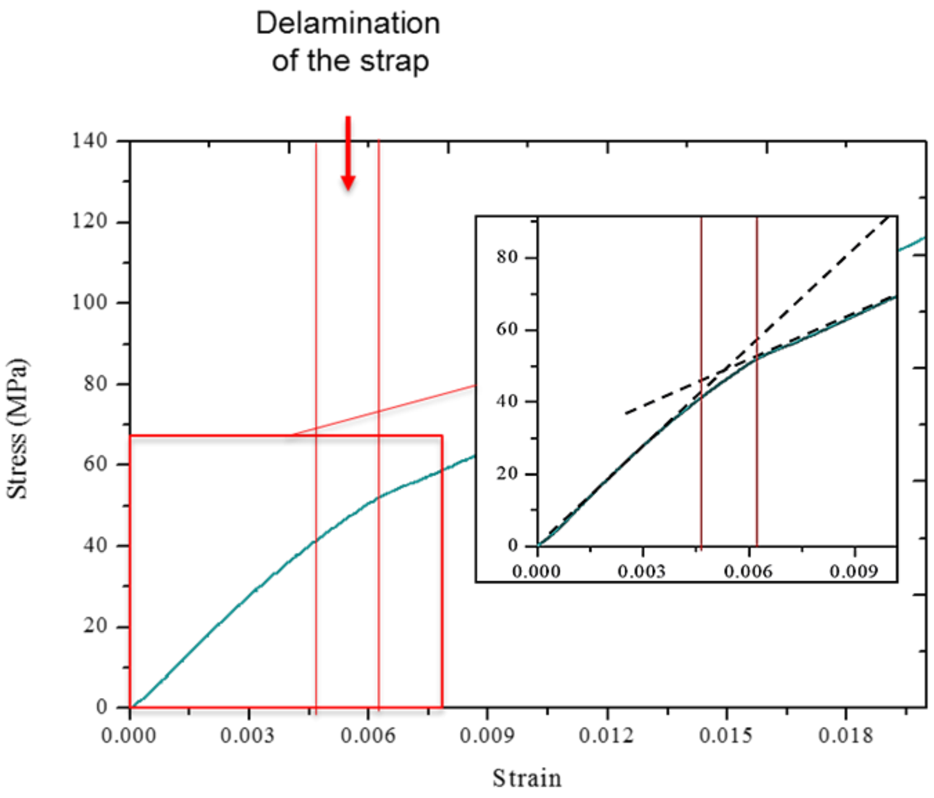

Figure 5.28 Typical stress versus strain curve for the lap-strap specimen. Failure of a ductile adhesive layer.

Figure 5.29 presents representative stress versus strain curves for the virgin and healed lap strap specimens that contain BMI-1500 as adhesive layer while Table 5-5 summarizes the calculated healing efficiency values in terms of Young's modulus and critical stress. As it can be observed, the material managed to almost fully regain its initial mechanical properties after several healing cycles. In detail, after the first healing event the healing efficiency values of the reversible adhesive layer, BMI-1500, was calculated at 97.05 % and 95.55 % in terms of Young's modulus and critical delamination stress recovery, respectively.

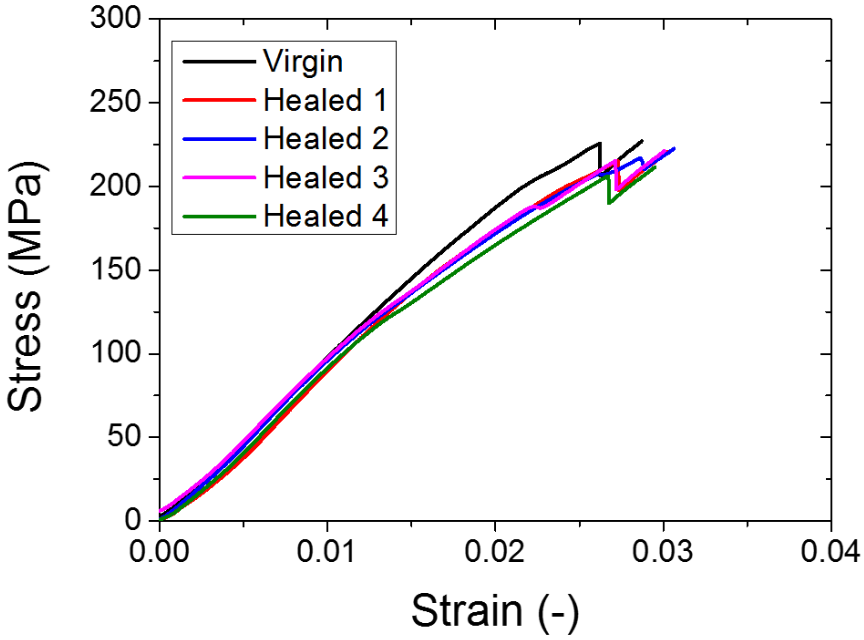

Figure 5.29 Representative stress-displacement curves for the reference, virgin and healed BMI-1500 lap strap specimens

Only a minor reduction in both the aforementioned quantities was calculated after the second and third healing event. Even after 4 healing cycles, the healing performance of the BMI-1500 was significantly high showing a recovery in Young's modulus at 92.20 % while in the case of critical delamination stress the healing efficiency reached at 91.55%.

Table 5-5 Critical stress, Young's modulus and the calculated healing efficiencies for the BMI-1500 lap strap specimens

Specimen	**E (GPa)**	**σ_{max} (MPa)**	**n_E (%)**	**n_σ (%)**
Virgin	9.75 ± 0.4	225.65 ± 22	-	-
Healed 1	9.46 ± 0.4	215.07 ± 20	97.05	95.55
Healed 2	9.45 ± 0.3	217.12 ± 18	96.91	96.40
Healed 3	9.42 ± 0.4	215.65 ± 21	96.09	95.50
Healed 4	8.99 ± 0.4	206.08 ± 20	92.20	91.55

Equally impressive with the previous case is the healing performance of the lap strap specimens incorporating BMI-1700 as adhesive. As can be seen in Figure 5.30 and Table 5-6, the healing efficiency values of the reversible polymer were n_E = 97.14% and

n_σ = 100.57% while after the fourth healing reached at 87.27 % and 122.25 %, thus demonstrating a successful recovery in performance.

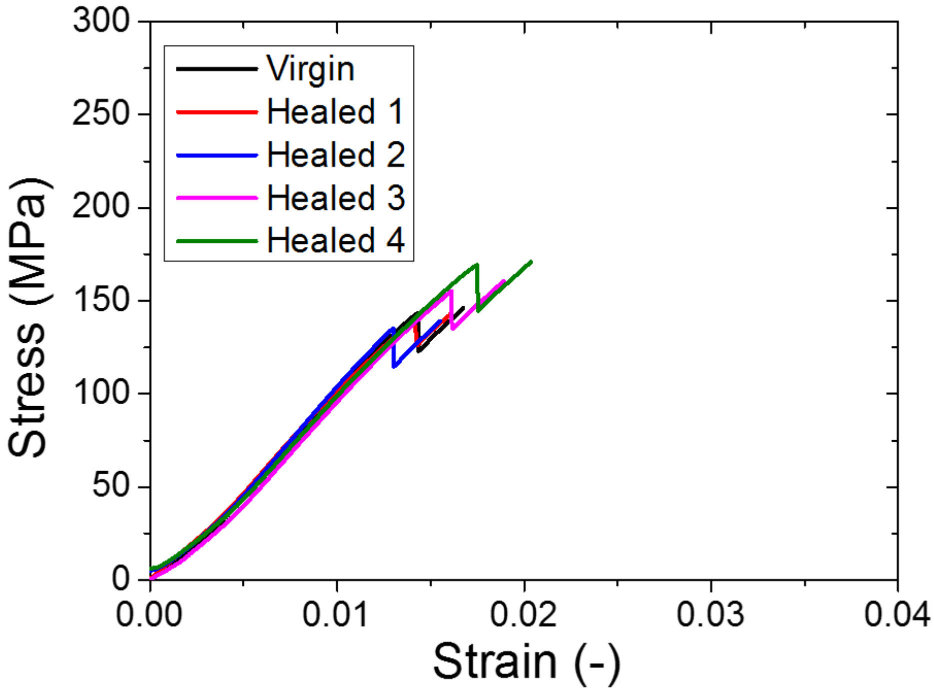

Figure 5.30 Representative stress-displacement curves for the reference, virgin and healed BMI-1700 lap strap specimens

Table 5-6 Critical stress, Young's modulus and the calculated healing efficiencies for the BMI-1700 lap strap specimens

Specimen	**E (GPa)**	**σ_{max} (MPa)**	**n_E (%)**	**n_σ (%)**
Virgin	10.14 ± 0.2	138.93 ± 15	-	-
Healed 1	9.85 ± 0.3	138.14 ± 20	97.14	100.57
Healed 2	9.59 ± 0.2	152.90 ± 17	94.57	110.79
Healed 3	9.04 ± 0.4	155.07 ± 22	89.15	112.31
Healed 4	8.85 ± 0.4	169.21 ± 21	87.27	122.25

The results from the mechanical testing of the BMI-3000 lap strap specimen are depicted in Figure 5.31, while Table 5-7 summarizes the calculated healing efficiency values n_E and n_σ. It is evident that the healing performance of the BMI-3000 is significantly high especially compared with the previous case where the same reversible polymer has been used as a matrix material and tested in a fracture toughness test.

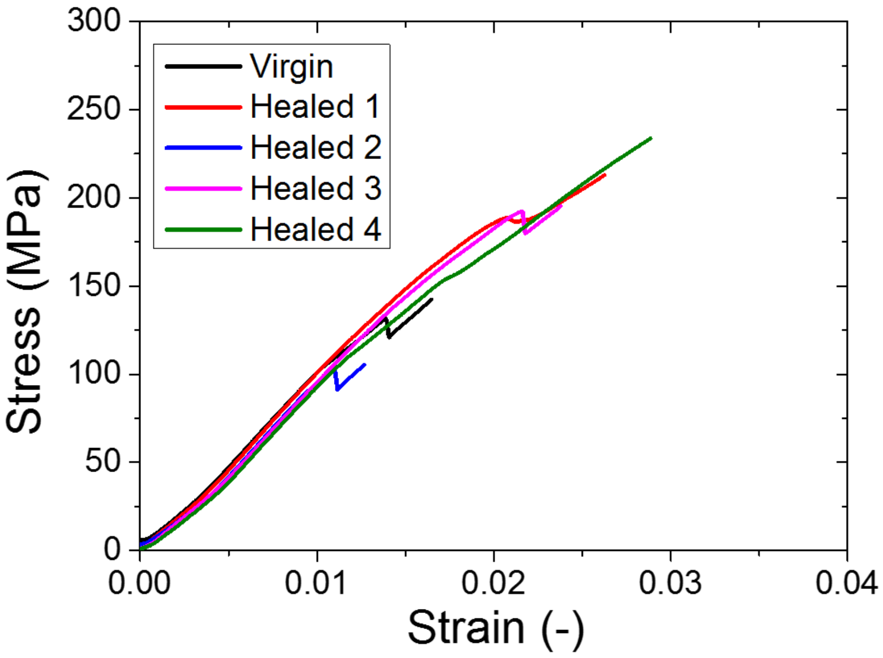

Figure 5.31 Representative stress-displacement curves for the reference, virgin and healed BMI-3000 lap strap specimens

After the initial healing, the stiffness was fully recovered and the stress level at which the delamination of the strap initiated was increased, resulting in a healing efficiency, n_σ = 143.51%. Even after four healing events the material exhibited a remarkable healing performance achieving a recovery of 86.84% and 118.32% in stiffness and critical delamination stress, respectively.

Table 5-7 Critical stress, Young's modulus and the calculated healing efficiencies for the BMI-3000 lap strap specimens

Specimen	**E (GPa)**	**σ (MPa)**	**n_E (%)**	**n_σ (%)**
Virgin	9.88 ± 0.3	131.45 ± 16	-	-
Healed 1	9.84 ± 0.4	188.60 ± 20	100.10	143.51
Healed 2	8.95 ± 0.3	102.16 ± 15	90.58	77.80
Healed 3	8.82 ± 0.3	192.36 ± 16	89.27	146.56
Healed 4	8.58 ± 0.4	155.48 ± 19	86.84	118.32

5.4. Conclusions

In this work, the successful synthesis of three reversible epoxy resins via a two-step reaction was presented. Using this methodology the side reactions occurrence during the thermal processing of the polymers was minimized. The characterization of the reversible polymers via DSC showed that the two oligomers BMI-1500 and BMI-1700 were successfully incorporated between the polymeric chains, via the Diels-Alder reaction, creating a reversible 3-D network. On the other hand, the increased molecular mass of the BMI-3000 had a detrimental effect on the creation of the reversible cross-linking. In addition, the irreversible radical polymerization of the BMI-3000 was enhanced at elevated temperature, thus compromising the healing performance of the system. The assessment of healing performance was initially achieved via a mode-II fracture toughness test. The three reversible polymers were employed as interlayers at the mid plane of GFRP coupons. The results indicated that the incorporation of BMI-1500 and BMI-1700 did not affect the fracture toughness of the system while a satisfying healing performance was also observed. However, in the case of BMI-3000 a significant knock-down effect on the fracture toughness was recorder. OM and AE revealed, that the reason behind this behavior was the weak interfacial bonding between the BMI-3000 and the glass fibers, resulting in an adhesive mode -II failure. The three reversible polymers have been also tested as adhesives in a lap strap specimen. In all cases, a remarkable stiffness and delamination stress recovery was recorded even after 4 healing events, indicating that these three reversible polymers are excellent candidates for the manufacture of composite structures with healing functionalities.

Reference

[1] C.B. Bucknall, I.C. Drinkwater, G.R. Smith, Hot plate welding of plastics: Factors affecting weld strength, Polym. Eng. Sci. 20 (1980) 432–440. doi:10.1002/pen.760200609.

[2] X. Chen, A. Dam, K. Ono, M. Ajit, H. Shen, S. Nutt, K. Sheran, F. Wudl, A Thermally Re-mendable Cross-Linked Polymeric Material, Science (80-.). 295 (2002) 1698–1702. doi:10.1126/science.1065879.

[3] S.R. White, N.R. Sottos, P.H. Geubelle, J.S. Moore, M.R. Kessler, S.R. Sriram, E.N. Brown, S. Viswanathan, Autonomic healing of polymer composites., Nature. 409 (2001) 794–7. doi:10.1038/35057232.

[4] V.B. Sundaresan, A. Morgan, M. Castellucci, Self-Healing of Ionomeric Polymers with Carbon Fibers from Medium-Velocity Impact and Resistive Heating, Smart Mater. Res. 2013 (2013) 1–12. doi:10.1155/2013/271546.

[5] J. Canadell, H. Goossens, B. Klumperman, Self-healing materials based on disulfide links, Macromolecules. 44 (2011) 2536–2541. doi:10.1021/ma2001492.

[6] Y. Xu, D. Chen, A Novel Self-Healing Polyurethane Based on Disulfide Bonds, Macromol. Chem. Phys. 217 (2016) 1191–1196. doi:10.1002/macp.201600011.

[7] V. Kostopoulos, A. Kotrotsos, S. Tsantzalis, P. Tsokanas, A.C. Christopoulos, T. Loutas, Toughening and healing of continuous fibre reinforced composites with bis-maleimide based pre-pregs, Smart Mater. Struct. 25 (2016). doi:10.1016/j.compscitech.2016.03.021.

[8] P.A. Pratama, M. Shari, A.M. Peterson, G.R. Palmese, Room Temperature Self-Healing Thermoset Based on the Diels − Alder Reaction, (2013).

[9] Y.-L. Liu, T.-W. Chuo, Self-healing polymers based on thermally reversible Diels–Alder chemistry, Polym. Chem. 4 (2013) 2194. doi:10.1039/c2py20957h.

[10] F. Herbst, D. Döhler, P. Michael, W.H. Binder, Self-healing polymers via supramolecular forces, Macromol. Rapid Commun. 34 (2013) 203–220. doi:10.1002/marc.201200675.

[11] G.M.L. Van Gemert, J.W. Peeters, S.H.M. Söntjens, H.M. Janssen, A.W. Bosman, Self-healing supramolecular polymers in action, Macromol. Chem. Phys. 213 (2012) 234–242. doi:10.1002/macp.201100559.

[12] S. Nojiri, H. Yamada, S. Kimata, K. Ikeda, T. Senda, A.W. Bosman, Supramolecular polypropylene with self-complementary hydrogen bonding system, Polym. (United Kingdom). 87 (2016) 308–315. doi:10.1016/j.polymer.2016.02.010.

[13] V. Kostopoulos, A. Kotrotsos, S. Tsantzalis, P. Tsokanas, T. Loutas, A.W. Bosman, Toughening and healing of continuous fibre reinforced composites by supramolecular polymers, Compos. Sci. Technol. 128 (2016) 84–93. doi:10.1016/j.compscitech.2016.03.021.

[14] V. Kostopoulos, Mode II fracture toughening and healing of composites using supramolecular polymer interlayers, Express Polym. Lett. 10 (2016) 914–926. doi:10.3144/expresspolymlett.2016.85.

[15] T. Kakuta, Y. Takashima, M. Nakahata, M. Otsubo, H. Yamaguchi, A. Harada, Preorganized hydrogel: self-healing properties of supramolecular hydrogels formed by polymerization of host-guest-monomers that contain cyclodextrins and hydrophobic guest groups., Adv. Mater. 25 (2013) 2849–53. doi:10.1002/adma.201205321.

[16] X. Hao, H. Liu, Y. Xie, C. Fang, H. Yang, Thermal-responsive self-healing hydrogel based on hydrophobically modified chitosan and vesicle, Colloid Polym. Sci. 291 (2013) 1749–1758. doi:10.1007/s00396-013-2910-4.

[17] U. Lafont, C. Moreno-Belle, H. van Zeijl, S. van der Zwaag, Self-healing thermally conductive adhesives, J. Intell. Mater. Syst. Struct. . 25 (2014) 67–74. doi:10.1177/1045389X13498314.

[18] N. Roy, E. Buhler, J.-M. Lehn, Double dynamic self-healing polymers: supramolecular and covalent dynamic polymers based on the bis-iminocarbohydrazide motif, Polym. Int. (2013) n/a-n/a. doi:10.1002/pi.4646.

[19] S.Y. An, S.M. Noh, J.H. Nam, J.K. Oh, Dual Sulfide – Disulfide Crosslinked Networks with Rapid and Room Temperature, Macromol. Rapid Commun. 36 (2015) 1255–1260. doi:10.1002/marc.201500123.

[20] W. Zhang, J. Duchet, J.F. Gérard, Self-healable interfaces based on thermo-reversible Diels-Alder reactions in carbon fiber reinforced composites, J. Colloid Interface Sci. 430 (2014) 61–68. doi:10.1016/j.jcis.2014.05.007.

[21] J.S. Park, T. Darlington, A.F. Starr, K. Takahashi, J. Riendeau, H. Thomas Hahn, Multiple healing effect of thermally activated self-healing composites based on Diels–Alder reaction, Compos. Sci. Technol. 70 (2010) 2154–2159. doi:10.1016/j.compscitech.2010.08.017.

[22] G. Postiglione, S. Turri, M. Levi, Effect of the plasticizer on the self-healing properties of a polymer coating based on the thermoreversible Diels-Alder reaction, Prog. Org. Coatings. 78 (2015) 526–531. doi:10.1016/j.porgcoat.2014.05.022.

[23] J. Kötteritzsch, S. Stumpf, S. Hoeppener, J. Vitz, M.D. Hager, U.S. Schubert, One-component intrinsic self-healing coatings based on reversible crosslinking by diels-alder cycloadditions, Macromol. Chem. Phys. 214 (2013) 1636–1649. doi:10.1002/macp.201200712.

[24] R. Araya-Hermosilla, a. a. Broekhuis, F. Picchioni, Reversible polymer networks containing covalent and hydrogen bonding interactions, Eur. Polym. J. 50 (2014) 127–134. doi:10.1016/j.eurpolymj.2013.10.014.

[25] J. Brancart, G. Scheltjens, T. Muselle, B. Van Mele, H. Terryn, G. Van Assche, Atomic force microscopy–based study of self-healing coatings based on reversible polymer network systems, J. Intell. Mater. Syst. Struct. . 25 (2014) 40–46. doi:10.1177/1045389X12457100.

[26] J. Ax, G. Wenz, Thermoreversible Networks by Diels-Alder Reaction of Cellulose Furoates With Bismaleimides, Macromol. Chem. Phys. 213 (2012) 182–186. doi:10.1002/macp.201100410.

[27] Y. Amamoto, H. Otsuka, A. Takahara, K. Matyjaszewski, Self-healing of covalently cross-linked polymers by reshuffling thiuram disulfide moieties in air under visible light, Adv. Mater. 24 (2012) 3975–3980. doi:10.1002/adma.201201928.

[28] C. Toncelli, D.C. De Reus, F. Picchioni, A. a. Broekhuis, Properties of Reversible Diels-Alder Furan/Maleimide Polymer Networks as Function of Crosslink Density, Macromol. Chem. Phys. 213 (2012) 157–165. doi:10.1002/macp.201100405.

[29] G. Rivero, L.T. Nguyen, X.K.D. Hillewaere, F.E. Du Prez, One-Pot Thermo-Remendable Shape Memory Polyurethanes, (2018).

[30] N. Bai, G.P. Simon, K. Saito, Investigation of the thermal self-healing mechanism in a cross-linked epoxy system, RSC Adv. 3 (2013) 20699. doi:10.1039/c3ra43746a.

[31] N. Bai, K. Saito, G.P. Simon, Synthesis of a diamine cross-linker containing Diels–Alder adducts to produce self-healing thermosetting epoxy polymer from a widely used epoxy monomer, Polym. Chem. 4 (2013) 724–730. doi:10.1039/C2PY20611K.

[32] Q. Tian, M.Z. Rong, M.Q. Zhang, Y.C. Yuan, Synthesis and characterization of epoxy with improved thermal remendability based on Diels-Alder reaction, Polym. Int. 59 (2010) 1339–1345. doi:10.1002/pi.2872.

[33] Q. Tian, Y.C. Yuan, M.Z. Rong, M.Q. Zhang, A thermally remendable epoxy resin, J. Mater. Chem. 19 (2009) 1289. doi:10.1039/b811938d.

[34] J.H. Aubert, Note: Thermally removable epoxy adhesives incorporating thermally reversible diels-alder adducts, J. Adhes. 79 (2003) 609–616. doi:10.1080/00218460309540.

[35] P.A. Pratama, A.M. Peterson, G.R. Palmese, The role of maleimide structure in the healing of furan-functionalized epoxy–amine thermosets, Polym. Chem. 4 (2013) 5000. doi:10.1039/c3py00084b.

[36] J.R. McElhanon, D.R. Wheeler, Thermally responsive dendrons and dendrimers based on reversible furan-maleimide diels-alder adducts, Org. Lett. 3 (2001) 2681–2683. doi:10.1021/ol0101281.

[37] D.H. Turkenburg, H.R. Fischer, Diels-Alder based, thermo-reversible cross-linked epoxies for use in self-healing composites, Polym. (United Kingdom). 79 (2015) 187–194. doi:10.1016/j.polymer.2015.10.031.

[38] T.S. Coope, D.H. Turkenburg, H.R. Fischer, R. Luterbacher, H. van Bracht, I.P. Bond, Novel Diels-Alder based self-healing epoxies for aerospace composites, Smart Mater. Struct. 25 (2016) 84010. doi:10.1088/0964-1726/25/8/084010.

[39] G. Socrates, Infrared and Raman characteristic group frequencies, 2004. doi:10.1002/jrs.1238.

[40] J.E. De Andrade, R. Machado, M.A. Macêdo, F.G.C. Cunha, AFM and XRD characterization of silver nanoparticles films deposited on the surface of DGEBA

epoxy resin by ion sputtering, Polímeros. 23 (2013) 19–23. doi:10.1590/S0104-14282013005000009.

[41] S.F. Parker, S.M. Mason, K.P.J. Williams, Fourier Transform Raman and infrared spectroscopy of N-phenylmaleimide and methylene dianiline bismaleimide, Spectrochim. Acta Part A Mol. Spectrosc. 46 (1990) 315–321. doi:10.1016/0584-8539(90)80100-D.

[42] D.G. Bekas, D. Baltzis, K. Tsirka, D. Exarchos, T. Matikas, A. Meristoudi, S. Pispas, A.S. Paipetis, Self-healing polymers: evaluation of self-healing process via non-destructive techniques, Plast. Rubber Compos. 45 (2016) 147–156. doi:10.1080/14658011.2016.1151987.

[43] A. Carpinteri, F. Cardone, G. Lacidogna, Energy Emissions from Failure Phenomena: Mechanical, Electromagnetic, Nuclear, Exp. Mech. 50 (2010) 1235–1243. doi:10.1007/s11340-009-9325-7.

[44] D.T.G. Katerelos, A. Paipetis, T. Loutas, G. Sotiriadis, V. Kostopoulos, S.L. Ogin, In situ damage monitoring of cross-ply laminates using acoustic emission, Plast. Rubber Compos. 38 (2009) 229–234. doi:10.1179/174328909x435348.

CHAPTER 6

Conclusions and Suggestions for Future Work

6.1. Conclusions

The current thesis lies at the intersection between damage detection (self-sensing) and damage repair (self-healing) in polymer composites. In the first part, a novel method has been developed for the structural integrity of nanomodified fibre reinforced composites using Impedance Spectroscopy (IS). The electrical properties of the interrogated system were tailored via the incorporation of MWCNTs, resulting in an increased signal-to-noise ratio. IS results indicated a direct correlation between the degradation of the material and the measure of the impedance, which proved extremely sensitive to the changes invoked in the material microstructure due to mechanical loading or hydrothermal exposure. As was shown, the electrical behavior of the system may be adequately modelled by simulating it as a simple RC circuit in parallel. Under this assumption, the resistance of the equivalent circuit was monotonically increasing due to the disruption of the conductive CNT network in the material. At the same time, the total capacitance of the material was decreased as the developed cracks at the nanoscale cumulatively affect the macroscopic capacitance of the material.

This step was essential in order to gain insight on the damage mechanisms that initiate and propagate within a composite material during its operating lifetime. The internal degradation of the material was counterbalanced by the development of several “tailor-on-demand” self-repairing scenarios that were capable of restoring specific functionalities of the composite.

In detail, in Chapter 3, the employment of a MWCNT-reinforced low-viscosity epoxy as a healing agent in vascular self-healing GRFP composites, was evaluated for the first time. The modification of the healing agent resulted in a remarkable healing performance, without compromising the rheological behavior of the system. SEM analysis revealed that the nano-reinforced healing agents enabled additional energy consumption mechanisms (e.g., crack bifurcation). The observed transition from adhesive to cohesive failure, indicated an enhancement of the adhesive strength between the nanomodified healing agents and the virgin fractured surface due to the beneficiary effect of MWCNTs on the epoxy/sizing coating of fibers interfacial strength.

The synthesis, characterization and evaluation of poly(urea-formaldehyde) microcapsules have been reported in Chapter 4. The developed capsule-based self-healing polymer was able to restore its initial fracture toughness at 72% while in the case of GFRP specimens, the healing efficiency was almost the same reaching at 77.84%. However, the incorporation of capsules at the midplane of a GFRP composite had a detrimental effect on the fracture toughness, thus showing that the employment of capsule-based methodologies remains a challenge. Finally, for the first time it has been proved that the modification of a polymeric adhesive using UF microcapsules, could be a reliable route towards up-scaling the employment of capsule-based self-healing methodologies to more complicated composite structures.

In the final main Chapter of this thesis, a novel study concerning the effects of three different thermo-reversible cross-linking agents on the thermal and mechanical properties of the resulted self-healing epoxy systems was conducted. The results derived from the DSC, showed that the two oligomers BMI-1500 and BMI-1700 were the most suitable candidates that can be successfully incorporated between the polymeric chains, via the Diels-Alder reaction, creating a reversible 3-D network. Regarding the healing performance, all the investigated reversible systems showed their remarkable ability to fully heal a delaminated lap strap geometry. It has been found that the fracture toughness and the healing temperature of the DA-based self-healing systems are inversely proportional quantities and are highly affected by the molecular weight of the crosslinker.

6.2. Suggestions for Future Work

Within the scope of this study, IS proved a highly efficient NDE method and produced impressive results. However, the experimental set up required access on both sides of the composite structure. The employment of interdigital sensors will be a reliable route towards the development of NDE system, based on IS, that will not require access to both sides of an aerospace composite structure. Compared with the full field sensors, interdigital sensors provide increased resolution and can be placed at critical areas of a composite structure. In addition, localization of a possible defect can be achieved by advancing from a 1D problem to a 2D one using Electrical Impedance Tomography (EIT). EIT is a well-established electrical-based method for characterizing processes in polymers and could be also employed for the quantification and localization of defects in advanced composite materials.

Regarding the self-healing concepts, the current thesis pushed the boundaries of our knowledge regarding the self-healing polymers and polymer composites. However, there are several issues that should be addressed before the self-healing concept can be adopted as a trustworthy technology in order to conform to the standardization demands of the aerospace industry. Further progress should be made towards the development of a fully autonomous self-healing system. For that purpose, efforts should be focused on novel healing chemistries that possess greater stability, increased reactivity, and faster kinetics. Another important issue that should be countered is the incorporation of the self-healing concepts on advanced composite structures without compromising their performance. Especially in the case of vascular self-healing composites, the creation of the vascular network usually decreases the composite performance. Therefore, efforts should be targeted on optimizing (i) the tube diameter, (ii) the processing conditions, (iii) the chemistry of the healing agent and (iv) the healing agent delivery mechanisms to the damaged site. Characterization of self-healing materials through various experimental techniques is naturally following the material production step. This study could provide useful information about the healing process and assist on the optimization of the healing conditions. More specifically, studying the reaction kinetics of the Diels-Alder reaction is of high importance since the healing conditions affect both the performance and the repeatability of the healing process. In addition, advanced characterization techniques such as Raman and Impedance spectroscopies could assess the healing process and provide an indirect measure of the healing efficiency of the system by measuring how the measured quantity deviates from the initial value.

CHAPTER 7

Publications and Curriculum Vitae

7.1. Publications in peer-reviewed journals

7.1.1. Published

1. D. Baltzis, **D.G. Bekas**, G. Tzachristas, A. Parlamas, M. Kabosi, N. Zafeiropoulos A. S. Paipetis, Hybrid multiphase reinforcement in epoxy composite materials: Dispersion and Electrical Impedance study, Composites Science and Technology, 157, 7-17, 2017
2. **D. G. Bekas**, D. Baltzis and A.S. Paipetis, Nano-reinforced polymeric healing agents for vascular self-repairing composites, Materials & Design, 116, 538–544, 2017
3. **D. G. Bekas**, G. Gkikas, G. M. Maistros, A. S. Paipetis, On the use of dielectric spectroscopy for the real-time assessment of the dispersion of carbon nanotubes in epoxy, RSC Advances, 6, 78838-78845, 2016
4. **D. G. Bekas**, A.S. Paipetis, Damage monitoring in nanoenhanced composites using impedance spectroscopy, Composites Science and Technology, 134, 96-105, 2016
5. **D. G. Bekas**, D. Baltzis, K. Tsirka, D. Exarchos, T. Matikas, A. Meristoudi, S. Pispas, A. S. Paipetis, Self-healing polymers: evaluation of self-healing process via non-destructive techniques, Plastics, Rubber and Composites: Macromolecular Engineering, 10, 147-156, 2016
6. **D. G. Bekas**, K. Tsirka, D. Baltzis, A.S. Paipetis, Self-healing materials: A review of advances in materials, evaluation, characterization and monitoring techniques, Composites Part B: Engineering, 87, 92-119, 2016
7. **D. G. Bekas**, A. S. Paipetis, Study of the Effect of Damage on the Electrical Impedance of Carbon Nanotube Reinforced Epoxy Nanocomposites, Journal of Sensors, 2015, 805303, 2015

7.1.2. Under revision

1. Carlos G. Berrocal, Karla Hornbostel, Mette. R. Geiker, Ingemar Löfgren, Karin Lundgren, **D. G. Bekas**, Electrical resistivity measurements in steel fibre reinforced cementitious materials, Cement and Concrete Composites, 2017

6.1.3. Articles in preparation

1. **D.G Bekas**, K. Tsirka, C. Gioti, M. Karabela, N. Zafeiropoulos, D. Papagiannis, A. W. Bosman A.S. Paipetis, Monitoring Healing Processes in supramolecular elastomer using Raman Spectroscopy
2. M. Kosarli, **D.G. Bekas**, D Baltzis, AS Paipetis, The effect of capsule size on the healing efficiency in extrinsic polymeric material
3. RR Alonso, **DG Bekas**, M Kosarli, AS Paipetis, SF Fernandez, A novel encapsulation process towards the development of PMMA capsules for self-healing applications
4. D. Vaimakis- Tsogkas, **D.G. Bekas**, A. S. Paipetis, N.- M. Barkoula, The effect of TiO_2 in thermal, mechanical, dielectric and photocatalytic properties on PDMS composites
5. X. Tsilimiga, **D. Bekas**, M. Kosarli, T. Loutas, A.S. Paipetis, V. Kostopoulos, Mechanical properties assessment of low-content capsule-based self-healing structural composites

6.1.4. Selected papers in peer-reviewed conference proceedings

1. **D.G. Bekas** and A.S. Paipetis, Impedance spectroscopy as an NDE technique for composite materials and structures, in proceedings of the 17th International Conference on Experimental Mechanics – ICEM 17, Greece, 2016
2. **D.G. Bekas**, K. Tsirka, D. Baltzis, A.S. Paipetis, Real time monitoring and evaluation of the self-healing process via the employment of Non-destructive evaluation techniques in proceedings of the 4th International Conference of Engineering Against Failure (ICEAF IV), Greece, 2015
3. **D.G. Bekas**, V. Melios, A.S. Paipetis, Impedance spectroscopy as a method to characterize damage initiation and progression in glass fiber reinforced polymers in proceedings of the 4th International Conference of Engineering Against Failure (ICEAF IV), Greece, 2015
4. **D.G. Bekas**, S.A. Grammatikos, C. Kouimtzi, A.S. Paipetis, Linear and non-linear electrical dependency of carbon nanotube reinforced composites to internal damage, IOP Conf. Ser. Mater. Sci. Eng. 74 (2015) 012002, 2015

5. **D.G. Bekas**, C. Couimtzi, A. Bousis, A.S. Paipetis, Electrical damage assessment of nanocomposites: DC & AC study in proceedings of the 22nd Annual International Conference on composites/nanoengineering-ICCE 22, Malta, 2014
6. G. Gkikas, **D.G. Bekas**, A.S. Paipetis, The reinforcement effect of carbon nanotubes in the interlaminar fracture toughness of a typical CFRP system under hydrothermal exposure in proceedings of the 22nd Annual International Conference on composites/nanoengineering-ICCE 22, Malta, 2014
7. **D.G. Bekas**, A.S. Paipetis, Hysteretic behavior of CNT reinforce composite under the effect of several levels of damage in proceedings of the 11th International Conference in Durability Analysis of Composite Systems-DURACOSYS, Japan, 2014
8. **D.G. Bekas**, A.S. Paipetis, Nonlinear electrical Behavior for Damage Analysis in Carbon Nanotube Reinforced Composite Materials in proceedings of the 5th International Conference on Structural Analysis of Advanced Materials- ICSAAM, Greece, 2013